UNIL | Université de Lausanne

Unicentre
CH-1015 Lausanne
http://serval.unil.ch

Year : 2017

The Origin of Terrestrial Carbonate Formations (Far North Cameroon, Chad Basin). Tracking Earth's Memories

Diaz Nathalie

Diaz Nathalie, 2017, The Origin of Terrestrial Carbonate Formations (Far North Cameroon, Chad Basin). Tracking Earth's Memories

Originally published at : Thesis, University of Lausanne

Posted at the University of Lausanne Open Archive http://serval.unil.ch
Document URN : urn:nbn:ch:serval-BIB_112C57E99A7C4

Droits d'auteur
L'Université de Lausanne attire expressément l'attention des utilisateurs sur le fait que tous les documents publiés dans l'Archive SERVAL sont protégés par le droit d'auteur, conformément à la loi fédérale sur le droit d'auteur et les droits voisins (LDA). A ce titre, il est indispensable d'obtenir le consentement préalable de l'auteur et/ou de l'éditeur avant toute utilisation d'une oeuvre ou d'une partie d'une oeuvre ne relevant pas d'une utilisation à des fins personnelles au sens de la LDA (art. 19, al. 1 lettre a). A défaut, tout contrevenant s'expose aux sanctions prévues par cette loi. Nous déclinons toute responsabilité en la matière.

Copyright
The University of Lausanne expressly draws the attention of users to the fact that all documents published in the SERVAL Archive are protected by copyright in accordance with federal law on copyright and similar rights (LDA). Accordingly it is indispensable to obtain prior consent from the author and/or publisher before any use of a work or part of a work for purposes other than personal use within the meaning of LDA (art. 19, para. 1 letter a). Failure to do so will expose offenders to the sanctions laid down by this law. We accept no liability in this respect.

The Origin of Terrestrial Carbonate Formations (Far North Cameroon, Chad Basin)

Tracking Earth's Memories

Faculté des Géosciences et de l'Environnement
Institut des Dynamiques de la Surface Terrestre
Mention Sciences de la Terre

Thèse de doctorat

présentée à la Faculté des Géosciences et de l'Environnement de l'Université de Lausanne
par

Nathalie Diaz

diplômée en MSc Biogéosciences, Lausanne

UNIL | Université de Lausanne

Jury

Directeur de thèse, Professeur Eric P. Verrecchia
Co-directeur de thèse, Docteur David Sebag
Expert externe, Docteur Pierre Deschamps
Expert externe, Docteur Georgina King
Expert externe, Professeur Alain Durand
Expert externe, Docteur Brian Chase

Sous la présidence du Professeur René Véron
Lausanne, UNIL, 2017

UNIL | Université de Lausanne
Décanat Géosciences et de l'Environnement
bâtiment Géopolis
CH-1015 Lausanne

IMPRIMATUR

Vu le rapport présenté par le jury d'examen, composé de

Président de la séance publique :	M. le Professeur Suren Erkman
Président du colloque :	M. le Professeur Suren Erkman
Directeur de thèse :	M. le Professeur Eric Verrecchia
Expert externe:	M. le Docteur David Sebag
Expert externe :	M. le Professeur Alain Durand
Expert externe:	M. le Docteur Pierre Deschamps
Expert externe :	M. le Docteur Brian Chase
Experte externe :	Mme la Docteure Georgina King

Le Doyen de la Faculté des géosciences et de l'environnement autorise l'impression de la thèse de

Madame Nathalie DIAZ

Titulaire d'une
Maîtrise ès Sciences en biogéosciences
de l'Université de Lausanne

intitulée

The Origin of Terrestrial Carbonate Formations (Far North Cameroon, Chad Basin) Tracking Earth's Memories

Lausanne, le 2 juin 2017

Pour le Doyen de la Faculté des géosciences et de l'environnement

Professeur Suren Erkman

La Science, mon garçon, est faite d'erreurs,
mais d'erreurs qu'il est bon de commettre,
car elles mènent peu à peu à la Vérité.
— 1864, Jules Verne,
Voyage au Centre de la Terre

To my family and my friends.

Acknowledgements

First, thanks to the persons who guided me during the last years with kindness and trust: my supervisors Eric and David, today my friends, I owe you so much. Thank you Prof. Ngounou Ngatcha for your welcome in Cameroon, for your guidance into the field and for having made this history begin. Thanks also to your group, we were more than welcome at the University of Ngaoundéré. Special thanks go to Simon, it was a pleasure to share your home in Ngaoundéré. Thank you Guillaume for your help in the field and your early support. Thank you Frédéric for your support and your kind words always said in crucial times, they counted a lot for me. Thanks to your group, kind of group of adoption, you ICE people were so kind that I sincerely felt part of you, I could have change of topic! Thanks Pierre for having followed me in my OSL adventure and for being my friend. You are my partner and we led this quest together, all the moments, discussions were precious, you were a perfect friend, thank you Fabienne. I would like to thank my group, you guys are the best, always there to make me smile again, I'll miss you a lot, Magma, Mike, Fina, Stéphanie and Pascal! And the former ones, Laurent, Gladys, Loraine, Olivier. Thank you John for everything. Life at UNIL would have been sad without you, S'T'Equipe of Donkeys, thanks to all of you for who you are, Gab, MG, Sté, Alexis, Papito, Elfie, Benji, Ignes, Momo, Borel, VV, Nadja, Leanne, Andrea, Gustavo, Mathieu, Gelare, Inigo, Nia, Iniaki, Ehsan, Hosna, Antoine, Lionel, Zoneibe, Renske, Marteen, Nico, Natan, Aline, Carmen, Christelle, Juila, Myriam, Naomis, Sassi, Nic, Erika... Thanks also to the ACIGE, it was a pleasure to be part of the commitee. Special thanks go to Femi who finished his PhD one week before me, you pulled me forward! Thanks to all others who were present during my life at UNIL, for coffees, beers at Zelig (thanks to Zelig!), Mélina, Anne-Cécile, Evelyne, Guillaume, Tanya, Nico, Goran, Lukas, Jean-Luc, Othmar, Martin... Thanks also to all IDYST people making the institute live. Thanks to all the persons who helped me during my lab work, you are essential during the way, Laetitia and Micaela, Benita, Laurent, Thierry, Jean-Claude. Thanks to Pierre for the SEM supervision but most of all for your friendship. Thanks to the students who helped me in the lab, Yohan, Marie-Jo, Loïc. Thanks to my family, my parents, Edith and Emilio, and my little sister Caroline, for their support and for never letting me go down! You are my piliars. Thanks to the McCarthy's family, Anders, Anna-Lena and Tom, Thomas, Caroline and Chloe, for their kindness and unfaded curiosity concerning my work. Thanks to my friends who remind me that life exists outside the UNIL! Marine, Joe, Nicky, Nathy, Jacky, Oli and co. Special thanks go to my cousin, friend and heart's sister, Stéphanie, always there for me, and for having chosen me as godmother for your son, Ryan. Thanks also to my pirates, Ines, Joelle, Pascale, Mél. Thanks to my Capoeira family, my mind is serene thanks to you, special thanks go to my forever guide, Mestre Papa. Thanks to my experts, Alain, for his great knowledge on the evolution of palaeoenvironments in West Africa, Brian, for his expertise on palaeoclimatology, Pierre, for the wonderful discussions and his geochemical approach, George, for her critical mind, her expertise in luminescence dating and her friendship, and Suren for his precious time.

Lausanne, 18 Mai 2017 N. D.

Abstract

Terrestrial carbonate formations have been observed along the Sudano-Sahelian belt. They occur in silicate watersheds, in calcium-poor and acidic settings, raising questions upon the mechanisms behind these calcium- and carbonate-rich accumulations. The investigated study site is located in Far North Cameroon, along the Mayo Tsanaga watershed. Carbonate nodules accumulate at the surface, and are associated with clay-rich pediments, having mound morphologies within stream networks. The questions addressed in this study are related to the origin of such formations and aim to give new clues upon: (i) their pedo-sedimentary nature, (ii) the processes of formation and the palaeoenvironment, and (iii) their age. Carbonate nodules are pedogenic in origin and associated with soils in disequilibrium with present-day conditions. Their properties are close to Vertisols and were thus termed Vertisol relics. Their various geomorphologic al settings show the role of erosion in their genesis. Present-day Vertisols are observed downstream in waterlogged areas. Vertisol areas were thus proposed to have been extended, parallel to waterlogged areas, during a past wetter climatic period, possibly the African Humid Period (AHP, 14.8 ka to 5.5 ka). The end of the AHP, accompanied by the increase of aridity, would have triggered the erosion of the landscape. Pedogenic carbonate nodule petrography and geochemistry revealed that they should have formed in soils affected by water-table fluctuations, at a time where an open forest was present and where hydric conditions were becoming drier. A parallel study showed that the calcium (Ca) from the nodules is mainly local, and was thus probably accumulated in the ecosystem before being transferred in the nodules. To precipitate, calcitic carbonate nodules need alkaline conditions. The discovery of oxalate crystals within the nodules showed that the engine of alkalinity could have been the Oxalate-Carbonate Pathway (OCP). This system links producer (vegetation, fungi) and consumers of oxalate (bacteria), leading to the alkalinisation of the surrounding environment, through oxalate oxidation. Consequently, Ca would have been weathered from the saprolite and further accumulated in the wet forest-soil ecosystem. Since the environmental conditions became drier, the vegetation decreased, freeing elements and oxalate, activating the OCP and leading to carbonate nodule precipitation. The chronological framework was time constrained and validated using multi-dating tools. It was showed that (i) the soil parent material deposited during a drier period, from 18 ka to 12 ka; (ii) the pedogenesis in a wet and forested environment occurred during the main humid period, from 11 to 8 ka cal BP, (iii) the carbonate precipitated from 7 to 5 ka cal BP, when climate was shifting toward drier conditions, and finally, (iv) the erosion should be post-carbonate formation, i.e. after 5 ka cal BP. Consequently, water balance changes linked to the monsoon system front migration during the Late Quaternary, controlled the pedo-sedimentary processes involved in Vertisol relics formation. Terrestrial carbonate formations are thus precious archives.

Résumé

Des formations carbonatées ont été observées le long de la zone Soudano-Sahélienne. Ces formations riches en calcium et carbonatées se trouvent paradoxalement dans des bassins versants silicatés, pauvres en calcium et en contexte acide. Se pose donc la question de savoir quels sont les mécanismes génétiques menant à ces formations carbonatées. Un site d'étude localisé dans l'Extrême Nord du Cameroun, dans le bassin versant du Mayo Tsanaga, a été étudié pour amener des éléments de réponse. Dans les zones en érosion, des nodules carbonatés sont accumulés à la surface de sols riches en argiles ayant des morphologies en dôme. Les questions abordées dans ce travail concernent l'origine de ces formations carbonatées et ont pour but d'étudier : (i) leur nature pédo-sédimentaire, (ii) les processus de formation et leur paléo-environnement, et (iii) leur âge. Les nodules carbonatés sont pédogéniques et associés à des sols en déséquilibre avec les conditions actuelles. Les propriétés de ces sols sont proches des Vertisols et peuvent donc être définis comme des reliques de Vertisols. Des Vertisols actuels peuvent être observés en aval des reliques de Vertisols dans des zones inondées. Il a donc été proposés que, durant une période plus humide, potentiellement la Période Humide Africaine (PHA, 14.8 ka to 5.5 ka), les zones à Vertisols étaient plus étendues, et ce, en concomitance avec les zones inondées. L'érosion du paysage serait liée à l'assèchement des conditions à la fin de la PHA. La pétrographie et la géochimie des nodules ont montré que, lorsque ils se sont formés, une forêt ouverte était présente, que les sols étaient soumis à des battements de nappe, et que les conditions hydriques étaient en train de s'assécher. Une autre étude a aussi montré que le calcium (Ca) était local et qu'il avait dû être accumulé dans l'écosystème avant d'être transféré dans les nodules carbonatés. Pour précipiter, les nodules carbonatés calciques doivent être en conditions alcalines. L'observation de cristaux d'oxalates dans les nodules suggère que la voie oxalate-carbonate pourrait être impliquée. Ce système lie des producteurs (végétaux, champignons) et des consommateurs (bactéries) d'oxalate, dont l'oxydation mène à l'alcalinisation du milieu. Ainsi, le Ca aurait été libéré de la saprolite et accumulé dans le système humide sol-végétation. Suite à l'asséchement des conditions, la végétation aurait décru, menant à la libération des éléments et de l'oxalate, activant la voie oxalate-carbonate et menant à la précipitation des nodules carbonatés. Cette chronologie a été validée avec différentes méthodes de datation. Il a été montré que (i) le matériel parental des sols s'est déposé pendant une période sèche entre 18 ka to 12 ka, (ii) la formation des sols en zones humide et arborée s'est faite pendant la période humide africaine entre 11 to 8 ka cal BP, (iii) les nodules carbonatés ont précipités à un moment où les conditions s'assèchaient, entre 7 to 5 ka cal BP, et finalement, (iv) l'érosion a dû avoir lieu après cet épisode carbonaté, soit après 5 ka cal BP. Des changements hydriques liés à la dynamique de la mousson pendant le Quaternaire récent seraient à l'origine de la succession des processus pédo-sédimentaires menant à la genèse des reliques de Vertisols. Les formations carbonatées terrestres sont donc de précieuses archives.

Contents

List of Figures

List of Tables

General Introduction Part I

1 State of the Art

This section gives an overview of the vast world of terrestrial carbonates and their importance in biogeochemical cycles. Terrestrial carbonate formations from the Sudano-Sahelian belt are then presented and their scientific challenges are addressed, according to the questions raised in this study. Finally, a description of the general setting of Far North Cameroon is given in the second part of this chapter.

1.1 What are terrestrial carbonates?

Terrestrial carbonates are continental carbonates forming in terrestrial environments without any marine influence (i.e. non-marine carbonates). They form in the vadose zone, i.e. the unsaturated zone, and are distinguished from aquatic carbonates, which are also continental carbonates, but formed in the saturated zone, such as lacustrine limestones or travertines (Flügel, 2004). Continental carbonates seem to have developed mainly since the Devonian, when vascular plants with root systemes started to colonise continental environments. Low pH levels, induced by the presence of organic and carbonic acids produced by root systems, led to an increase of weathering, and resulted in the release of elements in their ionic forms (Alonso-Zarza and Tanner, 2010; Brasier, 2011). Many depositional environments have been described and they are reviewed in Figure 1.1. When excluding reworking processes, the domain of surficial terrestrial carbonates mainly concerns the pedogenic carbonates, i.e. carbonates formed in the soils, and palustrine carbonates, i.e. carbonates formed in swamps or wetlands.

1.2 Relevance for the study of terrestrial carbonates

1.2.1 Terrestrial carbonates as palaeoenvironmental archives

Terrestrial carbonates are sediments deposited in terrestrial environments (Fig. 1.1). These environments are characterized by specific biological, chemical and physical settings, which influence the nature of the terrestrial carbonate. Consequently, the aim, when studying terrestrial carbonates, is to track the natural characteristics and to relate them to a depositional environment. In order to collect the information trapped in the carbonate properties, tools belonging to petrography (e.g facies study) and geochemistry (e.g isotopic and elemental compositions) are usually applied. Nevertheless, the identification of the natural characteristics, then used in the reconstruction of the depositional

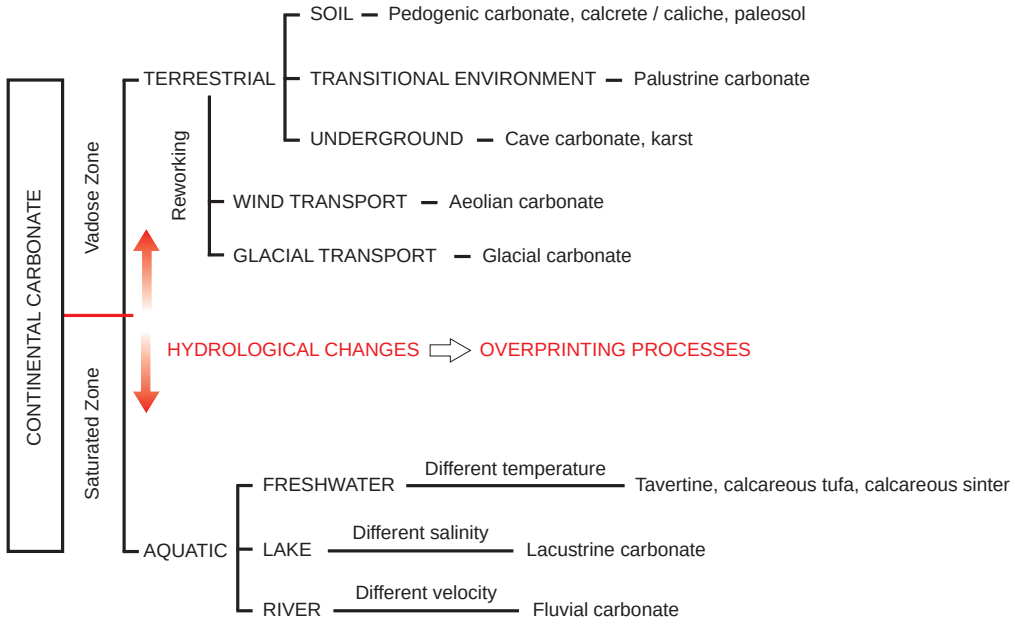

Figure 1.1 – Classification of continental carbonates in different depositional environments. Aquatic carbonates are found in water-saturated conditions and terrestrial carbonates in the vadose zone, i.e. unsaturated. Fast hydric changes can lead to overprinting processes (Freytet and Verrecchia, 1989; Flügel, 2004).

environment, remains challenging. First, properties, both physical and geochemical, can be modified since deposition, e.g. by diagenesis (Budd et al., 2002; Tanner, 2010). However, a common tool used to identify diagenetic imprint in carbonate rocks is cathodoluminescence (CL). This method uses the fact that trace elements, mainly manganese (Mn^{2+}) and iron (Fe^{2+}), induce cement zoning when included in minerals (Machel, 2000). Moreover, compared to marine settings, which are evolving slowly in terms of hydrological changes, continental settings can vary very quickly, inducing numerous variations. For example, according to hydrological changes, a palustrine depositional environment can evolve toward a lacustrine or a pedogenic environment. Resulting carbonate will be then characterized by lacustrine and pedogenic processes, which are overprinting palustrine processes (Fig. 1.1, Freytet and Verrecchia, 1989). However, knowing these limits, terrestrial carbonates have already proved their high value as palaeoclimatic proxies (Tanner, 2010), and are thus valuable terrestrial palaeoenvironmental archives.

Zamanian et al. (2016) recently reviewed pedogenic carbonate characteristics. Their morphologies are numerous and can be related to the surrounding environment in which they were precipitated, e.g. rhizoliths to root systems, biospheroliths to earthworms, or coatings to water-table fluctuations. However, some other morphologies cannot be directly related to a precise environment, such as laminar cements, cemented soil horizons, or nodular morphologies. Pedogenic carbonate precipitations as nodules are the most common form observed in many types of soils, but their formation processes are still unclear (Zamanian et al., 2016). The geochemistry of pedogenic carbonates, particularly stable carbon ($\delta^{13}C$) and oxygen ($\delta^{18}O$) isotopic compositions, can be used to trace the origin of carbon and oxygen, respectively (Fig. 1.2). In vadose environments, the $CO_{2(g)}$ content in the soil is mainly governed by the biological activity (i.e. soil respiration) and the diffusion processes leading to the mixing of atmospheric $CO_{2(g)}$ and respired $CO_{2(g)}$. Consequently, the precipitation of pedogenic carbonate from a soil solution ($HCO^{-}_{3(aq)}$) is considered to be in equilibrium with the soil $CO_{2(g)}$ (Cerling et al., 1989; Cerling and Wang, 1996; Deutz et al., 2001; Hasinger et al., 2015). It is thus possible to predict

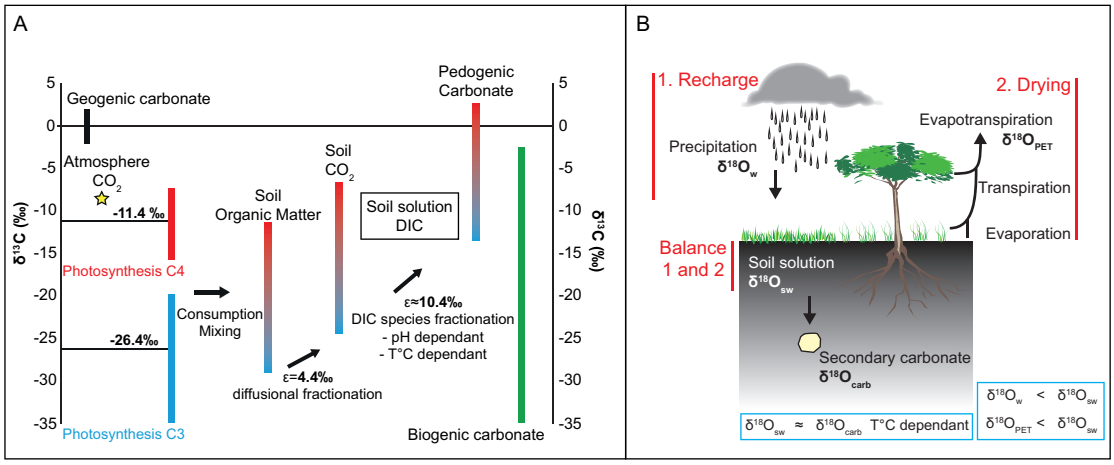

Figure 1.2 – Stable carbon (A) and oxygen (B) isotopic composition of soil carbonates. Stable C isotopic composition of pedogenic carbonate is in equilibrium with the C isotopic composition of the soil CO_2, which represents a mixing phase of CO_2 coming from the atmosphere and from the soil respiration. When the proportion coming from the respiration is dominant, the vegetation type can be assessed as there is a relationship between the soil CO_2 and the composition of the soil organic matter (modified after Zamanian et al., 2016). Stable O isotopic composition of soil carbonates reflects the O isotopic composition of water input (rain, water-table), intensity of the outputs (i.e. evapotranspiration), and the temperature at which the carbonate forms (Cerling and Quade, 1993; Hsieh et al., 1998).

the $\delta^{13}C$ of soil organic matter (SOM), soil $CO_{2(g)}$, dissolved inorganic carbon (DIC), and pedogenic carbonate, for given pH-T°C conditions (Clark and Fritz, 1997). Theoretically, there is a fractionation between the SOM $\delta^{13}C$ and the soil $CO_{2(g)}$ $\delta^{13}C$ of 4.4‰ (e.g. Cerling et al., 1991; Aravena et al., 1992). When water is infiltrating the soil (i.e. soil solution), the $CO_{2(g)}$ can be hydrated ($CO_{2(aq)}$) and quickly dissociated into bicarbonates ($HCO^-_{3(aq)}$) and carbonates ($CO^{2-}_{3(aq)}$) anions, whose concentrations are pH dependant. These processes are marked by different isotopic fractionation factors ($\varepsilon^{13}C$), which are temperature dependant. At 25°C, the $\varepsilon^{13}C$ from the $CO_{2(g)}$ to the $HCO^-_{3(aq)}$ is 7.9‰ and from the $HCO^-_{3(aq)}$ to the $CaCO_{3(s)}$ it is 2.4‰ (Clark and Fritz, 1997). Consequently, knowing the $\delta^{13}C$ of the pedogenic carbonate, the SOM $\delta^{13}C$ can be assessed, when making some assumptions of pH and temperature. As SOM results from a mixing of different OM sources (plants, microflore) and OM stabilities, it is generally possible to assess the proportion of the different types of plants (i.e. C3, C4, or CAM; Cerling, 2014). Indeed, their $\delta^{13}C$ signatures is related to their photosynthesis pathway (e.g. C3, C4, CAM) within the ranges given in Figure 1.2A. Finally, looking at the oxygen, the $\delta^{18}O$ of pedogenic carbonates is related to the $\delta^{18}O$ of the soil water, i.e. the soil solution, and to the soil temperature. The $\delta^{18}O$ of the soil solution depends on water inputs and outputs, i.e. the $\delta^{18}O$ of rainfalls and/or the water-table, and the extent of evapotranspiration (Cerling and Quade, 1993; Hsieh et al., 1998). Generally, under wet conditions, rainfall increases, evapotranspiration decreases, leading to lower soil solution $\delta^{18}O$, and *vice versa* (Cerling an Quade, 1993; Hsieh et al., 1998).

Palustrine environments are characterized by shallow waters, generally < 1m, being submerged by water or aerial exposed at different periods during the year. These characteristics differentiate them from lacustrine environments, i.e. with a water body depth > 1m and always submerged, and from inland environments, i.e. always emerged (Verrecchia, 2007). Palustrine carbonates are difficult to study because they often show features induced by pedogenic processes (Freytet and Plaziat, 1982). Due to these peculiar and changing hydric conditions, i.e. related to water-table fluctuations, palustrine

carbonates show many different facies and microfabrics (Freytet and Verrecchia, 2002):

- **Marmorization** is the mobilization of iron due to changes in redox conditions, which can accumulate in the carbonate and form pink, purple, red and/or yellow patches.
- **Cracking** can occur vertically, horizontally or can be curved.
- **Root traces**, or rhizoliths, are various and five major types were described by Klappa (1980): root moulds, root casts, root tubules, rhizoconcretions, and root petrification.
- **Vadose cements** are characterized by discontinuous coated pore walls.
- **Nodulization**.

Palustrine and pedogenic carbonates are thus sharing similar features, i.e. root fabrics, nodule occurrences, etc. Concerning their geochemistry, very commonly, palustrine carbonates $\delta^{13}C$ and $\delta^{18}O$ values are lower than in lacustrine carbonates and greater than in pedogenic carbonates (e.g. in Alonso-Zarza, 2003). However, this will depend on the degree of overprinting of pedogenic processes on palustrine carbonates. To summarize, the petrology and the geochemistry of terrestrial carbonates can provide pertinent information on paleo-environments in which they were formed. However, the precise processes behind their formations, is not yet entirely clear. To better understand the terrestrial carbonate genesis, it is necessary to look at the chemical properties of their constitutive carbonate minerals.

1.2.2 Their role in biogeochemical cycles

Terrestrial carbonates are part of the inorganic carbon reservoir of the continent in the global carbon cycle. Due to its low solubility product (Q_s, Equ. 1.1) at the surface of the Earth, calcite ($CaCO_3$) precipitates easily and is slightly soluble in water (Rotaru et al., 2006), making it the most stable carbonate mineral at the surface of continents. Formation, sedimentation, and erosion of $CaCO_3$ at the surface of the Earth are always associated with water (Geyssant, 2001) and precipitation of $CaCO_3$ can be approximated as:

$$Q_s = \frac{[HCO_3^-][Ca^{2+}]}{[10^{-pH}]} \tag{1.1}$$

$$Ca^{2+}_{aq} + 2HCO^-_{3(aq)} \rightarrow CaCO_{3(s)} + H_2O + CO_{2(g)} \tag{1.2}$$

This simple chemical reaction (Equ. 1.2) shows that terrestrial carbonates connect carbon, calcium and water cycles, all transient and exchanged compounds of different reservoirs, i.e. the hydrosphere, the atmosphere, and the geosphere. Element and molecule pathways between the reservoirs occur through various processes (Fig. 1.3). Carbon and water are transferred from the atmosphere to the biosphere by photosynthetic organisms (e.g. plants). Carbon transits from its inorganic and oxidized state ($CO_{2(g)}$) into its organic and reduced state (organic matter simplified as $< CH_2O >$).

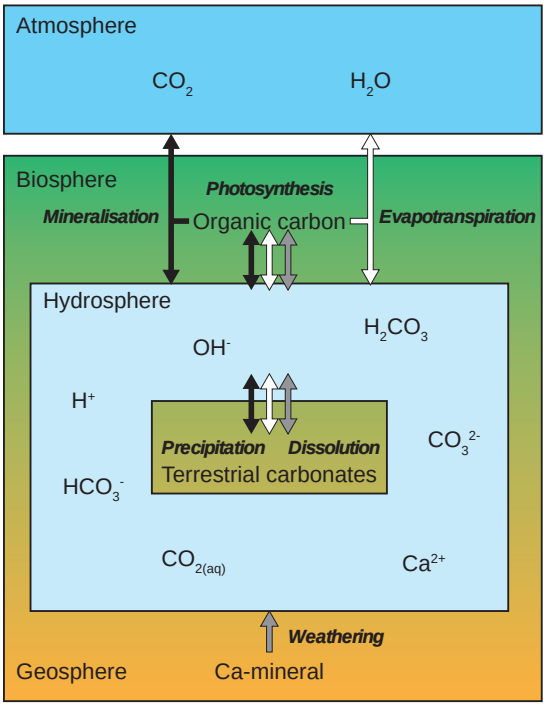

Figure 1.3 – Terrestrial carbonates precipitate from a solution enriched in elements originating from the Geosphere (Ca, grey arrow) liberated during weathering processes, from the Atmosphere, captured by photosynthetic organisms (C, black arrow) or coming from atmosphere and/or water (H_2O, white arrow). The three elements can be in transit through the Biosphere throughout the solution. C can return to the Atmosphere by mineralization processes and H_2O can be evapotranspirated as gazeous water.

Organic carbon can be mineralized by heterotroph organisms and transformed back into $CO_{2(g)}$, which can be transferred to the atmosphere or to the hydrosphere as an aqueous molecule $CO_{2(aq)}$. In the hydrosphere H_2O dissociates instantaneously and reversibly into H^+ and OH^- (Sposito, 1994). The aqueous form of CO_2 reacts quickly with water ions to form carbonic acid ($H_2CO_{3(aq)}$), which dissociates into bicarbonates ($HCO^-_{3(aq)}$) and carbonates ($CO^{2-}_{3(aq)}$) anions, according to pH and pCO_2 (Clark and Fritz, 1997). Water can also be transferred directly from the atmosphere to the hydrosphere through precipitation, i.e. rainfall, and can go back to the atmosphere from both biosphere and hydrosphere compartments through evapotranspiration processes. Calcium is mainly present in minerals and can be easily weathered, according to pH, and transferred to the hydrosphere as a soluble Ca^{2+} cation. Due to its divalent charge and relative abundance, Ca^{2+} from soils can be absorbed on the exchange complex or incorporated as a structural element of secondary minerals (Likens et al., 1998). It is also an essential nutrient for prokaryotes, fungi, plants, and animals (Likens et al., 1998), and consequently, it can be transferred to the organic pool. When conditions in the hydrosphere reach the equilibrium for calcite (e.g. saturation and $pH \approx 8.4$ (in standard conditions at the surface of the Earth: 20°C, pCO_2 = 3.3 atm, Cailleau et al., 2005), this mineral can precipitate (Clark and Fritz, 1997). Carbon and calcium are thus transferred into the terrestrial carbonates pool. The processes behind the precipitation of terrestrial carbonates are numerous and can be either abiotic or biotic. The abiotic pathway is related to supersaturation of the solution due to evaporation, temperature increase, and/or pressure decrease (in Brasier, 2011). The biotic pathways include (i) biomineralization of external or internal skeleton by some eukaryotes, (ii) the decrease of pCO_2 induced by autotrophic organism,

e.g. root uptake, cyanobacteria, methanogens, (iii) changes in alkalinity induced by prokaryotic heterotrophic organisms, e.g. ammonification, oxalotrophy, sulfato-reduction, and finally iv) fungal metabolism (in Brasier, 2011).

Thus, most of the carbon composing terrestrial carbonates originates from the atmosphere. However, the precipitation of $CaCO_3$ is also responsible of CO_2 production (Equ. 1.2). The last important point related to carbonate rocks (including both marine and continental carbonates), is the carbonate-silicate cycle described by the Urey reaction (Urey, 1952):

$$CaAl_2Si_2O_8 + 3H_2O + 2CO_2 \rightarrow Al_2Si_2O_5(OH)_4 + Ca^{2+} + 2HCO_3^- \tag{1.3}$$

where, $CaAl_2Si_2O_8$ is the anorthite and used as a proxy of silicate rocks. This cycle represents an important long-term global CO_2 balance (Berner et al., 1983). Moreover, if the calcium used to precipitate $CaCO_3$ is coming from the weathering of silicate rocks, two CO_2 are consumed during weathering and one is finally trapped in $CaCO_3$. Therefore, depending on the calcium sources, carbonate rocks can represent a significant C sink.

Consequently, not only acting as a palaeoenvironmental archives, terrestrial carbonates are integral parts of the global C cycle. By using a biogeochemical approach coupling carbon and calcium cycles, it appears that some terrestrial environments can trap C. As is the marine world, the continent may also be an important C trapping and its contribution should not be neglected.

2 The terrestrial carbonate formations from the Sahel

2.1 Topic and questions

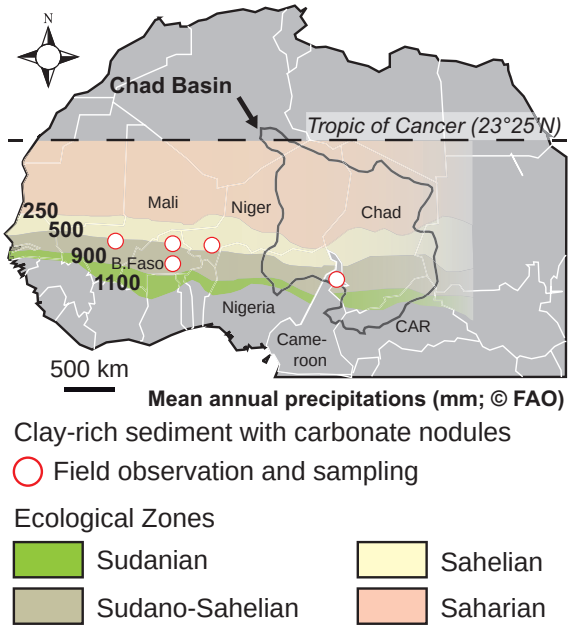

Figure 2.1 – Observation of terrestrial carbonates along the Sudano-Sahelian belt (not published: Durand, 1999; Rajot and Sebag, 2011; Cailleau et al., 2012). The Chad Basin is represented by the grey borders.

Terrestrial carbonate formations have been observed all along the Sudano-Sahelian belt (Fig. 2.1). In addition to their common latitudinal location, they also share the presence of large carbonate nodule accumulations at the soil surface, although they all belong to silicate watersheds. These types of carbonate formations are unexpected in such calcium-poor and acidic settings. In the Far North region of Cameroon (Chad Basin, Fig. 2.1), carbonate nodule accumulations can reach 11 kg m^2 at the soil surface. In the landscape, they are also associated with a clay-rich pediment forming mound morphologies within stream networks. The main lithology of the watershed is granitic and gneissic and thus poor in calcium (Table 2.1) and, as a paradox, the carbonate nodules are calcium-rich, with ~2000% more calcium than in the granite. Multiple questions are thus raised from these field observations.

How did such carbonate nodules form and in what kind of environment? Why are they accumulated at the soil surface and associated with clay-rich soils having mound morphologies? What is the source of calcium and how did this element accumulate in such an unfavourable chemical context? What is the importance of these accumulations in the continental carbon cycle? Are the carbonate formations found along the Sudano-Sahelian belt all genetically related? What is the time frame of their genesis?

Table 2.1 – Bulk chemical compositions of granite (Gr), soil (So), and carbonate nodules (No). So is compared to Gr and No to So and Gr, to emphasize elemental enrichment or depletion.

	Gr (wt-%)	**So (wt-%)**	**So/Gr (%)**	**Nod (wt-%)**	**Nod-Gr (%)**	**Nod-So (%)**
SiO_2	69.5	58.9	-15	13.5	-80	-77
Al_2O_3	15.9	19.0	19	4.2	-74	-78
CaO	1.7	2.1	24	45.2	2559	2052
MgO	0.5	1.6	220	0.9	80	-44
Na_2O	3.2	0.6	-81	0.2	-94	-67
K_2O	5.9	3.3	-44	0.8	-86	-76
Fe_2O_3	1.7	6.0	253	1.5	-12	-75
MnO	0.02	0.2	195	0.04	117	-27

All these questions emphasize how pertinent are the scientific inqueries related to such intriguing terrestrial carbonate formations. In the present work, a multi-scale approach, from the landscape to the mineral-lattice scale, is used with the aim of understanding the origin and the evolution of terrestrial carbonate formations through time. For this purpose, the following questions are addressed:

- **What** is the nature of terrestrial carbonate formations? What are the links with the other geomorphological units of the landscape?
- **How** did the terrestrial carbonate formations form? What are the processes and the paleo-environmental conditions involved in their genesis and accumulation?
- **When** did the terrestrial carbonate formations occur? What is their age and how did they evolve through time?

The study site is located in the Far North Region of Cameroon (Fig. 2.1). It has been investigated to provide new clues to help solving these questions. The results of this study are presented in separated parts of the manuscript and the methods used to address the questions are included in each specific part, explaining the absence of a single chapter dedicated to them. A synthesis is proposed before the general conclusions and perspectives of this work. Such a table of contents is also justified by the aim to value each portion of the research as scientific publications. The part II and the first chapter of part IV are already published (Annexe L).

2.2 Far North Cameroon: study site and general settings

2.2.1 Geology and Geomorphology

The Far North Region of Cameroon is located between the following latitudes and longitudes respectively: 10°04'N to 13°05'N and 13°34'E to 15°41'E. It belongs to the Sudano-Sahelian zone and its hydrological basin is the Chad Basin, an endorheic basin (Fig. 2.1). This region can be divided into four

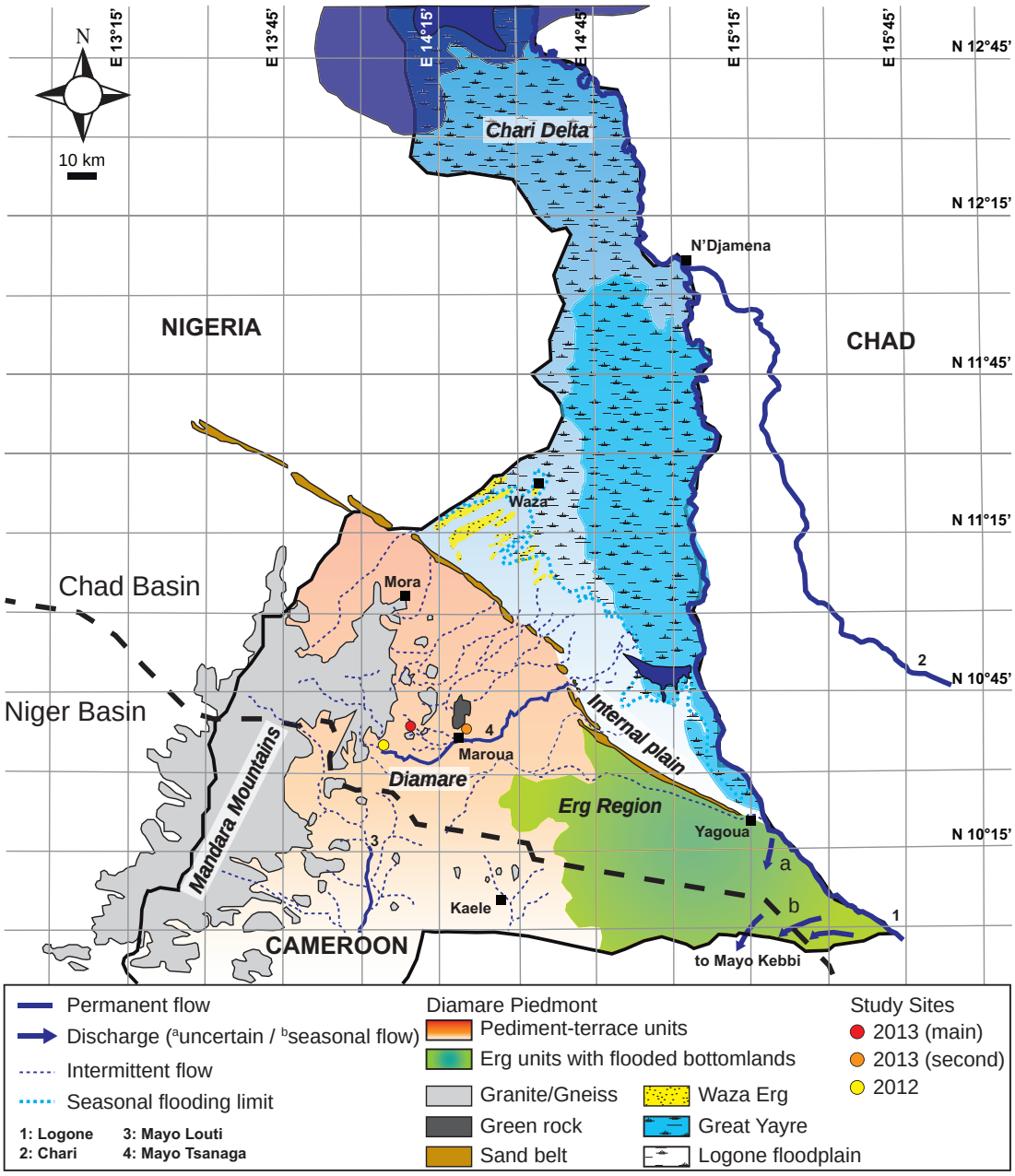

Figure 2.2 – In the W part, the Mandara Mountains are mainly granitic and gneissic; in the centre lies the Diamare piedmont, being a pediment-terrace unit, near Maroua, the lithology of the mountains are greenschist metabasalts (Green rocks of Maroua); in the SE, there is the Erg Region; the Internal Plain lies between the sand belt and the Logone-floodplain, whose parts differentiate by their flooding durations; in the N, there are the Chari Delta and Lake Chad. The Logone (1) and the Chari (2) feed Lake Chad (~84%) and flow from the southern Sudano-Guinean area. In the Diamare piedmont, streams are mainly intermittent, except for the Mayo Louti (3), which belongs to the Niger Basin, and the Mayo Tsanaga (4), which is part of the Chad Basin (black dashed line limit). In the Erg region, waters from the Logone can uncertainly flow (dark blue arrows) into the Mayo Kebbi, part of the Niger Basin. The slope is very gentle and decreases from 4-2% in the Diamare to 0.02% near Lake Chad. This leads to the formation of a floodplain, whose limits are given by the light-blue dashed line.

main areas: 1) the Mandara Mountains (1500-800 m a.s.l.) in the SW, 2) the Dry Plain (500-306 m a.s.l.), which includes the Diamare and the Internal plain, both units being separated by a quasi-continuous sand belt, orientated SSE-NNW, 3) the Logone floodplain (306-290 m a.s.l.), which includes the Yayres, and finally, 4) the Chari Delta, in the North (290-280 m a.s.l.). All the study sites are located in the Diamare piedmont within the Mayo Tsanaga watershed (Fig. 2.2).

The geological basement of Cameroon belongs to the Saharan Metacraton, i.e. a craton that was remobilized during an orogenic event but still recognizable (Abdelsalam et al., 2002). The craton is Paleo-Proterozoic in age and was affected by the Pan-African Orogeny during the Early Precambrian (Bertrand et al., 1983; Durand, 1995). The mountain ranges from Central Africa, such as the Hoggar, the Tibesti, the Aïr or the Mandara, were formed during this period and their lithology is composed of granite, gneiss, metasediments, migmatites, and granulites. The other parts of the Metacraton are overlaid by Cretaceous rocks or Saharan sands (Abdelsalam et al., 2002). In West Africa, subvolcanic intrusions, known as the Younger Granite, are post-Pan African Orogeny. During the Cretaceous, South America broke away from Africa, reactivating the Pan-African faults (Cratchley et al., 1984). The opening of the southern part of the Atlantic induced an important rifting in both West and Central Africa, i.e. the Western and Central African Rifts (Genik, 1992; Abderamane et al., 2013). It was proposed that the formation of basins, such as the Chad Basin, were related to the rifting processes (Louis, 1970). Consequently, the sedimentation in the Chad Basin began during the Late Cretaceous (Morin, 2000; Abderamane et al., 2013). Circa 56 Ma (Continental Terminal), the period of African lakes began, leading to the deposition of solely continental sediments. However, the sediments from this period poorly outcrop within the Chad Basin (Durand, 1995). The Benue trough has a Y-shape oriented SW-NE, and its northern branch, the Chad rift or the Gongola rift, disappears under the Chad Basin and its eastern branch, the Yola rift, can be followed until Sudan (Fitton, 1980, Ndougsa-Mbarga et al., 2007). The Cameroon Line, an alkaline volcano chain associated with this rift, started to form during the Eocene and lasted until the present-day in some areas (e.g. Mont Cameroon, Ngaoundere, Biu Plateau). The activity at the origin of the Mandara Mountains is dated from 40 Ma to 27 Ma (Fitton, 1980; Fitton and Dunlop, 1985). During the Miocene, the Chad Basin and the Chari-Logone drainage system are formed (Morin, 2000). The Mandara Mountains are mainly composed of granite and gneiss, and the greenschist facies of metabasalts, known as the green rocks of Maroua, constitute only a minor part of the intrusion around Maroua (Brabant and Gavaud, 1985). Tectonic structures are thus frequent in the basin; however, recent (Quaternary) tectonic activity, or neotectonics, in the basin remains poorly documented (in Durand, 1982). Nevertheless, in the northern part of the Chad Basin, differences between interdunal lake levels have been interpreted as the result of neotectonics (Servant-Vildary, 1978).

The Mandara Mountains are oriented SSW-NNE, they are steep and deeply incised by rivers. The highest altitudes are found in the North (until 1500 m a.s.l.), whereas the southern part reaches only 900 m a.s.l. (Morin, 2000). The transition from the Mandara Mountains to the Diamare piedmont is abrupt, with a decreasing slope from about 10% to 4-2%, which is a typical dryland landform associated with slopes called *pediment* (Morin, 2000; Goudie, 2013). The pediment infilling is heterogeneous and related to multiple pediment generations, which are the result of climate variations during the Quaternary (Morin, 2000). From the foot of the Mandara Mountains to the Yayres floodplain, the pediment evolves from a thin cover of weathered granitic sand, to a colluvium, and finally to an alluvium with a grain-size distribution skewed to finer sizes. However, these settings are complicated by evidence of lateral changes, such as a clay-rich intercalation pediment, possibly of palustrine origin, and sand lenses resulting from changes in the Mayo riverbed (Morin, 2000). The clay-rich pediment, with which carbonate nodules are often associated, outcrops along the southern bank of the Mayo

Tsanaga, or is overlain by either alluvium (for example near Mora) or various generations of fersiallitic pediments starting from the foot of granitic inselbergs, as observed around Maroua and in the region of Kaele (Sieffermann, 1967; Morin, 2000). In the SE, before the sand belt, sand dunes constitute two erg systems: 1) the Doukoula Erg oriented SSE-NNW, and 2) the Kalfou Erg oriented NNE-SSW, characterized by reddish sands. The bottomlands of these ergs are frequently flooded. Eastern of the ergs, the depression of Fianga forms in an ancient section of the Logone, where waters can flow either in the Niger Basin through the Mayo Kebbi or in the Chad Basin through the Logone (2.2, Morin, 2000). Further the sand belt, the slope is very gentle (0.5 to 0.2%). Before reaching the floodplain, emerged plains, i.e. the Internal plain, extends from 320 to 306 m a.s.l. In the northern part, the Waza Erg displays similar characteristics compared to the Kalfou Erg (e.g. grain size distribution and orientation). Southern of this erg, the most energetic Mayos bring alluvium on a sandy-clayey sediment. Below 306 m a.s.l., the area can be flooded by the Logone. Three areas are distinguished from this altitudinal limit towards Lake Chad, 1) the Little Yayre, a flooded meadow, 2) the Great Yayre, and 3) the Chari Delta. Slopes range between 0.16 and 0.1% in the Yayres and drops <0.05% in the delta. Dark clay deposits, which can be enriched in carbonates, characterize this floodplain. Coarser alluvium can interrupt these clay-rich sediments, their frequency being higher in the Chari Delta (Fotius, 2000; Morin, 2000).

2.2.2 Climate and hydrology

The climate in Far North Cameroon is regulated by the monsoon system (L'Hôte, 1998). The term monsoon comes from the old Arabic word *mausim*, which would mean season (Beltrando, 2004). This system is linked to the Intertropical Convergence Zone (ITCZ), which corresponds to the limit between the northern and the southern hemisphere circulations, generalized at the global scale. The ITCZ moves to the North during the boreal summer and to the South during the austral summer (Beltrando, 2004). According to the Köppen-Geiger climate classification (Peel et al., 2007), the Far North region of Cameroon belongs to the hot (h = mean annual temperature ≥18°C), steppic (S = mean annual precipitation ≥ $5*P_{threshold}$), arid (B) climate type, i.e. BSh. Summer is generally hot and there is a short well-marked wet season regulated by the monsoon. The weather station located in Salak, close to Maroua, records an average annual rainfall of 800 mm and an average annual temperature of 27.6°C (L'Hôte, 1998). The potential evapotranspiration is 2193 mm and the dry season lasts seven months with five months without any rainfall (Mahop et al., 1995). From January to April, the region is also marked by dry NE trade winds, called the "Harmattan" (L'Hôte, 1998).

Under these climatic conditions, streams are mainly ephemeral (*mayo* means ephemeral stream in *fulfulde*, in Seignobos and Tourneux, 2002) and their regime is mainly influenced by the intensity of the dry season (Olivry and Naah, 2000). The streams have a WSW-ENE-flow direction through the Diamare piedmont from the Mandara Mountains to the Yayres floodplain (*yayres* or *yaéré* means floodplain in *fulfulde*; in Seignobos and Tourneux, 2002) and are tributaries of the Chad Basin (L'Hôte, 2000). The Chad Basin is an endorheic watershed whose hydrological limit reaches the south of Maroua (2.2). Only several river tributaries to the Mayo Louti in the SE and the Mayo Kebbi in the SW contribute to the Benoue Basin, which belongs to the Niger Basin (Fig. 2.2). The rivers begin in the Mandara Mountains and, as the slopes are steep in these parts of the landscape, the runoff is important and lies directly on the bedrock. Between the mountains and the piedmont, the bedrock is patchily covered by granitic sands and the slope drops to 4-2%, enclosing river flows. In the alluvial plain, the slope is < 2% and riverbeds are less sharp due to frequent changes in flow directions and high alluvial load and reworking. The most energetic Mayos, such as the Tsanaga, go through the sand belt. However, water almost never reaches the Logone because slopes, as well as energy, continuously drop in this direction. The water

flow disappears in the floodplain, where the solid charge is finally trapped (Olivry and Naah, 2000).

2.2.3 Soil and Vegetation

Soils of Far North Cameroon are diverse and their distribution in the landscape depends on soil parent material and hydric conditions (Brabant and Gavaud, 1985). In the mountain area, the soils are coarse grained (arena), poorly developed and can be classified as Lithosol and Regosol, i.e with no significant profile development (IUSS Working Group, 2014). A mosaic of soils controlled by the variability of the hydric conditions are developing from the piedmont to Lake Chad (Brabant and Gavaud, 1985; IUSS Working Group, 2014):

- **Gleysol**, groundwater affected soils and/or underwater soils,
- **Vertisol (or *Karal in fulfulde***), soils under alternating wet-dry conditions and enriched in shrink-swell clays,
- **Planosol**, soils with stagnant water and abrupt grain size changes
- **Solonetz**, soils with high proportions of exchangeable sodium

The proportion of each type changes with hydric conditions, the Vertisols being favoured in the less weathered areas. In the Erg region, Ferralsols, i.e. kaolinite- and oxide-rich soils, are associated with sand dunes and a Gleysol-Vertisol-Planosol-Solonetz mosaic is also found in the lowlands. The same arrangement is observed in the northern part of the Internal plain in the Waza Erg (Fig. 2.2). Fersiallitic soils are observed around the massif of Maroua, i.e. on greenrocks of Maroua, but they evolve quickly toward a Gleysol-Vertisol-Planosol-Solonetz mosaic in the piedmont. Finally, the Fluviosol type is developing around the Mayos and the Logone-Chari rivers.

The particularity of soils observed in the Far North region of Cameroon is the fact that they were often mapped as degraded soils. The local term used to emphasize this soil degradation is *hardés*. This term characterizes soils that are very compact, with a low permeability, and a significant alkalinity. These conditions make these lands sterile and only sparse vegetation can grow on them. These areas are extensive, covering 886,500 ha, located mainly in the Diamare piedmont and in the Internal plain afore the Yayres (Brabant and Gavaud, 1985).

The vegetation associations of Far North Cameroon are diverse and related to water availability, soil types, and anthropic pressure (Fotius, 2000). Four ecological environments are distinguished, i) the mountains, ii) the dry plain, iii) the floodplain, and iv) the delta. The vegetation in the Mandara Mountains is of Sudanian type, but primary vegetation grows only at high altitudes (> 1200 m a.s.l) due to human occupation and pressure at lower altitudes (< 1200 m a.s.l). In the dry plain, the vegetation type evolves indistinctly from a Sudano-Sahelian / Sahelo-Sudanian type to a Sahelian type in the floodplain and the delta. In the Diamare piedmont, the "climacic" vegetation is characterized by *Anogeissus leiocarpus* (i.e. the African birch), *Sterculia setigera* and *Acacia hockii*. However, as stated above, the soils can be highly degraded (i.e. *hardés*) and characterized by variously intense hydromorphic conditions. Consequently, different vegetation associations are associated witn these two factors:

- ***hardés***: *Lannea humilis* formation

- ***Semi-hardés***: *Balanites aegyptica* formation
- **Intermediate Planosol-Vertisol**: *Acacia gerrardii* formation
- **Stony vertic soil**: *Acacia hockii* formation
- **Vertisol**: *Acacia seyal* formation

To summurize, terrestrial carbonates occur by definition in the vadose zone and are mainly related to soils and/or wetlands. They can be precious palaeoenvironmental archives and are part of the global *C* cycle. Terrestrial carbonate nodules were observed in silicate watersheds along the whole Sudano-Sahelian belt. In the Diamare piedmont, (Far North Region of Cameroon), they are associated with soils having mound morphologies within stream networks. The piedmont lies between the Mandara Mountains (granitic and gneissic) and the Logone-floodplain. The landscape is very flat leading to water riverbed changes in the piedmont and even to water riverbed disappearance in the floodplain. The infilling pediment in the piedmont is heterogeneous and evolves from a thin cover of weathered granitic sand, to a colluvium, and finally to an alluvium with a grain-size distribution skewed to finer sizes, which includes clay-rich intercalations. The climate is regulated by the monsoon system and is hot, steppic, and arid (BSh type). A strong anthropic pressure is observed in the region, inducing soil and vegetation degradation. In the following parts of this manuscript, questions addressed concerning the origin of the terrestrial carbonates (*what*, *how*, and *when*) from Far North Cameroon will be approached in distinctive parts.

Part II

Nature of terrestrial carbonate formations

SYNOPSIS

This part aims at the understanding of the nature of terrestrial carbonates, as well as their sedimentary and geomorphological relationships in the landscape. Non-anthropogenic earth mounds have been observed in non-carbonate watersheds along the Sudano-Sahelian belt in the Chad Basin. In the Diamare piedmont (Far North Cameroon), they are particularly well-developed within stream networks and can be defined as **mima-like mounds**. In less eroded areas, they occur as whaleback, flattened morphologies, or even as buried features. All these shapes are composed of clay-rich sediment associated with high proportions of secondary carbonate nodules and $Fe-Mn$ micro-nodules. Their soil structure is prismatic to massive and vertical cracks are observed locally. Grain-size distributions emphasize the clay-rich nature of the sediment, with average clay contents of 32% ± 12.8% (n=186, at $\pm 1\sigma$), which is significantly higher than the clay content in the adjacent sediments in the landscape (mean = 10% ± 4%, n=21, at $\pm 1\sigma$). Moreover, high proportions of smectite characterize the soil, with average contents of 34% ± 7% (n=25, at $\pm 1\sigma$). At the micro-scale, the groundmass has a cross-striated b-fabric, with embedded smooth subangular quartz and feldspar grains of the silt-size fraction. All the characteristics point to altered vertic properties in the clay-rich sediment composing the mima-like mounds. Mima-like mounds are thus interpreted as degraded Vertisols or **Vertisol relics**. Compared to present-day Vertisols occurring in the piedmont, mima-like mounds are located upstream. It is proposed that the Vertisol areas were more extensive during a former, wetter period. Subsequent changing climatic conditions toward drier conditions increased erosion, revealing the gilgai micro-relief by preferential erosion in micro-lows rather than in micro-highs. Mima-like mounds of the Chad Basin might thus result from pedogenesis combined with later erosion. These local processes can be **inherited** from regional climatic variations during the Late Quaternary and likely be related to the African Humid Period (14.8 ka to 5.5 ka).

3 The origin of mima-like mounds from Far North Cameroon

3.1 Introduction

Non-anthropogenic earth mounds occur in many parts of the world and the questions related to their origin make them exciting features (Cramer et al., 2012). The debate is generally centred upon the discussion of their abiotic or biotic origin. For example, earth mounds observed in South Africa (locally termed heuweltjies; Moore and Picker, 1991; Francis et al., 2012) and Brazil (Funch, 2015) are attributed to termite activity, but others provide some evidence they can result from differential erosion (Cramer et al., 2012). In North America, the geomyid pocket gopher may be involved in the mound (or mima mound) formation (e.g. Cox, 1984), but the debate on their real capability to produce them is still open (e.g. Butler, 1995). Silva et al. (2010) proposed that erosive processes combined with vegetation patterns are the cause of earth mounds (campos de murundus) observed in Brazil instead of resulting from termite activity. The origin of earth mounds changes from one region to another, but they have some common features, such as their regular spatial distribution or their size (Cramer et al., 2012). It was recently proposed that many of these different earth mounds, termed mima-like mounds, can be explained by the combination of erosion and/or aeolian processes with vegetation patterns (Cramer and Barger, 2014; Cramer and Midgley, 2015).

All along the Sudano-Sahelian belt, carbonate nodules have been observed in non-carbonate watersheds (Fig. 3.1A). In northern Cameroon (Fig. 3.1A), these nodules are associated with non-anthropogenic earth mounds (Fig. 3.2). These new features have not been studied up until now. In the Far North region of Cameroon (Chad Basin) they are frequently observed in the Diamare piedmont (Fig. 3.1B), and are particularly well developed within stream networks (10 m < diameter < 30 m and height up to 1 m). On Google Earth images (Fig. 3.2), they are distributed in eroded areas as regularly spaced (i.e. over-dispersed, Appendix A) round features. They can be defined as mima-like mounds due to their size and their spatial distribution. However, vegetation patterns do not play a main role in their formation, whereas erosion processes do. Generally, mima-like mounds are associated with sparse vegetation or none at all (Fig. 3.3). Consequently, the conditions under which they form still remain unclear. The clay- and carbonate-rich association composing the mima-like mound sediments was already described in the Diamare piedmont (Martin, 1961; Sieffermann, 1963; Brabant and Gavaud, 1985; Morin, 2000) and also farther away in the Chad Basin (Erhart, 1954; Pias, 1962; Bocquier, 1973). Compilation of former and new field observations raises questions on the potential links that could exist between these multiple locations. The clay-rich sediment, enriched in carbonate nodules, can be interpreted as a layer (or multi-layer?) forming residual mima-like mounds in highly eroded areas.

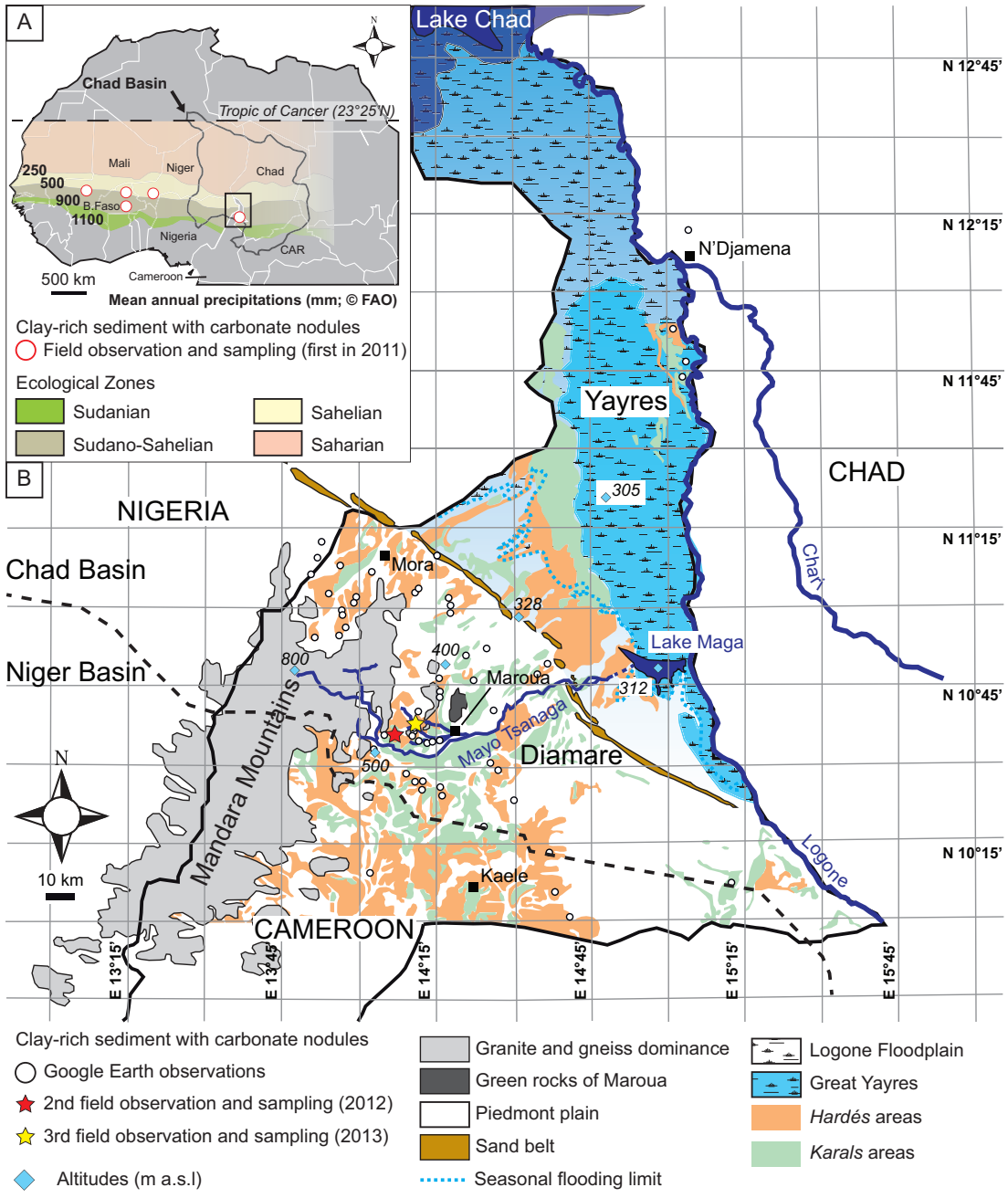

Figure 3.1 – A) Location of observed sediments associated with carbonate nodules (circles) along the Sudano-Sahelian belt (MAP 900-500 mm/yr); mean annual precipitation ranges are given for the three climatic zones; location of far North region of Cameroon (black rectangle). B) Far North region of Cameroon map showing, from SW to NE, the Mandara Mountains, the Diamare piedmont, separated from the Yayres floodplain by a sand belt, and finally, Lake Chad. Stars represent the study sites. They are located in the Mayo Tsanaga watershed, which belongs to the Chad Basin (large dashed-line; Olivry et al., 1996). Circles indicate the location of the clay-rich sediment outcropping as mima-like mounds within stream networks (Google Earth observations, Appendix A) and generally found in hardés areas or degraded soil areas found upstream Karal soils, i.e. Vertisols, reported by Brabant and Gavaud (1985).

Regarding the soils developing from this clay-rich parent material, there are mainly Planosol, Solontez and Vertisol (Brabant and Gavaud, 1985). However, these soils are often described and mapped as degraded soils (Brabant and Gavaud, 1985). Interestingly, mima-like mounds are typically observed in these degraded zones. This is consistent with their presence in eroded areas. However, could pedogenesis have a specific role in their genesis?

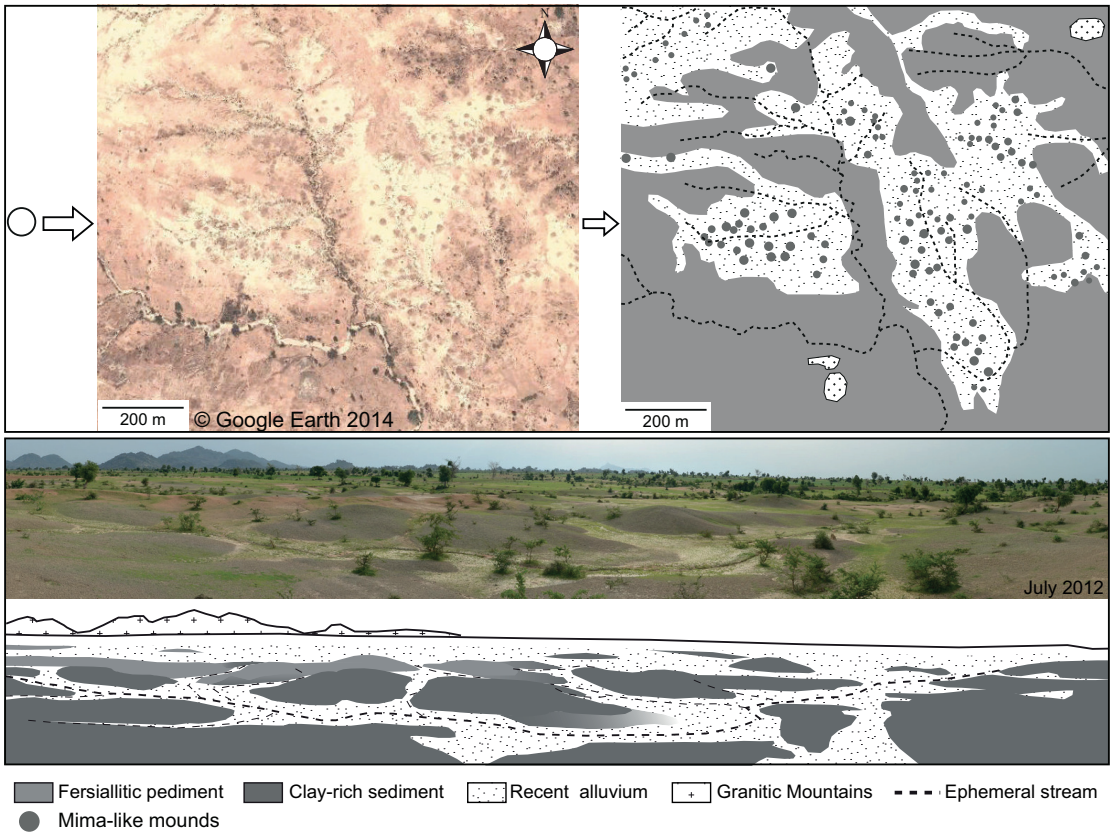

Figure 3.2 – Example of a Google Earth view (10°37'12.08"N, 14°11'13.55"E) showing regularly spaced (R=1.72, over-dispersion, Clark and Evans, 1954, Appendix A) mima-like mounds outcropping within stream networks. Beige alluvium surrounds them and less eroded areas display a reddish pediment interpreted as a fersiallitic pedolith (Retallack, 2001). In the landscape the clay-rich sediment outcrops as dark mima-like mounds at various stage in their development. The fersiallitic pediment is always observed overlaying the clay-rich sediment.

The aim of this study is to characterize sedimentological and geomorphological settings of mima-like mounds from the Far North region of Cameroon and to propose a possible origin of their formation. To achieve this goal, a multiple scale approach is used compiling (1) field observations, (2) grain-size distribution and clay mineralogy data at the mound scale, and (3) thin-section observations. Roles of pedogenesis and later erosion in the formation of mima-like mounds are investigated. Two main hypotheses are proposed: (i) mima-like mounds observed in northern Cameroon are relics of Vertisols associated with a gilgai micro-relief; and (ii) they result from abiotic processes related to the succession of pedogenesis and erosion-deposition phases associated with Late Quaternary regional climatic changes, and may thus be useful palaeoenvironmental indicators in the Chad Basin.

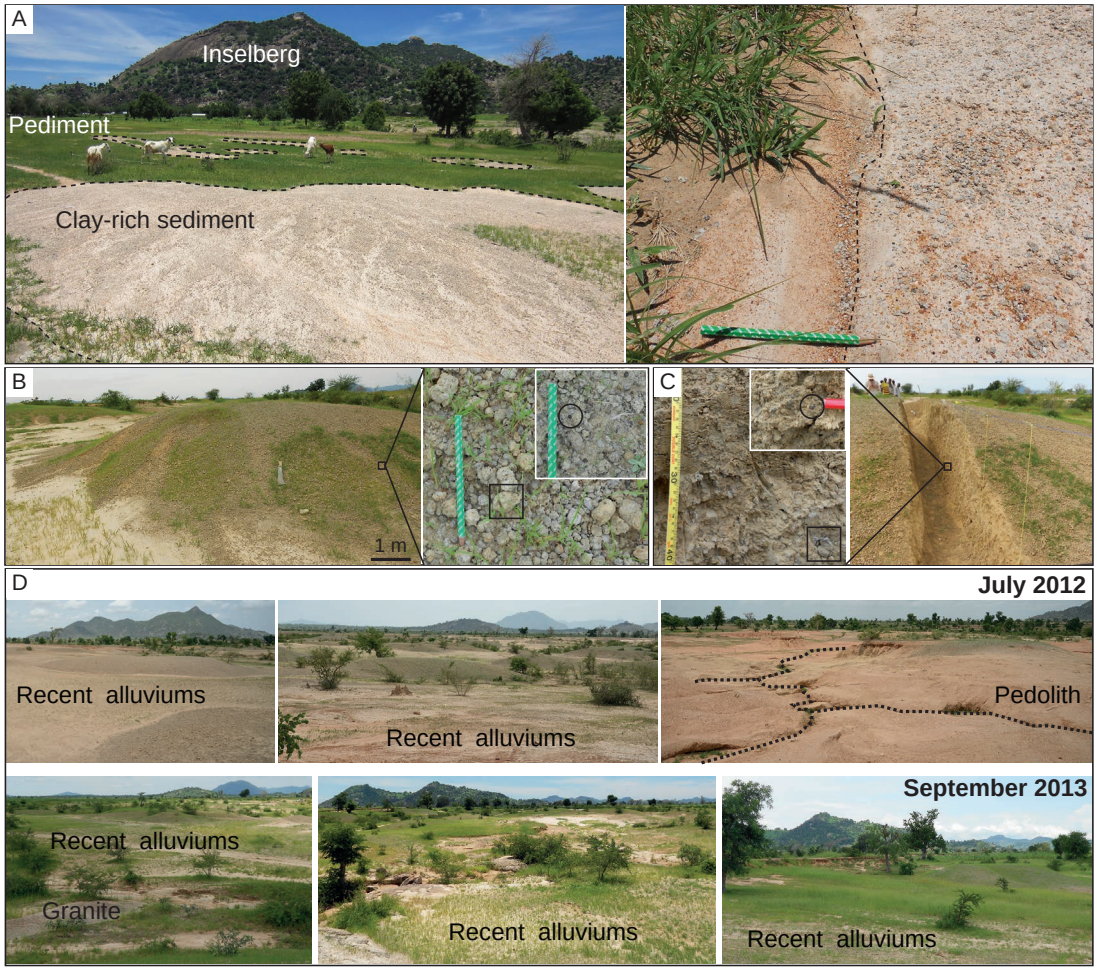

Figure 3.3 – A) Relationships between mima-like mounds and vegetation patterns. The clay-rich sediment is devoid of vegetation compared to surrounding sediments, and shows sharp limits (dashed line), which makes it easily recognizable in the landscape. B) Mima-like mound M1 located along the Mayo Tsanaga watershed (Fig. 3.1B, 2013 field observation) surrounded by a fine alluvium and covered by carbonate nodules and Fe-Mn micro-nodules. C) Trench through the mima-like mound M1 composed by a yellowish-grey, clay-rich and massive soil matrix. Carbonate nodules (black square) and $Fe-Mn$ micro-nodules (black circle) are also observed in the soil skeleton (>2 mm). Pictures taken in September 2013. D) Landscape view according to the season, showing the importance of erosion processes.

3.2 Material and methods

3.2.1 Sampling

Soil profiles are described according to the guidelines provided by the Food and Agricultural Organization of the United Nations (FAO, 2004). Depth, percentage and components of the skeleton (>2 mm), structure, relative abundance of carbonate (tested with 10% hydrochloric acid) and colour (determined in the field with a Munsell colour chart) are given in Table 3.1. Samples were collected at two main sites (Fig. 3.1B, stars). Trenches were opened through selected mounds. Soil profiles were described each meter along the trench. The site investigated in 2013 is located along an affluent stream of the

Mayo Tsanaga (Fig. 3.1B). A trench 12 m long and 1.30 m deep was opened through a well-developed mima-like mound (M1, Fig. 3.3B, 3.3C). Twelve soil profiles (A to L, Table 3.1) were described and sampled at 5-cm intervals in the first 10 cm from the top, and then every 10 cm. A second trench, 5 m long and 1.30 m deep, was opened through a less well developed and flattened mima-like mound partially buried by a coarse-grained alluvium interfingering with the clay-rich sediment (M2, Fig. 3.4B). Five soil profiles (N to R, Table 3.1) were described and sampled the same way as in mound M1. A last profile (T, Table 3.1) was described in a fersiallitic terrace (P, Fig. 3.4A) overlying the clay-rich sediment and sampled as in mounds M1 and M2. The site investigated in 2012 is located along the Mayo Tsanaga (Fig. 3.1B). A trench 7 m long and 1.30 m deep was opened in a mima-like mound from centre to perimeter (M3). Seven soil profiles (S, U to AB, Table 3.1) made at 1 m intervals were sampled every 5 cm. This second site was investigated during a different fieldwork campaign and soil descriptions are not as complete as at the first site (Table 3.1, nd=no data). All samples were dried at 45°C and sieved at 2 mm (fine earth fraction). A part of this fraction was crushed to a powder with an agate mortar (grain-size <10 μm). Carbonate nodules were collected as well, at various depths; some of them were crushed with an agate mortar in order to have both small pieces and powders. Soil samples were put in metallic boxes (8x8x4 cm) to make thin sections (thickness = 30 μm). They were collected from mounds M1, M2, and profile P at specific depths (Table 3.1). Samples were wedged in the best possible manner to keep the original soil structure.

3.2.2 Analytical methods

Measurement of pH_{H2O} was performed on the 2-mm sieved soil fraction. The soil was agitated in deionized water with a 1 : 25 soil to water ratio for 2 hours. The pH of the solution was then measured with a lab pH-meter (Metrohm SA).

Grain-size distributions were performed with the laser diffraction method ($Malvern^{TM}$ Mastersizer 2000). Carbonate and organic fractions were removed from the dried <2 mm soil fraction, using 10% hydrochloric acid (HCl) and 15-35% hydrogen peroxide (H_2O_2), respectively. Finally, mineral particles were dispersed with Na-hexametaphosphate (40 g/L). Samples are put in water suspension during the analysis (Hydro 2000S module). Due to their compositional nature, a centred log-ratio (clr) transformation was applied to the data:

$$x_n = \ln \frac{x_i}{G(x_i)} \tag{3.1}$$

where, x_n is the transformed data, x_i is the original data, and G the geometric mean of the x_i variable. Data resulting from the clr transformation were used to build a cluster tree by performing hierarchical cluster analysis (CA). The groups were obtained using the Euclidian distance between samples and the Ward algorithm for clustering. To compare the dissolution silicate residue trapped in carbonate nodules with the embedding soil matrix, this specific fraction was taken as a group without going through clr and CA processing. Each cluster is represented by its median and standard error of its median (σ_{median}):

$$\sigma_{median} = 1.253 \frac{\sigma}{\sqrt{n}} \tag{3.2}$$

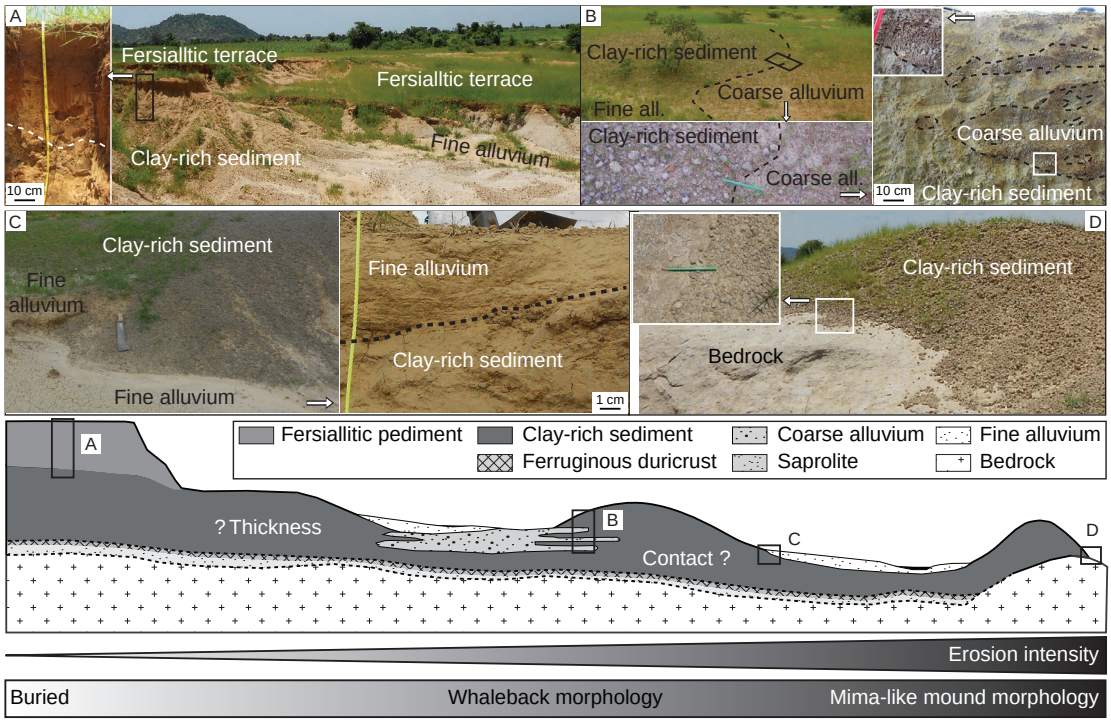

Figure 3.4 – Cross-section representing the various sediments observed in the landscape and the relationships to each other. Pictures illustrate different situations represented in the drawing (black rectangles). A) Detail of the fersiallitic pediment overlaying the clay-rich sediment (profile P). B) Example of a flattened mima-like mound (M2) in contact with a coarse alluvium interfingering the clay-rich sediment. C) Detail of the contact between the fine alluvium and the mima-like mound M1. D) Clear contact between a mima-like mound and the granitic bedrock. The thickness of the clay-rich sediment and its contact with a deep ferruginous duricrust described in the literature and/or the bedrock saprolite were not observed during the fieldwork. The clay-rich sediment outcrops as flattened mima-like mounds, whaleback morphologies, or mima-like mounds depending on the intensity of erosion, the fersiallitic pediment buries mounds in less eroded parts of the landscape.

where, σ is the standard deviation of samples composing a cluster and n the number of samples composing each cluster. For graphical reasons, the data are logarithmically transformed into phi (ϕ) values using the expression proposed by Krumbein in 1934 (Blott and Pye, 2001):

$$\phi = -\log_2 d \tag{3.3}$$

where, d is the grain-size in millimetres. Clay percentage interpolation (n=89) was performed using a cubic interpolation with Matlab (R2014a 8.3.0.532). X-Ray Diffraction (XRD) analyses were performed with both <2 μm and 2-16 μm fractions. Carbonate was removed from dried 2 mm-sieved soil samples with 10% HCl in an ultra-sonic bath for 3 minutes. The residual fraction was washed in order to remove the excess HCl. Separation of the <2 μm and 2-16 μm fractions was performed by centrifugation and deposited on separate glass plates. Five samples per cluster resulting from the CA analysis were selected and prepared for XRD analyses, which were performed using an ARL Xtra diffractometer (Thermo). Clay minerals were identified according to their diffraction properties, i.e. the spacing (d) between

rows of atoms and the angle of incidence (θ), defined by Bragg's law:

$$2d\sin\theta = n\lambda \tag{3.4}$$

where, $n\lambda$ is the number of wavelengths (Moore and Reynolds, 1997). The software PeakFit^{TM} (Systat Software Inc.) was used to deconvolve two parts of the diffractograms in order to discriminate between the different components combined in the signal (Velde and Meunier, 2008). The first part ranges from 4°2θ to 11°2θ and refers to smectite, illite and interlayered illite-smectite. The second part ranges from 23°2θ to 26°2θ and refers to the second peak of kaolinite and the fourth peak of the chlorite, which are overlapping. Kaolinite (cps) and chlorite (cps) were calculated as follows:

$$Kaolinite = CK001\frac{K002}{K002 + C004} \tag{3.5}$$

and,

$$Chlorite = CK001\frac{C004}{K002 + C004} \tag{3.6}$$

where, CK001 is the first peak of the kaolinite overlapping the second peak of chlorite occurring at about 12.5°2θ, K002 is the second peak of the kaolinite occurring at about 24.2°2θ, and C004 is the fourth peak of chlorite occurring at about 25.1°2θ (Moore and Reynolds, 1997). The signals were first smoothed and deconvolved with the residue method using the Pearson VII operator. Relative percentages were calculated for smectite, illite, chlorite and kaolinite.

3.2.3 Thin section descriptions

Thin section observations are used to identify pedogenic processes involved in the mima-like mound formation and to highlight the differences between sediments observed in the landscape. Thin section descriptions are performed according to the guidelines given in Stoops (2003). Particular attention is paid to the groundmass and the identification of pedofeatures, as they indicate lithology and weathering processes, as well as past and present pedogenic processes, respectively (Stoops, 2003). The characterization of the b-fabric, which is based on the patterns of orientation and distribution of interference colours in the soil micro-mass, is the main descriptor of groundmass, whereas, coatings, infillings, and nodules are mainly considered as pedofeatures (Stoops, 2003). Descriptors such as size, abundance, boundary, sorting, shape, sphericity, roughness, roundness, orientation, mineralogy, and colour, are used to differentiate the fabric units and patterns. The c/f related distribution, which is the ratio between individual fabric units, small fabric units, and associated pores (Stoops and Jongerius, 1975), is used to describe the relationships between coarse and fine elements of the fabric.

3.3 Results

3.3.1 Field and soil descriptions

Table 3.1 – Soil profile descriptions according to FAO (2006)'s descriptive codes for mima-like mound M1 (A to L), M2 (N to R), M3 (S to AB) and the fersiallitic pediment (T). Horizons marked in bold represent the locations where samples were collected to make thin sections. The pH_{H2O} was measured in the lab with a pH-meter.

	Horizon	Depth (cm)	Structure	Skeleton (%)	Skeleton comp.	Munsell (moist)	HCl %	pH_{H2O}
M1	AH2	9-24	AB to MA	1	Fe-Mn-ox/Cnod	2.5Y6/4	2-10	8.9
	AH3	24-44	AB to MA	1	Fe-Mn-ox/Cnod	?	0-2	8.8
	AH4	44-59	MA	0	-	2.5Y5/6	0-2	8.9
	BH1	0-5	SAB to SG	0	-	2.5Y5/6	2-10	8.6
	BH2	5-24	MA	0	-	2.5Y5/4	10-25	9
	BH3	24-64	MA	1	Cnod	2.5Y6/6	?	8.9
	CH1	0-1	SAB	1	Fe-Mn-ox	2.5Y5/4	>25	8.8
	CH2	1-9	SAB to MA	?		2.5Y6/4	0-2	8.9
	CH3	9-29	MA	1	Cnod	2.5Y5/4	10-25	9.1
	CH4	29-76	MA	1	Sil	2.5Y6/4	0-2	9
	DH1	0-3	AB	1	Cnod	2.5Y5/4	10-25	9.1
	DH2	3-24	MA	1	Fe-Mn-ox/Cnod	2.5Y5/4	0-2	9.1
	DH3	24-60	MA	1	Cnod	2.5Y5/4	0-2	9.1
	DH4	60-100	MA to SG	1	Cnod	2.5Y6/4	?	8.8
	EH1	0-5	SAB	5	Fe-Mn-ox/Cnod	2.5Y4/4	>25	8.9
	EH2	5-34	MA	1	Fe-Mn-ox/Cnod	2.5Y6/4	0-2	9.1
	EH3	34-114	MA	15	Fe-Mn-ox/Cnod	2.5Y6/4	0-2	8.9
	FH1	0-10	SAB	3	Cnod > Fe-Mn-ox	2.5Y5/4	10-25	8.7
	FH2	10-37	MA	2	Cnod	2.5Y6/3	?	9.1
	FH3	37-54	MA	15	Cnod	2.5Y5/4	0-2	9.6
	FH4	54-100	MA	20	Cnod	2.5Y5/4	0-2	9.1
	FH5	100-120	MA	5	Cnod	2.5Y5/4	0-2	8.7
	GH1	0-7	SAB	2	Fe-Mn-ox	2.5Y6/3	10-25	8.6
	GH2	7-32	MA	2	Fe-Mn-ox	2.5Y6/3	10-25	9.2
	GH3	32-112	MA	15	Cnod	2.5Y5/4	2-10	9.1
	GH4	112-128	MA	1	Cnod	2.5Y6/3	0-2	8.9
	HH1	0-7	SAB to MA	2	Fe-Mn-ox	2.5Y5/4	10-25	9.1
	HH2	7-96	MA	10	Cnod	2.5Y5/3	2-10	9.2
	HH3	96-120	MA to SAB	5	Cnod	2.5Y5/4	0-2	9
	IH1	0-20	MA	5	Fe-Mn-ox/Cnod	2.5Y6/4	0-2	8.5
	IH2	20-100	MA	0	-	2.5Y6/5	0	9
	JH1	0-17	MA	0	-	2.5Y6/3	0	8.7
	JH2	17-69	MA	1	Cnod	2.5Y6/3	0	9
	KH1	0-5	SAB	1	Cnod	2.5Y5/4	2-10	8.5
	KH2	5-35	MA	0	-	2.5Y6/2	0	8.3
	LH1	0-35	MA	0	-	2.5Y6/2	0	8.5
M2	NH1	0-8	SAB	0	Cnod	2.5Y6/3	0-2	9.3
	NH2	8-41	MA	20	Cnod	2.5Y6/4	0-2	9.5
	NH3	41-115	MA	10	Cnod	?	0-2	9.5
	OH1	0-7	SAB	5	Fe-Mn-ox/Cnod	2.5Y6/4	0-2	9.2
	OH2	7-39	MA	15	Cnod	2.5Y5/3	10-25	9.2
	OH3	39-110	MA	15	Cnod	2.5Y5/4	0-2	9.4
	PH1	0-13	AB to SG	2	Cnod	2.5Y6/4	>25	8.1
	PH2	13-45	SG	70	Mix	2.5Y6/4	0-2	9.1
	PH3	45-100	MA	5	Fe-Mn-ox/Cnod	2.5Y6/4	>25	9.2
	QH1	0-3	SG to SAB	70	Mix	10YR4/3	0	8.0
	QH2	3-50	SG	70	Mix	10YR4/4	0	8.1
	QH3	50-70	MA	2	Fe-Mn-ox/Cnod	2.5Y6/4	0-2	7.9
	QH4	70-100	MA	1	Fe-Mn-ox/Cnod	2.5Y6/3	2-10	8.5
	RH1	0-2	SG	70	Mix	7.5YR3/3	0	7.5
	RH2	2-34	SG	70	Mix > Sil	10YR5/6	0	7.8
	RH3	34-67	SG	70	Mix > Sil	10YR4/4	0	8.3
	RH4	67-83	SAB	50	Mix	2.5Y6/4	0-2	8.5
	RH5	83-95	MA	70	Mix	2.5Y5/4	0-2	8.2
	RH6	95-100	MA	2	Fe-Mn-ox/Cnod	2.5Y5/4	0-2	8.2
P	TH1	0-6	SG	0	-	10YR4/6	0	7.2
	TH2	6-21	SAB	1	Sil	10YR4/4	0	7.4
	TH3	21-42	SAB	2	Sil/Fe-Mn ox	10YR4/6	0	7.7
	TH4	42-54	SAB	3	Fe-Mn-ox	10YR4/6	0	7.8
	TH5	54-105	MA	3	Fe-Mn-ox	2.5Y5/6	0-2	8

M3	SH1	0-10	SG to AB	nd	nd	nd	10-25	9.3
	SH2	10-70	AB to P	nd	nd	nd	0-2	9.2
	SH3	70-100	AB to MA	nd	nd	nd	2-10	9.3
	SH4	100-120	AB to MA	nd	nd	nd	0-2	9.3
	UH1	0-16	SG to AB	nd	nd	nd	>25	9.2
	UH2	16-50	AB to P	nd	nd	nd	10-25	9.3
	UH3	50-110	AB to MA	nd	nd	nd	10-25	9.3
	WH1	0-4	SG to AB	nd	nd	nd	10-25	9.3
	WH2	4-80	AB to P	nd	nd	nd	2-10	9.3
	WH3	80-100	AB to MA	nd	nd	nd	2-10	9.3
	XH1	0-10	SG to AB	nd	nd	nd	>25	9.1
	XH2	20-40	AB to P	nd	nd	nd	10-25	9.3
	XH3	40-70	AB to MA	nd	nd	nd	10-25	9.4
	YH1	0-10	AB	nd	nd	nd	>25	9.3
	YH2	10-30	AB to P	nd	nd	nd	2-10	9.4
	YH3	30-60	AB to P	nd	nd	nd	10-25	9.4
	ZH1	0-20	SG to AB	nd	nd	nd	2-10	9.4
	ZH2	20-58	AB to P	nd	nd	nd	>25	9.4
	ABH1	0-14	SG to AB	nd	nd	nd	2-10	9.5
	ABH2	15-50	AB to P	nd	nd	nd	2-10	9.5

The studied mima-like mounds are located in the Mayo Tsanaga granitic watershed (Fig. 3.1B). They are distributed within stream networks and are regularly spaced (Fig. 3.1C) with R=1.72 (Appendix A) meaning over-dispersion (Clark and Evans, 1954). They are easily identified because of their sparse vegetation cover (Fig. 3.2A) and their darker colour (Fig. 3.3). The size of the mounds is up to 10 m in diameter and up to 1 m in height (Fig. 3.3B). Their nature can be referred to as the clay-rich pediment layer described by Sieffermann (1967) and Morin (2000), to which carbonate nodules are often associated (see Chapter 2). Field observations showed that mima-like mounds have various heights; some are flattened, whereas others have whaleback morphologies (Fig. 3.4A, 3.4B). A fine beige alluvium surrounds all the various types of mima-like mounds (Fig. 3.3, 3.4C). In less eroded and well-preserved areas, a red-brown fersiallitic pediment, described by Sieffermann (1967) and Morin (2000), overlies them (Fig. 3.2, 3.4A). Some flattened mima-like mounds are also partially buried by a coarse alluvium interfingering with the clay-rich sediment (Fig. 3.4B). The various observed morphologies are undoubtedly related to the intensity of erosion processes (Fig. 3.4). The peculiarity of mima-like mounds is that their surface is completely covered by carbonate nodules (2 cm < diameter < 10 cm) and Fe-Mn micro-nodules (Fig. 3.3B). These nodules can also be found in deeper horizons (Fig. 3.3C, Table 3.1).

In the studied areas, the thickness of the clay-rich sediment composing mima-like mounds is still unknown, as its base could not be reached. However, according to Morin (2000), it can be up to several meters (about 6 m) in the northwestern area of Mora. Nevertheless, field observations suggest that this clay-rich sediment has no genetic relationship with the granitic bedrock. Morin (2000) reported the following sedimentary and lithological succession in the region, from top to bottom: (i) clays with sand lenses, corresponding to the sediment composing the mima-like mounds, on (ii) a ferruginous duricrust, overlaying (iii) a saprolite directly developed from the cratonic rocks. However, the clay-rich sediment seems genetically related neither to the ferruginous duricrust nor the granitic bedrock. A mima-like mound deposited directly with a sharp unconformity on granitic inselbergs emphasizes the lack of any kind of causal relationship (Fig. 3.4D). However, more arguments are needed to strengthen this assumption.

Twenty-seven soil profiles were described along the trenches and descriptions are given in Table 1. The soils contain a very small amount of organic matter (less than 1%) and are essentially mineral (Fig. 3.5). The structure is single grain to angular blocky in the surficial horizons, becoming angular

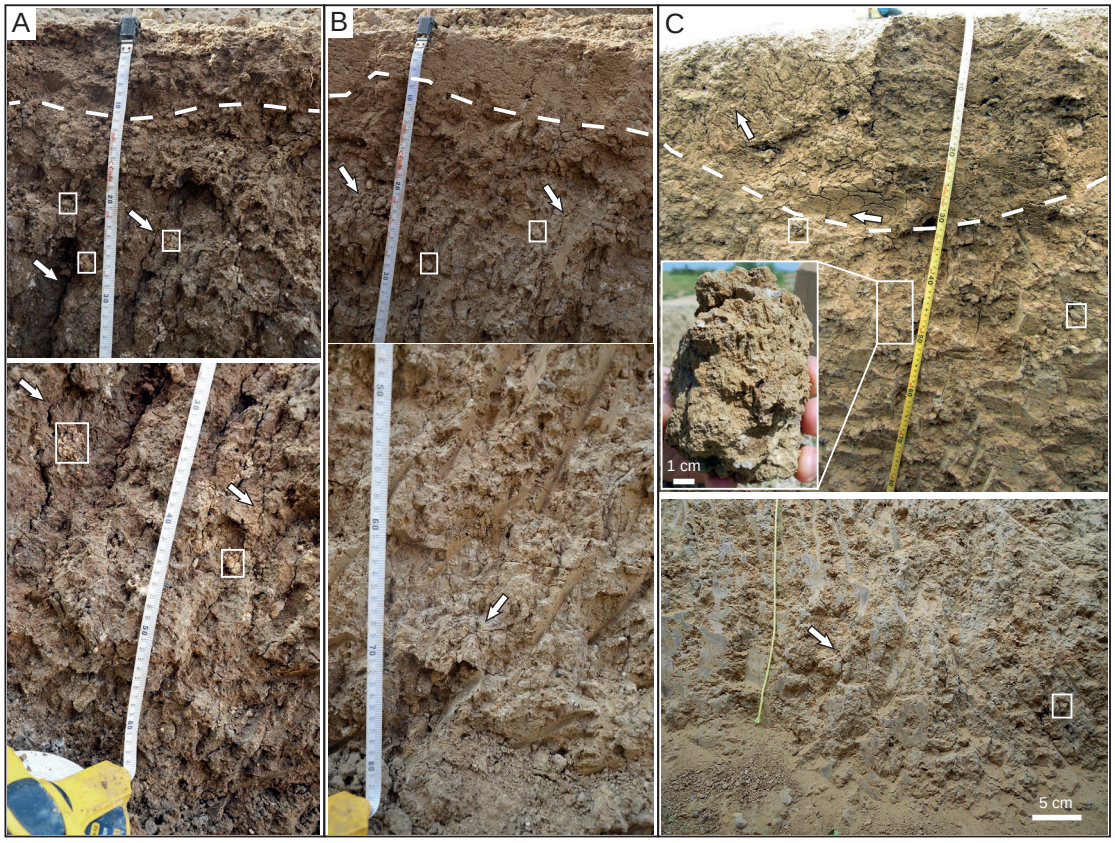

Figure 3.5 – A) Soil profile Y in mima-like mound M3. The structure is angular blocky from surface to 10 cm deep and angular blocky to prismatic below 10 cm (dashed line). Below 10 cm, slickensides are well developed and associated with vertical cracks (arrows). B) Soil profile W in mima-like M3. The structure is single-grained to angular blocky in the first 10 cm and angular blocky to prismatic below. Slickensides are also visible with vertical cracks (arrows). C) Top photo: soil profile D in mound M1. The structure is angular blocky in the first 30 cm and some preferentially oriented cracks are visible (arrows). The structure is massive below 30 cm and peds are blocky, although cracks are less visible. Bottom photo: soil profile J in mound M1. The structure is massive. Cracks, visible in the lower part of the profile, are not well developed (arrows). White squares highlight some carbonate nodules inside the soil profiles. Pictures of mound M3 were taken in July 2012 and mound M1 in September 2013.

blocky to prismatic or massive with depth. Some vertical cracks are visible in mound M3 below 10 cm (Fig. 3.5A, 3.5B, arrows). Mound M1 shows some preferentially orientated cracks, such as in profile D (Fig. 3.5C, top, arrows). However, the structure of M1 is angular blocky to massive in depth (Fig. 3.5C top, ped), and vertical cracks are locally visible but to a lesser extent compared to M3 (Fig. 3.5C, bottom, arrow). Carbonate nodules (Fig. 3.5, white squares) and Fe-Mn oxides compose the skeleton; soil colour is yellowish-grey and pH_{H2O} is alkaline ($8 < pH_{H2O} < 10$). The fine earth reacts to HCl indicating the presence of diffuse carbonate (Table 3.1). However, the coarse alluvium interfingering the clay-rich sediment in mound M2 has a single grained structure with a skeleton composed of silicate minerals, mainly quartz and feldspars, and a dark yellowish brown soil colour. The fine earth does not, or only weakly, react to HCl and pH_{H2O} are $7 < pH_{H2O} < 8$. The dark brown fersiallitic pediment has a sub-angular blocky structure with a skeleton composed of silicate minerals. The fine earth does not react to HCl, and pH_{H2O} is around 7. However, the lower part of the fersiallitic pediment displays the same properties as the mima-like mound soils, with a massive structure, a yellowish-grey soil colour, a

pH_{H2O} > 8 and a fine earth weakly reacting to HCl.

3.3.2 Grain size distribution

Cluster analysis of grain-size distributions of all sediment samples (Fig. 3.6) generates seven clusters (with a cophenetic correlation coefficient of 0.54, n=207). Each cluster is represented by its median (Fig. 3.6, black lines) and its associated standard error (Fig. 3.6, grey-shaded areas). The median and its error are plotted as an independent cluster (n=10, no clr and no CA processing) for the silicate residue trapped within the carbonate nodules, for comparison with other sediments. Six main modal classes (mci) have been recognized (Fig. 3.6): mc1) coarse-medium sands, mc2) medium-fine sands, mc3) very fine sands-coarse silts, corresponding to the desertic lœss window (Crouvi et al., 2010), mc4) fine silts, mc5) coarse clays, and, finally, mc6) fine clays. These modal classes display various relative amplitudes and are used to characterize each cluster type. The samples belonging to mound M3, especially those found on the lower edge of the mound, are in the first cluster (n=18). Cluster 1 is characterized by five modal classes, listed from higher to lower amplitudes: $mc5 > mc3 > mc1 > mc4 > mc6$. The second cluster (n=21) is fairly similar to cluster 1, with the same five modal classes characterized by similar amplitudes, except mc1, which is shifted toward the coarse sands. It groups samples from the upper edge of mound M3 and from both convex sides of mound M1. Cluster 3 (n=41) groups samples from the surface of mound M1 and five modal classes are identified: $mc5 \approx mc3 > mc1 > mc4 > mc6$. The alluvium deposited on the sides of mounds M1, M2, M3, and the transitional part between the fersiallitic pediment and the clay-rich sediment in P, are represented by cluster 4 (n=16). This cluster is characterized by four modal classes: $mc1 > mc3 > mc5 > mc4$. Samples from the core of mounds M1, M2, and the deeper part of P are grouped in cluster 5 (n=54). This cluster is characterized by five modal classes: $mc3 > mc5 > mc4 > mc1 > mc6$. Cluster 6 (n=52) is fairly similar to cluster 5, except that mc1 mode is shifted toward very coarse sand. Samples from the core of M3 are found in this cluster. Finally, surficial horizons from the fersiallitic pediment P are displayed in cluster 7 (n=5), with the following mode amplitudes: $mc3 > mc2 > mc4 > mc5$. The carbonate nodule residue group (n=10) is characterized by the following 4 modes listed from higher to lower amplitudes: $mc3 > mc5 > mc4 > mc1$.

Table 3.2 summarizes the mean, the minimal and maximal values of the clay, silt and sand contents (%) for each cluster and for the silicate residue trapped inside the nodules. The maximal clay proportions in the clay-rich sediment are > 30% and can reach 67% (e.g. in cluster 2). However, the clay content can also be fairly low, e.g. in clusters 3, 5, and 6. In clusters 5 and 6, mean values are close to 20%. As expected, alluvium and fersiallitic pediment have high proportions of sand, i.e. $47.6 \pm 6\%$ and $63.2 \pm 10.1\%$ in average, respectively. The silt-fraction is high, between 30 and 55% in all the clusters. The silicate residue trapped inside the nodules has a high silt fraction content (52.2±3.5%) and displays a maximal clay value of 39.2%. The sand proportion is around 20%.

At the mound scale, highest proportions in the clay fraction (50-70%) are found in both convex sides and in the deepest layers of mound M1 (Fig. 3.7, mound M1 see Fig. 3.3B). The lowest values of clay content (< 20%) are concentrated in a belt located in the middle part of the mound and at both extremities.

3.3.3 Clay mineralogy

Smectite and kaolinite are the main clay minerals composing the clay-rich sediment, the alluvium, and the silicate residue trapped in the carbonate nodules, whereas kaolinite is clearly dominant in

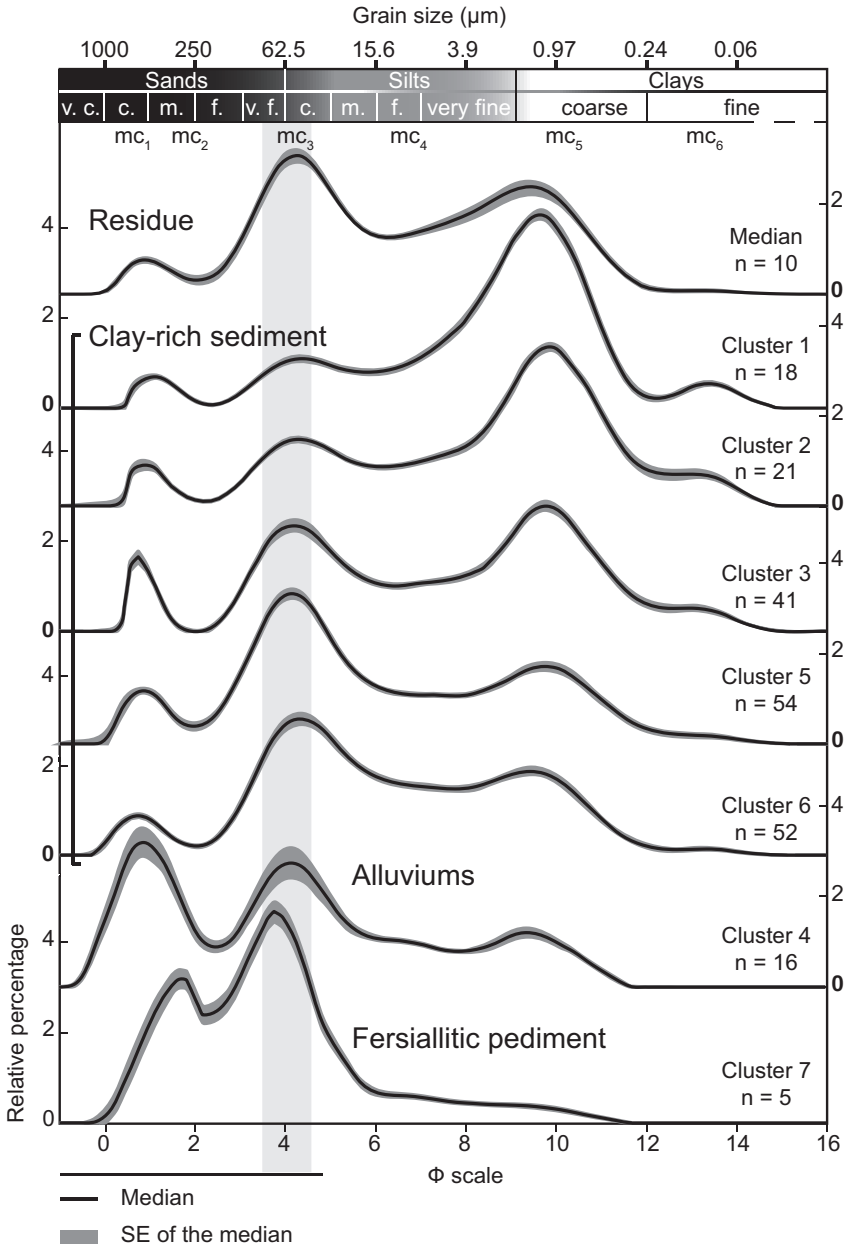

Figure 3.6 – Grain-size distributions grouped in seven clusters represented by their median (black line) and its associated standard error (grey-shaded areas). Clusters were processed according to the Euclidian distance between the samples (n=207) using the Ward agglomeration algorithm (with a cophenetic correlation coefficient of 0.54). Data were previously transformed using the centred log-ratio method. Six modal classes (mci) are identified. Their respective presence and amplitudes are used to characterize each cluster. The dark rectangle around 4 ϕ represents the desertic lœss window (20-80 μm) according to Crouvi et al. (2010). The cluster representing the silicate residue of carbonate nodules (n=10) has not been included in the hierarchical clustering analysis in order to directly compare this particular group with other sediments from the landscape. In order to provide a maximum of information, the descriptive terminology used for sands and silts is adapted from the GRADISTAT program (Blott and Pye, 2001) and the one for the clays from the United States Department of Agriculture. Abbreviations: v for very, c for coarse, m for medium and f for fine.

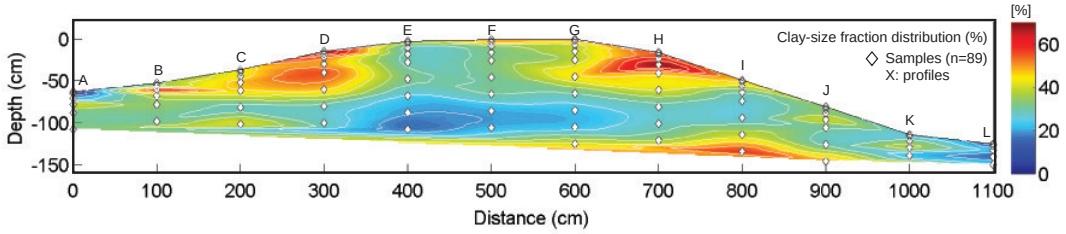

Figure 3.7 – Distribution of the clay-size fraction (%) in mima-like mound M1 according to a cubic interpolation (n=89). Capital letters refer to profile names.

the fersiallitic pediment (represented by cluster 7; Table 3.2). Regarding the smectite/kaolinite ratio (S/K) of samples belonging to each grain-size cluster and carbonate nodule residues (Table 3.2), their mean values are above 1 in clusters 1, 6 and for carbonate nodule residues. They range from 0.5 to 1 in clusters 2, 5, and 4, and are < 0.5 in clusters 3 and 7. In terms of absolute values, the lowest S/K is about 0.04 in the fersiallitic pediment. High ratio values are < 1 in clusters 3 and 7, between 1 and 1.5 in clusters 2, 5, 6, and 4, and finally < 2 in cluster 1 and in carbonate nodule residues.

3.3.4 Soil micromorphology

Soil thin sections from mound M1 were sampled between 10-18 cm and 90-98 cm, respectively (Fig. 3.8A, 3.8B). Thin sections were also made in coarse and fine alluvium sediments (Fig. 3.8C, 3.8D, respectively), and the fersiallitic pediment (Fig. 3.8E, 3.8F). The aggregate microstructure of the soil composing the mima-like mound (Fig. 3.8A) is angular blocky, with long horizontal and vertical channel voids between aggregates. The groundmass is composed of a very fine and unrecognizable clay fraction, with a pale yellow and striated b-fabric (Fig. 3.8A, white arrows). The cross-striated nature of the b-fabric is better observed at higher magnification (Fig. 3.8B, white and grey arrows). The groundmass also includes a coarse silt fraction: the grains are essentially composed of quartz and sparse epidote, feldspar, and biotite. The grains display a weakly weathered pattern, with a high sphericity, smooth edges, but an angular roundness. The two major pedofeatures are Fe-Mn oxyhydroxide nodules and carbonate nodules. They both are disorthic nodules, enclosing skeleton grains of similar nature to their surrounding matrix, but with sharp boundaries. The coarse alluvium partially burying the flattened mound M2 was sampled between 23 and 30 cm for thin sections (Fig. 3.8C). Peds are subangular blocky. The groundmass is yellowish-brown, displayed as coatings around mineral grains but also as broken coatings floating between the grains (Fig. 3.8CII). The coarse material is sandy and composed of microcline, quartz, epidote, biotite, and feldspars. The only pedofeature is an anorthic Fe-Mn oxyhrydroxide nodule. Finally, the c/f related distribution is chitonic. The structure of the fine-grained alluvium surrounding mound M1 (2-10 cm) is horizontal and laminated (Fig. 3.8D). The coarse fraction (mainly silt-sized) in the groundmass is well sorted and composed of quartz, feldspars, epidote, and biotite. There is no fine material in the groundmass, except that associated with some rare relic peds (yellowish-brown b-fabric). Anorthic $Fe-Mn$ oxyhydroxide nodules and fibrous organic components are the only observed pedofeatures. Finally, the c/f-related distribution is coarse monic. The structure of the peds in the fersiallitic pediment (40-48 cm) is angular blocky (Fig. 3.8E). The colour of the groundmass varies from pale yellow to yellowish-red. It is granostriated and porostriated, and coatings are randomly orientated. Two classes of grain-sizes are observed, one in the fine silt fraction and another in the fine sand fraction. Grains are mainly quartz and feldspars (weakly weathered), with a smooth angular shape. Epidote and biotite are also present as accessory minerals. The b-fabric of the

Table 3.2 – Mean percentages, standard errors of the mean (SEM), minimum (min) and maximum (max) clay, silt, and sand contents (relative %), smectite, and kaolinite contents (relative %), and ratios of smectite/kaolinite (S/K) in each cluster and silicate residue of carbonate nodules (= Residue).

		Clay-rich sediment					**Alluvium**	**Fersial. ped.**	**Residue**
		Cluster 1	Cluster 2	Cluster 3	Cluster 5	Cluster 6	Cluster 4	Cluster 7	-
	n	18	21	41	52	54	16	5	10
Clay (%)	Mean	49.5	52.4	39.2	23.9	22.8	12.0	4.5	26.2
	SEM	2.2	2.2	1.4	1.0	1.0	1.0	0.8	2.8
	Min value	36.7	45.5	28.1	14.0	9.1	7.6	3.3	22.1
	Max value	56.2	67.0	48.6	35.0	33.0	16.4	6.3	39.2
Silt (%)	Mean	40.6	34.3	42.1	46.0	55.0	40.4	32.3	52.2
	SEM	1.9	1.4	1.3	0.8	1.1	3.0	3.9	3.5
	Min value	34.5	26.0	35.3	40.2	48.0	32.3	25.7	29.3
	Max value	53.0	39.7	51.4	52.8	68.4	55.3	39.5	47.9
Sand (%)	Mean	9.8	13.3	18.7	30.1	22.2	47.6	63.2	21.6
	SEM	0.8	1.2	1.0	1.4	0.9	6.0	10.1	3.0
	Min value	7.1	7.1	14.2	22.1	16.0	37.1	54.2	10.6
	Max value	14.9	17.0	22.4	41.6	29.4	53.7	70.9	20.4
	n	5	5	5	5	5	5	3	12
S/K	Mean	1.4	0.7	0.5	0.7	1.0	0.8	0.2	1.8
	SEM	0.4	0.1	0.1	0.2	0.1	0.1	0.1	0.2
	Min value	0.4	0.4	0.3	0.5	0.8	0.4	0.0	0.7
	Max value	2.9	1.0	0.6	1.3	1.3	1.2	0.3	3.8
Smectite (%)	Mean	42.9	30.4	25.1	29.8	40.7	33.8	12.2	46.0
	SEM	8.9	3.6	2.8	7.3	2.8	4.6	0.8	4.2
	Min value	15.8	20.2	14.1	4.5	35.0	23.8	10.2	24.1
	Max value	70.1	42.4	29.1	47.9	48.4	49.4	13.1	71.5
Illite (%)	Mean	13.1	16.9	18.4	14.8	11.6	12.6	23.1	17.8
	SEM	4.5	2.0	1.8	2.9	1.7	2.1	3.6	2.3
	Min value	4.7	10.2	13.2	8.3	8.3	7.7	15.1	10.0
	Max value	30.6	22.0	23.9	25.0	18.1	18.2	29.1	34.0
Kaolinite (%)	Mean	37.4	45.4	48.1	46.7	40.2	46.1	54.1	30.6
	SEM	4.6	1.9	1.9	4.1	2.1	2.9	3.1	2.3
	Min value	21.4	40.5	43.1	35.5	35.9	34.9	48.9	16.2
	Max value	46.8	49.2	53.5	60.4	46.7	50.4	60.9	44.1
Chlorite (%)	Mean	6.5	7.2	8.5	8.7	7.5	7.6	10.6	5.6
	SEM	1.0	0.7	0.3	0.4	0.5	0.7	1.4	0.9
	Min value	3.8	4.8	7.7	7.9	6.5	5.8	8.9	2.3
	Max value	9.6	8.7	9.2	10.1	8.9	9.6	13.7	10.7

groundmass in the fersiallitic pediment (between 14 and 20 cm) is granostriated and its colour varies from yellow to red (Fig. 3.8F). There are two major grain-sizes, a fine silt and a fine sand fraction. In the silt fraction, angular quartz and feldspar grains are mainly smooth. The sand fraction displays the same mineralogy, with smooth- and subangular-shaped grains. Both fractions are weakly weathered.

3.4 Discussion

The presence of mima-like mounds in eroded areas of the landscape supports that erosion processes are involved in their morphology. Field observations suggest that vegetation patterns do not play a role in mound formation (Fig. 3.2, 3.3A). The question of another biotic factor (termite activity?) may be involved is not totally ruled out, especially as the over-dispersion spacing of the mounds may support a biotic origin (Cramer and Midgley, 2015). Nevertheless, thus far, observations indicate an abiotic origin for mima-like mounds from northern Cameroon. Interestingly, the clay- and carbonate-rich sediment composing mima-like mounds has already been described. It was observed (i) at various depths in all the Diamare piedmont (i.e. in the Mora and Kaele plains), (ii) outcropping on the southern bank

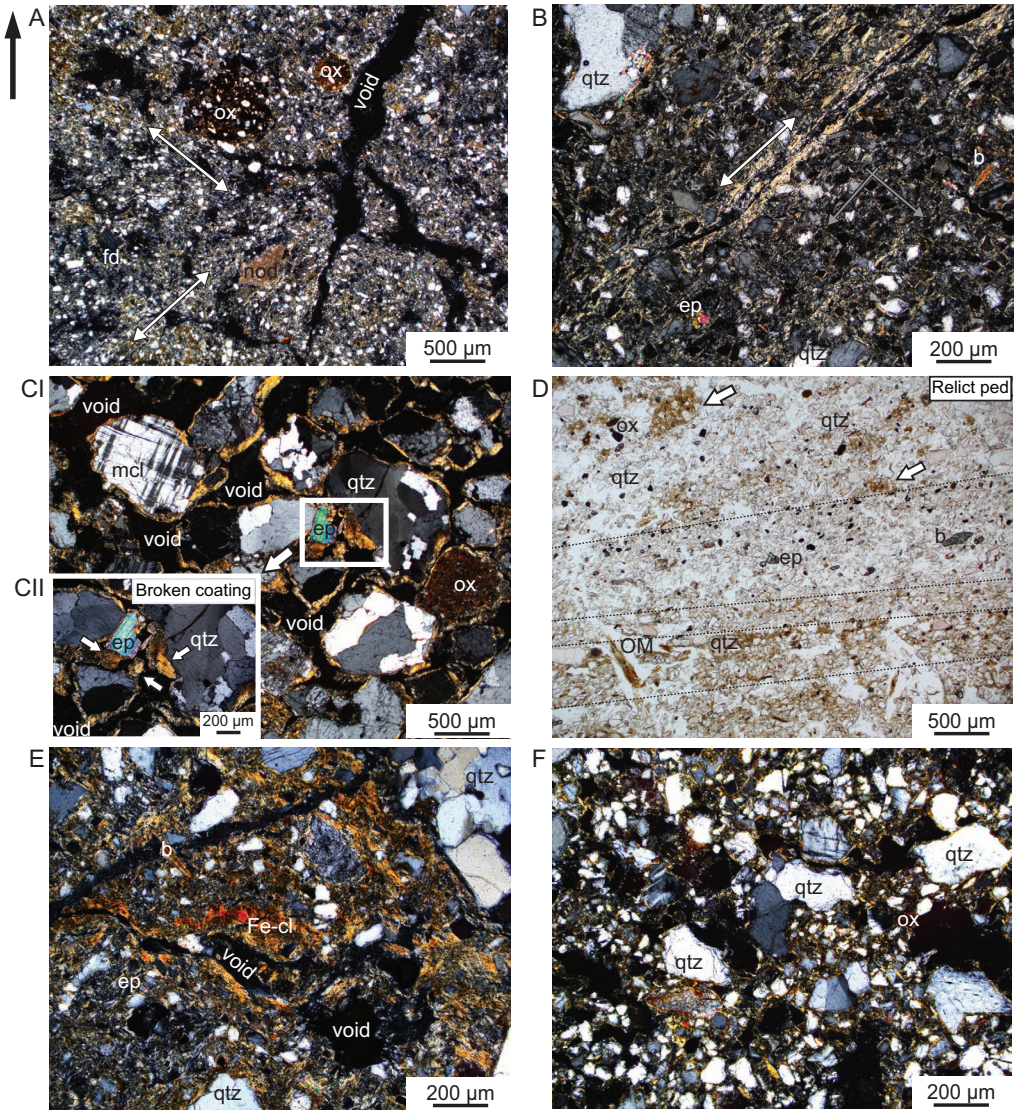

Figure 3.8 – Illustrations of soil thin sections, the black arrow refers to the top. Ox for Fe-Mn oxide nodule, nod for carbonate nodule, fd for feldspar, mcl for microcline, qtz for quartz, ep for epidote, b for biotite, OM for organic matter, Fe-cl for iron-clay coating, PL for polarized light and CPL for crossed-polarized light. A) Mima-like mound (M1) between 10-18 cm: the groundmass is pale yellow and has a striated b-fabric, whose orientation is illustrated by the white arrows (CPL). B) Mima-like mound (M1) between 90-98 cm: the grey and white arrows show the cross-striated and striated orientation of the groundmass, respectively (CPL). The striated and cross-striated nature of the b-fabric in the mima-like mounds (A and B) can be referred to as slickensides, which are typical features resulting from shrink-swell processes. C) Coarse alluvium interfingering the clay-rich sediment in M2 (23-31 cm): a broken coating is shown in a white box (CPL); the c/f related distribution is chitonic with a fine yellow birefringence layer surrounding all minerals. D) Fine alluvium (2-10 cm) surrounding M1: several horizontal deposits are shown and highlighted by black dashed-lines; relict peds (white arrows) show a c/f single-spaced porphyric, (PL) and are found in a c/f coarse monic material. E) Fersiallitic pedolith between 40-48 cm (CPL): the groundmass varies from yellow to yellowish-red and coatings are randomly orientated. F) Fersiallitic pedolith between 14-21 cm (CPL): the groundmass is yellow to yellowish-red and displays a granostriated b-fabric.

of the Mayo Tsanaga (Siefferman, 1967; Brabant and Gavaud, 1985; Morin, 2000), and (iii) was even

observed farther away in the Chad Basin between the Logone and Chari rivers (Erhart, 1954; Pias, 1962; Bocquier, 1973). Consequently, these repeated occurrences have led this sediment to be interpreted as an extended layer, possibly associated to a specific regional deposition event (aeolian, palustrine?). But how can mound morphologies be explained? Another interesting point is that mima-like mounds systematically occur in areas described as *hardés* or degraded soil (Fig. 3.1B), questioning the role of pedogenesis in their formation.

3.4.1 Mima-like mounds as Vertisol relics

Vertisols are clay-rich soils with a content ≥ 30% in the <2 μm size fraction (Wilding, 2004; Southard et al., 2011; FAO, 2014). The smectitic group of swelling clays (e.g. montmorillonite) represents the main soil clay mineralogy. Consequently, soils swell and shrink when they undergo marked changes in their soil moisture content (Hubble, 1984, Dudal and Eswaran, 1988; Mermut et al., 1996; Southard et al., 2011). Swell-shrink processes induce important volume variations in the soil (Southard et al., 2011). They can shape the ground surface with an alternation of knolls and depressions, known as gilgai micro-relief (Prescott, 1931; Oakes and Throp, 1950; Hallsworth et al., 1955; Mermut et al., 1996). They also lead to characteristic macro-features in the solum, such as vertical cracks, slickensides (or grooved shear planes), and cyclic horizons, organised in micro-low, micro-high, and intermediate parts at all depths (Wilding and Tessier, 1988; Eswaran et al., 1988, Wilding et al., 1990). The presence of a vertic horizon characterized by these macro-features is needed to define a soil as a Vertisol (FAO, 2014). According to Wilding et al. (1990), micro-lows have deep A and Bss horizons, while micro-highs have a thin A horizon, without any Bss horizons. When present, a Bk horizon in the micro-highs is characterized by a higher content in hard secondary carbonate than in micro-lows.

Today, climatic conditions in northern Cameroon (chapter 2) are favourable for Vertisol genesis. In terms of their global distribution, about 60% are found in the Tropics (Wilding, 2004). Brabant and Gavaud (1985) described and mapped some Vertisols in the Diamare, but most of them are in the south bank of the Mayo Tsanaga, near Kaele, or downstream near the sand belt. In the studied sites where mima-like mounds are observed, Planosol, associated with Solonetz, is generally the soil type. However, independently of the nature of soil, the striking feature is that mima-like mounds are observed in degraded areas, i.e. *hardés*. Soil descriptions, grain-size distributions, clay mineralogy, and thin-section observations suggest that mima-like mounds can be interpreted as *degraded Vertisols* or *Vertisol relics*, which could possibly have evolved toward Planosol or Solonetz.

Soil observations demonstrate that cycling and vertical cracks are present in some parts of the mima-like mounds (Fig. 3.5). Vertical cracks are observable in the mound M3 (Fig. 3.5A, 3.5B). In soil profile D (M1), what can be interpreted as a Bss horizon seems to have been truncated (Fig. 3.5C, top). Interestingly, the clay content in micro-lows can be slightly higher than in micro-highs (Yule and Ritchie, 1980; Mermut et al., 1996). The truncated Bss horizon is located on the perimeter of the mound M1, where the clay fraction reaches 67% (Profile D, Fig. 3.7). It may thus be interpreted as an ancient micro-low. Cracks are less visible in the profile J (Fig. 3.3C, down) compared to what is seen in M3. This could be due to the season in which the pictures were taken. In M3, they were taken during the dry season of July 2012 and in mound M1 in September 2013, during the wet season. The cracks generally occur during the dry season; it is likely that they were less visible in September. Nevertheless, the soil structure observed in mima-like mounds is typical of swell-shrink processes. Fe-Mn oxides and carbonate nodules are significant components of mima-like mounds (Fig. 3.3B, 3.3C) and they are known to be common features in Vertisols (Wieder and Yaalon, 1974; Ahmad, 1983). Regarding grain-size distributions and clay mineralogy of the soil residue trapped in carbonate nodules,

it is similar to the surrounding soil (Fig. 3.6, Table 3.2). Consequently, these nodules are secondary pedogenic carbonate nodules precipitated inside the mima-like mound soil matrix. However, in Vertisols, secondary carbonate nodules are generally observed in the Bk horizon, which occur at about 20 cm deep in micro-highs, or about 100 cm deep in micro-lows (Wilding et al., 1990, Kovda et al., 2003, 2006). In mima-like mounds, even if some nodules are observed in deep horizons, they accumulate in large amounts at the surface, forming a cover (Fig. 3.3B, 3.3C). It is likely that the erosion of the surficial horizons, leaving only the Bk horizon at the surface, explains this surficial nodule accumulation.

Regarding the grain-size distributions and the clay mineralogy in mima-like mounds, they are similar to what is generally expected in Vertisols. The clay content in mima-like mounds is high, with an average proportion of 32% (standard error of the mean = 0.935, n=186) and with maximum values reaching 67% (Table 3.2). In addition, they contain a high proportion of smectite (Table 3.2), which is significantly higher than in the overlaying fersiallitic pediment (mean S/K ratio = 0.2±0.1). However, even if these components seem to be key features of the sediment forming mima-like mounds, they do not strictly correspond to Vertisol characteristics. First of all, in some cases, the clay content can be < 30% (Table 3.2). The grain-size distribution shows that coarse clays are more abundant that fine clays, which is generally the opposite in Vertisols well-structured (McGarry, 1996). Moreover, kaolinite can be the main clay mineral composing the clay-size fractions, which is often the case at the mound surface (cluster 3, Table 3.2). But a potential and progressive denaturation of smectite or an exogenic and aeolian contribution can explain this. Regardless of the reasons why kaolinite is dominant, these observations show that smectite is not always the main clay mineral in the clay-rich sediment, whereas it should be in Vertisol (Coulombe et al., 1996a). At the microscale, the b-fabric is striated to cross-striated (Fig. 3.8A, 3.8B), which is common in clay-rich soils subject to shrink-swell processes (Dalrymple and Jim, 1984; Jim, 1990). These features are particularly observed in mima-like mounds and absent in the alluvium or the fersiallitic pediment. All these observations point to Vertisols, but not exclusively. Consequently, mima-like mounds from the Diamare piedmont are interpreted as *degraded Vertisols* or *Vertisol relics*.

3.4.2 From gilgai micro-relief to present-day mima-like mounds

The mima-like mounds from the Diamare piedmont may thus be interpreted as Vertisol relics. Vertisol degradation implies that there was a phase during which the Vertisols developed and another phase when they were degraded and eroded. The Bio-Rhexistasy theory, proposed by Erhart (1967), illustrates this conjecture. He described two major environmental phases: (i) Biostasy phases are stable periods characterized by dense vegetation cover, high soil development and biogeochemical weathering, during which leaching processes, and biogeochemical deposits prevail. In contrast, (ii) Rhexistasy phases are characterized by unstable periods due to drastic changes in ecosystems (*rhêksis* means *to break up*). The decrease of vegetation cover and the destabilization of soils due to hydric changes favour erosion and detrital sedimentary deposits. It is demonstrated that there is a critical threshold of 55% vegetation cover, below which erosion rates increase rapidly (Snelder and Bryan, 1995, in Goudie, 2013). At the regional scale, Vertisols are perfectly adapted to present-day climatic conditions and can easily develop in the Diamare piedmont because of the presence of clay-rich sediment. However, Vertisols are located at lower altitudes compared to mima-like mounds (Martin, 1961; Siefferman, 1967; Bocquier, 1973; Brabant and Gavaud, 1985). It can be hypothesized that the topography plays an important role for Vertisol genesis in this region. This is explained by their chemical properties. Vertisols must have a high content of clay with high surface area and usually be highly alkaline (Coulombe et al., 1996a). The cation exchange capacity in Vertisols is typically high, saturated with Ca^{2+}, Mg^{2+}, and Na^{+}, depending on the clay mineralogy and the parent material. Moreover, the pH is often neutral to

alkaline. These conditions, and a high silica activity, favour the stability and the formation of smectite (Eswaran and Wong, 1978). On the contrary, leaching processes and acidic conditions induce the denaturation of smectite and the formation of kaolinite, leading to the development of other types of soils (Eswaran et al., 1988). The mima-like mounds are presently located in eroded and degraded areas (hardés), but it is possible that these areas were not always degraded. Consequently, it is proposed that the extent of the area favourable to Vertisol genesis varied through time and reached mima-like mound locations under different climatic conditions. To explain the link between Vertisol genesis and

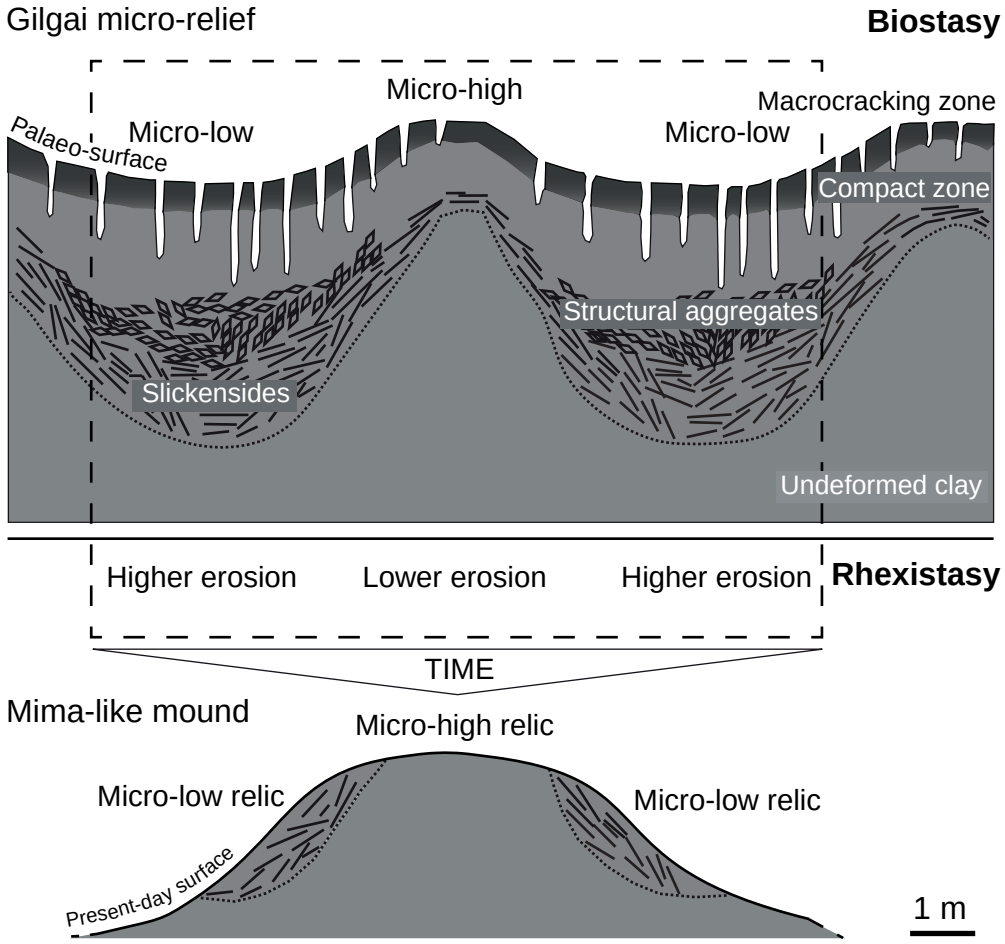

Figure 3.9 – Hypothetical erosion scenario leading to mima-like mound formation. Top: this figure is modified from Coulombe et al. (1996b) and shows Vertisol genesis associated with a gilgai micro-relief characterized by alternations of micro-highs and micro-lows. Secondary carbonate nodules form during Vertisol genesis in a Bk horizon, developing at 20 cm in micro-highs and at 100 cm in micro-lows. Bottom: mima-like mound, or residual gilgai micro-relief, after a phase of erosion and composed by relics of micro-lows and micro-highs (compare with Fig. 3.7). Vertisol genesis at mima-like mound locations may occur during a Biostasy phase, characterized by wetter conditions than in present-day; onset of erosion may correspond to a Rhexistasy phase, characterized by drastic changes in climatic conditions.

mound formation, it is interesting to note that the diameter of mima-like mounds, which can reach up to 10 m, is consistent with what is commonly observed in a gilgai landscape. The common distance from the micro-high to the micro-low, or the radius, ranges from 2 to 5 m (Miller and Bragg, 2007). Consequently, Vertisol genesis could have been associated with a gilgai micro-relief, during a period

when Vertisol areas were extensive. This period of widespread occurrence can be defined as a Biostasy phase (Fig. 3.9). Precipitation of secondary pedogenic carbonate nodules and Fe-Mn micro-nodules are linked to Vertisol genesis, and thus, to this phase as well. Then, a Rhexistasy phase occurred as a response to climatic changes, inducing a decrease in favourable areas for Vertisol genesis, and an increase in erosion processes (Fig. 3.9). The gilgai micro-relief might have favoured preferential runoff in micro-lows rather than in micro-highs, inducing pejoration of landscape irregularities. Consequently, mima-like mounds observed in the present-day landscape are interpreted as residual micro-highs and micro-lows inherited from the gilgai micro-relief and resulting from differential erosion (Fig. 3.9). Furthermore, the wind has probably played a determinant role as an erosion agent. The Sahel of West Africa is a place for high-velocity winds produced by intense baroclinal gradients. In these sub-humid to arid areas, wind erosion is important and creates a diverse mosaic of morphologies such as inverted relief or yardangs, for example, which are the result of wind deflation erosion (Goudie, 2013). The mima-like mounds might be the result of contemporary interactions of both aeolian and fluvial erosion systems. This erosion association is a topic of significant discussion (Goudie, 2013) but seems to be effective particularly under short-term climate changes (Bullard and Livingstone, 2002). Independently of the type of erosion agent, erosion of fine fractions from surficial horizons can explain the relative accumulation, or pavement, of secondary carbonate nodules and Fe-Mn micro-nodules, normally found in a deeper Bk horizon, as a layer at the mima-like mound surface (Fig. 3.3B). It also explains the high clay content in both sides of the mounds (Fig. 3.7), which are the remaining parts of ancient micro-lows (Fig. 3.9).

3.4.3 Sediments adjacent to mima-like mounds and landscape changes

Analyses of sediments adjacent to mima-like mounds provide evidence of landscape geomorphogenesis. The grain-size distributions in the alluvium (both fine and coarse) and in the fersiallitic pediment are represented in clusters 4 and 7, respectively (Fig. 3.6). These two clusters lack a clay fraction (Fig. 3.6, mc6). They are also different from each other with the presence of mc2 in cluster 7 and a significant higher amplitude of mc5 in cluster 4. These variations can be explained by different sources of sediments and/or transportation parameters (Vandenberghe, 2013). From their mineralogy observed in thin sections (Fig. 3.8), they definitely differ in terms of transportation parameters rather than sources of sediment. Coarse alluvium includes some broken clay coatings and a fine yellow birefringence rim surrounds all mineral grains (Fig. 3.8C). This type of chitonic c/f related distribution corresponds to periods of high energy (coarse fraction) followed by slow water flow, which resulted in impregnations by fine material (Mücher et al., 2010). Field observations showed that the coarse alluvium was interfingering the clay-rich sediment of mound M2 (Fig. 3.4B), suggesting contemporaneous deposition. In the fine alluvium (Fig. 3.8D), the fine fraction is only present as relic peds, demonstrating the contribution of some reworked soils. Moreover, the S/K ratio in the alluvium varies between 0.45 and 1.23, which is close to the values observed in the clay-rich sediment, emphasizing the reworking of this proximal sediment. The fersiallitic pediment shows a complete disorganization of the clay-Fe coatings in the deepest horizon (Fig. 3.8E), while they are poorly marked in the surficial horizon (Fig. 3.8F). This disorganization indicates that fersiallitic pedofeatures are probably inherited and the soil material reworked. Therefore, the fersiallitic pediment may instead be a fersiallitic pedolith (Retallack, 2001). In the landscape, this pedolith is always found above the clay- and carbonate-rich sediment (Fig. 3.2, 3.4). This suggests they were reworked at the same time as the Vertisol surficial horizons, during gilgai micro-relief erosion. This means that the fersiallitic soil developed during the same period as Vertisols, but upstream. These interpretations strengthen hypotheses of high erosion events (Rhexistasy phase) occurring in northern Cameroon after a phase favourable for soil development

(Biostasy phase). Moreover, they emphasize the complexity of erosion-deposition processes in such terrestrial environments. Finally, grain-size distributions (Fig. 3.6) for all the sediments, including the clay-rich sediment, show a common modal class belonging to the desertic lœss window (20-80 μm) defined by Crouvi et al. (2010). At the micro-scale, well-sorted, smooth, and angular quartz, feldspars, and a few epidote grains characterize this fraction (Fig. 3.8). These observations raise questions about a possible aeolian contribution to the sediments. Maley (1981) already proposed an allochtonous contribution of sediments to explain the wide extent of the clay-rich sediment layer in the Far North region of Cameroon. Later, Mpeck (1994) studied the formation of Doyang, located in the south bank of the Mayo Tsanaga, between Maroua and Kaele, a formation already studied by Sieffermann in 1967. Mpeck (1994) proved the aeolian origin for this silty clay-rich deposit and emphasized its probable reworking after deposition. As previously demonstrated, field observations suggest the absence of a genetic relationship between the granite bedrock and the clay-rich sediment (Fig. 3.4D), making its origin as a simple result of granite bedrock weathering unlikely. Nevertheless, more investigations are needed to strengthen the hypothesis of an aeolian contribution to the mima-like mound area.

3.4.4 Are mima-like mounds inherited from Late Pleistocene-Holocene climatic changes?

Two main phases can thus explain mima-like mounds (Fig. 3.9); (i) during Biostasy, the Vertisol area was extended, and (ii) during Rhexistasy erosion increased, leading to Vertisol degradation in areas corresponding to the present-day mima-like mound locations. The shift from one phase to another probably results from changes in regional climates. It is proposed that the extent of Vertisol areas were related to wetter than present conditions. An increase in erosion, and thus the formation of mima-like mounds, can result from a serious decrease in the vegetation cover induced by climate change from wetter toward drier conditions. With these two environmental constraints, it is possible to discuss the potential role of Quaternary climatic changes in the Chad Basin area. During the Quaternary (Fig. 3.10), the main climatic changes in the African tropics are related to the intensity and the latitudinal position of the monsoon front, which is a thermodynamic heat response to orbital forcing (deMenocal et al., 2000; Mayewski et al., 2004; Wanner et al., 2008; Lezine et al., 2011; Shanahan et al., 2015). From ca. 14.8 to 5.5 ka, a strengthening and a northward expansion of the African monsoon system, due to a gradual increase of the Northern Hemisphere summer insolation, led to a climatic optimum, known as the African Humid Period (AHP; deMenocal et al., 2000; deMenocal and Tierney, 2012; Shanahan et al., 2015). This period is characterized by a higher rainfall rate and a general northward displacement of the vegetation zonation by 400-500 km, in conjunction with the monsoon system shift (Lézine, 1989; Hély et al., 2009). However, the climatic conditions during Holocene were unstable and marked by hydrological variations (Mayewski et al., 2004). Several studies showed differences between Early Holocene (9.5-8 ka cal BP) and mid-Holocene (6.5-5 ka cal BP; Maley, 1983, 2010; Gasse, 2000; Lézine et al., 2011). Lézine et al. (2011) examined more than 1500 palaeohydrological records collected between 10° and 28°N in the Sahara and the Sahel in Africa and demonstrated that a reduced and fragmented geographical extent of lakes and wetlands occurred during the Early Holocene (9.5-8 ka cal BP) compared to mid-Holocene (6.5-5 ka cal BP). The widespread extent of humid sectors in the mid-Holocene can be attributed to high groundwater levels, which might have been filled during Early Holocene, when maximum rainfall was recorded. In these conditions, the humid areas might have been widespread during the mid-Holocene, even if rainfall decreased (Lézine et al. 2011). Therefore, it is likely that the extent of Vertisol areas associated with a gilgai micro-relief has varied in the Diamare piedmont during the AHP. These variations may be concomitant with humid sector variations. Vertisol genesis in the Diamare piedmont might therefore be related to palustrine areas.

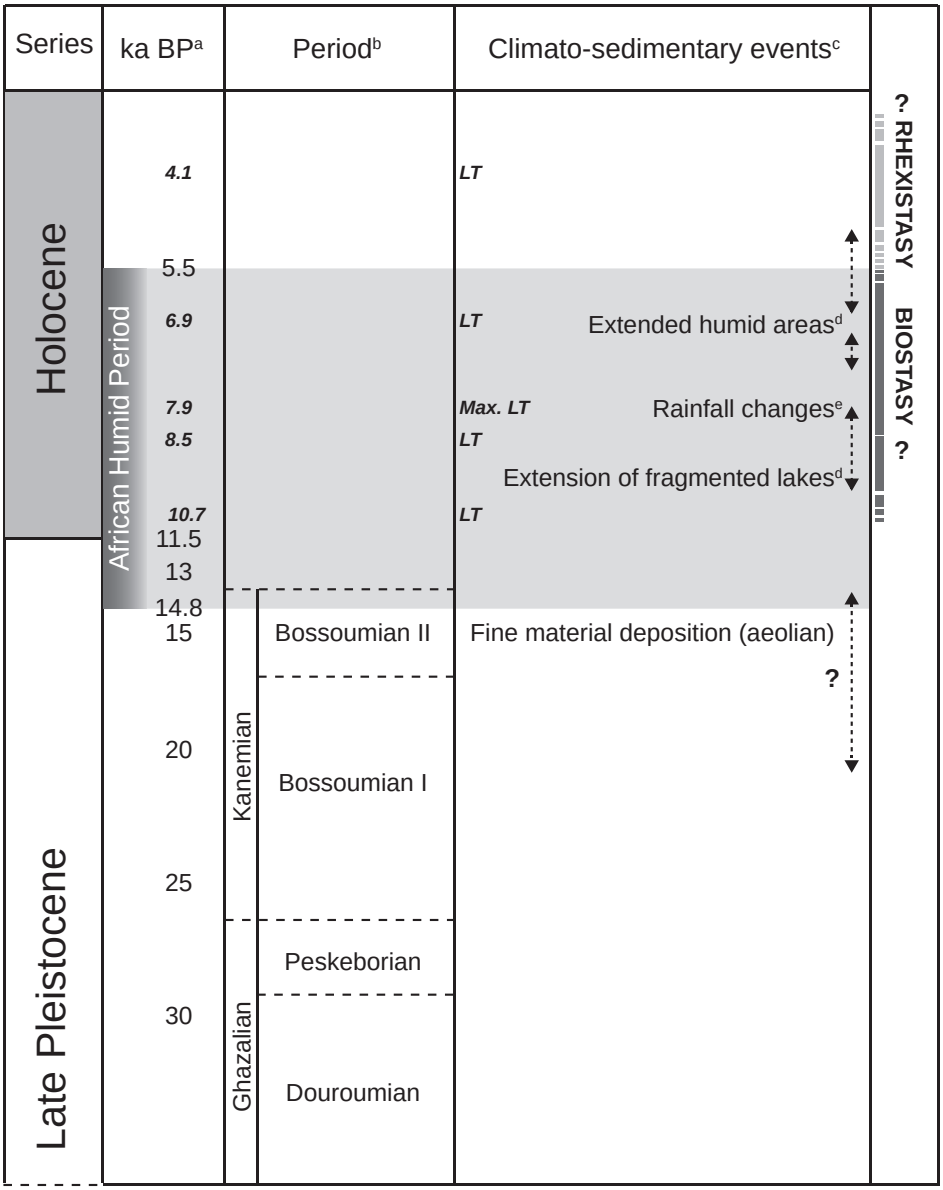

Figure 3.10 – Summary of the main events that occurred in the Chad Basin during the Late Pleistocene-Holocene period and relationships with mima-like mound formation ([a]deMenocal et al., 2000; [b]Hervieu, 1970, Brabant & Gavaud, 1985; [c]Hervieu1970, Maley, 1981, Maley, 2004; Morin, 2000; [d]Lézine et al., 2011; [e]Servant, 1983). Abbreviations: LT for lacustrine transgression; Max for maximum. The African Humid Period lasted from 14.8 ka to 5.5 ka cal BP; the extent of Vertisol areas in the Diamare piedmont is hypothesized to have varied during this period in concomitance with different climatic events (e.g. lake-level changes, extent of humid areas) and may have been larger than in the present-day. This period can be referred to as a Biostasy phase. A climate change, inducing an increase of erosional processes characterized the end of the AHP. Vertisol erosion in a gilgai micro-relief is likely at the origin of the present-day mima-like mound landscape. This period can be referred to as a Rhexistasy phase. The time limits of all these phases are uncertain and illustrated by dashed lines and arrows. N.B. The ages represented here are calibrated, they are not in the publication (Appendix L).

The contemporaneous deposition of the coarse alluvium and the clay-rich sediment implies changes in transportation energy. As demonstrated above, climate was not stable during the AHP. Servant

(1983) already identified rainfall changes c. 8 ka cal BP, due to the slight migration of the monsoon front position towards the south (Fig. 3.10). The rainfall regime is directly associated with this front. Dhonneur (1974) demonstrated that cumulonimbus clouds are dominant preceding the monsoon front and associated with big raindrops (>2 mm); on the other hand, cumulus clouds are dominant behind the front, and their associated raindrops are smaller (<2 mm). Consequently, before c. 8 ka cal BP, fine sedimentary deposits are favoured, whereas after c. 8 ka cal BP, coarse-grained sediments are dominant (Maley, 1983; Servant, 1983). Another process can be related to variations in the Lake Chad water level, which is the base level of rivers draining into the Chad Basin, such as the Mayo Tsanaga (Fig. 3.1B). Leopold and Bull (1978) defined the base level of a river as the elevation below which a stream cannot flow. The base level changes would have caused disequilibrium in river profiles: if it rises, the whole profile will tend to be raised by increasing accommodation space and then favouring deposition processes and fine material production; if it lowers, the profile will tend to be lowered by increasing erosion and coarse material production (Davis, 1902). Several studies showed that the lake level would have varied several times during the Holocene (Durand, 1982, 1995; Ghienne et al. 2002; Maley, 2004; Bouchette et al., 2010). Both runoff change processes due to rainfall and/or base level changes might have induced transportation energy changes able to explain the coarse alluvium/clay-rich sediment interfingering.

The AHP ended around 5.5 ka cal BP (Fig. 3.10), mainly because of the weakening and the southward migration of the monsoon front (Kröpelin et al., 2008; deMenocal and Tierney, 2012; Shanahan et al., 2015). Even if it is known that another humid phase occurred between 3.5-2.5 ka cal BP (Lézine, et al., 2011), it never reached the same maximum of rainfall. Nevertheless, efficient Vertisol genesis cannot be excluded during this period as well, and another erosion period might have been initiated again at the end of this second wet phase. However, it is likely that erosion might have increased with drier conditions and a decrease in vegetation cover. Consequently, it is probable that the Rhexistasy phase might be related to the end of the AHP.

Finally, the question remains of the potential aeolian origin of the material composing all the sediments. It was demonstrated that aeolian sediments are generally mobilized under dry conditions and stabilized during wet conditions, due to the increase of vegetation cover and soil moisture (Kocurek, 1998; Swezey, 2001; Vandenberghe, 2013). McTainsh (1984) showed that the isohyet of 400 mm/yr is the minimum for dust stabilization. It is recognized that during the climato-sedimentary event, known as the Bossoumian II (from 17 to 14 ka cal BP; Hervieu, 1970; Maley, 1981; Brabant and Gavaud, 1985; Morin, 2000), fine aeolian deposits were favoured (Fig. 3.10). However, Durand (1995) showed that aeolian stabilization might have already been possible since 26 ka cal BP (beginning of the Kanemian climato-sedimentary event). He demonstrated that the ergs observed in northern Cameroon and northeastern Nigeria, which represent the maximal extent of the Sahara, were probably formed before 30 ka cal BP and thus much older than the Kanemian. Consequently, the Kanemian was not as dry as was previously thought, and it is not excluded that the 400 mm/y isohyet might have been reached since 26 ka cal BP, leading to the possible stabilization of aeolian material.

In summary, the following chronological succession is proposed: (i) a pre-AHP period, during which aeolian material is deposited and probably reworked and mixed with the local material along the slopes, (ii) an AHP period, during which Vertisol developed, associated to gilgai micro-relief and secondary mineral precipitation; the extent of Vertisol was larger than nowadays, and during this period, fersiallitic soils were developing upstream Vertisols; and finally, (iii) a post-AHP period, during which erosion increased, forming the present-day mima-like mounds and reworking the fersiallitic soil above the clay-rich sediment. However, dating constraints are needed to support and improve the proposed chronology. Nevertheless, mima-like mounds and their adjacent sediments offer a great potential for

the sedimentary record of the Chad Basin.

3.5 Conclusion

Investigations on newly observed earth mounds in the Chad Basin led to new interpretation of their formation. According to their size and spatial distribution, they can be defined as mima-like mounds (Cramer and Barger, 2014). Recently it was postulated that mima-like mound shapes result from the combination of erosion and/or aeolian and vegetation patterns. Mima-like mounds observed in northern Cameroon are strongly linked to erosion, and there is no evidence that vegetation patterns play or played any particular role. Field observations and analytical results, such as grain-size distribution, clay mineralogy, and thin section observations show mima-like mounds to be degraded Vertisols or Vertisol relics developed in a former gilgai micro-relief. Erosional processes induced the stripping of surficial horizons of Vertisols and the accentuation of the gilgai micro-relief. They also induced the formation of a large accumulation of pedogenic nodules at the mound surface, remains of a former Bk horizon. In addition, a fersiallitic pedolith (e.g. reworked soil) buries them at some places in the landscape and this highly supports the occurrence of erosion events at some points. Present-day climatic conditions in the region of northern Cameroon are favourable to Vertisol genesis. But locally, climatic changes in the region during the Quaternary may have modified the extent of the Vertisol area. Larger areas of Vertisol can be related to widespread humid fields during the second part of the AHP during the Mid-Holocene (Biostasy phase). At the end of the AHP, climatic conditions became drier, inducing a decrease in vegetation cover and an increase in erosional processes (Rhexistasy phase). Moreover, water level fluctuations of Lake Chad and/or changes in the rainfall regime also occurred during the AHP, which might have influenced transportation-deposition processes in the Diamare piedmont. These changes would explain the occurrence of coarse alluvium interfingering the clay-rich sediment in a mima-like mound, which indicates a concomitant formation. Some questions are still pending regarding the origin of some fractions in the sediments from this landscape: all of them include a modal class corresponding to an aeolian component. Therefore, the possibility of a substantial aeolian contribution occurring before the AHP is proposed but this hypothesis remains open. Finally, the mima-like mounds from the Chad Basin have a significant potential as a regional sedimentary record.

Part III

Soil relics as palaeoenvironmental archives

SYNOPSIS

In the last chapter, terrestrial carbonate nodules from Far North Cameroon were demonstrated to be pedogenic in origin and related to Vertisol genesis. The present-day mima-like mound landscape probably resulted from this inherited pedogenesis combined with later erosion; they can thus be termed Vertisol relics; *soil relics* being unburied soils but in disequilibrium with present-day conditions. Processes involved are pedo-sedimentary in nature and were hypothesized to be linked to climatic variations that occurred during the Late Quaternary. Consequently, these processes can be attributed to a Biostasy phase, i.e. a stable phase characterized by pedogenesis, followed by a Rhexistasy phase, i.e. an unstable phase, characterized by erosion. Mima-like mounds and associated pedogenic carbonates, i.e. Vertisol relics, have thus a great potential as palaeoenvironmental indicators in the Chad Basin. This part is dedicated to the understanding of the processes involved in the formation of Vertisol relics, in order to **reconstruct palaeoenvironments** and their **evolution through time**. The origin of Ca in pedogenic carbonate nodules was showed to be mainly local, i.e. from plagioclases of the granite. Ca was thus transferred from Ca-poor granite into a Ca-rich nodule. To explain such an enrichment, Ca must have been accumulated in distinct pools (or compartments), which could have been associated with the soil, i.e. the clay minerals and/or the organic matter. The petrography and the geochemistry of the nodules showed that they were probably formed in a wetland soils affected by water-table fluctuations, with the presence of an open forest, but in a environmental context evolving toward drier conditions. Moreover, to form calcium carbonates, conditions have to be **alkaline** and the processes behind the soil alkalinization remains still unclear. **Oxalate** was observed in the nodules. This mineral is ubiquitous in vascular plants and is a source of C for some bacterias. Its oxidation occurs as soon as it is transferred into the soil, and this process is known to increase the pH. It is thus proposed that wet soil-vegetation ecosystem formed during a humid period and accumulated C, Ca, and oxalate. Then conditions became drier leading to the decrease of vegetation and the liberation of the elements and oxalate. The oxidation of the latter led to an alkalinization of the soil environment, and to the precipitation of carbonate nodules. Consequently, the Vertisol relics resulted from complex processes linked to pedogenesis and biota, and to sedimentary processes, in turn related to hydric conditions.

4 From pedo-sedimentary processes to palaeoenvironments reconstruction

4.1 Introduction

4.1.1 The pedo-sedimentary approach

In the previous chapter, it was demonstrated that the mima-like mounds from Far North Cameroon resulted from past pedogenesis and later erosion. They can thus be considered as pedo-sedimentary archives. Such a similar concept exists in soil geomorphology coined as polygenic soils (Johnson et al., 2005). Soils evolve through time, and as they are affected by external factors, they can be seen as *palimpsests* (Schaetzl and Thompson, 2015). Another point of view, close to the latter, but in a different context, is the *sediment-soil continuum* used by pedo-archaeologists (Walkington, 2010). These approaches clearly share the link between sedimentology and pedology. Both scientific fields are studying and addressing different questions, but it is necessary to link them to understand the evolution of a geosystem through time (Fig. 4.1). Two main sets of processes, which are related, are involved in a pedo-sedimentary system: (i) the physical sedimentation processes (Fig. 4.1, red box), and (ii) the biogeochemical sedimentation processes (Fig. 4.1, blue box). At the scale of the watershed, the first type corresponds to the transportation/deposition of material (clay, silt, sand particles) by various external agents (wind, water, ice), leading to the formation of sediments (or surficial formations; see below): these processes belong to the field of sedimentology. The second type concerns processes transforming sediments and occurring at larger scales, through chemical reactions and recombination of atoms, and leading to secondary mineral formation (i.e. clay minerals, oxides, carbonates). Acting at Earth's surface, they are intimately related to biological processes, and thus to the field of pedology. Processes belonging to both fields are regulated by external factors, such as climate and topography, in turn related to tectonics at a longer time scales. Consequently, at smaller scales, these terrestrial processes are closely related to the regional and even global water cycle (Willmott and Rowe 1985).

Water, in a watershed, is regulated by the climate and the topography, which influence its quantity and state, and its distribution, respectively. The amount and the state of water (vapour, liquid, solid) are related to atmospheric rules controlling precipitations and temperature. Topography, characterized by the morphology of the landscape and the distribution of slopes (i.e. geomorphology), influences patterns and supply of water, expressed as rivers morphology, creation of lakes or swamps, etc. The scientific field dealing with water dynamics is hydrology. The hydrology of a watershed directly impacts sediment transportation/deposition processes. These processes are numerous in a landscape and related to different agents such as (i) gravity in piedmont and slopes, leading to colluvial sediments,

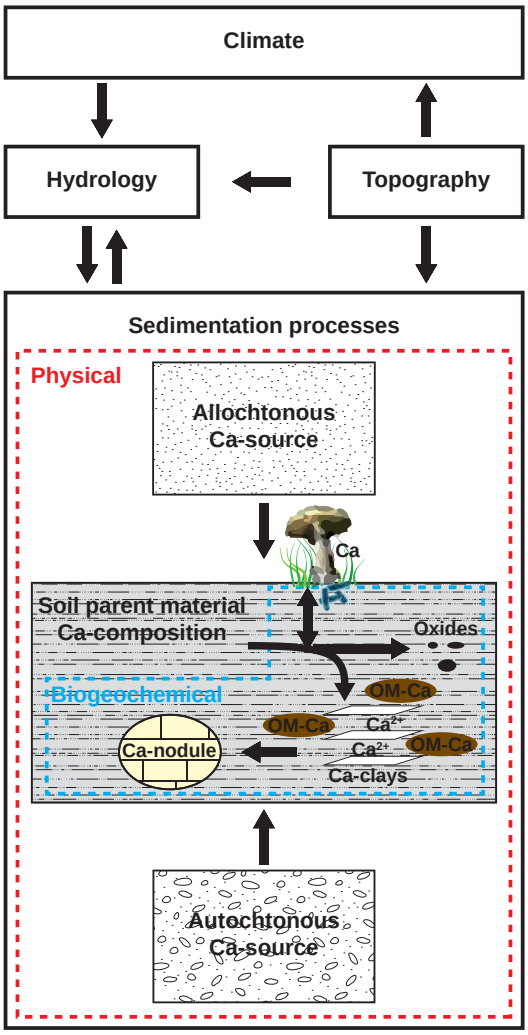

Figure 4.1 – Environmental relationships and processes involved in a pedo-sedimentary geosystem. Two kinds of sedimentation processes are ruling a continental geosystem at different scales; the physical sedimentation processes (red box), including the transport of mineral material (clay, silt, sand, and > 2 mm material) and their deposition; and the biogeochemical sedimentation processes (blue box), corresponding to the biogeochemical transformation of this sediment and to soil formation. These processes are related to water amount and distribution in the watershed, which are controlled by climate and topography.

(ii) wind, leading to aeolian sediments, (iii) running and concentrated water of rivers, leading to alluvial sediments, or (iv) more stagnant and shallow water of swamps and lakes, leading to palustrine and lacustrine sediments, respectively. All these sediments are considered as superficial formations, which are defined as *continental formations, soft or secondary hardened, whose origin is due to the mechanical or chemical rock disintegration and, which can be variously reworked* (Dewolf and Bourrié, 2008). A superficial formation represents commonly the soil parent material, whose origin is, either autochthonous, para-autochthonous (i.e. autochthonous material mixed with allochtonous material), or allochtonous (Campy and Macaire, 2003). Autochthonous materials can be as heterogeneous and varied as the landscape geomorphological and lithological settings. Allochtonous material can be brought and deposited in the watershed, its transportation/deposition depending on climate, i.e.

wind trade, soil moisture favourable for dust stabilization (e.g. Kocruek, 1998), and topography (i.e. mountains acting as dust traps due to surface roughness and/or wind speed decrease; Pye and Tsoar, 1987).

Once the soil parent material is stabilized, water transforms it through biogeochemical processes, i.e. the biogeochemical sedimentation processes (Fig. 4.1, blue box). The chemical weathering of the soil parent material leads to the liberation of ions into the soil solution (Kolka et al., 1996). These elements can (i) recombine to form secondary minerals, such as clays and/or oxides, (ii) be used by living forms (bacteria, vegetation, fungi) as nutrient compounds, i.e. they enter the biogenic cycle of elements (Giesler et al., 2000), or (iii) be leached out of the geosystem. The living forms are sources of organic matter, structured by many different molecules containing macro-elements, other than C, H, O, and N, such as calcium (Ca), magnesium (Mg), iron (Fe), etc. This organic matter can bond with clays to form the clay-humus complex (Duchaufour, 1990). Elements can thus remain in various forms in the ecosystem, i.e. clay-humus complex, the living organic matter, etc., which are characterized by large variety in residence time, according to factors influencing the stability-evolution of a given ecosystem. The elements can be transferred from a form to another and lead to secondary minerals precipitation, such as oxides or carbonate minerals, depending to hydrological and biogeochemical settings, mainly the soil water balance and the soil solution chemistry. The soil water balance concept was proposed by Thornthwaite (1948) (i.e. P/PET) who defined it as a ratio between water inputs in the soil (P) and loss due to the potential evapotranspiration (PET). The degree of aridity can be expressed with the Aridity Index (AI) expressed as MAP/MAE, where MAP=Mean Annual Precipitation and MAE=Mean Annual potential Evapotranspiration (UNEP, 1997).

Consequently, the sediments and the soils are connected and form a continuum in the landscape. Depending on the scale, they are controlled by the water characteristics (e.g. amount, phase), and the distribution, and thus related to climate and topography. A soil can be seen as the transformation of sediment through time under the influence of biological processes. The sediment evolution is interrelated to biotic and abiotic chemical changes and thus to larger scale processes. The concept of evolution integrates intrinsically the notion of time. A geosystem evolves, i.e. changes, through time and these changes may be gradual or abrupt. Erhart (1967) proposed to call these two modes of change as “Evolving Biostasy” and “Rhexistasy”. Changes occur in both modes, but the second one is characterized by an environmental crisis. The shift toward a crisis occurs at a moment known as a *tipping-point*. It refers to a situation during which the forces creating stability are overcome by the forces bringing instability, leading the system to shift or tip over into disequilibrium (Cairns, 2004). The challenge lies thus in recognizing if changes in the geosystem were gradual or abrupt, and in identifying the causes of such changes.

4.1.2 Vertisol relics as pedo-sedimentary geosystems

Terrestrial carbonate nodules from Far North Cameroon are pedogenic in origin and related to Vertisol genesis (Diaz et al., 2016a). Today, soils are Vertisol relics, i.e. unburied soils in disequilibrium with present environmental conditions (Retallack, 2001), emphasizing the inherited nature of vertic characteristics. The mima-like mound landscape are the result of past pedogenesis and subsequent erosion. Consequently, these features can be seen as pedo-sedimentary geosystems resulting from succession of sedimentary and pedogenic processes. A four-step (S) chronological succession (Fig. 4.2) has been proposed (Diaz et al., 2016a). The soil parent material, i.e. the sediment in which soils developed, deposited in the Diamare piedmont (S1). According to grain size distribution (Diaz et al., 2016a) the reworked regolith has also been mixed with aeolian dust input (20 μm < desertic lœss < 80 μm; Crouvi

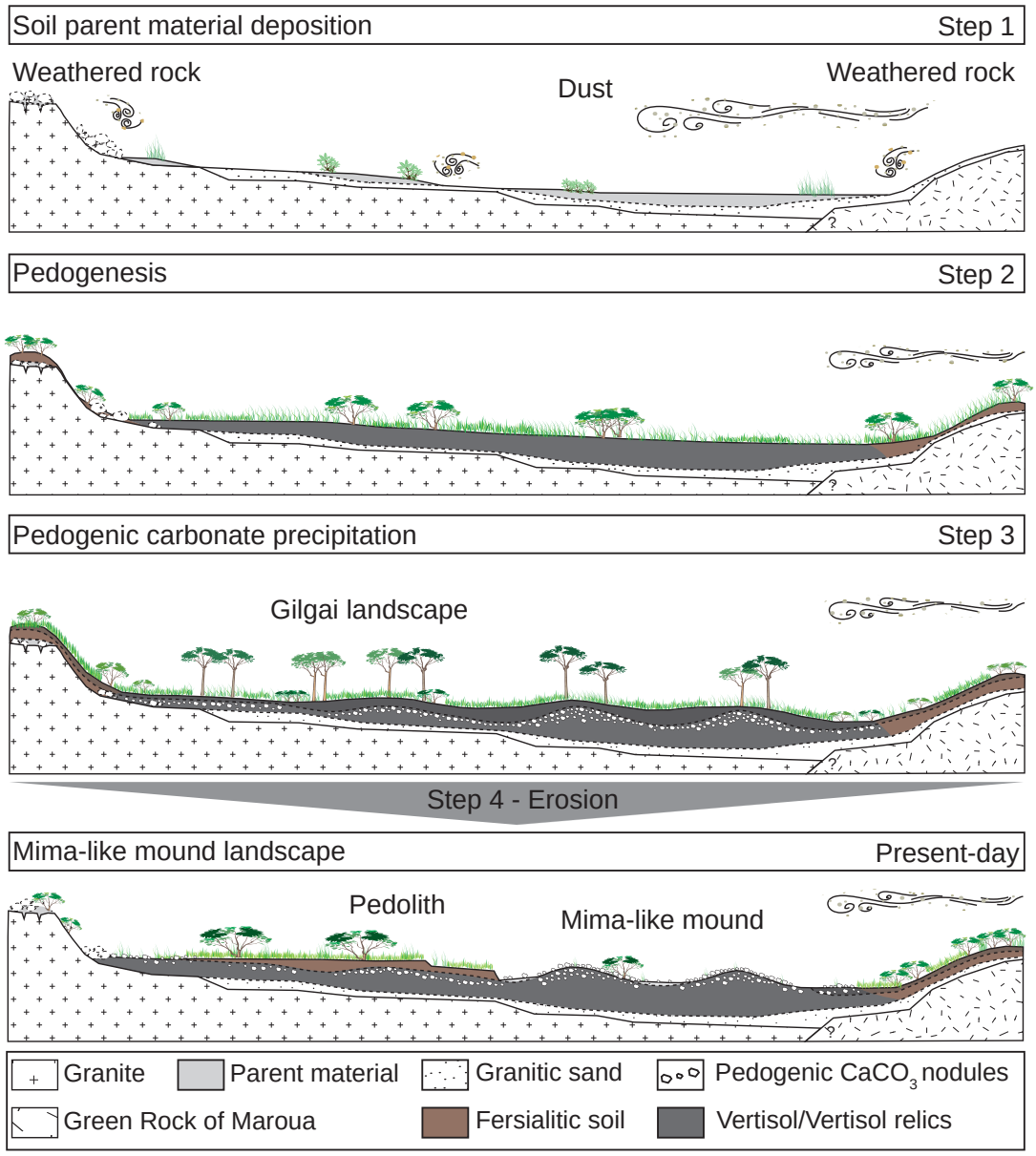

Figure 4.2 – Chronological hypothesis of mima-like mound formation. Succession of pedo-sedimentary processes in four steps, leading to the present-day mima-like mound landscape: S1=deposition of soil parent material, S2=pedogenesis, S3=pedogenic carbonate nodule formation in Vertisols, S4=Erosion.

et al., 2010). Strontium and neodynium isotopic results (see below) support this statement showing signatures similar to Saharan dusts (Dietrich et al., 2017). It was thus proposed that S1 occurred during a dry period, possibly before the African Humid Period (AHP), lasting from 14.8 to 5.5 ka (deMenocal et al., 2000). Then, wetter conditions triggered weathering and the development of denser vegetation cover, leading to soil development (S2). During this period, the organic matter production is high and was integrated in the soil. This phase was proposed to occur during the AHP. Later in the AHP, Vertisols would have become better developed, and during their pedogenic processes, new features such as pedogenic carbonate nodules and gilgai micro-relief occurred (S3). Finally, due to environmental

condition changes, the vegetation would have decreased leading to the onset of erosion, shaping the present-day landscape (S4). This phase would have been occurred during the Late Holocene when climatic conditions are becoming drier. Vertisol relics are thus clearly resulting from a succession of sedimentary and pedogenic processes through time, which can be related to the Bio-Rhexistasy theory from Erhart (1967), explaining the landscape as successsion of stable and unstable phases linked to climate.

The pedogenic carbonate nodules associated with mima-like mounds represent huge amounts of Ca and C accumulated as terrestrial carbonate in the Diamare piedmont, 65±20 kgm^3 and 20±6 kgm^3, respectively (Appendix B). As the geological settings are granitic, with Ca content of only 1.65±0.02 wt-% (n=1), the questions upon the Ca dynamic (e.g. sources, biogeochemical cycle) need to be addressed, in order to give new clues on the mechanisms responsible for such accumulations. Geochemical conclusions from the PhD work of Fabienne Dietrich are thus used to better understand the pedo-sedimentary geosystem. Her results are exposed in the following section.

4.1.3 Dynamic of calcium: unexpected sources and a trapping organo-mineral pool

Strontium (Sr) isotopes ($^{87}Sr/^{86}Sr$ ratio) were used to trace Ca (Dietrich et al., 2017). Four soil profiles were selected, three of them are in the granitic area and one is in the green rock area (i.e. greenschist metabasalt facies, see Chapter 2, Part I). Sr isotopes were measured on (i) plagioclases extracted from each soil profile, (ii) the soil carbonate phase, (iii) the soil non-carbonate phase, (iv) the nodule carbonate phase, and (v) the nodule non-carbonate phase. Results showed that the Ca composing the soil carbonate and the nodule carbonate phases originates from the same sources. The Ca source of secondary carbonates comes mainly from plagioclases supplied during bedrock weathering (granite or green rock) and local reworking. The $^{87}Sr/^{86}Sr$ ratio of plagioclases and the nodule carbonate phase are distinct and proper to each profile, revealing a very local Ca source, i.e. at the scale of the soil profile. However, $^{87}Sr/^{86}Sr$ ratios of the nodule carbonate phase are more radiogenic than plagioclases (+0.0032±0.0004 ppm), indicating the contribution of another Ca source (Dietrich et al., 2017).

The origin of the soil parent material, characterized by a clay-rich component and high amounts of smectitic clay minerals (Diaz et al., 2016a), is still unclear, but many indices point to an aeolian component. The parent material grain size distribution displays a typical mode corresponding to desertic lœss (Diaz et al., 2016a). Moreover, it was proposed that this material could have been deposited before the AHP. Interestingly, in many other areas in the region the second part of the Kanemian (21 ka to 14 ka cal BP) is suggested to have been a period favourable for dust stabilization (Hervieu, 1967; Bennett, 1980; Maley, 1981). This period had favourable environmental conditions, i.e. soil moisture, vegetation cover, wind trade, etc., for dust input and stabilization in the studied areas (Kocurek, 1998; Swezey, 2001; Vandenberghe, 2013). These optimal conditions were proposed to be related to mean annual rainfall of 400 mm/yr (Mc Tainsh, 1984). Neodymium (Nd) isotopes were performed on the soil parent material and compared with Sr isotopes in order to identify their origin (Dietrich et al., 2017). Results showed that the parent material is a mix between the local bedrock and Saharan dust. The proportion of dust in the parent material depends on the position in the landscape, i.e. topographic factor; however, in the main study site, results show a mixing of 50% of an aeolian component and 50% of local saprolite (Dietrich et al., 2017). The Sr signature of this mixed sediment is also more radiogenic than the nodules, suggesting that the second Ca source for secondary carbonates is potentially the dust component. However, it would provide a small proportion of Ca for carbonate nodules. It was not possible to calculate these proportion, nevertheless, the local

contribution proportion is clearly greater than the allochtonous contribution proportion (Dietrich et al., 2017).

The study of geochemical dynamics of elements in the landscape identified different pools enriched in specific elements, which reflect the way these elements are influenced by the processes ruling the pedo-sedimentary geosystem (Dietrich et al., *in prep*). Silica (Si), sodium (Na) and potassium (K) are mainly found in granite and saprolite, i.e. first stage of bedrock weathering; *sapros* meaning *decomposed* in Greek. Aluminium (Al), magnesium (Mg) and iron (Fe) are the main elemental components of the < 2mm soil fraction of Vertisol relics. Finally, Ca and manganese (Mn) are the elements characterizing pedogenic processes associated with Vertisol genesis.

At a starting point, the bedrock is affected by weathering and the saprolite can form. It is then mixed with an aeolian component leading to a para-autochthonous superficial formation (Campy and Macaire, 2003): the soil parent material. This mixed sediment is further weathered following various intensities according to the position in the landscape. Bocquier (1973) showed that fersiallitisation, i.e. 1 : 1 clay mineral neogenesis (kaolinite), preferentially occurs upstream, in higher areas, where weathering is greater, whereas bisiallitisation processes, i.e. 2 : 1 clay mineral neogenesis (e.g. smectite), dominate in downstream, rather in lower areas with low weathering conditions and element accumulation (e.g. alkaline cations and silica). The elements in the soil (Al, Mg, Fe) are mainly related to clay minerals and oxides (Dietrich et al., *in prep*). Al is one of the two main components of clays, and during bisiallitisation processes, beidellite and/or montmorillonite can form, explaining also the presence of Mg and Fe. Fe is present in oxides as well, identified as goethite by XRD. Finally, Ca and Mn are related to particular secondary mineral precipitation; calcium carbonate nodules and $Fe-Mn$ micro-nodules, respectively. Dietrich et al., *in prep* demonstrated that the Ca has been relocated from the granite to secondary carbonate nodules. Consequently, the environment evolved from Ca-poor (granite: 1.65±0.02 wt-%, n=1) to a Ca-rich (carbonate nodules: 45±0.8 wt-%, n=5) environment. It is thus necessary to explain how Ca is concentrated in the geosystem. Dietrich et al., *in prep* suggested that the smectitic pool can efficiently fix Ca (Coulombe et al., 1996; Velde and Meunier, 2008). However, its role would have been mainly related to a transient pool constantly exchanging with the soil solution. They proposed a second possible pool: the organic pool. Vegetation and soil organic matter should have been a system able to trap huge amounts of Ca. As the conditions were wet, vegetation should have been well developed and Ca would likely have been biocycled in plants. Some studies emphasized that, in tropical forest ecosystems, nutrients are easily recycled and work in quite-closed cycles, resulting in an ecosystem delivering low nutrient outputs (e.g. Bruijnzeel, 1991).

Sr isotopic results emphasized the local source of Ca and its relocation from the bedrock to pedogenic carbonate nodules. Consequently, the geosystem started to develop in a granitic environment with a low Ca content (1.65±0.02 wt-%, n=1) and ended as a geosystem with large accumulations of Ca (45±0.8 wt-%, n=5). Regarding Ca dynamics, the study of the geochemical elements (major, traces, REE) showed that it has been necessary to trap Ca in order to accumulate it before its relocation inside pedogenic carbonate nodules. The compartment able to trap Ca might have been mainly the organic pool (biomass and necromass), whereas the smectitic clay minerals would have acted as a transient pool. This process should have occurred during wet climatic conditions, which were efficient for plant development. However, due to topographic characteristics (low slopes), they were not powerful enough for large leaching outputs. These settings led thus to an *in situ* Ca pool building.

4.1.4 The alkalinity issue

The Ca dynamic in the pedo-sedimentary geosystem is well constrained, however, other questions are emerging concerning the palaeoenvironments. Which were the types of environmental conditions able to lead to such peculiar Ca dynamics? Ca was accumulated in the geosystem, showing that losses were low, but how did such a preservation occurred and why? It seems clear that climate, influencing soil water balance, has an important role but what exactly? The most important question concerns the alkalinity. The main mineral composing pedogenic carbonate nodules is calcite. This mineral is stable under alkaline conditions, and usually when $pH \approx 8.4$ (in standard conditions at Earth surface: 20°C, pCO_2 = 3.3 atm, Cailleau et al., 2005). However, it has been inferred that pedogenic carbonate nodules were formed during a wet period. This means high weathering and high organic matter production. Consequently, the conditions in the soil should have been rather acidic (including the high respiration rate, i.e. CO_2 production). How can edaphic conditions be alkaline and favourable for $CaCO_3$ precipitation in such a context?

In the present-day, alkaline soils are generally observed in semi-arid and arid regions, i.e. with low P/PET (Global Soil Data Task Group, 2002). They mainly group saline soils (i.e. Solonchak) and sodic soils (i.e. Solonetz). In Solonchak and Solonetz, pH values are high (> 8.5) and this is generally related to the presence of sodium salts or sodium cations saturating the cation exchange capacity (CEC), respectively (Schaetzl and Thompson, 2015). However, if alkalinity related to the presence of sodium cations seems probable in the present-day mima-like mounds, this was much less likely in the past, when climatic conditions were wetter (i.e higher P/PET). Consequently, dryness is not a satisfying explanation for past alkaline pH conditions. However, high amounts of smectitic clay minerals, i.e. 2 : 1 clay minerals, characterize Vertisol relics. This group of clay mineral mostly forms in waterlogged areas with low weathering (bisiallitisation, Bocquier (1973)). Such hydromorphic conditions preserve elements in the reactor, such as silica, iron and alkaline cations (Ca^{2+}, Mg^{2+}, etc.), stabilizing smectitic clay minerals. This is generally accompanied with alkaline pH values (Eswaran and Wong, 1978). Vertisols, which need smectitic clay minerals to develop, are thus frequently observed in lowlands and waterlogged areas, i.e. Vertisol genesis linked to the topography. Consequently, despite the fact that Vertisols developed during a wet period favouring weathering, did waterlogged conditions lead to alkaline pH? Were these waterlogged areas alkaline enough to reach stability conditions for calcite?

The aim of this present study is thus to explain the alkalinity of the geosystem at the time of pedogenic carbonate nodules formation. What kind of palaeoenvironment and what associated processes could explain alkaline soil pH? To track information upon the palaeoenvironment, a multi-scalar approach is used with tools belonging to petrography and geochemistry. The study of carbonate micro-facies can give information on the context of precipitation and thus on the environmental conditions. Geochemical tools, mainly stable C and O isotopes ($\delta^{13}C$ and $\delta^{18}O$), can help to recognize the processes of formation. More precisely, C isotopes give information on the sources of C (organic, vegetation type), and O isotopes can inform on hydrological processes, i.e. fractionation linked to water inputs and/or outputs. Once the environment for pedogenic carbonate nodule genesis is well constrained, a reconstruction of the pedo-sedimentary geosystem evolution through time will be proposed.

4.2 Materials and Methods

The main study site is located in the Diamare piedmont in Far North Region of Cameroon (Fig. 4.3). Pedogenic carbonate nodules were collected at different depths in a mima-like mound area from the soil profiles described in Diaz et al., 2016a (i.e. M1, M2 and M3; Table 4.1). Moreover, mima-like

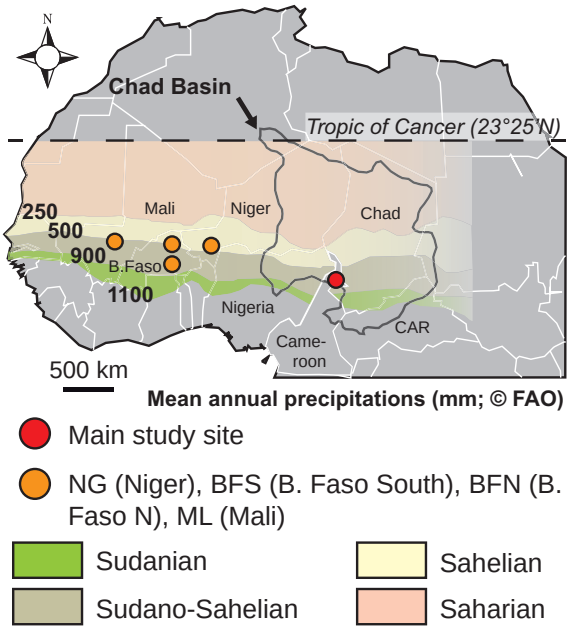

Figure 4.3 – Geographical location of sites along the Sudano-Sahelian belt, where carbonate nodules were observed and collected. In red is the main study site, with the most complete data set and in orange are the additional sites for comparison. Grey line represents the hydrological limits of Chad Basin.

mounds are generally well distributed in the landscape within stream networks, and surrounded by alluvial systems having various grain sizes (Diaz et al., 2016a). A surficial transect was performed from a mima-like mound to its surrounding alluvial system (Fig. 4.4), from which nodule morphologies were described. Finally, similar carbonate nodules were also collected in sites located in Mali (ML), Burkina Faso (South=BFS and North=BFN) and Niger (NG). They were also investigated and compared to Far North Cameroon nodules in order to highlight possible genetic relationships (Table 4.1).

Petrographic tools were used to identify, describe, and interpret cements and facies in order to provide evidences on the conditions of formation of pedogenic carbonate nodules and their palaeoenvironment. Moreover, the aim was also to identify the different type of nodules: are they all the same or, if they are different, why so? Consequently, pedogenic carbonate nodules were observed and characterized at different scales: i) in the field, ii) in thin sections, and iii) with a scanning electron microscope (SEM) coupled with an elemental analyser (based on energy dispersive X-ray spectroscopy, i.e. EDS). Furthermore, diagenesis certainly affected carbonate nodules. The question is: how severe was the diagenesis? Cathodoluminescence (CL) was used to highlight recrystallization and redistribution processes. Finally, C and O stable isotope analyses were performed on (i) the carbonate fraction of nodules and soils (< 2 mm, i.e. diffuse carbonate), and the organic matter trapped within the nodules and in the surrounding soil (only stable C isotopes in these cases). The aim was to be able to track the sources of C and, as the organic pool seems to be an important point to explain the Ca trapping, to provide some new clues regarding the palaeovegetation. Stable O isotopes were used to investigate hydrologic conditions at the time of nodule precipitation (Cerling and Quade, 1993). Finally, radiocarbon dating on the carbonate fractions ($^{14}C_{inorg}$) was performed on bulk nodules from Far North Cameroon and from Mali, Burkina Faso and Niger (Table 4.1) to give new clues on timing relationships.

Table 4.1 – Carbonate nodule samples from three study sites in Cameroon; M1=10°37'60.00"N, 14°11'16.70"E; M2=10°37'57.30"N, 14°11'20.40"E; M3=10°34'49.37"N, 14°4'45.14"E; in Burkina Faso=14°0'48.16"N, 0°8'4.35"O; in Mali=14°37'52.20"N, 10°48'32.66"O and in Niger=13°33'1.51"N, 2°40'1.89"E. Thin sec. for thin sections, Inorg. isotopes for C-O on carbonate, Org. isotope for C on organic matter

		Profile	Code	Depth (cm)	Size (cm^3)	Thin sec.	SEM	Inorg. isotopes	Org. isotope	Remarks
Cameroon	M1	F	B2.1	0-20	1.521	-	x	x	-	Grey - oxide - Mn dendrite
Cameroon	M1	F	B2.2	0-20	3.9	-	-	x	-	Grey - oxide - Mn dendrite
Cameroon	M1	F	-	20-40	-	x	-	-	-	Septarian cracks, grey
Cameroon	M1	H	B4.2	40-80	2.66	-	x	x	-	Reddish
Cameroon	M1	G	B6	120-130	4.5	-	-	x	-	Grey and reddish
Cameroon	M1	G	-	0-20	-	x	-	-	-	Septarian cracks, grey
Cameroon	M1	G	-	20-40	-	x	-	-	-	-
Cameroon	M1	G	-	40-60	-	x	-	-	-	Reddish
Cameroon	M1	G	-	60-120	-	x	-	-	-	Septarian cracks, reddish
Cameroon	M1	-	C1	0	943	-	-	x	x	Aggregated
Cameroon	M1	G	C2	0	164	-	-	x	x	Bulk analysis
Cameroon	M1	H	C3	5-10	70	-	-	x	x	Bulk analysis
Cameroon	M1	E	C4	30-40	139	-	-	x	x	Bulk analysis
Cameroon	M1	H	C5	40-50	151	-	-	x	x	Bulk analysis
Cameroon	M1	H	C6	50-60	154	-	-	x	x	Bulk analysis
Cameroon	M1	H	C7	80-90	158	-	-	x	x	Bulk analysis
Cameroon	M1	H	C8	90-100	145	-	-	x	x	Bulk analysis
Cameroon	M1	G	C9	100-110	51	-	-	x	x	Bulk analysis
Cameroon	M1	G	C10	120-130	34	-	-	x	x	Bulk analysis
Cameroon	M2	O	C.2	5-10	1.95	-	-	x	-	Septarian cracks, grey and reddish
Cameroon	M2	O	C.3	20-40	2.34	-	-	x	-	Grey, white - Mn dendrite
Cameroon	Transect	Transect	D3	0	28	-	-	x	-	Coarse silicate minerals
Cameroon	M3	S	E1.2	115	5.76	-	-	x	-	Grey, reddish - Mn dendrite
Cameroon	M3	U	E5.3	10	4.86	-	-	x	-	Grey - Mn dendrite
Burkina Faso	-	-	BFS	0	15	x	x	x	x	Grey - oxide
Burkina Faso	-	-	BFN	0	9.75	-	-	x	-	Grey
Burkina Faso	-	-	BFN	0	7.225	x	-	x	-	Grey - oxide
Burkina Faso	-	-	BFN	0	3.6	-	-	x	-	Grey
Mali	-	-	ML	0	49.5	x	x	x	-	Grey
Niger	-	-	NG	0	12.6	x	x	x	-	Reddish
Niger	-	-	NG	0	27	-	-	x	x	Reddish - Mn dendrite

Thin sections were made at the Institute of Earth Sciences (ISTE, University of Lausanne). They were observed with standard microscopes at the Institute of Earth Surface Dynamics (IDYST, University of Lausanne) to study the facies, as well as with a cathodoluminescence device to identify specific diagenetic features, if present (ISTE, University of Lausanne). Moreover, mima-like mounds soil thin sections were observed to study the associations between the carbonate fractions and the surrounding soil. For SEM observations (ISTE, University of Lausanne), the nodules were broken and the internal parts were mounted on small stubs. They were coated with a gold thickness of c. 23 μm. EDS measurements were used in order to characterize qualitatively the chemical composition of observed cements and minerals. Samples were compared with standard compounds from Sigma Aldricht to define more precisely the potential type of mineral. Standards were also prepared on stubs and coated with the same gold thickness. EDS measurements were performed directly on samples and standards under the same conditions, i.e. with a current of 68 μA, a voltage of 15 kV, a probe current (PC) of 8 and at a working distance (WD) of 23 mm.

For stable isotope measurements, the samples were crushed with an agate mortar to get fine powders. Sub-aliquots were collected in different areas of the nodules (Fig. 4.5) to assess the isotopic variability within a sample, i.e. parts with different colours, in veins or not, inside the external borders, etc. These sub-aliquots were then compared with bulk analyses, which were also dated with radiocarbon (see below). Finally, some of the powders were treated with HCl (32%) in order to remove the carbonate fraction and isolate the organic carbon fraction. HCl was removed after washing the powders three times with deionized water. Stable *C* and *O* isotopic compositions of the carbonate fractions were performed by a Gasbench II coupled to a ThermoFinniganplusXL isotope ratio mass spectrometer (IRMS) at the Stable Isotope Laboratory (IDYST, University of Lausanne) using the method of acid digestion at 70°C (Spötl and Vennemann, 2003). An internal laboratory standard (Carrara Marble)

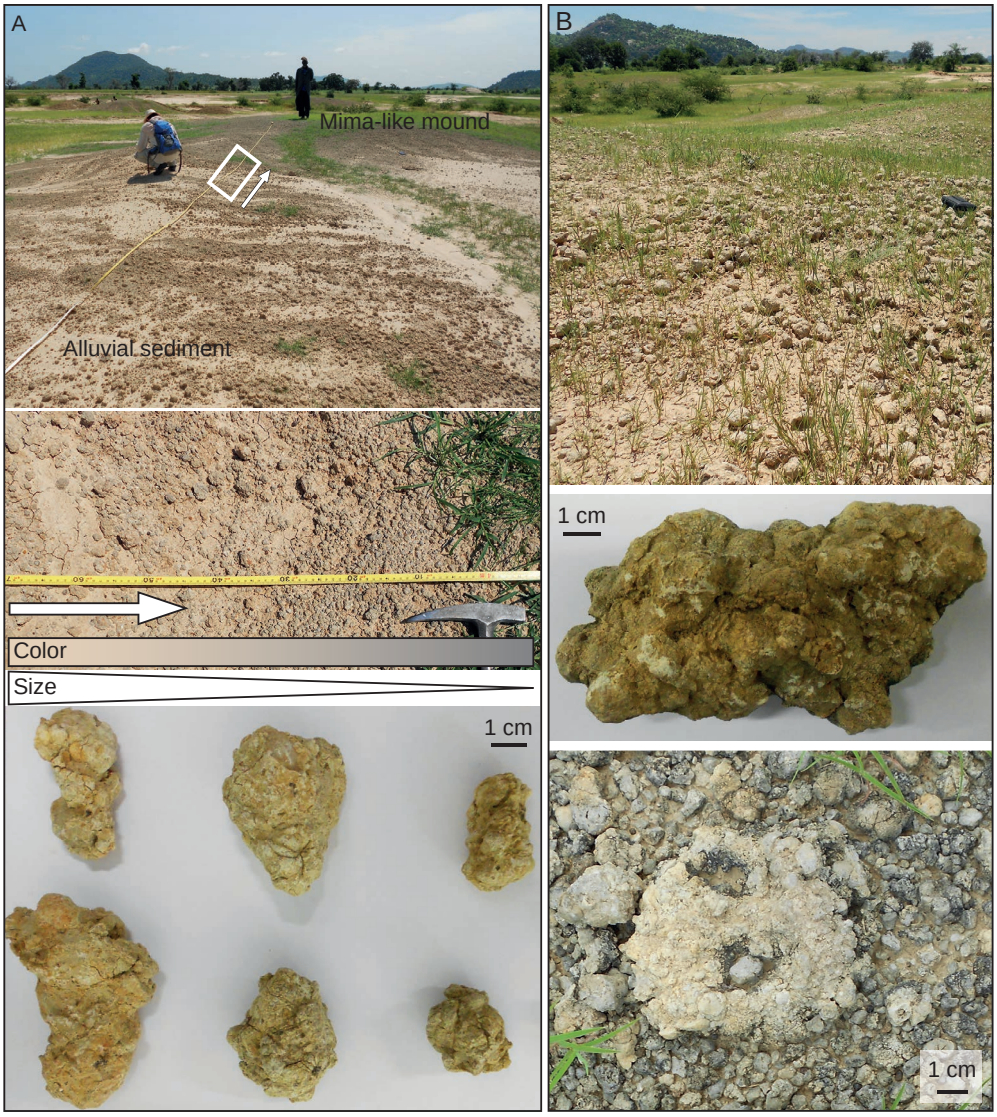

Figure 4.4 – Pedogenic carbonate nodules in the field in the Diamare piedmont (Far North Cameroon). A) Transect from a mima-like mound to the alluvial sediment, the nodules evolved from small, grey, rounded nodules, to bigger, reddish, elongated nodules. B) 10 cm diameter nodules showing an aggregation of smaller nodules.

calibrated to VPDB was used to normalise the final δ-values. The standard deviation of the internal standard is ≤0.05‰ and ≤0.18‰ for $\delta^{13}C$ and $\delta^{18}O$, respectively (n=13). The C isotopic composition of the organic C was performed on HCl treated powders with an elemental analysis-isotope ratio mass spectrometry (EA-IRMS) with a Carlo Erba 1108 connected to a Thermo Fisher Delta V IRMS (IDYST, University of Lausanne). The standard error was 0.1‰. The isotopic compositions are reported in the δ-notation as the per mil (‰) deviation relative to the Vienna Pee Dee Belemnite limestone (VPDB) as followed:

$$\delta X = (\frac{R_{sample}}{R_{standard}} - 1) * 1000 \tag{4.1}$$

and,

$$R = \frac{X^{hi}}{X^{li}} \tag{4.2}$$

where, δX is the isotopic composition of the sample (‰) for element X (C or O), and R is the molar ratio of the heavy (X^{hi}) to the light (X^{li}) isotope of the sample and the international standard, respectively.

The inorganic radiocarbon measurements were performed with an accelerator mass spectrometer (AMS) at the Ion Beam Physics Laboratory (ETHZ, Zurich). Sample treatment procedure and inorganic radiocarbon dating, are referred in Hajdas (2008). The fractionation of carbon isotopes ($^{14}C/^{13}C$ and $^{13}C/^{12}C$) is also measured in order to take into account the natural fractionation of the sample and the fractionation due to sample treatment (Table 1). The mass fractionation is used to correct the ^{14}C activity of the sample (F14C). The uncalibrated radiocarbon age (T) is given by (Stuvier and Polach, 1977):

$$C^{14}Age = -8033 ln(F^{14}C) \tag{4.3}$$

Finally, the radiocarbon ages need to be calibrated due to the atmospheric ^{14}C content variability through time. The IntCal13 calibration data (Reimer et al., 2013) and the program OxCal (version 4.2, Ramsey, 2009) was used to obtain calibrated ages at 95% confidence.

4.3 Petrography and geochemistry of pedogenic carbonate nodules

4.3.1 A multi-scalar diversity

Pedogenic carbonate nodules are diverse and complex at each scale of observation. Nodules can be directly associated with mima-like mounds or be found at the surface of alluvial sediment. Along this transect, the nodules vary in size, colour and roundness (Fig. 4.4). Figure 4.4A shows that the nodules evolve from small (Ø = 1cm), grey (5Y8/2 to 5Y7/1), rounded nodules, to bigger (Ø = 3 cm), reddish (2.5Y8/3 to 7.5YR7/4), elongated nodules. These reddish and elongated nodules have also trapped coarser silicate primary minerals (Appendix C). Furthermore, in some areas, the nodules can reach bigger diameters (Ø = 10 cm) and they seem to be small grey nodules aggregated together (Fig. 4.4B).

Pedogenic carbonate nodules are very porous and they often show septarian cracks and/or micropores. The trapped secondary oxides, mainly composed by iron and manganese, i.e. $Fe-Mn$ oxides (Appendix C), having black or reddish colours (Fig. 4.5). The reddish oxides are concentrated in circular features around black circular features or can be diffused in some patches or in the whole nodule, giving to the calcitic cement a reddish colour (Fig. 4.5A, 4.5C). The black oxides are concentrated as micro-nodules

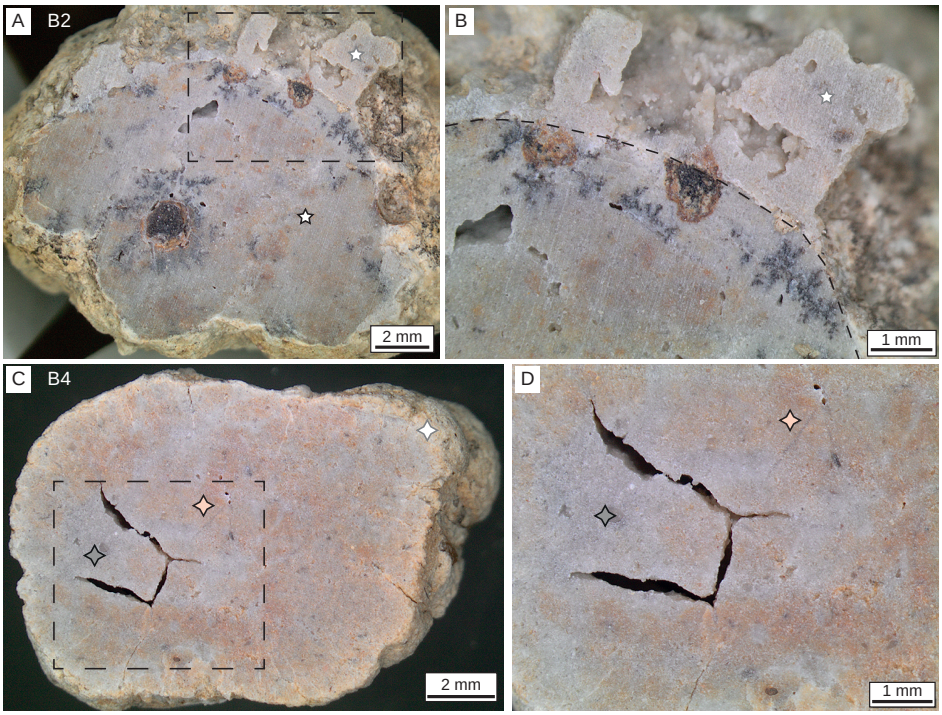

Figure 4.5 – Macro-observation of nodule sections.A) Nodule B2 showing greyish cement with reddish patches, dendritic black areas and oxides nodules are trapped within it. B) Zoom on the external par of nodule B2 showing the clear border (dashed line) between the external lighter cement around the darker cement. C) Nodule B4 with reddish cement, greyish patches and septarian cracks in the left-centre. D) Zoom in on the septarian crack area. The four- and five-branched stars correspond to the areas where sub-samples were taken for isotopic analyses and are used in Figure 4.11.

or show dendritic features. The borders (1-2 mm) of the carbonate nodules (e.g. B2 and B4) have a lighter colour and can show a net limit with the internal part (Fig. 4.5B, dashed lines). Oxides from this border is black and surrounded by a reddish aureole, which is more diffuse and discontinuous at more most external part (Fig. 4.5A, 4.5B).

Some carbonate fractions are also present in soils forming mima-like mounds (see Chapter 3, part II); carbonate can thus be diffused in the soil fine fraction (< 2 mm). This diffused fraction is mainly distributed in void channels (Fig. 4.6A, 4.6B1, 4.6B2 red arrows), with microsparitic crystals (> 5 μm), or impregnates the plasma, giving it a bright yellow birefringence colour (Bullock et al., 1985). The carbonate fraction can also be observed in hard nodules, in which calcite crystals are either very small (Fig. 4.6C, 4.6D), i.e. as micrite (< 5 μm), or clearly visible, as sparite (Fig. 4.6E, 4.6F). Some hard nodules seem to impregnate the soil fraction and are aureoled by thin white needles (Fig. 4.6C, 4.6D, red arrows). Other nodules show however angular and sharp borders, well separated from the surrounding soil (Fig. 4.6E, 4.6F, red arrow). In addition, rounded $Fe-Mn$ oxides are present in the surrounding soil matrix. These oxides nodules have diameters ranging from 1 to 5 mm. They can be dark with sharp borders, corresponding to disorthic or anorthic nodules, or lighter coloured, with fuzzy borders, corresponding to orthic nodules (Wieder and Yaalon, 1974; Fig. 4.6E, 4.6F, green arrows).

Thin sections of hard nodules (Fig. 4.7) generally show three different calcitic features: 1) a micritic phase (Mc), 2) a sparitic fibrous cement (Fc), and 3) a sparitic cement (Sp). Mc and Fc are dominant

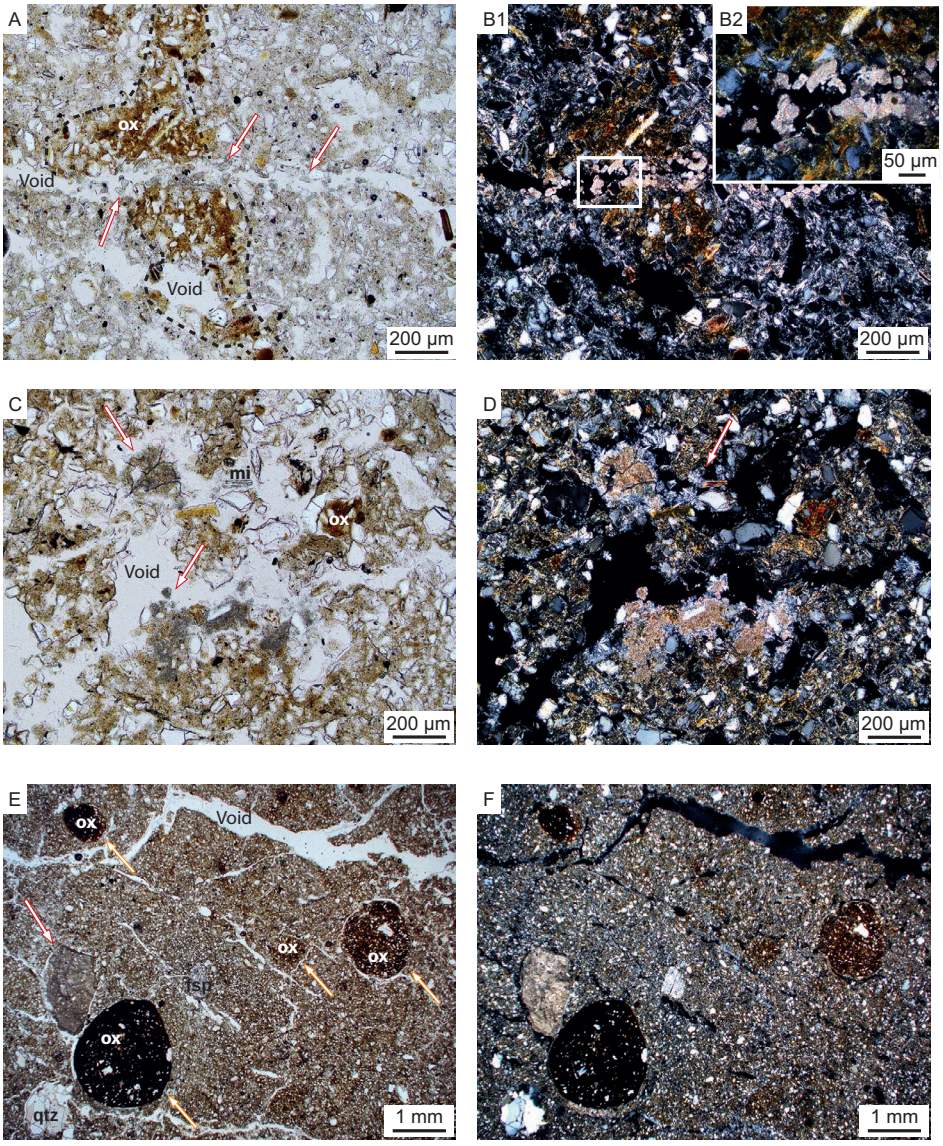

Figure 4.6 – Vertisol relic thin sections. A) Depth: 10 cm, PL. Sparitic minerals (red arrows) distributed in a horizontal void going through an iron-rich groundmass (dashed lines). B1) A in CPL. B2) Zoom on the sparitic minerals. C) Depth: 10 cm, PL. Micritic nodules occurring near the voids (red arrows). D) C in CPL. Small white needles are occurring around the micritic nodules (red arrow). E) Depth: 15 cm, PL. Different generations of $Fe-Mn$ oxides in the soil matrix (orange arrow) and fragment of carbonate nodule (red arrow). F) E in CPL. Abbreviations: PL for polarized-light, CPL for crossed-polarized light, ox for oxides, mi for mica, qtz for quartz, fsp for feldspar.

in the nodules and appear as patches. The Mc phase is dark and brownish. Primary minerals (mainly quartz and feldspars) are trapped within this Mc matrix and are aureoled by palisadic sparitic calcite (Fig. 4.7E, 4.7F). SEM pictures of nodule B2 illustrate typical aureoled quartz; the mineral is rounded having numerous percussion marks, and is surrounded by calcitic crystals (5-10 μm). The aureoled quartz is embedded in a matrix composed of micritic crystals (Fig. 4.8A, 4.8B). Fc cements display fan-like features, or cone-in-cone structures (Shaub, 1937), but the primary minerals trapped in them

are not aureoled (Fig. 4.7G, 4.7H). The colour of this cement is lighter and yellowish. Crystals are sparitic and have elongated morphologies. SEM observations show that the crystals are microsparitic (5-10 μm), rectangular and stacked up (Fig. 4.8C). Finally, very small crystals (2-5 μm), without any specific orientation, are composing the Mc phase (Fig. 4.8D). The Sp cements are located around voids and/or appear as veins and generally represent a small proportion of the whole nodule (Fig. 4.7). The crystals are sparitic (~20 μm), clear and white in the natural light. Their observation with the SEM shows nice rhombohedric crystals coating voids (Fig. 4.8B, 4.8G). Some of them can have nice step-like growth features (Fig. 4.8E), or being etched, and showing dissolution patterns (Fig. 4.8F, arrow). Cements react differently to the exposition of an electron beam in a cathodoluminescence devise (Fig. 4.9). Sp cements remain dark blue and are sometimes surrounded by a luminescent orange layer (Fig. 4.9B, 4.9D, 4.9F). Fc cements with flake-like patterns have borders slightly more luminescent and orange (Fig. 4.9F). Mc phase is bluish (Fig. 4.9D) but some parts are showing highly luminescent mushroom-like patterns (Fig. 4.9B). These patterns are particularly well expressed in the external border part of some nodules (Fig. 8H). Finally, a few unidentifiable traces of organic matters are entombed in the carbonate nodules, but they are neither shells nor rests of living forms, such as plants. $Fe-Mn$ oxides trapped in the matrix can be affected by septarian cracks and be secondary filled with Sp calcite. The oxides can also diffuse inside the cements (Fig. 4.7C, 4.7D) or form dendritic features (Fig. 4.7E, 4.7F). SEM observations show that these $Fe-Mn$ oxides trap primary minerals in an amorphous, i.e. crypto-crystalline or microcrystalline matrix (Fig. 4.8H, 4.8I, 4.8J).

Small and thin needles (5-10 μm) were observed with the SEM in the microporosity of some carbonate nodules (Fig. 4.10A). According to EDS analyses, the chemistry of these crystals is composed by C, O, and Ca, such as calcite (Fig. 4.10B). However, their habitus is very different from the one of calcite, or even aragonite, both minerals using the same elemental composition (C, O, Ca) and expected to be found in such an environment. Nevertheless, other minerals have the same elemental composition and display the observed habitus (Frey-Wyssling, 1981): calcium oxalates (as monohydrated, dehydrated, or polyhydrated CaC_2O_4). By comparing C/Ca and O/Ca ratios of pure calcite and pure calcium oxalate standards (Sigma Aldricht), it is possible to differentiate clearly both mineral species (Fig. 4.10B). The ratios related to the proportions of C and O compared to Ca in calcite ($CaCO_3$) and calcium oxalate (CaC_2O_4), are different. Results show that the small needles trapped in the pedogenic carbonate nodules are closer to the calcium oxalate standards, whereas the matrix is clearly similar to calcite (Fig. 4.10B). The large uncertainties are due to the fact that the measurements are not performed on flat surfaces, but in 3D, giving some imprecise results. In addition, needles are very small. Nevertheless, it is still possible to differentiate the needles from the matrix. Mineral habitus and chemistry suggest thus quite confidently that the needles observed in the microporosity of the carbonate nodules are calcium oxalate ($CaOx$).

4.3.2 Interpretations

4.3.3 Stable isotopic composition and ages of pedogenic carbonate

Pedogenic carbonate nodules are associated with Vertisol genesis (Diaz et al., 2016). Their formation with rounded $Fe-Mn$ oxides in Vertisol is very common (e.g. Wieder and Yaalon, 1974; Ahmad, 1983; Mermut et al., 1996) and was often described in recent Vertisol (e.g. Kovda et al., 2003) and Paleovertisols as well (e.g. Driese and Mora, 1993; Kovda et al., 2006; Violette et al., 2010). The different morphologies and colours of carbonate nodules in the field suggest that *primary* nodules (small, grey and rounded) can be reworked and affected by later dissolution-precipitation processes leading to *secondary* nodule morphologies (bigger, reddish and elliptic). Nevertheless, the *secondary* nodules trap

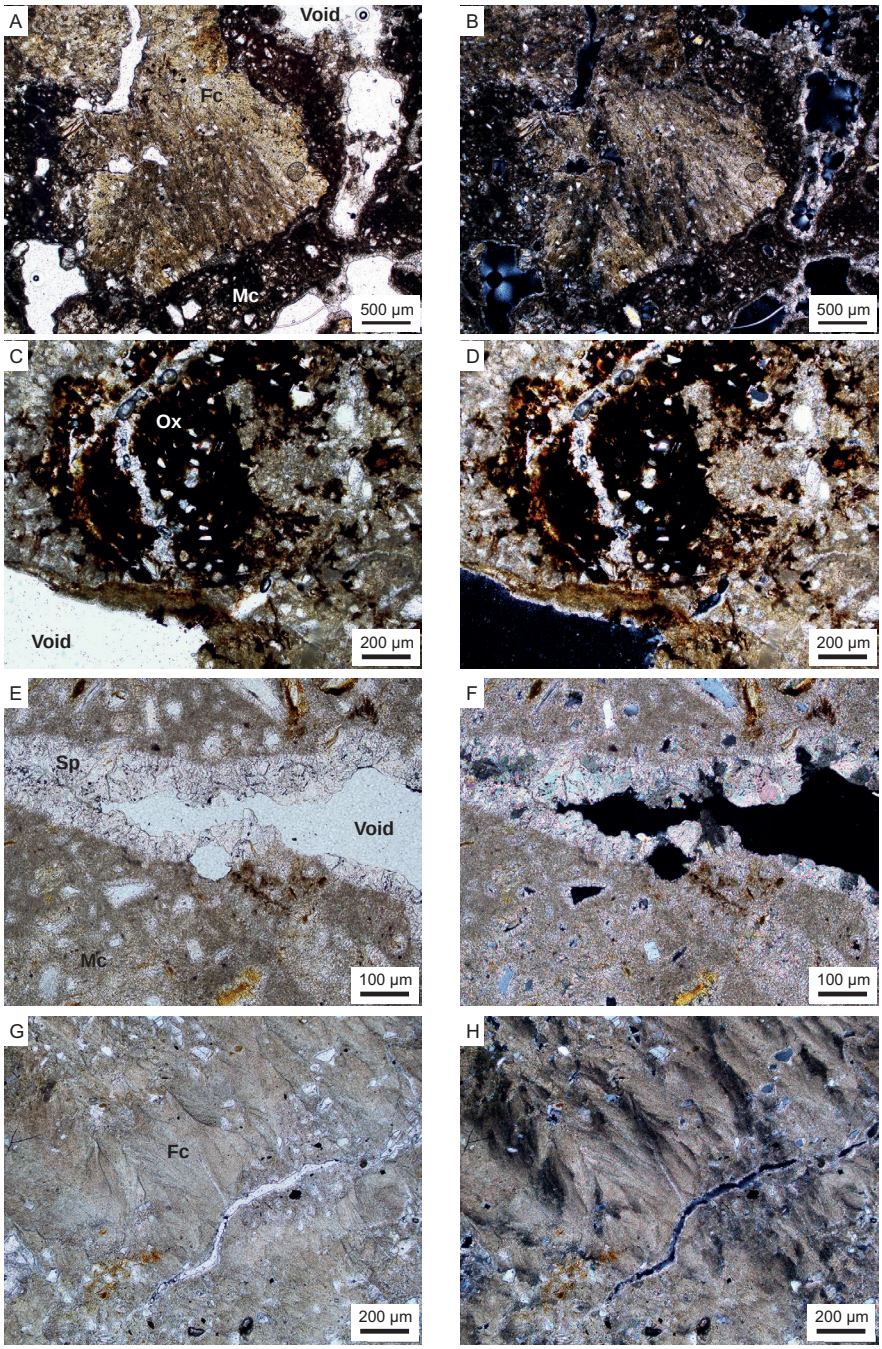

Figure 4.7 – A-B) Depth: 20-40 cm in profile F, PL and CPL. Yellowish fibrous calcite surrounded by darker micritic phase. The voids in the micritic phase are coated by sparitic and white crysltals. C-D) Depth: 0-20 cm in profile G, PL and CPL. Rounded Fe-Mn oxide trapped within micritic cement and cut by a void later filled by sparite. The oxide can also be diffused and have dendritic pattern in the micrite. E-F) Depth: 0 cm, PL and CPL. Micritic phase with nice aureoled minerals, sparitic cement are growing in the septarian crack. G-H) Depth: 0 cm, PL and CPL. Fibrous calcite showing fan-like structures or cone-in-cone. Abbreviations; Fc for fibrous calcite, Mc for mictritic phase, Ox for oxids.

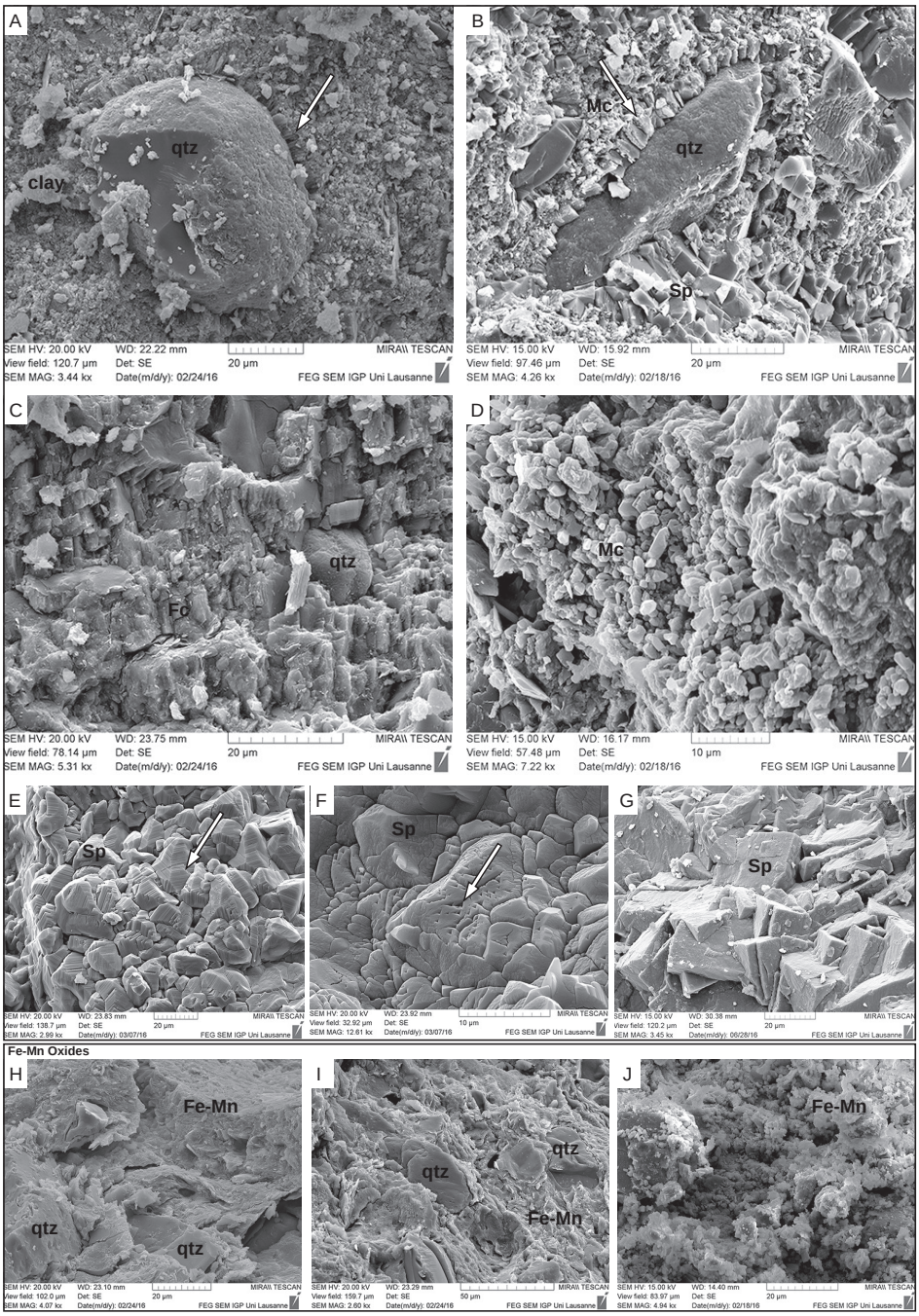

Figure 4.8 – Secondary Electron Microprobe images (SEM) on samples B2 and on $Fe-Mn$ oxides. A) Aureoled quartz within a Mc phase, clay component are visible. B) Aureoled quartz within a Mc phase, in the bottom Sp crystals infilling a former void. C) Fc calcite showing micro-sparite minerals stack up and unaureoled quartz. D) Mc crystals without any particular orientation. E) Step-like Sp cement. F) Etched Sp with traces of dissolution. G) Sp crystals. H-I) $Fe-Mn$ oxide matrix around primary minerals. J) Mico-crystalline $Fe-Mn$ oxide matrix.

also a coarser silicate mineral fraction. Is there thus really a difference between *primary* and *secondary* nodules related to reworking, or is it a consequence of two different environments of formation, i.e.

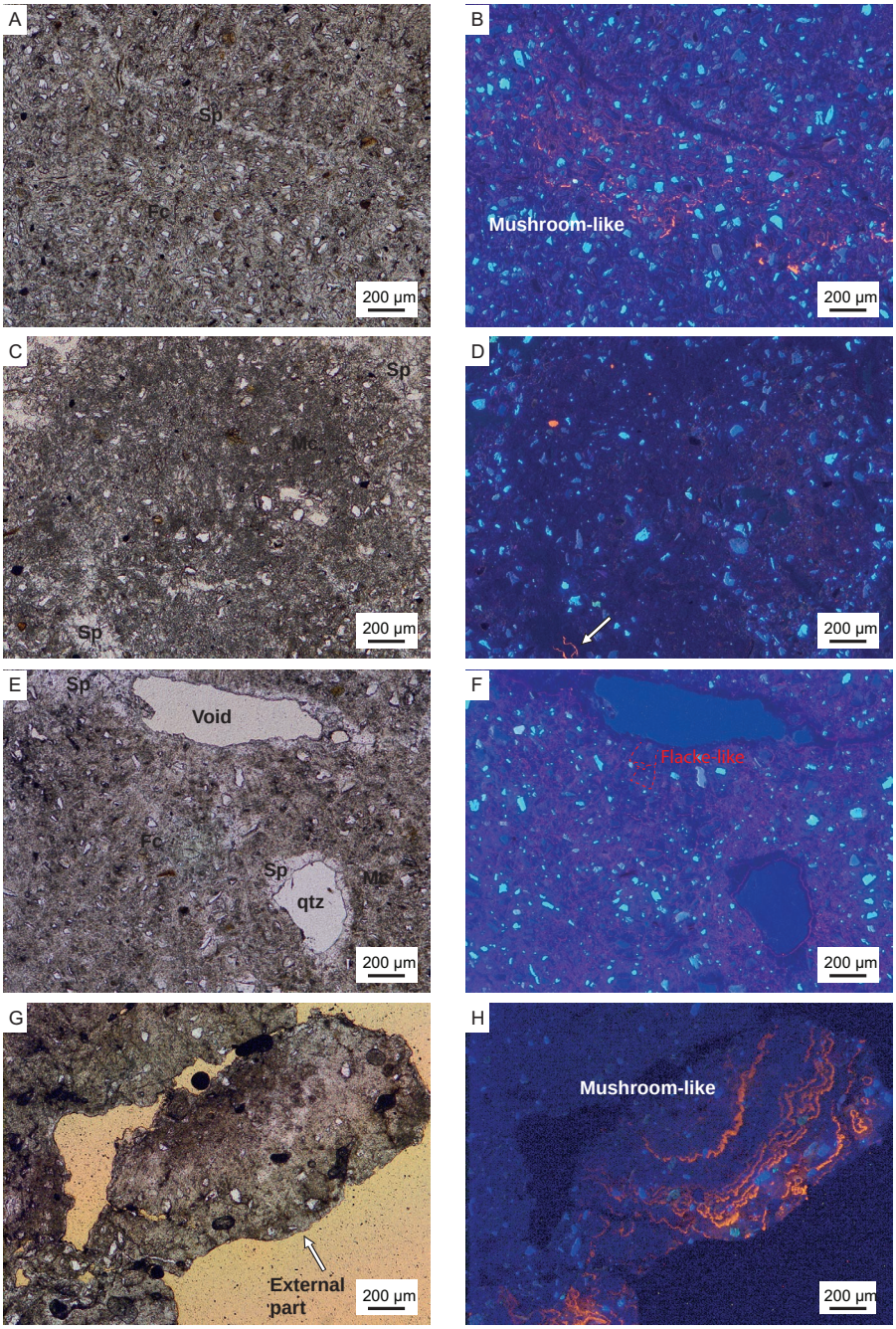

Figure 4.9 – Carbonate nodule thin section and cathodoluminescence (CL). A-B) PL and CL images of Fc crossed by Sp vein. The Fc cement can have mushroom-like pattern parallel to the Sp vein having dark blue colour. C-D) PL and CL images of Mc and Sp areas. The Mc is dark and blue to slightly reddish colours, the Sp is dark blue, except one area showing an orange luminescent internal border. E-F) PL and CL images of Fc crossed by Sp cement filling a septarian void. To the right part of the images, aureoled quartz in a Mc phase can be observed. The Fc cement shows blue-reddish colours with flacke-like pattern whose borders are more luminescent. The Sp cement is dark blue and the Mc phase is blue-reddish but without flacke-like patterns. G-H) PL and CL images of the external part of a nodule showing developed mushroom-like patterns.

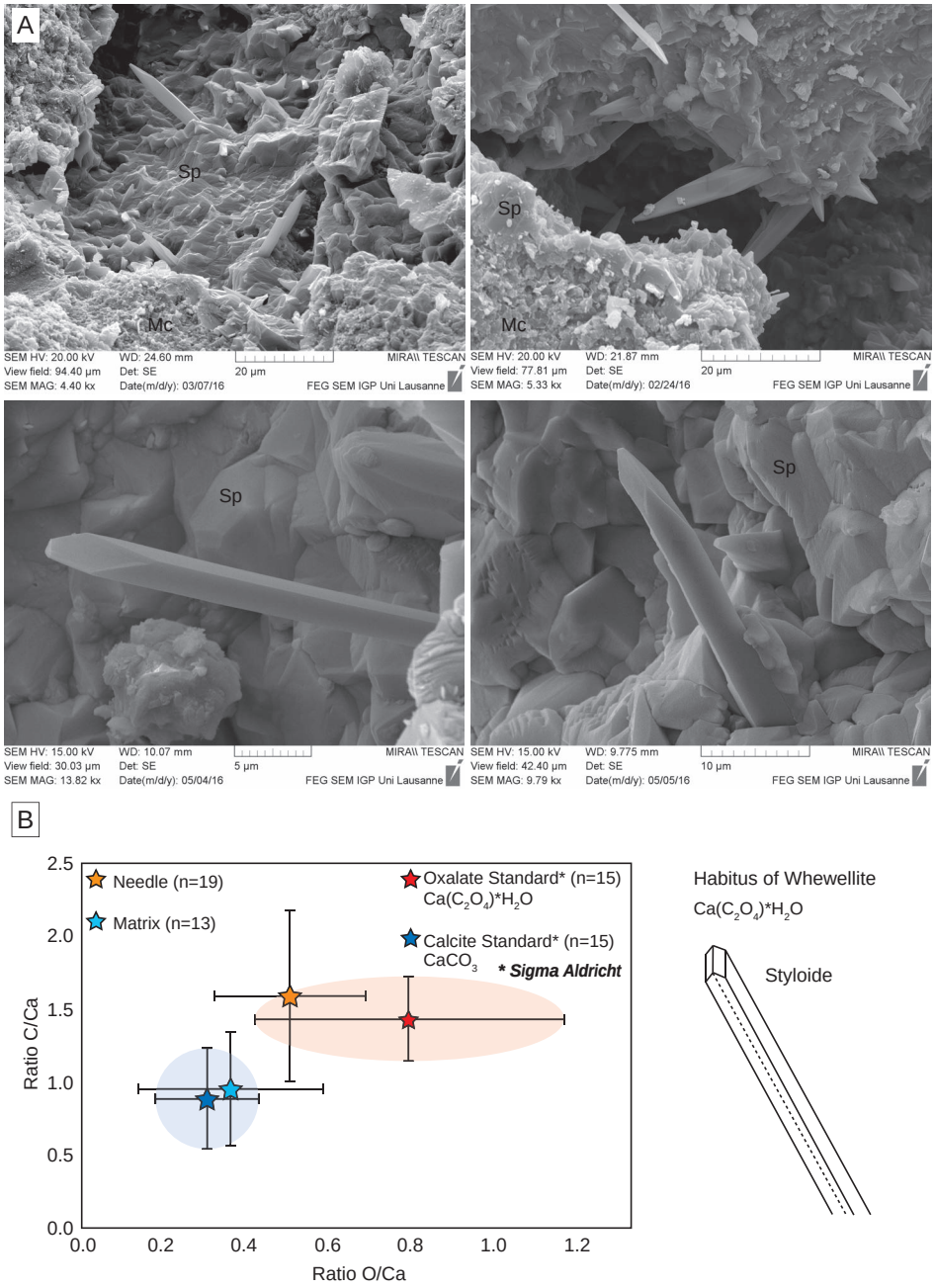

Figure 4.10 – Secondary Electron Microprobe (SEM) images and Energy Dispersive X-ray Spectroscopy (EDS) analyses. A) Micrometric needles developing in the micro-porosity, which is coated by sparite (Sp). Micrite (Mc) surround the coated pores. B) EDS results on the needles (n=19), the matrix, i.e. Sp and Mc phases, (n=13), and on the monohydrated oxalate and calcite standards (n=15). The needles are clearly closer to the oxalate and the matrix is closer to the calcite. On the right, is represented the habitus that can take Whewellite, a monohydrated oxalate (Frey-Wyssling, 1981).

alluvial or not alluvial? Small nodules can also be aggregated together to form larger nodules with diameters reaching 10 cm. Kovda et al. (2003) observed such nodules and showed that they were related to dissolution-precipitation processes mainly occurring in microlow parts of Vertisol Gilgai microrelief

(see Chapter 3, for definitions). Figure 4.4B suggests that this could occur at the soil surface, although there is little evidence of this occurring. Nevertheless, this aggregation can result from reworking, partial dissolution and precipitation processes.

Carbonate nodules are very porous and often show septarian cracks (Fig. 4.5). The occurrence of these cracks is highly debated but is generally proposed to be the result of dehydration, diagenetic processes and/or tensile failures (e.g. Raiswell and Fisher, 2000). In Vertisols, numerous physical stresses result from swelling clays and hydric changes (Mermut et al., 1996). These stresses may also affect the nodules inducing desiccation and creating septarian cracks. The redistribution of calcite as sparite in these voids (Fig. 4.5C) clearly shows later dissolution-precipitation processes (e.g. Zhou and Chafetz, 2009; Violette et al., 2010). Moreover, the dendritic pattern of oxides can also be related to Fe and Mn redistribution within the nodule due to percolation of internal fluids (Swartzlow, 1934). These processes are also visible at the borders of the nodules (Fig. 4.5B). Consequently, the micro-stratigraphy suggests that this $Fe-Mn$ oxide was 1) trapped within the nodule, i.e. during carbonate precipitation I; 2) partially dissolved with the carbonate cement, i.e. during dissolution I; and 3) some of the residue of this oxide was trapped again in a new calcitic cement, i.e during carbonate precipitation II. Obviously, $Fe-Mn$ oxides were formed before the carbonate nodule. However, in the soil matrix, many generations of $Fe-Mn$ oxides, reworked (i.e disorthic or anorthic nodules) or formed *in situ* (i.e orthic nodules), are present, suggesting that many different periods were favourable for their genesis (Wieder and Yaalon, 1974).

The different cements composing the nodules, as well as the micritic phase, suggest an environment sharing characteristics from swamps (i.e. palustrine and/or paludal), and soils (i.e. pedogenic). Micrite embedding aureoled quartz, but also septarian cracks and dendritic oxides are typical features of palustrine and floodplain limestones (Freytet and Verrecchia, 2002; Alonso-Zarza, 2003; Wanas and Soliman 2014). However, some typical biogenic features are missing suggesting rather a genesis related to water-table fluctuations (Wright and Peeters, 1989). The fibrous calcite, as *cone-in-cone* structures (Shaub, 1937), also suggests wet conditions, even if aureoled quartz minerals are absent. Indeed, this cement was found associated with algal systems (Freytet and Verrecchia, 1989) and thus to wet conditions. Moreover, a study also showed that *cone-in-cone* structures could be associated with root-bacteria systems in hydromorphic soils (Aassoumi et al., 1992). Despite the doubts concerning the crystallogenesis, both micritic (Mc) and fibrous calcitic (Fc) crystals should have grown in thermodynamic disequilibrium, otherwise they should have formed euhedral rhombohedra. Thermodynamically, Fc and Mc crystals are supposed to result from a rapid growth in a supersaturated solution (West et al., 1988; Wright and Peeters, 1989). It was also proposed that micritic crystals were positively associated with the clay mineral abundance (Wieder and Yaalon, 1974). Though, it is possible to conclude that the environment in which carbonate nodules formed would have been Vertisols being seasonally waterlogged and affected by water-table fluctuations. These hydric changes affected the nodule growth and its early and later diagenetic processes. Cathodoluminescence properties of the cements reflect these changes in both Eh and pH during precipitation due to hydric changes (Wright and Peeters, 1989). Mn, as the main activator ion in its Mn^{2+} form inducing calcite luminescence (Machel, 1985), underwent reduction, common in suboxic and hydromorphic environments such as Vertisols.

Finally, even if unobserved within the carbonate nodules, biological features were however detected at the carbonate-soil interface. The diffuse carbonate within the horizontal channel (Fig. 4.6A, 4.6B1, 4.6B2) is very similar to calcified root cells (Jaillard et al., 1991). First of all, the horizontal void itself can be interpreted as a root pass breaking into the iron-rich soil area (Fig. 5A, dashed lines). Second, the equigranular size (60-80 μm) and shape of the calcite crystals seem to correspond to original parenchymatic cells or xylem vessels (Alonso-Zarza et al., 1998; Jaillard et al., 1991; Kosir, 2004).

However, the crystals are very dispersed suggesting an inherited feature. The diffuse carbonate can also occur as fine needles around the nodular micritic phase (Fig. 4.6C, 4.6D). These occurrences are similar to unstable aragonite needles quickly recrystallized as calcite needles observed in calcareous soils (Ducloux and Butel, 1983), or to mineralized fungal filaments observed in calcrete (Verrecchia et al., 1993). These filaments were shown by the authors to be calcium oxalate, which can be secondary recrystallized in calcite. Similar mineralized filaments were observed in the external part of some carbonate nodules (Appendix C).

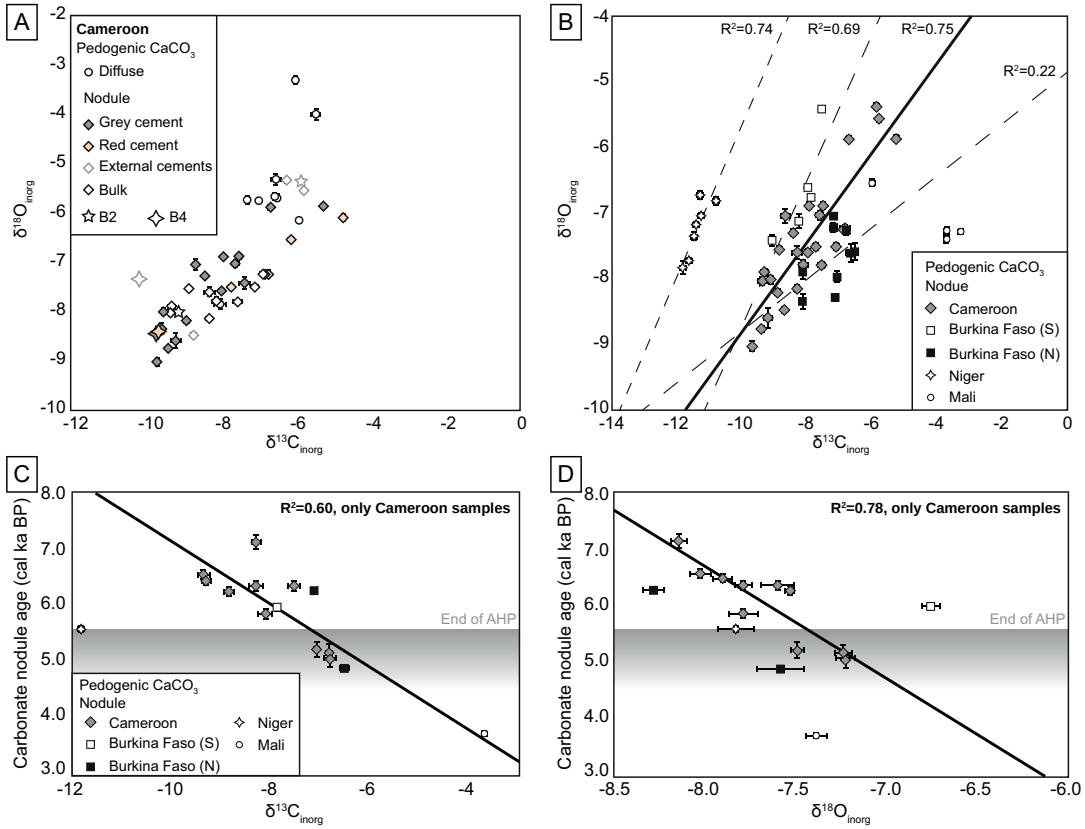

Figure 4.11 – A) Plot of $\delta^{13}C_{inorg}$ versus $\delta^{18}O_{inorg}$ of Cameroon samples, on the diffuse phase (circles) and the nodule phase (diamonds). Sub-samples were taken in the nodules, to compare the grey cements (grey diamonds), the reddish cements (light orange diamonds) and the external parts (grey border diamonds). Bulk analyses are represented by the white diamonds. Finally, as a sub-sampling example, are also represented the results of samples B2 and B4 (see Fig. 4.5), by the five-branched and four-branched stars. B) Plot of $\delta^{13}C_{inorg}$ versus $\delta^{18}O_{inorg}$ of samples of Cameroon (grey diamonds = data in A) compared with bulk analyses on samples from Burkina Faso (S, white squares and N, black squares), Niger (stars) and Mali (circles). C) $\delta^{13}C_{inorg}$ versus radiocarbon ages of bulk analyses on samples from Cameroon (grey diamonds), and few samples from Burkina Faso (S, white squares and N, black squares), Niger (stars) and Mali (circles). The linear regression (bold line) R^2 is for Cameroon samples only. The grey area represents the end of the African Humid Period varying depending the regions. D) Same than C but with $\delta^{18}O_{inorg}$ versus radiocarbon ages.

Stable isotopes (Fig. 4.11, Appendix D) show variability between the different cements, the internal and external parts of the carbonate nodules, and the different phases in the soil (hard nodules and diffuses soil carbonate). Comparing the internal part of nodule B2 with its external part (Fig. 4.5A, 4.5B), which shows dissolution-precipitation processes, the $\delta^{13}C_{inorg}$ values are -9.5‰ and -6.2‰, respectively, and the $\delta^{18}O_{inorg}$ are -8.0‰ and -5.3‰, respectively (Fig. 4.11A, five-branch star). For nodule B4 (Fig.

4C, 4D), comparing the grey and the reddish areas, the $\delta^{13}C_{inorg}$ values and the $\delta^{18}O_{inorg}$ values are not different with values of -9.7‰ and -8.4‰, respectively (Fig. 4.11A, four-branch star). However, the external part of nodule B4 shows different isotopic composition in both the $\delta^{13}C_{inorg}$ and the $\delta^{18}O_{inorg}$, with values of -10.2‰ and -7.3‰, respectively (Fig. 4.11A, four-branch star). The diffused carbonate has different isotopic compositions at different depths, $\delta^{13}C_{inorg}$ = -6‰ and $\delta^{18}O_{inorg}$ = -5.7‰ at 0-5 cm; $\delta^{13}C_{inorg}$ = -7‰ and $\delta^{18}O_{inorg}$ = -5.7‰ at 20 cm; $\delta^{13}C_{inorg}$ = -8‰ and $\delta^{18}O_{inorg}$ = -8‰ at 60 cm. Looking at all analyses, it is interesting to see that internal cements have $\delta^{13}C_{inorg}$ ranging between -10 and -6‰, and $\delta^{18}O_{inorg}$ ranging between -9‰ and -7‰. The bulk analyses are in this range as well (Fig. 4.11A, white diamond). It is different from the diffused soil carbonate and some external cements with $\delta^{13}C_{inorg}$ values ranging between -7‰ and -4‰ and $\delta^{18}O_{inorg}$ values ranging from -7‰ and -5‰ (Fig. 4.11A). There is a link between $\delta^{13}C_{inorg}$ and $\delta^{18}O_{inorg}$ values with R^2 of 0.75 (Fig. 4.11B).

Carbonate nodules radiocarbon ages range from 7 to 5 cal kBP (Appendix D). For the Cameroon samples, there is a relationship between these ages and both the bulk $\delta^{13}C_{inorg}$ and $\delta^{18}O_{inorg}$ values, with R^2 of 0.60 and 0.78, respectively (Fig. 4.11C, 4.11D). Both $\delta^{13}C_{inorg}$ and $\delta^{18}O_{inorg}$ values are becoming heavier with time. Finally, the *C* isotopic composition of the trapped organic matter (Appendix D) ranges between -20 to -25‰ (n=10), and it seems to become lighter with depth. The *C* isotopic composition of the surrounding soil organic *C* ranges between -18 and -20‰ (n=3).

4.3.4 Comparison with nodule samples from the Sahel

Figure 4.12 shows pictures from nodules collected along the Sudano-Sahelian belt (Fig. 4.3), in Niger (NG), Burkina Faso (South=BFS and North=BFN) and Mali (ML). The nodules are porous with a trapped oxide fraction as dendrite (NG), small nodule (BF) or patches (ML). The colour of the calcitic cement is reddish (NG) or greyish (BF and ML). Thin section observations reveal their micritic and brownish nature for NG and ML samples. Obvious aureoled primary minerals are visible inside the matrix. For sample BF, micrite is also present but highly affected by further dissolution-precipitation processes demonstrated by the numerous veins infilled with sparitic crystals, corresponding to former septarian cracks. Dendritic oxides are present within the three nodules. SEM observations revealed the presence of small needles in samples NG and ML, very similar to those observed in the nodules from the Diamare piedmont (Fig. 4.10). They were not observed in sample BF; however, this sample shows aureoled quartz within calcitic cement.

$\delta^{13}C_{inorg}$ and $\delta^{18}O_{inorg}$ signatures of these samples are given in figure 4.11B and compared with samples from Cameroon. BF samples are close to those from Cameroon. NG samples are shifted toward more negative ^{13}C values, whereas ML samples are shifted toward more positive ^{13}C values. There is also a correlation between $\delta^{13}C_{inorg}$ and $\delta^{18}O_{inorg}$ values for samples NG and BFS, with a R^2 = 0.74 and 0.69, respectively. This relationship is less strong for BFN samples and not expressed in ML samples, probably due to the lack of points. Some samples from the Sahel were also dated using radiocarbon and the ages are in the same order of magnitude than samples from Far North Cameroon (between 7 ka and 3 ka cal BP, Appendix D). When the ages are compared with $\delta^{13}C_{inorg}$ and $\delta^{18}O_{inorg}$ values, they seem to follow a similar trend as the samples from Cameroon (Fig. 4.11C, 4.11D). Consequently, many features and characteristics observed within the carbonate nodules from Far North Cameroon are also observable in three different sites along the Sudano-Sahelian belt.

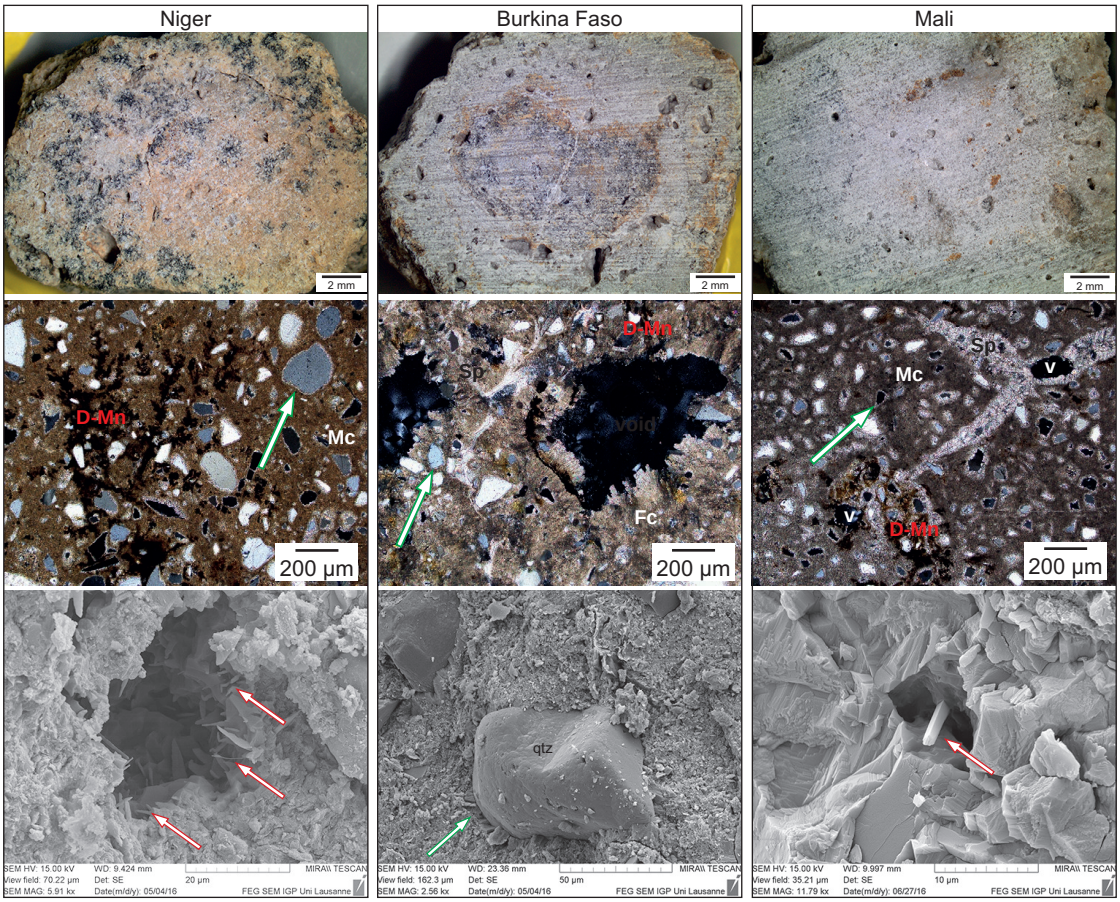

Figure 4.12 – Comparison with nodules from the Sahel. Macro-observations, thin sections and SEM images of nodules from Niger, Burkina Faso and Mali. Thin sections images in cross-polarized light. Green and red arrows emphasize the aureoled quartz and small needles in the micro-porosity, respectively. D-Mn for dendritic manganese, Mc for micrite phase, Sp for sparite and Fc for fibrous calcite.

4.4 Discussion

4.4.1 Chemical changes and secondary mineral stabilities

$Fe-Mn$ oxide micro-nodules can be trapped within pedogenic carbonate nodules, suggesting that they were formed first. The occurrence of hard $Fe-Mn$ oxide micro-nodules is the result of seasonal changes in the redox potential (Eh) and pH (Gasparatos et al., 2005). They are secondary minerals and thus result from weathering. Their main constituents are soluble in anoxic conditions and insoluble in oxic conditions (Schwertmann, 1988). Consequently, water-table fluctuations in the soil environment are needed in order to mobilize Fe and Mn from primary minerals and to then precipitate them as secondary oxides. As both oxide minerals (goethite, hematite, etc.) and calcitic cements refer to wet edaphic conditions, could they be contemporaneous? Occurrence of $Fe-Mn$ oxides implies that redox conditions varied. Moreover, calcite is the main mineral composing the pedogenic carbonate nodules. Looking at the stability conditions of both minerals, they are both occurring in oxic conditions, although the pH seems to be the parameter making the difference. If pH conditions are < 8, $Fe-Mn$ oxides are dominant, whereas calcite dominates at pH conditions > 8 (Krumbein and Garrels, 1952;

Ashley et al., 2013). Calcite can also occur in anoxic conditions if pH is > 8; nevertheless, the study of rare earth elements in the carbonate fraction of the nodules showed a negative cerium (Ce) anomaly, confirming that the carbonate nodules precipitated in oxic conditions (Dietrich et al., *in prep*). In the present-day, both carbonate nodules and $Fe-Mn$ nodules are widely accumulated in the mima-like mound landscape. Therefore, as they should not be dominant in the same chemical conditions, it seems that there was a period of time very favourable for $Fe-Mn$ oxide formation and another period of time more favourable for carbonate nodule precipitation. It is not excluded that carbonate nodules began to form at the same time than $Fe-Mn$ oxides; nonetheless, they would not have been preserved, maybe because there was too much water in the system or because the alkalinity was not high enough, etc. On the other hand, it is not excluded that $Fe-Mn$ oxides were forming at the same time as carbonate nodules (Krumbein and Garrels, 1952; Ashley et al., 2013; Appendix E). Looking at $Fe-Mn$ oxides in the soils, their patterns clearly show many different generations. Disorthic to anorthic $Fe-Mn$ oxide nodules are clearly reworked, whereas diffuse oxide nodules, i.e. orthic ones, are formed in situ and are younger than disorthic and anorthic oxides (Stoops, 2003).

These waterlogged conditions also provide suitable conditions for authigenesis of smectitic clays. Smectitic clays, more precisely montmorillonite, can result from plagioclase weathering in case of mild hydrolysis (Meilhac and Tardy, 1970). In hydromorphic conditions, biotite and muscovite were also observed to be completely or slightly altered into smectite, respectively (Aoudjit et al., 1995). All these minerals compose the granitic bedrock in Far North Cameroon and smectitic clays may likely be a by-product of in situ weathering. It is more likely that the conditions would have been seasonally hydromorphic, such as suggested by the occurrence of $Fe-Mn$ oxides and by the petrography of carbonate nodules. In these settings, silica and alkaline cations are present, leading to montmorillonite formation in both temperate and tropical regions (Boquier, 1973; Tardy et al., 1973). Moreover, in the present-day, the chemistry of the water from the Mandara Mountains and the Diamare piedmont evolved into the stability domain of kaolinite, and the waters in the Yayres are in the stability domain of kaolinite and Na-montmorillonite (Ketchemen et al., 1993). These results suggest that in present-day hydromorphic areas, smectitic clays are stable minerals. Therefore, if hydromorphic areas were extended, the area of stability for smectitic clays would have followed this trend as well.

Consequently, the petrology showed that the environment of Vertisol was a wetland, seasonally waterlogged. These hydric conditions led to mobilize elements and to precipitate them as secondary minerals (smectite, oxide, carbonate). By looking at the stabilities of these secondary minerals, it is possible to state that conditions were first rather favourable for the formation of $Fe-Mn$ oxides, and then of carbonate nodules. A change in the pH conditions may explain the shift of the geosystem from a chemistry dominated by Fe and Mn to a chemistry dominated by Ca and C. Waterlogged and alkaline conditions were very favourable for smectitic clay authigenesis and stability, giving to the background a chemical composition dominated by Al and Mg. Though, why did the pH conditions shift?

4.4.2 The alkalinity engine

A way to increase soil pH is the influence of processes related to microorganism metabolisms (Chafetz and Buczynski, 1992; Kazmierczak et al., 2015). Small needles were observed with SEM within the carbonate nodules. EDS measurements and habitus of crystals suggest that these needles are calcium oxalates ($CaOx$). Two hypotheses can be suggested in order to explain their presence in the microporosity of the nodules: 1) $CaOx$ needles are diagenetic products formed concomitantly with sparitic crystals within the septarian cracks. $CaOx$ was first trapped within the nodules; during hydric

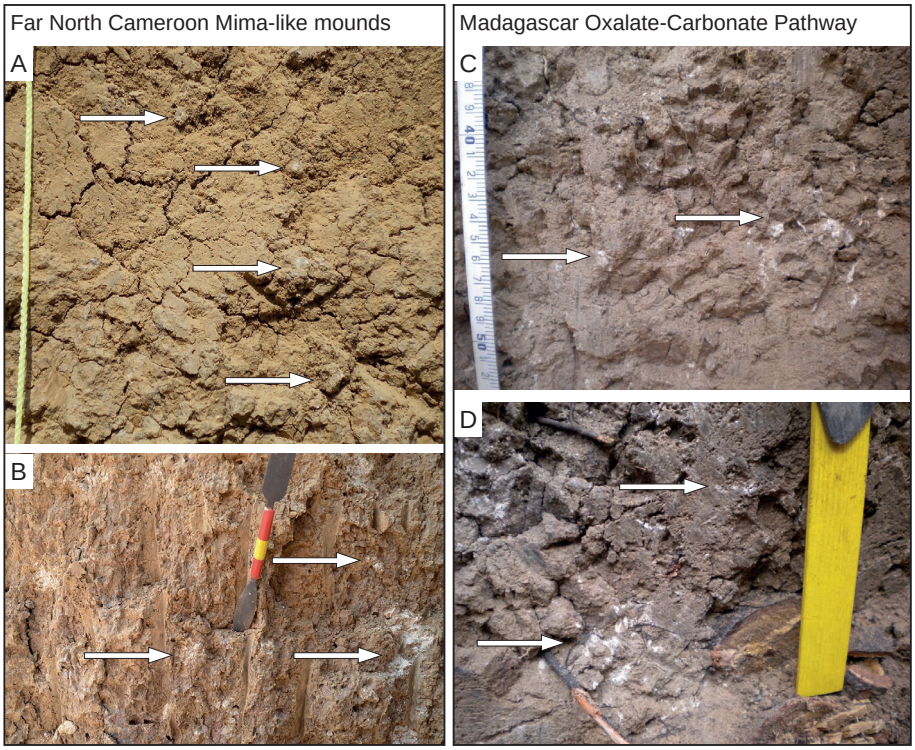

Figure 4.13 – Comparison of pedogenic carbonate in Mima-like mounds from Far North Cameroon (left) with pedogenic carbonate in soils where the Oxalate-Carbonate Pathway (right) was detected (Madagascar, courtesy of Fina Randevoson)

changes, which induced septarian cracks, internal percolated fluids inducing dissolution-precipitation processes led to the formation of rhombohedral sparite and to the dehydration of polyhydrated $CaOx$ into monohydrated $CaOx$ needles (Verrecchia et al., 1993); 2) the internal fluid was enriched in oxalic acid ($(COOH)_2$) and reacted with the carbonate phase as follows:

$$(COOH)_2 + 2CaCO_3 \leftrightarrow Ca^{2+} + (HCO_3^-)_2 + C_2O_4^{2-} + Ca^{2+} \leftrightarrow CaCO_3 + CaC_2O_4 + H_2O \tag{4.4}$$

From this oxalic-rich solution, the two Ca belonging to the carbonate phase at the beginning was then used to form a new calcium carbonate crystal (Sp cement) and a $CaOx$ crystal. Indeed, the pK of calcite and $CaOx$ are very close with values of $2.8 * 10^{-9}$ and $2.7 * 10^{-9}$, respectively. Nevertheless, independently of the type of process, in both cases oxalate (as a crystal or as an acid), had to be present in the environment at the time of carbonate nodule formation. Oxalic acid ($H_2C_2O_4 * nH_2O$) forms through biotic and abiotic processes, but mainly comes from the decomposition of larger C-compounds (Applin et al., 2016). It can also be secreted by a wide variety of fungi (Gadd et al., 2014). Calcium oxalate mineral ($CaOx$) is the most common form and is generally found as whewellite ($Ca(C_2O_4) * H_2O$), which is thermodynamically the most stable form in the environment. It was shown to be strongly associated with life and occurs in biological interfaces, but it was also observed in hydrothermal settings or as a diagenetic product (Nakata, 2003; in Baran, 2014). $CaOx$ as a synthesized biomineral was first reported in plants but was observed in animals, fungi, lichen, algae and even in human kind (as kidney

stones). $CaOx$ is ubiquitous in higher plant families (Franceschi and Nakata, 2005), calcium being provided by the environment (Nakata, 2003). Consequently, it is hypothesized that a direct link between oxalate and presence of life exits.

Despite its ubiquitous occurrence and its stability in the environment at geological time scales (Applin et al., 2016), $CaOx$ do not accumulate in sedimentary sequences (Verrecchia et al., 2006). Consequently, their simple occurrence in the pedogenic carbonate nodules is already extraordinary. The reason behind oxalate absence in sediment sequences is the presence of oxalotrophic bacteria using oxalate as a carbon source for their metabolism (Martin et al., 2012). It was found that this metabolism was coupled with the secondary formation of calcium carbonate (Verrecchia et al., 2006). This process is known as the Oxalate-Carbonate Pathway (OCP). The coupling between these two minerals occurs mainly because the oxidation of oxalate by oxalotrophic bacteria induces the increase of pH by the production of hydroxyl anions (OH^-) by the oxidation of calcium oxalate (Verrecchia et al., 2006):

$$CaC_2O_4 * nH_2O + \frac{1}{2}O_2 \rightarrow Ca^{2+} + 2CO_2 + (n-1)H_2O + 2OH^- \tag{4.5}$$

Then, if the adequate pH is reached, calcite can precipitate:

$$Ca^{2+} + 2OH^- + CO_2 \rightarrow CaCO_3 + H_2O \tag{4.6}$$

The final balance is thus (Verrecchia et al., 2006):

$$CaC_2O_4 * nH_2O + \frac{1}{2}O_2 \rightarrow CaCO_3 + CO_2 + H_2O \tag{4.7}$$

Consequently, the OCP can produce alkalinity in oxic conditions and lead to secondary carbonate precipitation. Figure 4.13 shows pictures of pedogenic carbonate accumulations in Vertisol relics from Far North Cameroon, compared with similar carbonate accumulation in soils located in Madagascar where the OCP was detected. It is likely that the $CaOx$ within the carbonate nodules and the large amounts of secondary carbonate accumulations are pointing to the involvement of the OCP in the genesis of pedogenic carbonate nodules. This pathway can explain the shift of pH, making the geosystem evolve from a $Fe-Mn$ chemical reactor toward a $Ca-C$ one.

4.4.3 An open forest 10 ka ago

The involvement of the OCP to explain the shift in pH in the geosystem implies the presence of life in the environment. The geochemistry of the nodules, especially the $\delta^{13}C_{org}$ and $\delta^{13}C_{inorg}$ can provide some clues concerning the origin of C. The $\delta^{13}C_{inorg}$ values of pedogenic carbonate reflect the $\delta^{13}C$ of the soil CO_2. In a non-calcareous soil, the soil CO_2 is a mix between the CO_2 resulting from organic matter oxidation (soil CO_2 respiration) and the CO_2 from the atmosphere (Cerling, 1984). The $\delta^{13}C$ of soil CO_2 reflects this mix, with values generally enriched of 3-7‰ compared to soil organic matter

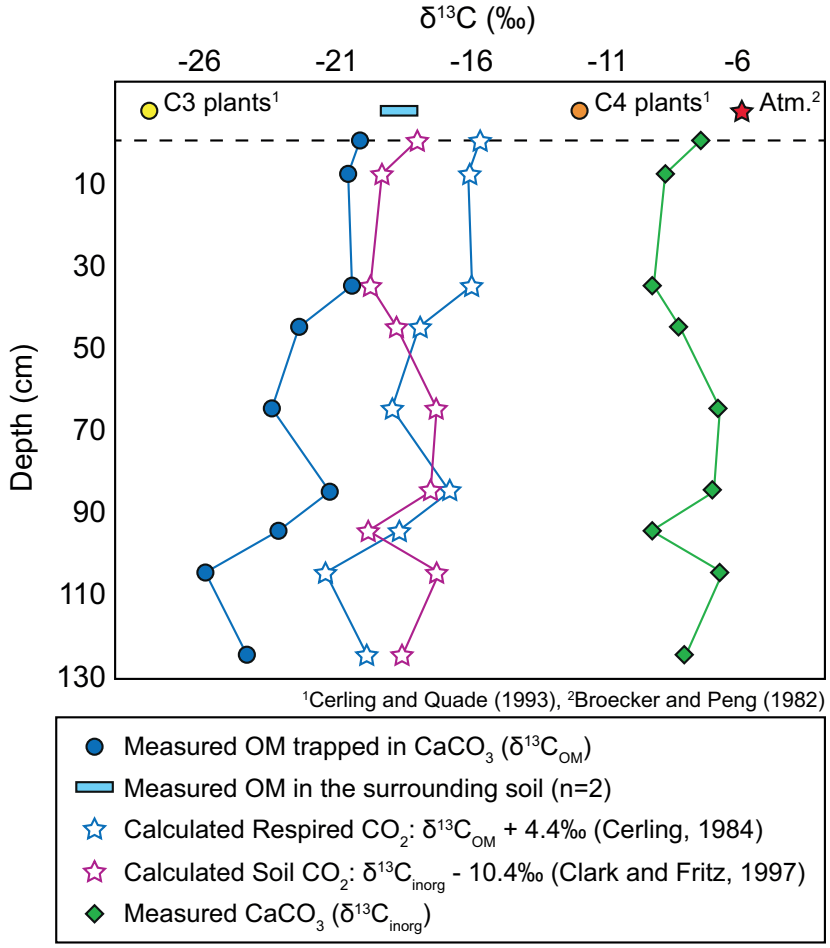

Figure 4.14 – Stable C isotopic composition of carbonate ($\delta^{13}C_{inorg}$) and organic matter ($\delta^{13}C_{OM}$) for samples collected at different depth in Mima-like mound M1 (Table 4.1). Are represented measured $\delta^{13}C_{OM}$ of OM trapped in the carbonate nodules (dark blue), measured $\delta^{13}C_{inorg}$ of carbonate nodules. Calculated respired CO_2 (blue stars) is calculated from the $\delta^{13}C_{OM}$ adding the diffusion fractionation of 4.4‰ (Cerling, 1984) and the calculated soil CO_2, i.e. respired CO_2 mixed with atmospheric CO_2, (purple stars) is calculated from $\delta^{13}C_{inorg}$ values adding fractionation constants in the soil carbonate system at 25°C (Clark and Fritz, 1997). The CO_2 atmospheric values for the pre-industrial period (Broecker and Peng, 1982), and the C3 and C4 plant values (Cerling and Quade, 1993) are also given.

(Cerling, 1984). This range shows that the $\delta^{13}C$ of soil CO_2 is variable. Indeed, it is function of the soil respiration rate, i.e. the proportion of CO_2 coming from soil organic matter oxidation, and the soil depth, i.e. the proportion of atmospheric CO_2 entering the soil (Cerling and Quade, 1993). At the soil-atmosphere interface, and during low production rates, the $\delta^{13}C$ of soil CO_2 is shifted toward atmospheric CO_2 $\delta^{13}C$ values (-6.5‰ in the pre-industrial times, Broecker and Peng, 1982). The results show that the $\delta^{13}C_{inorg}$ values of the internal parts, i.e. the least affected by diagenesis, of pedogenic carbonate nodules range from -10‰ to -6‰. Assuming a temperature of 25°C, the fractionation between CO_2 and DIC is +8.0‰ and from DIC and $CaCO_3$ +2.4‰ (Clark and Fritz, 1997). It is thus possible to reconstruct the $\delta^{13}C$ of soil CO_2 at the time of precipitation, and calculations show that $\delta^{13}C$ of soil CO_2 values should range between -20.4 and -16.4‰. The sources of this CO_2 are thus biogenic

and atmospheric. The trapped organic matter has a $\delta^{13}C_{org}$ signature ranging from -25.7‰ to -20.1‰. The resulting $\delta^{13}C$ of soil CO_2 coming from the oxidation of this organic matter is 4.4‰ enriched due to the diffusion effect (Cerling, 1984) and thus ranges from -21.3‰ to -15.7‰. Consequently, the CO_2 trapped in the pedogenic carbonate nodules should mainly come from the oxidation of organic matter (Fig. 14). This result implies that the nodules are formed in deep horizons and/or during a period characterized by high respiration rates. This also implies that pools must provide enough Ca^{2+}, as high CO_2 concentrations should favour $CaCO_3$ dissolution rather than precipitation (Drever, 1973).

The $\delta^{13}C$ composition of soil organic matter should reflect a mix between organic matter pools of different origin (fresh, humified, inherited) and sources (C3 and C4 plants). Due to different photosynthesis pathways, the $\delta^{13}C$ of C3 plants range from -40‰ to -23‰, with average value of -27.1‰; the $\delta^{13}C$ of C4 plants range from -19‰ to -9‰, with average value of -12‰ (Balesdent et al., 1987; Cerling and Quade, 1993). The $\delta^{13}C$ of soil organic matter in an ecosystem dominated by C3 plants (e.g. temperate forest) ranges from -29‰ to -24‰, and in an ecosystem dominated by C4 plants, from -14‰ to -12‰ (Balesdent et al., 1987). Assuming that the mean values of both ranges, i.e. -26.5‰ (C3) and -13‰ (C4), it is possible to reconstruct the vegetation proportions from measured $\delta^{13}C$ of the soil organic matter. The function of this relationship is shown in Table 4.2, and corresponds to the equation y=-13.5x-13, or x=(-13-y)/13.5. The measured $\delta^{13}C$ average value of organic matter trapped in the carbonate nodules is -22.30‰ (n=10). According to the previous relationship, this represents an organic matter mixing 70% of C3 and 30% of C4 plants. By applying the same relationship to the surrounding soil organic matter ($\delta^{13}C$ = -18.68‰, n=2), it represents a mix of 40% of C3 and 60% of C4 plants. These results suggest that the trapped organic matter has an isotopic composition coming from an open forest dominated by C3 plants. Therefore, such ecosystem is very favourable to the presence of oxalogenous species and to the presence of the OCP.

Table 4.2 – Relationship between soil organic matter (SOM) sources and $\delta^{13}C$ of SOM

C3 SOM %	C4 SOM %	$\delta^{13}C$ SOM
100	0	-26.5
90	10	-25.15
80	20	-23.8
70	30	-22.45
60	40	-21.1
50	50	-19.75
40	60	-18.4
30	70	-17.05
20	80	-15.7
10	90	-14.35
0	100	-13

Figure 4.11C shows that the $\delta^{13}C_{inorg}$ of pedogenic carbonate varied linearly with time towards heavier values. This trend could reflect vegetation changes, and more precisely, a decrease of C3 plants in favour of C4 plants through time. The problem to directly relate $\delta^{13}C_{inorg}$ of pedogenic carbonate to organic matter was discussed above, and results are clearly suggesting that the source of CO_2 is mainly the oxidation of organic matter, whose $\delta^{13}C$ signatures should reflect the proportion of C3 and C4. Consequently, this trend may likely reflect an increase of C4 with time. This conclusion suggests a shift toward drier conditions, as C4 plants are more adapted to dryness. Therefore, a relationship between variability in dryness, vegetation change, and the formation of pedogenic carbonate nodules can be drawn.

4.4.4 Hydrological changes

Interestingly, $\delta^{18}O_{inorg}$ values are significantly shifting toward heavier compositions through time (Fig. 4.11D). The $\delta^{18}O_{inorg}$ of carbonate can be interpreted as a proxy of the soil water balance (Cerling and Quade, 1993; Hsieh et al., 1998). It is a function of the oxygen isotopic composition of water inputs, mainly the rainfall ($\delta^{18}O_{rain}$) and the water-table ($\delta^{18}O_{wt}$), and outputs, i.e. evapotranspiration ($\delta^{18}O_{PET}$). The temperature at which the carbonate precipitates has also an impact on the $\delta^{18}O_{inorg}$ of carbonate. Consequently, changes in $\delta^{18}O_{inorg}$ values can be explained by changes in either, 1) the rainfall regime, 2) the evapotranspiration, and/or 3) the temperature. Geochemical studies of precipitation in the tropics showed that the $\delta^{18}O_{rain}$ is mainly controlled by the amount of precipitation, i.e. the amount effect; consequently, high values must correspond to less rainfall (Dansgaard, 1964). However, some studies emphasized the importance of the atmospheric circulation patterns on the seasonal cycles of isotopic compositions (Feng et al., 2009). The seasonal rainfall distribution in the Diamare piedmont is associated with the monsoon system and shifts of the ITCZ (L'Hôte, 1998). Risi et al. (2008) showed that the $\delta^{18}O_{rain}$ values in Niger were recording the monsoon onset and large-scale convective variability in the Sahel. Indeed, the values appeared to drop significantly at the monsoon season onset. A recent study modelled the $\delta^{18}O_{rain}$ changes during the Holocene at 9 ka, 6 ka and 3 ka BP (LeGrande and Schmidt, 2009). By comparing with present-day data, this study showed that the $\delta^{18}O_{rain}$ values were lighter in the past in West Africa. However, even if the model resulted in a decrease of rainfall through the Holocene due to shifts and weakening of the ITCZ, this study showed that $\delta^{18}O_{rain}$ values were not following this trend and stayed very negative. This would be mainly due to the strong relationship between $\delta^{18}O_{rain}$ and vapour flux on land (LeGrande and Schmidt, 2009). Nevertheless, terrestrial $\delta^{18}O$ of waters are complex to interpret because of the evapotranspiration effect. Fantong et al. (2010) studied different pools of water (spring, groundwater, rain, etc.) in the Mayo Tsanaga watershed (Diamare piedmont, Far North Cameroon) and they showed that the spring waters have heavier $\delta^{18}O$ compared to $\delta^{18}O_{rain}$. Consequently, it is very challenging to find the reason for such an increase in carbonate $\delta^{18}O_{inorg}$ values with time, but this is beyond the scope of this study. Most important is the fact that carbonate nodules seem to record changes in the hydrological regime. The reasons behind these changes are various and can have a climatic origin, a hydrological origin (watershed scale) and/or a pedo-climatic origin (soil scale).

To sum up, chemical conditions, principally pH and water balance conditions, changed through time and this is accompanied by a vegetation change. It seems that the OCP was present in the ecosystem, explaining the increase of alkalinity. However, what is the link between all these environmental parameters.

4.4.5 Involved processes and evolution of the palaeoecosystem through time

Synthesizing all the conclusions, it is possible to propose a scenario of the pedo-sedimentary geosystem evolution through time (Fig. 4.15). The soil parent material has an aeolian component, which was mixed with the saprolite, i.e the local granitic sand (Dietrich et al., 2017). The occurrence of aeolian deposition suggests that the mean annual rainfall should have been ≥ 400 mm/yr (Mc Tainsh, 1984), and a period known with those climatic conditions is the Kanemian (Durand, 1995), lasting from 26 to 14 ka cal BP (Servant, 1973). Interestingly, Barshad (1966) showed that under mean annual rainfall of ~400 mm/yr, the proportion of smectite in the soil resulting from an acid igneous rock, i.e. a granite, is ~40% (Appendix F). Consequently, were the smectitic clay minerals already forming during the Kanemian?

From this parent material, soil can develop. It was demonstrated that the soil environment was in waterlogged conditions, seasonally affected by water-table fluctuations. In those conditions, the Eh is low (anoxia), leading to the mobilization of Fe and Mn. The precipitates of these elements are rounded $Fe-Mn$ oxide nodules formed in oxic conditions, i.e. when the water-table dropped. Waterlogged conditions are also very favourable to bisiallitisation processes (Bocquier, 1973) and smectitic clays (e.g. montmorillonite, beidellite) might thus likely have been formed from the weathering products of feldspars and micas (Meilhac and Tardy, 1970; Aoudjit et al., 1995). The vegetation was also showed to be an open forest dominated by C3 plants. In this large organic pool, it is highly possible that calcium was accumulating by biocycling and thus stored in the ecosystem (Bruijnzeel, 1991). This ecosystem is thus a mineral world dominated by $Al-Mg$ (smectite) and $Fe-Mn$ (oxide), and an organic world dominated by C and Ca. The climatic conditions should thus have been wet during this period, and it is tempting to propose that this wet period was the AHP.

A change in pH would have led the ecosystem shift to a mineral world dominated by C and Ca. What is the trigger for this pH shift? The OCP was proposed to be involved in soil alkalinization. Was the open forest ecosystem already producing $CaOx$? Plants capable to biomineralize CaOx are ubiquitous; consequently, this is a plausible hypothesis. However, why are the carbonate nodules, which need alkaline pH, only mainly producing in a second time, i.e. after $Fe-Mn$ oxides, and not as soon as the forest is present? Is it because the conditions were not favourable for secondary carbonate preservation (too much water)? Or was the alkalinity not high enough? Stable C and O isotopic compositions suggested that the vegetation began to change in favour to C4 plants, and that hydrological conditions began to shift toward drier conditions with time. Is it possible that the decrease of C3 plants, i.e. mainly trees due to dryness, would have increased the inputs of $CaOx$ in the soil and thus amplify the OCP? The engine of alkalinity was thus accelerated and pH drastically shifted toward calcite stability. Consequently, C and Ca, first accumulated in the forest ecosystem, were then transferred from the vegetation and the clay pools to the pedogenic carbonate nodules. During the period of carbonate nodule formation, the water-table continued to fluctuate as showed by petrographic facies and the nodules were forming following alternating precipitation-dissolution processes. Another parameter, also related to dryness, can be the lowering of the water-table and/or the decrease in frequency of water-table fluctuations, which could have favoured the preservation of pedogenic carbonate nodules. It is also highly possible that these condition changes were linked to the end of the AHP. At some point, the geosystem stopped or fossilized, due to the occurrence of one or several erosion events. The trigger for these events may likely be deforestation, but is such a process related to climate and/or human? Nevertheless, the geosystem entered into a Rhexistasy phase, leading to the present-day mima-like mound landscape and to degraded Planosols (*hardés*).

It can be noted that the large accumulation of smectite in the Diamare piedmont could be due to the fact that they were continuously in stable conditions, but for different hydrological reasons. At the time of soil parent material deposition, possibly during the Kanemian, smectite neogenesis is favoured by climatic reasons, i.e. mean annual rainfall of 400 mm/yr (Barshad, 1966, Appendix F). A the time of soil genesis, smectite neogenesis is favoured by hydrological conditions, i.e. waterlogged (Aoudjit et al., 1995). In the present-day, kaolinite is the most stable clay mineral in the Diamare piedmont (Ketchemen et al., 1993) due to mean annual rainfall of 800 mm/yr (Barshad, 1966).

4.4.6 An occurrence at the West African scale?

In some regions along the Sudano-Sahelian belt, such as Mali, Burkina Faso, and Niger, carbonate nodules were observed and sampled. They have been dated and are in the same age range than the

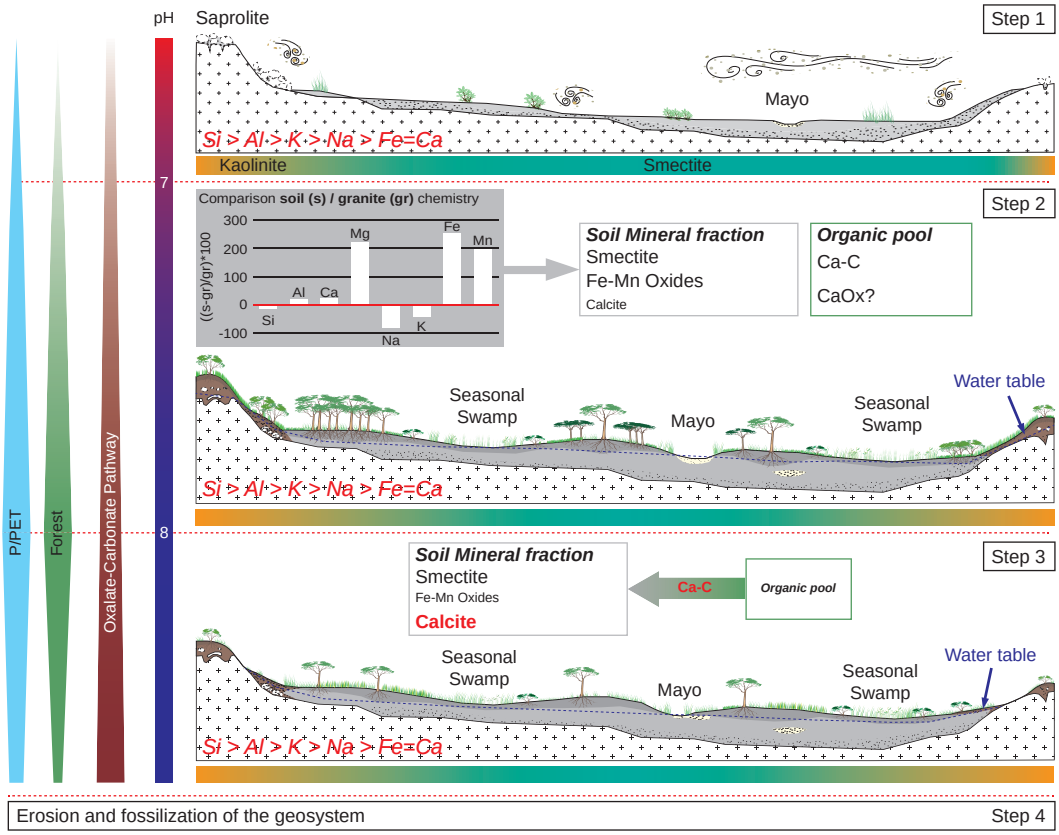

Figure 4.15 – Evolution of the geosystem. Step 1) The soil parent material deposited in low P/PET conditions (light blue), in an environment poorly forested (sahelian?; green), with the likely absence of the oxalate-carbonate pathway (dark red) and thus soil pH close to the alkalinity (reddish-purple) in the lowland areas. The elements in the granite (red) are mixed with an aeolian component and weathered to form kaolinite in higher areas, with greater weathering, and smectite in the lowlands, with lower weathering (Bocquier, 1973). Step 2) P/PET conditions are increasing, the forest is thus growing, likely producing oxalate, water-tables are higher and waterlogged areas (seasonal swamps) can develop in lowlands, which are favourable for smectite neogenesis. Kaolinite and fersiallitic soils are rather developing in the higher areas. The elements from the granite are transferred in secondary minerals, i.e. smectite, Fe-Mn oxides and few calcite, and in the organic pool. Step 3) When P/PET are shifting to lower values, the forest is retreating and the water-table fluctuates less frequently. Oxidation of the organic matter enhanced the OCP and induced an increase of pH, calcite precipitation becomes dominant when pH are 8.4. The other minerals like smectite and $Fe-Mn$ oxides can still produce. Step 4) As P/PET are more lowering, the system reached a critical point leading to its erosion and fossilization (Fig. 4.2).

nodules from Far North Cameroon (Appendix D). This present study exposed in details the petrography and geochemistry of the nodules from Far North Cameroon. They display striking similarities in their petrographic and geochemical aspects with the nodules from Mali, Burkina Faso and Niger. These observations are not by chance, and suggest a possible genetic relationship at the scale of the Sudano-Sahelian belt. Obviously, there is some variability in several parameters, e.g. in the C and O isotopic compositions, but these slight differences can certainly be related to regional factors. More field observations and data are needed to constrain these geosystems and to clearly discriminate regional from global responses. Therefore, are carbonate nodules, observed in Mali, Burkina Faso, Niger, and probably even in other places if confirmed, relics of past forest and wetland ecosystems? This study suggests that a comparison of geosystems at the West African scale could provide major information

on their response to climate change and on the relationships between a large panel of different scales (from the mineral to the continent) including their timescale.

4.5 Conclusion

Vertisol relics from Far North Cameroon are pedo-sedimentary geosystems. They resulted from 4 steps of formation, 1) the soil parent material deposition, 2) the pedogenesis, 3) the carbonate nodule precipitation and 4) the erosion. It was suggested that this events succession could be linked to climatic variations during the Late Quaternary. A geochemical study of associated pedogenic carbonate nodules showed that the Ca is mainly coming from the plagioclase of local saprolite. To explain the transfer from a Ca-poor rock (saprolite) to a Ca-rich rock (carbonate), the Ca should have been accumulated in the geosystem first. It was proposed that the soil, more precisely the smectitic clays and organic matter, would have stock Ca. However, alkaline soil conditions are needed to precipitated $CaCO_3$ and processes behind this are unclear. The petrography showed that the nodules were mainly formed in waterlogged soil environments affected by water-table fluctuations. The associated $Fe-Mn$ oxides were formed before the carbonate nodules and in different chemical conditions, more precisely less alkaline. Oxalate crystals ($CaOx$) were discovered in the carbonate nodules suggesting that the Oxalate-Carbonate Pathway (OCP) could be involved in the alkalinization of the environment. $CaOx$ is ubiquitous produced by vegetation and stable C isotopes of pedogenic carbonate and trapped organic matter showed that an open forest dominated by C3 plants should have been present at the time of pedogenesis. Consequently, $CaOx$ could have been produced at that time. However, the carbonate nodules are only forming in a second time, i.e. after $Fe-Mn$ oxides. Isotopic composition of carbonate suggested that the hydrological conditions are changing the nodules are forming. At the same time, stable C isotopic compositions suggest vegetation change with the increase of C4 plants proportion. Consequently, it seems that at the time of pedogenic carbonate nodule formation, the environmental conditions are becoming drier. It was proposed that this change was responsible of the vegetation decrease and $CaOx$ liberation, activating the OCP and increasing the pH. $CaCO_3$ nodules can then precipitate. From step 1 to step 3, the elements stayed in the geosystem (or were poorly exported). Al and Mg are transferred in the smectitic clay minerals, stable during the whole period of time, Fe and Mn are transferred in the oxides, and Ca is accumulated in the organic matter (as $CaOx$?) before being translocated in the carbonate nodules. Finally, the system fossilized due to the strengthening of dry conditions and/or anthropic activities (deforestation?) leading to one or several erosion event(s). Vertisol relics from Far North Cameroon are thus valuable pedo-sedimentary palaeoenvironment archives.

Part IV
Chronology and stratigraphy of Vertisol relics

SYNOPSIS

It has been demonstrated that the mima-like mounds from Far North Cameroon were Vertisol relics. The associated terrestrial carbonate nodules are pedogenic in origin, and related to Vertisol genesis. Vertisol relics are pedo-sedimentary features resulting from a four-steps events succession. The soil parent material is made of an aeolian component mixed with a local regolith and supposed to have been deposited as a sediment (S1) during a dry period, potentially before the African Humid Period (AHP). The soils, which were developing from this material (S2), were showed to have been seasonally waterlogged (favourable for Vertisol genesis). In these hydric conditions, $Fe-Mn$ oxides and smectitic clays formed. Results obtained from the trapped organic matter showed that an open forest, dominated by C3 plants, was probably present at that time. When climatic conditions became drier, the C3 vegetation decreased in favour of C4 plants, and hydrological conditions changed inside the soil. These new conditions would have been favourable to the precipitation and the preservation of carbonate nodules. The alkalinisation of the soils was explained by the enhance of the Oxalate-Carbonate Pathway (OCP). The organic pool built previously would have been Ca-, C-, and oxalate-rich. Organic matter oxidation led to the liberation of the elements and to increase of pH through the oxalate consumption. Ca and C would have thus been transferred into an inorganic carbon pool, such as carbonate nodules. At some point, the system fossilized, after its erosion, leading to the present-day mima-like mound landscape. It was suggested that pedogenesis was inherited from the African humid Period and that carbonate nodule formation, and later erosion, were linked to the end of this wet period.The aim of this part is to address the questions related to the **timing of mima-like mound formation**. Are mima-like mounds inherited from climatic variations during Late Quaternary in West Africa? To achieve this, it is proposed to use Optically Stimulated Luminescence dating (OSL) to date the soil parent material deposition (S1) and radiocarbon to date the soil organic matter (S2) and the last event of carbonate nodule precipitation (S3). As the soil samples were not collected properly to be dated by OSL, it was necessary to develop a method in order to use the minerals trapped within the carbonate nodules. Trapped minerals have a complex history related to pedogenesis and sedimentary processes since their deposition. It was thus necessary to first identify a suitable mineral population. The environmental dose rate has also changed through time following carbonate precipitation and the radionuclide decay series may be in disequilibrium. Consequently, the first chapter of this part deals with these methodological issues related to OSL dating and **proposes a methodology** to obtain satisfying OSL ages. In the second chapter, Vertisol relics are showed to be **relevant pedo-sedimentary terrestrial archives**. By combining the dating methods, it was possible to constrain the four-steps of formation through time, i.e. during the **last 20 kyr**: 1) soil parent material deposition occurred between 18 ka and 12 ka, 2) strong vertisol pedogenesis operated from 11 to 8 ka cal BP, 3) carbonate nodules precipitated between 7 and 5 ka cal BP, and finally 4) erosion acted after 5 kyr. This succession of processes through time can be associated with the evolution of the soil water balance in turn linked to the climate evolution during the Late Quaternary. Vertisol relics are thus valuable palaeoenvironmental archives, recording events linked to climate variations, and in this case spanning the African Humid Period.

5 Pedogenic carbonate nodules as sedimentary time archives

5.1 Introduction

Pedogenic carbonates comprise $CaCO_3$ accumulations in soil horizons (Lal and Kimble, 2000; Tanner, 2010), which can have various morphologies such as nodular, laminar, tubular, and also different strengths (e.g. Durand et al., 2007). They are widespread and their geochemical properties (e.g. stable carbon and oxygen isotopic composition) can be used as proxies for reconstructing palaeo-climatic conditions (e.g. Dworkin et al., 2005; Retallack, 2005; Yang et al., 2014), palaeo-elevations (Quade et al., 1989; Quade et al., 2007) and also for assessing palaeo-vegetation (Cerling, 1984; Ding and Yang, 2000). The occurrence of pedogenic carbonate is generally observed in soils where there is enough water to provide ions in solution (e.g. Ca^{2+}) and, at the same time, where the moisture regime can be sufficiently xeric (i.e. dry) to reach calcite supersaturation and lead to secondary carbonate precipitation and accumulation (Deocampo, 2010; Gocke et al., 2012; Zamanian et al., 2016). Consequently, pedogenic carbonates are characteristic soil features of arid to sub-humid climatic conditions or where soil moisture conditions alternate strongly (Cerling, 1984; Gocke et al., 2012). Pedogenic carbonates also comprise an important part of the global soil carbon budget (around 30-40% of the global soil carbon inventory is soil inorganic carbon; Eswaran et al., 2000), and, in addition to understanding the processes of their formation, it is also important to constrain the time scale of carbonate precipitation. Numerical dating is possible with methods such as U/Th dating (e.g. Durand et al., 2007; Violette et al., 2010) and radiocarbon dating (e.g. Williams and Polach, 1971; Achyuthan et al., 2010). Furthermore, pedogenic carbonates may also contain a substantial non-carbonate fraction and we show here that this fraction can give important temporal constraints for sedimentary processes and soil formation.

In the Far North Region of Cameroon (Fig. 5.1A), pedogenic carbonate nodules formed in clay-rich soils have been investigated in granitic watersheds belonging to the Chad Basin. These soils are highly eroded and degraded (Fig. 5.1B), and have been interpreted as Vertisol relics (Diaz et al., 2016a) likely inherited from the African Humid Period (AHP), which lasted from c. 15 ka to c. 5 ka (deMenocal et al., 2000). Consequently, the carbonate nodules may be important continental palaeo-environmental archives for this region (Alonso-Zarza and Tanner, 2010), where major precipitation variations occurred in relation to the northern migration of the ITCZ (deMenocal et al., 2000; deMenocal and Tierney, 2012; Shanahan et al., 2015). The aim of this study is to explore the potential of the carbonate nodules as time archives using the mineral fraction trapped within them. The nodules are pedogenic in origin (Diaz et al., 2016a), i.e. were formed in situ in the host soil, meaning that primary minerals trapped within them represent a residual soil fraction (Fig. 5.1C). Singhvi et al. (1996) previously explored this trapped

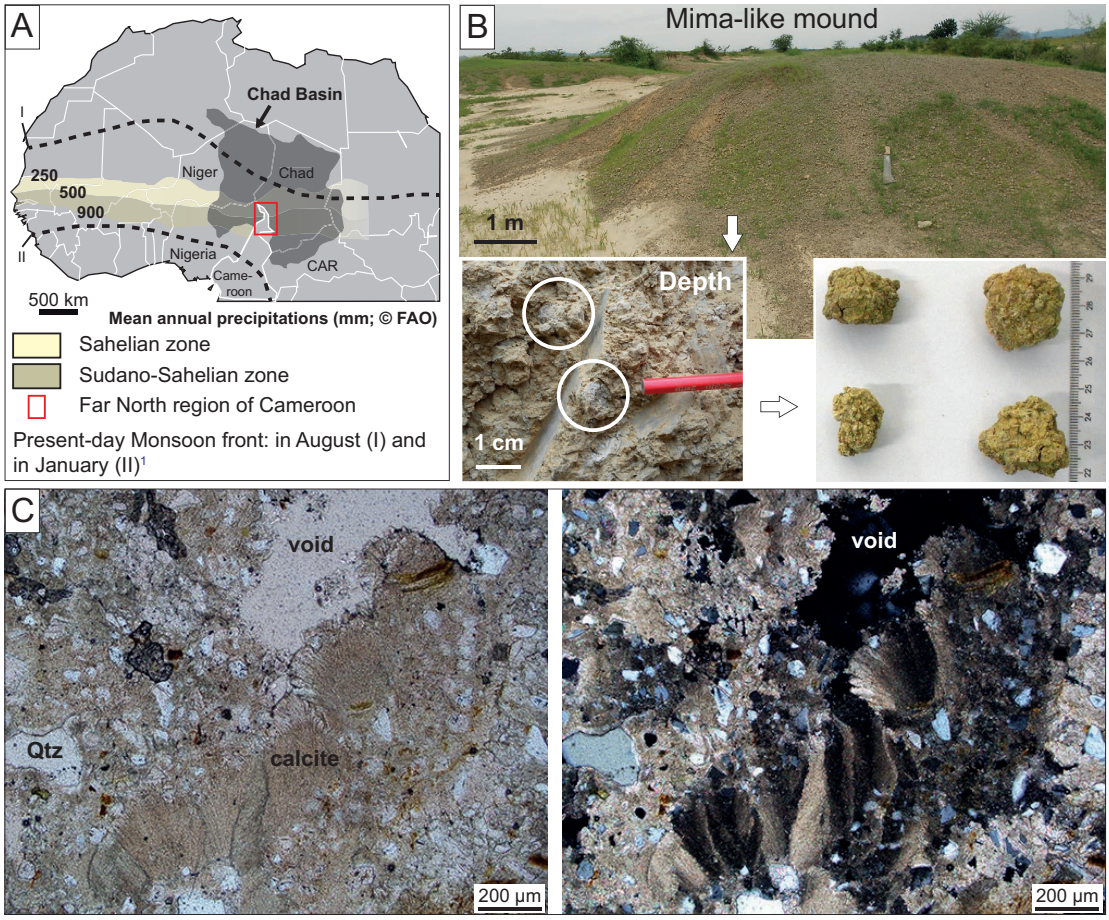

Figure 5.1 – General setting and samples. A) Far North region of Cameroon (red square) study site location along the Sudano-Sahelian belt and within the Chad Basin (dark grey). Dashed lines are the present-day average latitudinal position of the ITCZ in August (I) and January (II) (Nicholson, 2009), controlling wet and dry season occurrences during the year. B) Clay-rich soils forming mima-like mounds and covered by large amounts of carbonate nodules (up to 11 kgm^{-2}). Insets show nodules found within the soil and representative nodules. C) Thin section of a pedogenic carbonate nodule in polarized light (left) and cross-polarized light (right). Calcite precipitated around soil components, i.e. primary minerals (e.g. quartz, feldspars), secondary minerals (clays, oxides) and organic matter.

mineral fraction in carbonate nodules using thermoluminescence (TL) dating, to assess the age of carbonate precipitation. Here we aim to use this trapped mineral fraction for dating the deposition time of the soil parent material, i.e. the sediment from which Vertisols and then carbonate nodules formed, through the measurement of optically stimulated luminescence (OSL). The trapped minerals have a complex post-deposition history linked to pedogenesis (i.e. Vertisol genesis) and subsequent geomorphological processes (i.e. erosion; Diaz et al., 2016a). This needs to be carefully addressed for accurate interpretation of the luminescence measurements and OSL age calculations.

Luminescence dating is a useful method for establishing absolute Quaternary chronologies in continental sedimentary sequences. It is widely used to determine the time that has elapsed since buried sediments were last exposed to sunlight. During burial, trapped electrons accumulate in the minerals in response to environmental radiation (α-, β-particles and γ-rays) emitted by the decay of radiogenic

elements present in the host sediment and by cosmic rays. These electrons recombine when the minerals are exposed to light or heat, resulting in the emission of light (luminescence), and can thus be used to date the deposition time of the sediment (Aitken, 1998). In luminescence dating, an age (ka) is derived from:

$$Age = \frac{D_e}{\dot{D}} \tag{5.1}$$

where, D_e is the equivalent dose (Gy) and relates to the natural dose received by the mineral, and $\dot{D}$ is the environmental dose rate (Gy ka^{-1}).

Successful OSL dating of trapped minerals within pedogenic carbonate nodule requires two main challenges to be addressed. First, the D_e value of the sample needs to be carefully determined, as some nodules were brought at the surface following erosion processes and were thus exposed to light. Consequently, there is a risk that the OSL signal of the trapped minerals has been partially reset, which would result in an underestimation of the sediment depositional age. Moreover, the investigated soils are Vertisol relics. Vertisols are clay-rich, smectitic-rich soils and are affected by swelling-shrinking processes due to soil moisture changes (Wilding, 2004; Southard et al., 2011). These processes induce vertical crack structures leading to the input of surficial soil material in deeper horizons (FAO, 2014). Consequently, these pedoturbation processes can potentially cause a mixing between younger and older sedimentary grains. Both partial bleaching, due to erosion, and sediment mixing, due to pedoturbation, are expected to induce some variability in the D_e distribution (Bateman et al., 2003). The second challenge is to accurately characterize the environmental dose rate ($\dot{D}$). Carbonate accumulation must have led to chemical changes in the soil environment. The concentration of radionuclides surrounding the trapped minerals has thus changed since carbonate precipitation, affecting the $\dot{D}$ (Aitken, 1998). Environmental radiation is mainly emitted following the decay of the uranium (U) and thorium (Th) series and the simple decay of potassium (K) and rubidium (Rb), as well as an additional cosmic dose component. In luminescence dating, the decay series are generally assumed to be in secular equilibrium, implying that the dose rate is constant through time (Olley et al., 1996; Aitken, 1998). However, in the case of carbonate nodules, it is likely that disequilibrium has occurred due to the precipitation of carbonate (Ferronsky and Polyakov, 2012). Finally, as relic soils have been subsequently eroded, the contribution from cosmic rays may have also changed through time, which should also be assessed.

To summarize, two main questions are investigated in this study: (1) is there a suitable population of trapped minerals within the pedogenic carbonate nodules for luminescence dating, and (2) can the $\dot{D}$ changes through time and potential disequilibrium effects be adequately accounted for? Overcoming both challenges would enable the minerals trapped within the carbonate nodules to be used to date the deposition time of the soil parent material. This would also set a maximum age for the onset of pedogenesis, constraining the carbonate nodule genesis that related to the formation and evolution of the Vertisols. As such, pedogenic carbonate nodules can be used as sedimentary archives in a multi-proxy approach using not only the carbonate fraction but also the silicate fraction, which is the objective of this study.

5.2 Material and methods

5.2.1 Sample preparation

For logistical reasons, soil samples were not collected under light-safe conditions and thus cannot be directly used for luminescence dating. Consequently, we propose to explore an alternative approach by using the trapped mineral fraction within the carbonate nodules to assess the time of soil parent material deposition. In the mima-like mound settings, the carbonate nodules are found both as a cover at the surface and within the soil matrix (Fig. 5.1B). Thin sections show that a significant fraction of the carbonate nodules comprises a residual soil component (Fig. 5.1C). X-ray diffraction measurements also confirm this observation, with averages (n = 5) of 57±8% calcite ($CaCO_3$) and of 43±8% other minerals (e.g. quartz, feldspars, phyllosilicates, oxides). These non-carbonate minerals have been shown to represent the surrounding host sediment mineralogy (Diaz et al., 2016a). However, in such settings, this trapped mineral fraction has experienced a complex history from grain deposition to sampling for OSL analysis. Several steps can describe the trapped mineral history (Fig. 5.2). First, the mineral grains are deposited and buried to constitute a sediment sequence (step I). From this sediment deposit, soils (e.g. Vertisols) have then developed during step II. Vertisol genesis induced favourable conditions for secondary carbonate accumulation (Wieder and Yaalon, 1974; Ahmad, 1983) with pedogenic carbonate nodule precipitation that trapped a host soil fraction (step III). Note that there are unknown time gaps between steps I and II, and between steps II and III. Finally, erosion affected the Vertisols leading to the present-day mima-like mound Vertisol relics with some nodules brought to the surface (step IV). As already stated, this complex history has direct implications for the equivalent dose data and for the dose rate assessment.

To investigate the possibility of using trapped minerals for OSL dating despite the complex setting, two carbonate nodules were selected. One nodule was collected at the surface (NO1, diameter (Ø) = 10 cm) and a second nodule was collected at 100 cm depth in a mima-like mound (NO2, Ø = 4 cm). Due to its surficial position, sample NO1 was exposed to light for an unknown duration. To assess the influence of sunlight exposure on the luminescence signal, the outer most layer of sample NO1 ($NO1_{Ext}$, 2-3 cm thick) was removed under red light conditions using a diamond saw and isolated from the central part ($NO1_{Int}$). The luminescence properties of grains from both NO1 subsamples and the buried sample NO2 were then compared. A non-light-safe mineral population should exhibit partial bleaching, following sample exposure to sunlight after carbonate precipitation, and thus a scatter in the equivalent dose (D_e) distribution should be expected. Consequently, a scatter in the equivalent dose distributions could be induced by pedoturbation processes (Bateman et al., 2003), affecting $NO1_{Ext}$, $NO1_{Int}$, and NO2, while we expect sunlight exposure to preferentially affect $NO1_{Ext}$.

The nodules were treated with HCl (35%) to remove carbonates and with H_2O_2 (20 vols) to remove any organic material. Samples were then sieved to isolate the 90-180 μm fraction, which was selected for further analysis because of the abundance of grains in this range. The minerals were then separated by density using sodium polytungstate to isolate quartz (2.7-2.62 gcm^{-3}), plagioclase (2.62-2.58 gcm^{-3}) and K-feldspar (<2.58 gcm^{-3}). A low abundance of quartz led us to the use the K-feldspar fraction, which was not etched (Duller, 1992). Each sample preparation step was performed under subdued red light conditions.

5.2.2 Luminescence measurements

Luminescence measurements were performed using a Risø TL/OSL-DA-20 reader (dose rate ≈ 0.1 Gy s^{-1}) at the Institute of Earth Surface Dynamics (University of Lausanne). To assess the D_e, a single-aliquot regenerative post-IR IRSL protocol was used to access a high temperature signal from feldspars, which is in theory less affected by anomalous fading (Thomsen et al. 2008; Buylaert et al., 2009). A pre-heat of 250°C for 60 seconds was followed by an IR stimulation at 50°C for 100 seconds (IR_{50}) and a post-IR IRSL stimulation at 225°C for 100 seconds ($pIRIR_{225}$). This $pIRIR_{225}$ protocol was chosen instead of the $pIRIR_{290}$ protocol to limit high potential residual doses from partial resetting and thus age overestimations (Thiel et al., 2011, Roberts, 2012). The measured responses of the aliquot to a regenerative dose (L_x) and to a test dose (T_x) were integrated over 3 seconds, and the background signals were integrated over the last 10 seconds of stimulation. Measurements were done using small aliquots (SA, Ø = 1 mm, 100-150 grains measured per aliquot), mounted on stainless steel discs, and single grain measurements were done using aluminium discs (hole diameter Ø = 300 μm, 10-20 grains per hole). Due to a high number of grains in the single grain disks, we refer to these as pseudo-single grain (PSG) measurements. However, SA and PSG comparison still allow us to further investigate the possibility of partial bleaching through reducing the number of analysed grains by one order of magnitude (Duller, 2008). The measurement protocol was validated using a dose-recovery test (Murray and Wintle, 2003) and PSG measurements (n = 3 discs, ≈ 120 measurements), whereby samples were exposed for 4 hours to direct sunlight in Lausanne prior to measurement. Samples were given a dose approximately equal to the equivalent dose (~ 30 Gy) and dose recovery ratios were calculated following subtraction of measured residuals (n = 3 discs ,≈ 120 measurements).

Although the post-IR IRSL protocol reduces the effects of anomalous fading, a fading test was done for both samples (n = 3 SA discs) following Huntley and Lamothe (2001). Previously measured aliquots were given a dose approximately equal to the equivalent dose (~ 30 Gy) and measured following increasing delays (n = 4) between 100 and 800 minutes. The resulting g-values (%/$decade$) were calculated following Auclair et al. (2003) and were normalised to 2 days (Huntley and Lamothe, 2001).

Finally, the D_e values were determined using Analyst v.4.31.7 (Duller, 2015) according to the following acceptance criteria: recycling ratios within 5 and 10% of unity for SA and PSG measurements respectively, maximum test dose and palaeodose error <10%, and maximum recuperation <10% of the natural luminescence signal. The D_e values of the samples were calculated using the central age model (CAM; Galbraith et al., 1999) and are cited at 1σ uncertainty. The sample residual doses and the dose recovery test D_e values are reported with standard error (SE) and 1σ uncertainties, respectively.

5.2.3 Environmental dose rate assessment

The external dose rate ($\dot{D}_{Ext}$, in Gy ka^{-1}) is defined as:

$$\dot{D}_{Ext} = \dot{D}_{\alpha} + \dot{D}_{\beta} + \dot{D}_{\gamma} + \dot{D}_{cos} \tag{5.2}$$

where, $\dot{D}_{\alpha}$, $\dot{D}_{\beta}$ and $\dot{D}_{\gamma}$ are the energy emitted by α-, β-particles and γ-rays, respectively, and $\dot{D}_{cos}$ is the cosmic ray dose rate. As K-feldspars are used in this study, it is also necessary to consider the contribution of the internal dose rate ($\dot{D}_{int}$) resulting from the internal K decay. The combination of the external and internal doses gives the environmental dose rate ($\dot{D}$). The soil and nodule U

(ppm), Th (ppm), K (%) and Rb (ppm) compositions were assessed by X-Ray fluorescence at the Institute of Earth Sciences (University of Lausanne) and by ICP-MS at Actlabs (Activation Laboratories, Ancaster). The internal K-content (%) was measured on individual feldspar grains (n = 187) with a JEOL 8200 Superprobe at the Institute of Earth Sciences (University of Lausanne). The calculations of and were done with the online dose rate calculator DRAC v1.1 (Durcan et al., 2015). The beta grain size attenuation factors of Guérin et al. (2012) and alpha grain size attenuation factors of Bell (1980) were used. The cosmic ray dose rate contribution was assessed using the protocol outlined by Prescott and Hutton (1994) corrected for the geomagnetic latitude (11.789°N; F = 0.39, J = 0.55 and H = 4.35), and taking into account the cosmic-ray attenuation with depth (0 and 100 cm for nodules NO1 and NO2, respectively). We used the water content attenuation factors of 1.5 (α), 1.25 (β) and 1.14 (γ) following Zimmerman (1971) and Aitken and Xie (1990).

External dose rate changes through time

Due to carbonate precipitation, the chemical environment surrounding the minerals varied since the time of deposition (t_0), resulting in external dose rate ($\dot{D}_{Ext}$) changes (Fig. 5.2). During the time period , environmental radiation is solely derived from the radionuclides within the soil matrix and the cosmic dose rate ($\dot{D}_{Ext1}$). However, following carbonate precipitation (i.e. during the time period T_2), the α- and β-contributions are derived from radionuclides composing the carbonate nodule, whilst the γ-dose is derived from both the surrounding soil and the carbonate nodule (Aitken 1985). As nodule diameters are 10 cm (NO1) and 4 cm (NO2), the nodules cannot be seen as an infinite matrix, and γ-rays emitted by the host sediment have to be considered. The γ-dose contribution thus needs to be scaled by the nodule size. To summarize, the carbonate nodule formation results in a different external dose rate ($\dot{D}_{Ext2}$). However, beyond this simple time frame, there are some potential complexities that still need to be investigated:

- During the time period T_1, pedogenesis begins followed by potential carbonate accumulation, leading to a different soil chemical environment (step II). How does this affect the $\dot{D}_{Ext1}$ assessment?
- When the minerals become trapped in a nodule (step III), the nodule growth rate is unknown. The nodule size has most likely increased incrementally through time with different precipitation events, resulting in an uncertainty on the scaled γ-dose. This may also influence the β-dose, but only at the early onset of precipitation when the carbonate size was <3 mm (Aitken, 1985); we thus assume this effect to be negligible. Concerning the γ-dose, can the nodule growth rate affect the $\dot{D}_{Ext2}$ assessment?
- Has the cosmic ray contribution changed through time, due to late-stage erosion (step IV), which would then affect the $\dot{D}_{Ext2}$?

These different points need to be addressed in the assessment of the environmental dose rate changes, and will be individually discussed in the next sections.

Decay chain disequilibrium

In typical silt-sand alluvium, the U and Th decay chains can contribute up to approximately 50% of the external dose rate $\dot{D}_{Ext}$ (Olley et al., 1996). In most luminescence dating applications, the decay chains are assumed to be in secular equilibrium with $\dot{D}_{Ext}$ constant over Quaternary timescales (Armitage,

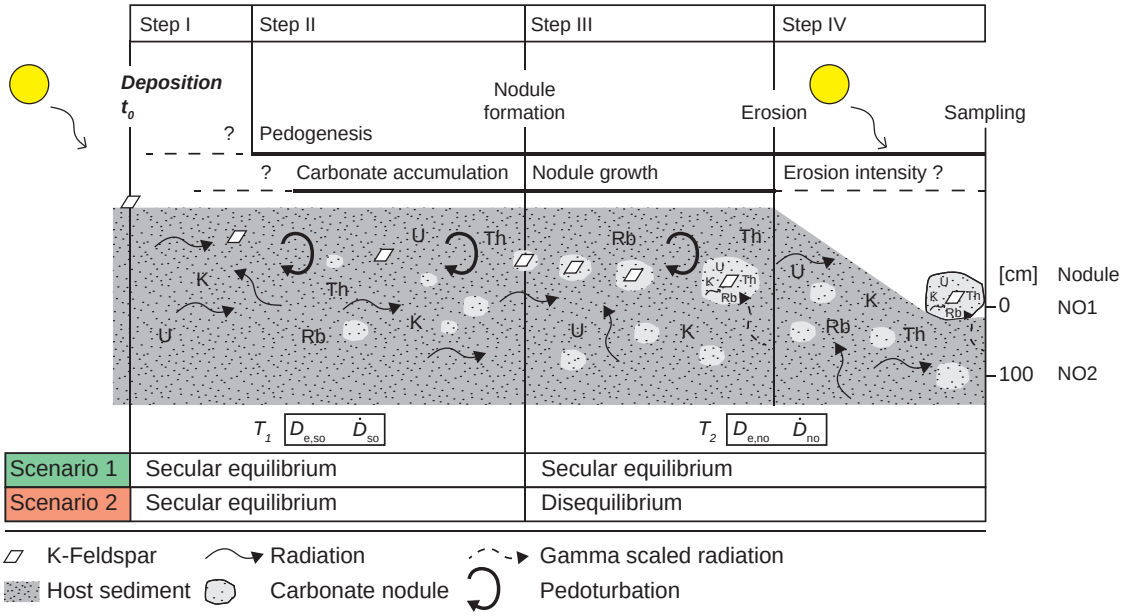

Figure 5.2 – After deposition (t_0), K-feldspars are buried in the sediment (step I), from which the soil will form during period of time T_1 (step II). The luminescence signal ($D_{e,so}$) results from the environmental dose rate ($\dot{D}_{so}$), to which the decay of radionuclides (U, Th, K, Rb) composing the sediment (U, Th, K, Rb) contributes. After carbonate nodule precipitation (step III), the K-feldspars are trapped, and the luminescence signal ($D_{e,no}$) results from the environmental dose rate during time T_2 ($\dot{D}_{no}$), to which the decay of radionuclides composing the nodule and the sediment contribute (γ-dose rate is scaled). Finally, erosion brought some nodules (e.g. NO1) to the surface leading to their exposure to sunlight (step IV). Radionuclides are assumed to be in secular equilibrium during both T_1 and T_2 in scenario 1 (green). Some radionuclides are likely to be in disequilibrium since T_2 in scenario 2 (red).

2015). However, because some radionuclides are mobile, in surficial sediments the ^{238}U decay chain is likely to be in disequilibrium (e.g. Osmond et al., 1983; Short et al., 1989, Olley et al., 1996), and this disequilibrium is very common in environments where carbonates are present or where weathering processes occur (e.g. Guibert et al., 2009; Zander and Hilgers, 2013). Therefore, in the context of pedogenic carbonate nodules, the disequilibrium is linked to the incorporation of U within carbonate during nodule precipitation. In oxic environments, U exists mainly as uranyl species ($UO_2 2+$) and in waters it can form uranyl carbonates ($UO_2(CO_3)_2 2-$) (Chabaux et al., 2008). The disequilibrium of U is mainly caused by the α-recoil of ^{238}U in minerals, inducing the ejection of ^{234}Th at the mineral boundaries. This radionuclide will decay rapidly to ^{234}U, and due to high U solubility it will be leached in pore fluids (DePaolo et al., 2006; Dosseto et al., 2008). Another process is the preferential release of ^{234}U from crystal lattices that are damaged by α-recoil (e.g. Andersen et al., 2009). Consequently, natural surficial waters are generally enriched in ^{234}U compared to ^{238}U.

As secondary carbonate precipitates from a supersaturated soil solution, the U incorporated in the secondary mineral has similar disequilibrium; because U is a heavy element, further fractionation can be assumed to be negligible. In most natural river waters the ($^{234}U/^{238}U$) activity ratio is close to unity when chemical weathering processes are dominant (Chabaux et al., 2003), higher than unity (up to 4) when physical erosion processes are dominant (e.g. Vigier et al., 2001; Andersen et al., 2009) or when groundwaters are contributing to surficial waters (Andersen et al., 2009; Chkir et al., 2009), and lower than unity if there is no renewal of sediment and thus a strong depletion in ^{234}U (Israelson et al., 1997;

Riotte and Chabaux, 1999). In this study, low material availability prevented high-resolution gamma spectrometry to directly determine the degree of U-series disequilibrium. Consequently, following the literature summarized above, different ($^{234}U/^{238}U$) activity ratios between 0.5 and 3 have been investigated. Moreover, in order to illustrate the effect of the most extreme disequilibrium scenario on the environmental dose rate, we have assumed that all the daughter radioisotopes of ^{234}U are absent following carbonate precipitation.

Table 5.1 – Thorium and Uranium composition (XRF and ICP-MS) of the granite bedrock, soil and carbonate ($CaCO_3$) nodule. n is the number of measurements.

	n	**K (%)**	**Rb (ppm)**	**Th (ppm)**	**U (ppm)**	**Ratio Th/U**
Granite	1	5.0±0.07	215.8±1	12.0±2	3.4±1	4/1
Soil	35	2.7±0.03	126.6±1.2	20.1±0.3	4.3±0.1	5/1
$CaCO_3$ nodule	12	0.7±0.03	36.1±0.9	6.1±0.1	5.4±0.2	6/5

As a carbonate nodule precipitates within a soil, U is also derived from minerals within the residual soil fraction trapped in the nodule. This fraction of U is assumed to be in secular equilibrium, unlike the U included as $UO_2(CO_3)_2^{2-}$. In contrast to U, as chemical processes, such as ion leaching and secondary mineral formation, have no or very little effect on Th, this radionuclide should not accumulate in secondary minerals as a soluble phase (Ferronsky and Polyakov, 2012). A comparison of the granite, the soil and the carbonate nodule chemistry (Table 5.1), shows that Th is four to five times more abundant than U in the granite and soil, whereas the Th and U contents are approximately equal in the carbonate nodule. Uranium is thus in excess in the carbonate nodules, which is a consequence of U inclusion as $UO_2(CO_3)_2^{2-}$ during carbonate precipitation; whereas all Th within the carbonate nodule is a component of the trapped residual soil fraction. Consequently, considering the Th/U ratios of the soil ($(\frac{Th}{U})_{so}$ and nodule ($(\frac{Th}{U})_{no}$ given in Table 1, it is possible to distinguish the proportion of U derived from the residual soil fraction (f_{so}) included in the nodule, as follows:

$$\frac{Th}{U}_{no} = [(\frac{Th}{U})_{so} * f_{so}] + [(\frac{Th}{U})_W * f_W] \tag{5.3}$$

where f_{so} is the U fraction of the residual soil fraction trapped within the nodule, and f_W is the authigenic U fraction from water as $UO_2(CO_3)_2^{2-}$, and,

$$f_{so} + f_W = 1 \tag{5.4}$$

$$\frac{Th}{U}_{W} = 0 \tag{5.5}$$

so,

$$f_{so} = \frac{(\frac{Th}{U})_{no}}{(\frac{Th}{U})_{so}} \tag{5.6}$$

The sum of the two fractions represents the total U in the nodule (Equ. 5.4) and as all Th within the nodule is derived from the trapped residual soil fraction, the second term of Equation 5.3 is equal to zero (Equ. 5.5). The fraction of U included in the nodule as a soil detrital fraction, and thus assumed to be in secular equilibrium, can thus be calculated according to Equation 5.6.

For the nodule samples and hypothesizing that the carbonate precipitation event is the main factor affecting disequilibrium, we can assume that only the ^{238}U-series is in disequilibrium. Concerning the ^{235}U-series, it comprises only 0.07% of total natural U. Its contribution to the total U dose rate is relatively small: ~4% (α-decay), ~2% (β-decay) and ~1% (γ-decay) (Guérin et al., 2011). Consequently, we assumed this decay chain to be in secular equilibrium, while a potential disequilibrium (if present) would be negligible relative to the total U dose rate. Finally, as all Th is derived from the trapped residual soil fraction, i.e. not to the carbonate precipitation event, the ^{232}Th-series is also assumed to be in secular equilibrium.

Proposed burial scenarios

To assess the effect of disequilibrium from carbonate precipitation on the $\dot{D}$ (Gy ka^{-1}) and thus on the resulting OSL ages, two end-member scenarios have been considered (Fig. 5.2): (1) the surrounding environment of the minerals has changed through time but radionuclides have remained in secular equilibrium during both time periods T_1 and T_2; and (2) the surrounding environment of the minerals has changed through time, and, in addition, carbonate precipitation induced disequilibrium of the ^{238}U-series during time period T_2. The relationships between the measured equivalent doses, the dose rates, and the time periods are as follow:

$$D_e = D_{e,so} + D_{e,no} = T_1 * \dot{D}_{so} + T_2 * \dot{D}_{no} \tag{5.7}$$

and,

$$\dot{D}_{so} = \dot{D}_{int} + \dot{D}_{ext1} \tag{5.8}$$

$$\dot{D}_{no} = \dot{D}_{int} + \dot{D}_{ext2} \tag{5.9}$$

where, D_e (Gy) is the equivalent dose, $D_{e,so}$ (Gy) is the dose received during the time period T_1, which thus results from $\dot{D}_{so}$; and $D_{e,no}$ (Gy) is the equivalent dose received during the time period T_2, which thus results from $\dot{D}_{no}$. The internal dose rate ($\dot{D}_{int}$) does not change through time whereas the external dose rate is different during time T_1 ($\dot{D}_{ext1}$) and time T_2 ($\dot{D}_{ext2}$) as explained above. During T_1, the soil

environment also varied through time as carbonate progressively accumulated. In the present-day soil, the proportion of carbonate nodules is 7% maximum. To assess this potential influence on the dose rate, the external dose rate for $\dot{D}_{so}$ was also calculated as mixture of a 7% $\dot{D}_{ext2}$ and 93% $\dot{D}_{ext1}$. Moreover, during time T_2, the cosmic ray contribution varied following late-stage erosion (step IV). As the intensity and the timing of the erosion event are unknown, a mean $\dot{D}_{cos}$ was calculated assuming erosional removal of 30 cm of soil during approximately 30% of the total time period, i.e $T_1 + T_2$. Finally, the nodule growth rate during time T_2 remains unconstrained. As the nodule size is expected to increase incrementally through time, this would result in an uncertainty on the scaled γ-dose ($\dot{D}_{\gamma}$), which was calculated with varying nodule diameters from 0.5 to 10 cm.

5.2.4 Calculations

External dose rate

To assess the relative contributions of the different decay series to the external dose rate ($\dot{D}_{ext}$, Gy ka^{-1}), the method outlined by Stokes et al. (2003) and later applied by Armitage (2015) was used. It is possible to calculate the external dose rate for both time periods T_1 and T_2 (i.e. $\dot{D}_{ext1}$ and $\dot{D}_{ext2}$, respectively), either assuming secular equilibrium (scenario 1) or taking into account various degrees of ^{238}U-series disequilibrium during T_2 ($^{234}U/^{238}U$ ratios from 0.5 to 3, scenario 2). The resulting environmental dose rates calculated for scenarios 1 and 2 will then be compared to highlight the potential effect of disequilibrium on calculated environmental dose rates and OSL ages.

In the following section, each step leading to the calculation of the α-, β- and γ-event contributions to the $\dot{D}_{ext}$ are detailed. For the simple decay of K and Rb, the β and γ-dose contributions are calculated according to the conversion factors reported by Guérin et al. (2011). However, for the ^{238}U-series, the radioisotope specific activity (k) needs to be calculated for each radiation event in order to account for potential disequilibrium.

The following calculations must be done for the α-, β- and γ-decays of each radioisotope. Here we detail a representative example for the α-decay contribution (k_{α}) of a radioisotope x ($k_{x\alpha}$):

$$k_{x\alpha} = \left(\sum_{parent}^{ndaughters} E_{x\alpha} \right) * a * b * c_{\alpha} \tag{5.10}$$

where, $E_{x\alpha}$ is the decay energy (MeV/Bq s^{-1}) of a radioisotope x and for an α-decay (Appendix G), a is the number of seconds per ka, b is the number of joules (J) per MeV and c_{α} is the grain size attenuation factor for α-radiation (e.g. Bell, 1980). The k factor is thus expressed in J/Bq ka^{-1}. As U comprises two decay chains with different abundances in nature (99.29% for ^{238}U and 0.07% for ^{235}U), the k factors for each decay event (α, β, and γ) must be adjusted by their relative abundance. The k factor for a given decay chain varies with the number of daughter radioisotopes that are considered, i.e. for a decay chain in secular equilibrium, all daughters will be considered in $E_{x\alpha}$ (i.e. the total energy of all α-particles for a given parent, listed in Appendix G).

As a result, the attenuated radiation (Gy ka^{-1}) for an α-decay event of an element X is calculated as follows:

$$X_\alpha = [X] * A_x * k_{x\alpha} \tag{5.11}$$

where, $[X]$ is the element concentration in ppm (or in % for K), A_x is the isotopic activity of the radioisotope x in Bq/kg ppm (i.e. the number of decays occurring in a given time for a specific number of atoms), and $k_{x\alpha}$ is the specific activity of radioisotope x for an α-decay event (Equ. 5.10).

Both ^{238}U and ^{235}U radionuclides have to be added and scaled by their respective activities (A) and factors$k$ for a given U content $[U]$ (Equ. 5.12). Finally, for α-decay events, it is necessary to take into account the effectiveness of the α-particles (Aitken, 1985; Aitken, 1998) and thus to multiply the outcome of Equation 8 by the a-value (a_{val}). Balescu and Lamothe (1993) measured the α efficiency of 150-250 μm K-feldspar grains for their samples, estimating an a_{val} of 0.11±0.03, which we use in this study. The final equation to assess the energy of the U α-decay event (Gy ka^{-1}) is:

$$U_\alpha = ((A_{238U} * k_{238U\alpha} * [U]) + (A_{235U} * k_{235U\alpha} * [U])) * a_{val} \tag{5.12}$$

This calculation is valid for U series in secular equilibrium. However, for scenario 2 the ^{238}U-series is in disequilibrium; we can assume that all daughter radioisotopes below ^{234}U are absent, and that ^{234}U may be in excess or in deficit. Consequently, only the parent radioisotopes are considered in the calculation of E_x (Equ. 5.10), and [U] is scaled by its ($^{daughter}X/^{parent}X$) activity ratio μ, which represents the excess or lack of $^{daughter}X$ compared to $^{parent}X$. Consequently, the U α-decay dose rate, where ^{234}U is in disequilibrium with ^{238}U, is:

$$U_\alpha = ((A_{238U} * k_{238U\alpha} * [U]) + (A_{234U} * k_{234U\alpha} * [U] * \mu) + (A_{235U} * k_{235U\alpha} * [U])) * a_{val} \tag{5.13}$$

Furthermore, even in scenario 2, not all U within the nodule can be considered to be in disequilibrium because some is derived from the residual soil fraction (Equ. 5.6). Consequently, the U_α dose rate needs to be calculated for both equilibrium and disequilibrium, and the U concentrations [U] must be multiplied by the relative proportions calculated in Equation 5.6.

After the calculation of the contribution for each element, the same decay events' contribution must be added together and corrected for water attenuation using the appropriate factor (here for α = 1.49; Aitken and Xie, 1990). The following equation shows an example for the total α-dose rate contribution ($\dot{D}_\alpha$):

$$\dot{D}_\alpha = \frac{U_\alpha + Th_\alpha}{(1 + 1.49 * \frac{WF}{100})} \tag{5.14}$$

where, U_α and Th_α are the attenuated doses calculated in Equations 11 or 12, depending on the scenario (1 or 2), and WF is the water content (%) of the sample (estimated here to be 10±2%). Finally,

the γ-dose rate ($\dot{D}_\gamma$) needs to be scaled during the time period T_2. Because the nodule diameter is <30 cm, a nodule cannot be considered as an infinite matrix (Fig. 5.2). The final $\dot{D}_\gamma$ then accounts for the self-dose from the nodule and a contribution from the host sediment (Aitken, 1985):

$$\dot{D}_\gamma = \frac{p}{100}\dot{D}_\gamma^i + (1 - \frac{p}{100})\dot{D}_\gamma^{ex} \tag{5.15}$$

where, the self-dose p (%) is calculated by multiplying the diameter of the nodule (cm) by its density (2.7 gcm^{-3}, as estimated for the nodules (n = 5)), $\dot{D}_\gamma^i$ is the gamma dose emitted by the decay of radionuclides present in the carbonate nodule, and $\dot{D}_\gamma^{ex}$ is the gamma dose emitted by the decay of radionuclides present in the soil.

OSL ages

The OSL age (ka) of trapped minerals, reflecting the deposition time of the soil parent material (t_0), can be calculated as follows:

$$t_0 = T_1 + T_2 = \frac{D_{e,so}}{\dot{D}_{so}} + \frac{D_{e,no}}{\dot{D}_{no}} \tag{5.16}$$

so,

$$t_0 = (\frac{D_{e,so}}{\dot{D}_{so}}) + T_2 \tag{5.17}$$

The length of T_2, or the age of carbonate nodule formation, is thus important to assess. The objective here is to evaluate the effect of different T_2 durations on the OSL age (t_0) for both scenarios. As already specified, the pedogenic carbonate nodules are expected to form in Vertisols inherited from the AHP from c. 15 to 5 ka BP; deMenocal et al., 2000). Moreover, it is not excluded that carbonate is still precipitating in the present-day, as the soil chemical conditions are still favourable (Diaz et al., 2016). Consequently, the two end-members, represented by the minimum and maximum deposition ages, are:

$$t_{min} = \frac{D_e}{\dot{D}_{so}} \tag{5.18}$$

$$t_{max} = \frac{D_e}{\dot{D}_{no}} \tag{5.19}$$

where, t_{min} considers that the carbonate nodule never precipitated, i.e = 0, and t_{max} considers that

the carbonate nodule always existed, i.e $T_2 = t_0$. The true sediment age should lie between these two unlikely end-members, i.e. some residence time in the soil followed by a second phase trapped in the nodule (Equ. 5.16 and 5.17). For the disequilibrium scenario, the OSL ages are first calculated with a ($^{234}U/^{238}U$) activity ratio of 1.31, assuming that the ^{234}U daughters are absent. This ratio value is used following the $^{234}U/^{238}U$ ratios measured for Holocene pedogenic carbonate nodules from a similar environment in India (Violette et al., 2010). Different activity ratio values are also tested in subsequent calculations in order to more specifically determine this effect on the OSL ages.

5.3 Results

5.3.1 Luminescence results

A summary of the luminescence results is given in Table 5.2 for nodules NO1 and NO2. The SA overdispersion values (OD) for subsample $NO1_{Ext}$ are much higher than for subsample $NO1_{Int}$ for both the IR_{50} (19.4±0.6 % and 8.6±0.3 %, respectively) and $pIRIR_{225}$ (8.4±0.3 % and 1.1±0.8 %, respectively) signals. PSG measurements have higher OD values than SA measurements, but follow the same trends. The $IR_{50}/pIRIR_{225}$ ratios, which represent the relationship between the doses derived by the IR_{50} and the $pIRIR_{225}$ signals, are 0.50 and 0.41 for PSG and SA respectively for $NO1_{Ext}$. For $NO1_{Int}$, they are 0.74 and 0.64, while for NO2 they are 0.66 and 0.60. This ratio is expected to be less than unity as the IR_{50} signal is more affected by anomalous fading (Thomsen et al., 2008). This is supported by the measured g_{2days} values (n=3), which are 4.5±0.9 %/decade (NO1) and 5.0±0.7 %/dec (NO2) for the IR_{50} signals, and 1.7±0.6 %/dec (NO1) and 1.9±0.6 %/dec (NO2) for the $pIRIR_{225}$ signals. Moreover, the $pIRIR_{225}$ signal has been shown to bleach more slowly than the IR_{50} signal (Buylaert et al., 2012), supported for these samples by the residual doses measured after sunlight bleaching (~4 Gy for the IR_{50} signal and ~8 Gy for the $pIRIR_{225}$ signal, Table 5.3). The dose recovery ratios (measured dose - residual dose/given dose) measured using PSG for both samples show acceptable deviations from unity within 10% (Table 5.3). The OD values for the PSG dose recovery test range between 10 and 24% (Table 5.3). The D_e values determined using the PSG and SA measurement approaches are within uncertainties for all samples, and only the $NO1_{Ext}$ IR_{50} signal has a ratio beyond 10% of unity, i.e. 1.3 (Table 5.2 and Fig. 5.3). The kernel density estimate (KDE) plots illustrate the SA D_e distribution for $NO1_{Ext}$ and $NO1_{Int}$, with both IR_{50} (Fig. 5.4A) and $pIRIR_{225}$ (Fig. 5.4B) signals. The difference between the two sample D_e values is smallest for the $pIRIR_{225}$ signal.

Table 5.2 – Comparison of pseudo-single grain (PSG) and small aliquot (SA) measurements for samples $NO1_{Ext}$, $NO1_{Int}$ and NO2. The D_e values were calculated according to the central age model (CAM; Galbraith et al., 1999) with uncertainties expressed at $\pm 1\sigma$. The $IR_{50}/pIRIR_{225}$ ratio illustrates the difference between investigated signals. The PSG/SA ratio compares the two measurement approaches. n is the number of aliquots/grains measured.

	Signal	**Pseudo-Single grain (PSG)**				**Small aliquot (SA)**				**PSG/SA**
		n	D_e (Gy)	$IR_{50}/pIRIR_{225}$	OD (%)	n	D_e (Gy)	$IR_{50}/pIRIR_{225}$	OD (%)	
$NO1_{Ext}$	IR_{50}	63	33.9±15.2	0.50	38.1±0.4	24	25.5±6.3	0.40	19.4±0.6	1.3
	$pIRIR_{225}$	25	67.3±11.8		15.0±0.5	24	63.1±7.0		8.4±0.3	1.1
$NO1_{Int}$	IR_{50}	125	57.3±13.3	0.74	22.8±0.1	24	56.4±6.9	0.64	8.6±0.3	1
	$pIRIR_{225}$	54	77.8±10.4		11.3±0.2	24	88.3±5.2		1.1±0.8	0.9
NO2	IR_{50}	148	52.2±15.6	0.66	29.9±0.2	24	53.6±4.0	0.60	5.1±0.3	1
	$pIRIR_{225}$	24	78.9±16.8		23.1±0.7	24	90.5±5.5		2.2±0.5	0.9

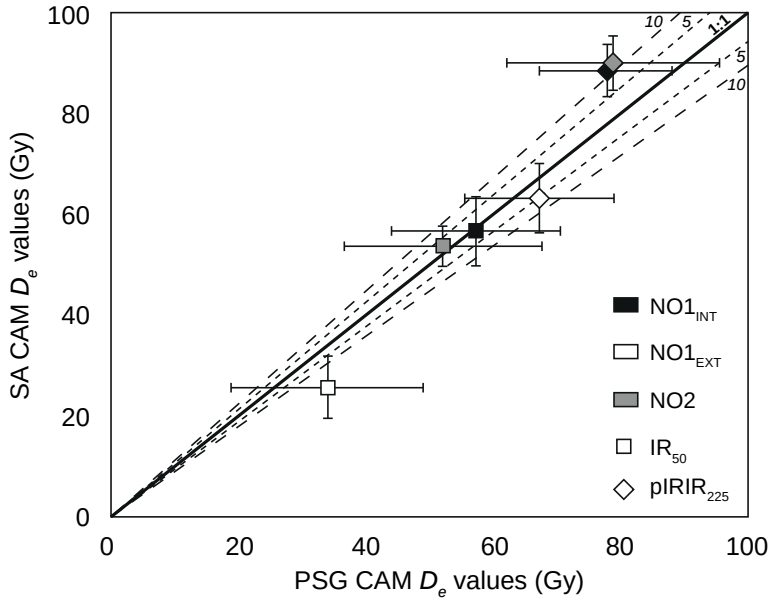

Figure 5.3 – Sample $NO1_{Int}$ (black), $NO1_{Ext}$ (white) and NO2 (grey) are represented by their IR_{50} (square) and $pIRIR_{225}$ (diamond) signals. Dashed lines show the deviation percentage (5 and 10%) from the 1:1 line (bold). Uncertainties are shown at one standard deviation ($\pm 1\ \sigma$).

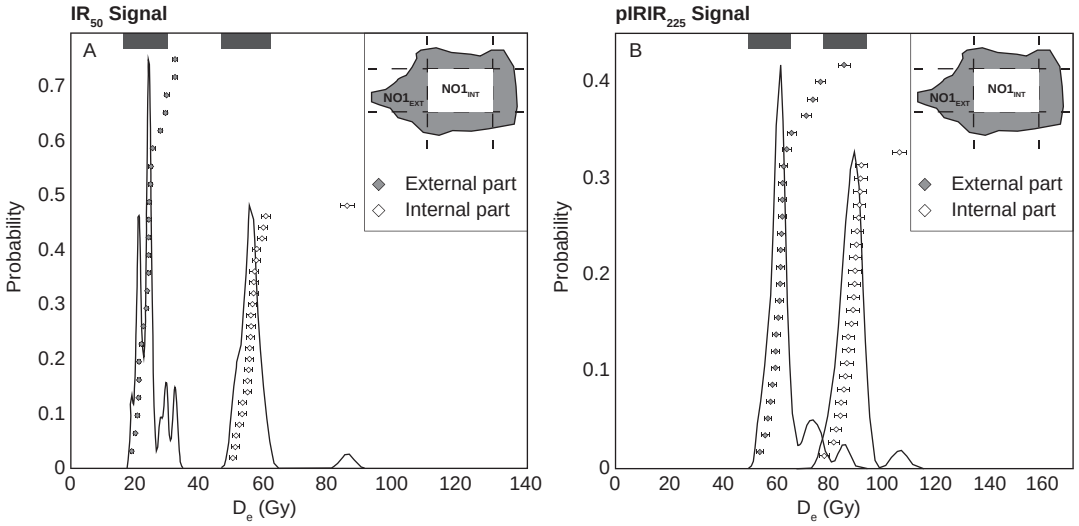

Figure 5.4 – Comparison of the SA equivalent dose (n=24) for the external part of nodule NO1 ($NO1_{Ext}$) with its internal part ($NO1_{Int}$), for both IR_{50} (A) and $pIRIR_{225}$ (B) signals. The equivalent doses for both signals are significantly different between $NO1_{Ext}$ and $NO1_{Int}$. This difference is greater for the IR_{50} signal than the $pIRIR_{225}$ signal.

5.3.2 Dose rate assessement

Electron microprobe micro-analysis on individual grains indicated that the <2.58 gcm^{-3} mineral extract comprises 30% K-poor plagioclases (Oligoclase, K-content <5%) and 70% K-rich feldspars (Orthoclase),

Table 5.3 – Residuals and dose recovery test results from pseudo-single grain (PSG) measurements. The residual D_e values were calculated according to the central age model (CAM; Galbraith et al., 1999) represented with uncertainties expressed at ±SE (standard error). The dose recovery ratio is calculated as the recovered dose - mean residual ($D_{(e-res)}$) divided by the given dose (D_{eg}) and are expressed at ±1 σ.

	Signal	**Residual dose**		**Recovery test**		
		n	$D_e \pm SE$ (Gy)	n	$D_e \pm SE$ (Gy)	OD (%)
$NO1_{Ext}$	IR_{50}	98	3±0.3	48	1.03±0.30	22±0.4
	$pIRIR_{225}$	59	8±0.6	22	1.13±0.25	10±0.6
$NO1_{Int}$	IR_{50}	106	4±0.4	149	1.03±0.23	16±0.1
	$pIRIR_{225}$	75	8±1.0	81	0.97±0.58	24±0.2
NO2	IR_{50}	194	3±0.2	211	0.93±0.14	10±0.1
	$pIRIR_{225}$	168	6±0.3	96	0.94±0.19	14±0.1

resulting in a mean K-content of 12.65±0.10% (±1σ) for the K-rich feldspar fraction. Assuming the K-rich feldspars contribute mostly to the measured signal, the calculated $\dot{D}_{int}$ is 0.45±0.09 Gy ka^{-1} for both NO1 and NO2. The $\dot{D}_{cos}$ may have varied during T_2 following late-stage erosion (Step IV, Fig. 5.2). The extent of erosion is unknown but if we assume a total erosion of 30 cm, $\dot{D}_{cos}$ changes from ~0.21 Gy ka-1 (before erosion) to ~0.29 Gy ka^{-1} (after erosion) for NO1, and from ~0.17 to 0.18 Gy ka-1 for NO2. The other unconstrained parameter is the proportion of time affected by the change in the $\dot{D}_{cos}$, i.e. when the erosion event occurred. As proposed by Diaz et al. (2016), this event occurred after nodule formation and could therefore have been initiated towards the end of the African Humid Period. The proportion of time affected by the change in $\dot{D}_{cos}$ should then be ~30%. Consequently, $\dot{D}_{cos}$ values of 0.25±0.03 Gy ka^{-1} and 0.17±0.02 Gy ka^{-1} are obtained for NO1 and NO2, respectively, for the whole time period, i.e. $T_1 + T_2$.

The external dose rates in the nodule ($\dot{D}_{ext2}$) were calculated for both scenarios. Continuing with the example of α-decay as developed in sections 5.2.4, the energy values for an α-decay ($E_{x\alpha}$) of the ^{238}U-series in equilibrium is 42.87 MeV/Bq s^{-1}, whereas in disequilibrium, $E_{x\alpha}$ is reduced to 4.19 MeV/Bq s^{-1} (Appendix G). The resultant k factors (Equ. 5.10) are thus 0.036 and 0.003, for the equilibrium and the disequilibrium scenario, respectively. This represents a one order of magnitude reduction in $\dot{D}_{U\alpha}$ (Appendix G). All the attenuated radiation values, for each element and radiation type, in the soil and nodule and for both scenarios, are given in the supplementary material (Appendix G).

Following Equations 5.3 to 5.6 and geochemical measurements (Table 5.1), the calculation of the U fraction included in the carbonate nodule as a soil detrital fraction, and thus assumed to be in secular equilibrium, is 0.24. This implies that 76% U was included as $UO_2(CO_3)_2^{-2}$ and can thus be assumed to be in disequilibrium. The resulting external dose rate during the time period T_1 ($\dot{D}_{ext1}$, i.e. from the soil and cosmic ray dose during step I), is 5.36±0.34 Gy ka^{-1} and 5.28±0.34 Gy ka^{-1} for NO1 and NO2 respectively. The external dose rate during the time period T_2 ($\dot{D}_{ext2}$, i.e. from the nodule and the soil), is 3.67±0.34 Gy ka^{-1} and 3.79±0.34 Gy ka^{-1} for NO1 and NO2, respectively, when assuming secular equilibrium (scenario 1). If disequilibrium is accounted for (scenario 2), the $\dot{D}_{ext2}$ is 3.00±0.34 Gy ka^{-1} and 3.18±0.34 Gy ka^{-1} for NO1 and NO2, respectively (Table 5.4).

The total environmental dose rate, i.e. taking into account the $\dot{D}_{int}$, for the time period T_1 ($\dot{D}_{so}$) is thus 5.81±0.34 Gy ka^{-1} (NO1) and 5.73±0.34 Gy ka^{-1} (NO2). For the time period T_2 ($\dot{D}_{no}$), when assuming secular equilibrium, it is 3.92±0.34 Gy ka^{-1} (NO1) and 3.96±0.34 Gy ka^{-1} (NO2), while it is reduced to 3.25±0.34 Gy ka^{-1} (NO1) and 3.35±0.34 Gy ka^{-1} (NO2) if disequilibrium is accounted for (Table 5.4).

The effect of different nodule diameters on the dose rate shows an increase of ≈0.3 Gy between nodule diameters of 0.5 and 10 cm, which represent a maximum error of c. 8%. Moreover, different ($^{234}U/^{238}U$) activity ratio values, ranging from 0.5 to 3 assuming that ^{234}U daughters are absent, were explored in the calculation of $\dot{D}_{ext2}$. Resulting dose rates range from 3.04 to 3.10 Gy ka^{-1} inducing a maximum change of 0.06 Gy ka^{-1} (~2%). Finally, the potential accumulation of carbonate during T_1 induced a maximum change of 0.2 Gy ka^{-1} (~8%) if we consider a concentration of 7% carbonate nodules in the soil according to the present-day observations. Regarding the lack of real quantitative constrains of these factors and the negligible effect on the calculated dose rates, we did not consider them in the age calculations.

Table 5.4 – Internal ($\dot{D}_{int}$), cosmic ($\dot{D}_{cos}$) and environmental dose rates ($\dot{D}$?) for NO1 and NO2, for the equilibrium (1) and disequilibrium (2) scenarios.

				Scenario 1		**Scenario 2**	
	$\dot{D}_{int}$ Gy ka^{-1}	$\dot{D}_{ext}$ Gy ka^{-1}	$\dot{D}_{so}$ Gy ka^{-1}	$\dot{D}_{ext2}$ Gy ka^{-1}	$\dot{D}_{no}$ Gy ka^{-1}	$\dot{D}_{ext2}$ Gy ka^{-1}	$\dot{D}_{no}$ Gy ka^{-1}
NO1	0.45±0.09	5.36±0.34	5.81±0.34	3.67±0.34	3.92±0.34	3.00±0.34	3.25±0.34
NO2	0.45±0.09	5.28±0.34	5.73±0.34	3.79±0.34	3.96±0.34	3.18±0.34	3.35±0.34

5.3.3 OSL ages

Figure 5.5 illustrates the anomalous fading corrected and uncorrected ages for NO1. It shows the ages calculated for the secular equilibrium scenario (scenario 1) and between the end-members (Equ. 5.17-5.18-5.19). According to the g_{2days} values (%-dec), the correction is more important for the IR_{50} ages than the $pIRIR_{225}$ ages (Fig. 5.5A, 5.5B). The corrected IR_{50} ages are in good agreement, i.e. on the 1:1 line, with the uncorrected $pIRIR_{225}$ ages (Fig. 5.5C). Greater deviation between values is observed when comparing the corrected IR_{50} ages with the corrected $pIRIR_{225}$ ages (Fig. 5.5D). Even if the residual doses are subtracted from the $pIRIR_{225}$ value and the IR_{50} value, the corrected $pIRIR_{225}$ ages are ~25% greater than the corrected IR_{50} ages. The agreement between IR_{50} ages and $pIRIR_{225}$ ages is good when $pIRIR_{225}$ ages are uncorrected by anomalous fading.

Figure 5.6 illustrates the equilibrium and disequilibrium OSL ages for samples NO1 and NO2, calculated with time period T_2 ranging from 0 to 15 ka. The represented ages are the uncorrected $pIRIR_{225}$ ages. The OSL age (t_0) ranges from 15 ka to 22 ka. The difference between the equilibrium and disequilibrium OSL ages is <5% if the carbonate nodule precipitation age is <7 ka, and between 5 and 10% if the nodule precipitation age is 7 to 15 ka. This is represented by the deviation from the 1:1 line, which increases with the carbonate nodule age. The OSL ages shown in Figure 5.6 were calculated with a ($^{234}U/^{238}U$) activity ratio of 1.31 for scenario 2. However, if the effect of different ($^{234}U/^{238}U$) activity ratios (0.5 to 3), as a function of different T_2 durations, is added (Fig. 5.6, inset), this increases the difference between equilibrium and disequilibrium OSL ages by only 1%. Figure 5.7 shows the resulting OSL ages of sample NO1 and NO2 calculated as a function of the carbonate nodule age. The black bold line and grey bold line represent the disequilibrium and the secular equilibrium scenarios, respectively. The minimum OSL ages (white stars) are obtained for a carbonate nodule age of 0 ka, i.e. the carbonate nodule never precipitated (=no disequilibrium effect on the dose rate), and are 15.2 ka (NO1) and 15.8 ka (NO2). However, when the carbonate nodule precipitates, the $\dot{D}_{ext}$ will differ according to the different scenarios. This results in two different age-accumulation rates (Figure 5.7), which deviate from one another with time, i.e. with increasing the carbonate nodule age. The slope of the lines assuming decay chain equilibrium for nodules NO1 and NO2 (~0.3) is lower than the disequilibrium lines (~0.4), which is a consequence of the greater $\dot{D}$. The maximum OSL ages (black stars) are c. 23 ka

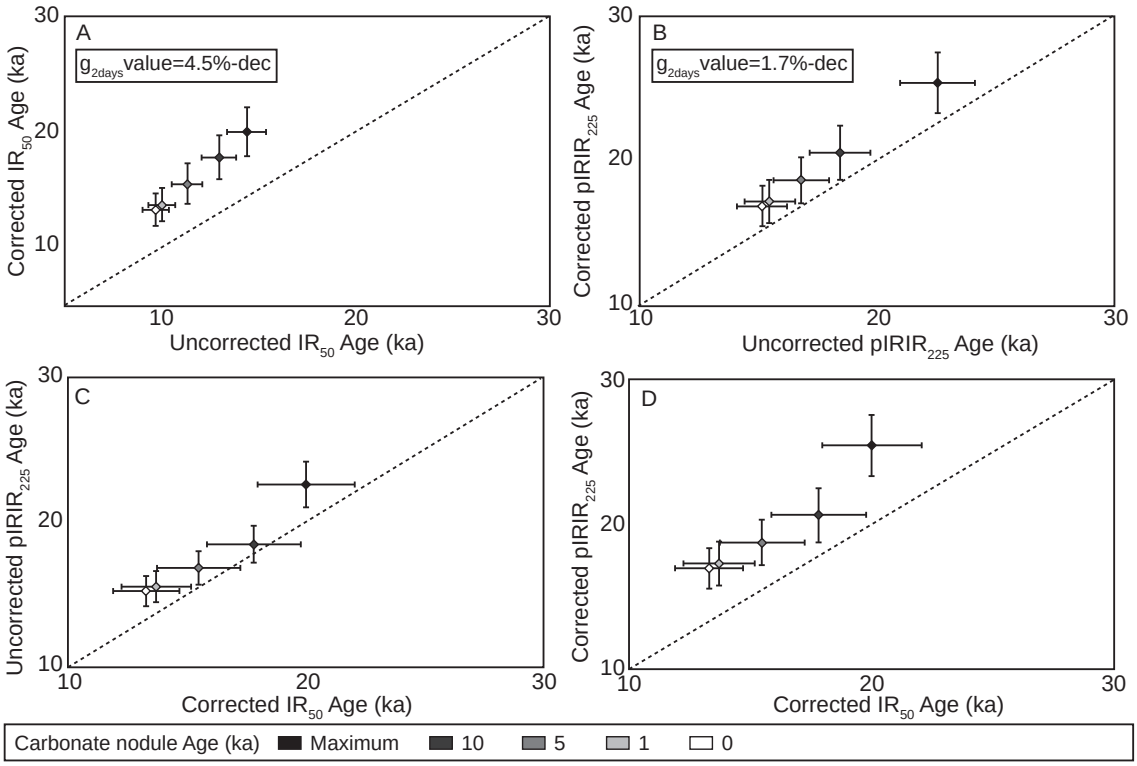

Figure 5.5 – Ages calculated for NO1, using different carbonate nodule ages (grey scale) and assuming secular equilibrium (scenario 1). A) Uncorrected IR_{50} age versus fading corrected IR_{50} age, B) Uncorrected $pIRIR_{225}$ age versus fading corrected $pIRIR_{225}$ age; the g-values are given in the boxes. C) Fading corrected IR_{50} age versus uncorrected $pIRIR_{225}$ age, D) Corrected IR_{50} age versus corrected $pIRIR_{225}$ age.

for scenario 1 and c. 27 ka for scenario 2, with a maximum deviation of 18%. These maximum ages imply that the OSL age is equal to the carbonate age (i.e. the carbonate nodule already existed at the deposition time). The grey area in Figure 5.7 represents the African Humid Period (AHP, c. 5 ka to c. 15 ka); if we consider that the carbonate nodule formed during the AHP (Fig. 5.7, white arrow), giving plausible OSL age ranges between c. 16 to 22 ka.

5.4 Discussion

5.4.1 Suitable mineral population

In this study, we investigated the potential issue of partial bleaching using PSG instead of strict SG. The number of grains is sim10-20 but chemical measurements of the <2.58 gcm^{-3} fraction showed that 70% of the grains were K-rich feldspars and 30% K-poor feldspars. Consequently, as K-rich feldspars are brighter, the number of responding grains is sim7-14 for each PSG measurement. Except for the IR_{50} signal of $NO1_{Ext}$, the OD values are <30%. For PSG measurements, the high OD in the values can be attributed to intrinsic factors, such as measurement uncertainties, thermal transfer, variable rates of fading and extrinsic factors, such as partial bleaching, post-depositional processes and potentially variable micro-dosimetry (e.g. Duller, 2008; Lamothe et al., 2012; Reimann et al., 2015; Mayya et al., 2006). As the grains might have been mixed by pedoturbation after deposition, and as the carbonate

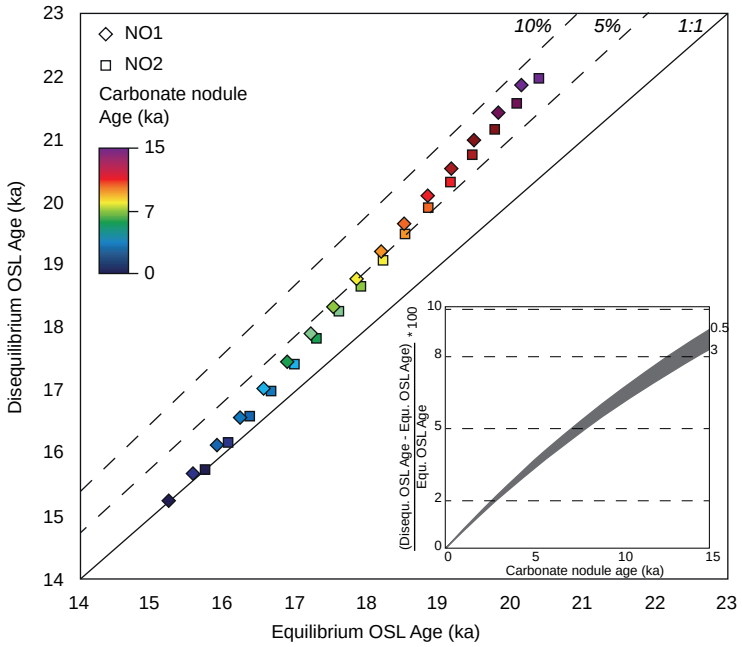

Figure 5.6 – OSL ages were calculated for $NO1_{Int}$ (diamond) and NO2 (square) considering either thean equilibrium or disequilibrium scenario. An activity ratio ($^{234}U/^{238}U$) of 1.31 was taken in the calculations. The difference between both scenarios increases with the carbonate nodule age (i.e. the duration of T_2). The inset shows the effect of changing the ($^{234}U/^{238}U$) activity ratio from 0.5 to 3 on OSL ages as a function of carbonate nodule age and duration of time T_2. Calculations were done taking the most extreme scenario, i.e. assuming that all ^{234}U daughters were lacking. The error is <10% irrespective of the ($^{234}U/^{238}U$) activity ratio if the nodule age is 15 ka. The error associated with different ($^{234}U/^{238}U$) activity ratios (ranging from 0.5 to 3, grey area) increases with the carbonate nodule age but is negligible compared to the effect of the absence of ^{234}U daughters. If these were present, the disequilibrium scenario would get closer to secular equilibrium.

nodules were exposed to light after precipitation, scatter in the equivalent dose (D_e) distributions relating to partial bleaching, is anticipated.

Overdispersion from the dose recovery experiment should enable scatter caused by intrinsic factors only, to be characterised (Reimann et al., 2015), and for single-grain feldspar the OD values measured in other studies range from 6 to 22% (Neudorf et al., 2012; Reimann et al., 2012; Trauerstein et al., 2014; Smedley et al., 2015). The OD values of the dose recovery experiments for NO1 and NO2 (PSG) range between 10 and 24% (Table 5.3); which is significantly greater than the measured instrument reproducibility (<10% for PSG measurements). This could be explained by variability in rates of anomalous fading between grains from the same sample (Lamothe et al., 2012), or variations in the rate of signal bleaching (Buylaert et al., 2012; Smedley et al., 2015). When the OD values recorded for the natural measurements are contrasted with those from the dose-recovery measurements, it is apparent that most signals and samples contain some scatter attributed to extrinsic factors. Heterogeneous carbonate accumulations could result in micro-dosimetric variations that partly explain this apparent excess in dispersion. This would be true during step I (Fig. 5.2), however during step II, thin section analyses (Fig. 5.1C) indicate a near-homogeneous distribution of detrital minerals in the nodules. $NO1_{Ext}$ has the greatest OD and had the greatest degree of sunlight exposure (nodule surface, sampled from the surface of a mima-like mound), which suggests that partial bleaching may be a key cause of the overdispersion that we observe. This interpretation is supported by the $IR_{50}/pIRIR_{225}$ ratio,

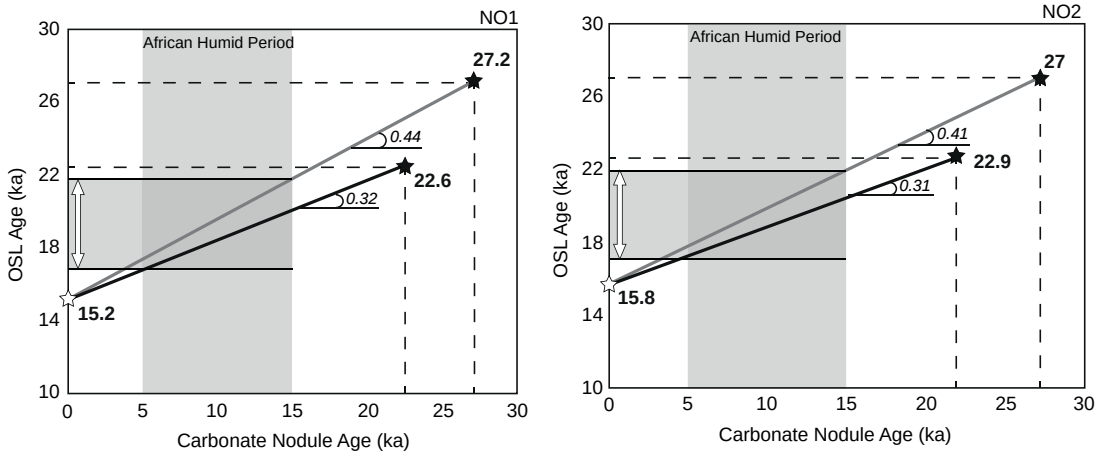

Figure 5.7 – OSL ages for NO1 (left) and NO2 (right) as a function of the carbonate nodule age. The bold black line represents the equilibrium scenario (1) and the bold grey line represents the disequilibrium scenario (2). The end-members calculated assuming that the nodule has always existed (maximum OSL age, black stars) and late, instantaneous nodule precipitation until a nodule age of 0 ka, i.e. carbonate nodule never existed (minimum OSL age, white stars), calculated with Equations 17 and 18. The plausible OSL ages should thus range between these two end-members. As carbonate nodules are expected to form during the African Humid Period (grey area), the most plausible OSL age should range between 16 to 22 ka (white arrows).

which is significantly smaller (~0.2) for $NO1_{Ext}$ (0.50) compared to $NO1_{Int}$ (0.74), indicative of greater reset of the fast-bleaching IR50 signal (e.g. Thiel et al., 2011; Buylaert et al., 2012). Furthermore pedoturbation processes, which are characteristic of Vertisols, may also have induced some of the observed scatter (Bateman et al., 2003). The OD value of NO2 is 29.9±0.2% for the IR_{50} signal, but the NO2 $IR_{50}/pIRIR_{225}$ ratio is similar to $NO1_{Int}$ (0.66 and 0.74, respectively), suggesting that the luminescence signals have not been partially reset. Nevertheless, the OD values for both $NO1_{Int}$ and NO2 assessed by PSG measurements suggest that any partial bleaching is not significant (i.e OD values are ≤30%) and the minerals from the internal part of the nodule are considered suitable for luminescence dating.

Contrasting the PSG and SA measurements indicates that although some SA values are higher than the PSG values, they are within errors and the difference between both approaches is ≤10% (Fig. 5.3). The difference is greater (>10%) for the IR_{50} signal of $NO1_{Ext}$, emphasizing that post-deposition bleaching affects the exterior of surficial nodule NO1 and that the IR_{50} signal bleaches most rapidly. Consequently, as PSG measurements are time consuming and technically challenging (Duller, 2008; Trauerstein et al., 2014), and as they do not significantly change the values determined for these samples, it is suggested that the SA approach is both sufficient and appropriate.

Finally, comparing the SA measurements for $NO1_{Ext}$ and $NO1_{Int}$ (Fig. 5.4), the difference in values between the internal and external parts is significant for both the IR_{50} and $pIRIR_{225}$ signals, but is greatest for the IR_{50} signal. This may be explained by the slower bleaching of the $pIRIR_{225}$ signal in comparison to the IR_{50} signal (Buylaert et al., 2012), as also evidenced by our residual measurements (Table 5.3). Differences between the IR_{50} and $pIRIR_{225}$ values are explained by anomalous fading (Thomsen et al., 2008; Buylaert et al., 2012). Fading corrections were done using the luminescence package (v.0.3.4) in RStudio (Kreutzer et al., 2012) following Huntley and Lamothe (2001). According to Figure 5.5, the IR_{50} and $pIRIR_{225}$ ages are in good agreement when $pIRIR_{225}$ ages are uncorrected

for anomalous fading (Fig. 5.5C). However, when $pIRIR_{225}$ ages are corrected for anomalous fading, they overestimate the age compared to corrected IR_{50} ages (Fig. 5.5D). Subtraction of the residual measured following 4 h of sunlight exposure in Lausanne cannot reduce the fading-corrected $pIRIR_{225}$ age overestimation, relative to the fading corrected IR_{50} ages. The g_{2days} values measured for the $pIRIR_{225}$ signal are close to 1.5%/dec within error, measuring such low fading rates accurately is difficult. Therefore, fading correction may not necessarily give more accurate ages (Wallinga et al., 2007; Roberts, 2012). Moreover, the residual dose was measured after sunlight exposure in Lausanne, which may be considerably different from the natural depositional environment in Cameroon. Finally, as discussed previously, our results suggest that the $pIRIR_{225}$ signals of $NO1_{Int}$ and NO2 were not affected by partial bleaching. Consequently, regarding (i) the challenge of accurately constraining low rates of anomalous fading, (ii) the lack of an appropriate residual dose analogue, and (iii) the good agreement between fading-corrected IR_{50} ages and uncorrected $pIRIR_{225}$ ages, the latter are regarded as being the most representative of the true age (Fig. 5.5C).

5.4.2 Effect of carbonate nodule formation on the environmental dose rate

The carbonate nodule formation event induced two different effects: (1) a change in the radionuclide concentration, and (2) as assumed in this study, a disequilibrium in the ^{238}U-series. Consequently, the $\dot{D}$ is 50% lower during T_2 than during T_1, as the respective radionuclide concentrations also reduced. Moreover, if the ^{238}U-series is considered to be in disequilibrium (scenario 2) during T_2, the $\dot{D}$ is reduced by a further 19±3% (~0.7 Gy ka^{-1}) than when secular equilibrium is assumed (scenario 1). This is a maximum estimate because we assume that all ^{234}U daughters are absent. However, this difference is significant and two times more important than the uncertainties induced by different ($^{234}U/^{238}U$) activity ratios or different carbonate nodule diameters, which exert maximum changes of 2% (0.07 Gy ka^{-1} between $^{234}U/^{238}U$ activity ratios of 0.5 and 3) and 8±1% (0.3 Gy ka^{-1} between diameters of 0.5 and 10 cm), respectively. Finally, the progressive accumulation of carbonates during T_1 could induce a change in the infinite matrix dose rate. Calculating the dose rate assuming a maximum probable carbonate accumulation of 7% (as presently observed in the soil), results in maximum change of $\dot{D}$ during T_1 of 3% (0.2 Gy ka^{-1}). Consequently, all combined, the maximum total uncertainty, without the disequilibrium effect, on the environmental dose rate may be ~10% (~0.5 Gy ka^{-1}).

5.4.3 Soil parent material deposition age

The significance of the disequilibrium effect depends directly on the age of the carbonate nodule, i.e. the duration of time period T_2. Thus, whilst the environmental dose rate ($\dot{D}$) may change considerably, the effect on the OSL age may be relatively limited. The uncertainty induced by the disequilibrium is <10% for nodule ages ranging from 0 to 15 ka. As $\dot{D}_{no}$ is lower than $\dot{D}_{so}$, when the $\dot{D}_{no}$ contribution increases, i.e. T_2 increases, the OSL age becomes older (Fig. 6). This is also apparent within the disequilibrium scenario. The effect of different ($^{234}U/^{238}U$) activity ratios (0.5 to 3) on the OSL age (Fig. 6, inset), as a function of different T_2 durations, is even less significant (~1%) than the absence of ^{234}U daughters (<10%). If some ^{234}U daughters were present, the difference between the equilibrium and disequilibrium OSL ages would be smaller. Furthermore, regarding Figure 7, it is possible to state that both minimum (c. 15 ka) and maximum (c. 23 or 27 ka) OSL ages are improbable: $T_2 = 0$ is impossible as the nodule exists, and $T_2 = t_0$ is unlikely as the carbonate nodule formed within the host soil. It is thus certain that the deposition event preceded carbonate accumulation (i.e. $T_2 < t_0$). The time of mineral deposition (t_0) should thus range between these two end-members (Fig. 7). Finally, the nodule growth rate is unknown but this effect on the final age would induce a maximum uncertainty of 5% (c.

2 ka). However, this is for t_{max}, if we look at OSL calculated ages between the expected T_2 range, the error would be less than 2% on the OSL age (<1 ka), which is considered negligible as it is within errors.

Consequently, the maximum difference between the two scenarios is 15.5±1.5% on average for both samples (Fig. 5.7). As the carbonate nodules are expected to form during the AHP (Fig. 5.7; grey area), the uncertainty induced by disequilibrium should be less than 10%. Nevertheless, even in this range, the most probable OSL age ranges are 17-20 ka and 17-22 ka for the equilibrium and the disequilibrium scenarios, respectively. The OSL age uncertainty is thus still ~20%, which is significant. Consequently, it is crucial to independently assess the duration of T_2 to calculate accurate OSL ages. The uncertainty attributed to the carbonate nodule age is higher than the uncertainty attributed to the disequilibrium. Finally, the uncertainties related to other parameters, such as the nodule growth rate, the degree of disequilibrium or the progressive accumulation of carbonate during t_1, are even lower than the disequilibrium. Since these parameters have a negligible influence on the palaeoenvironmental interpretation, they are not considered further.

5.4.4 Mineral fractions within pedogenic carbonate nodule as time archives

The minerals trapped in the pedogenic carbonate nodules can be used to assess the age of the soil parent material deposition. Despite the amount of uncertainty induced by the carbonate nodule age and the associated disequilibrium, calculated OSL ages show that the deposition of the soil parent material may have occurred before the AHP, i.e. before 15 ka. Such ages would suggest that the soil parent material was deposited during a drier period, termed the Bossoumian (Hervieu, 1970). This information is important and confirms the hypothesis that the soils may have been initiated during the AHP (Diaz et al., 2016a) following the Bossoumian and thus the deposition of the soil parent material. However, to strengthen this statement the deposition ages need to be calculated more accurately, and in order to achieve this, the carbonate nodule precipitation ages must be determined independently with other methods (i.e. U/Th or radiocarbon dating). Nevertheless, pedogenic carbonate nodules are important time archives and can be used to get temporal information on the soil parent material deposition constraining the onset of pedogenesis, to which carbonate precipitation is related.

5.5 Conclusion

Carbonate nodules in soil relics can be used as time archives. As they are pedogenic in origin, the minerals trapped within them are representative of the soil parent material. Luminescence dating of these minerals can provide information on the deposition time of the sediments from which the soils developed. In this study, pedoturbation and post-deposition partial bleaching can affect the OSL signal of the minerals. We show that the minerals from the internal part of a nodule have low overdispersion values using either pseudo-single grain or small aliquot measurements, which suggests that this mineral population is unaffected by partial bleaching and/or pedogenic processes and is thus suitable for OSL dating. Moreover, the carbonate precipitated from surficial waters and, in this context, the ^{238}U-series is likely to be in disequilibrium. We found that only 76% of U could be considered in disequilibrium, the other 24% being derived from the trapped residual soil fraction and thus assumed to be in secular equilibrium. Considering this context, the worst-case disequilibrium scenario is when all ^{234}U daughters are absent, which results in a decrease of the environmental dose rate by 19±3% (~0.7 Gy ka^{-1}), irrespective of the ($^{234}U/^{238}U$) activity ratio value included in the calculations (from 0.5 to 3). However, the effect of disequilibrium on the final OSL age is shown to be strongly dependent on the carbonate nodule precipitation age. As the carbonate nodules are expected to have precipitated

during the AHP, the maximum uncertainty on the OSL ages should be ~20% and the maximum error induced by the disequilibrium should be <10%. To conclude, the assessment of the carbonate nodule age is important for OSL age calculations, when using minerals trapped within carbonate nodules. It is advisable to combine independent methods to assess the time of carbonate formation. However, this alternative dating approach is useful when fieldwork/logistical issues prevent the possibility of collecting soil or sediment samples for OSL dating. Moreover, our proposed method is promising and has the potential to constrain soil formation and associated pedogenic processes inducing secondary carbonate precipitation. Beyond being geochemical proxies, pedogenic carbonate nodules are thus also sedimentary time archives.

6 The valuable legacy of soil relics

6.1 Introduction

Environmental changes can be reconstructed through the study of different sedimentary archives, using multiple proxies and adequate dating techniques. These tools improve our understanding of environmental processes evolution through time and are thus important for the prediction of ecosystem evolution. In the tropical zone of West Africa, the major climatic changes since the Last Glacial Maximum (LGM, 26.5-19 ka) have been documented owing to marine (e.g. deMenocal et al., 2000; Lézine and Cazet, 2005; Weldeab et al., 2007) and lacustrine sedimentary sequences (Salzmann et al., 2002; Shanahan et al., 2015). Sequences usually show that, while cold and hot periods alternated in the northern hemisphere, respective dry and wet periods were recorded in Africa (deMenocal et al., 2000). These climatic variations directly influenced the water budget at the continental surface, impacting dynamics of landscapes in both aquatic (rivers, lakes) and terrestrial (vegetation, soils) environments. These changes are tracked in various continental sedimentary sequences, such as lacustrine, alluvial, or palustrine environments (e.g. Gasse, 2000; Lézine et al., 2011; Sangen et al., 2011).

In the semi-arid/arid areas, such as the Sudano-Sahelian belt of West Africa, the observation of discontinuous and/or incomplete continental records make the palaeo-environmental interpretations challenging due to little organic matter preservation and aeolian erosion during dry periods (Chase, 2009; Bristow and Armitage, 2016). Beyond the preservation issue observed in continental settings, it is also important to take into account the response of the different geosystems and to understand how they record environmental fluctuations. The interpretations can be biased by the inertia effect affecting the water table, its level varying slower than the climate. There is also a threshold effect, implying that the disappearance of the water table does not necessarily signify an absence of precipitations but rather the occurrence of a minimal level, which is site dependant (Durand and Lang, 1986). These issues are obviously depending on the type of geosystem studied. The Chad Basin (Fig. 6.1A) includes a very sensitive climatic area, the Sahel, i.e. a zone of transition between the desert and wooded savannahs. This sedimentary basin represents therefore an ideal place to study the response of continental geosystem to climate change during the Quaternary. In the whole basin, the study of partial sedimentary sequences located in various places (e.g. Pias, 1968; Hervieu, 1970; Sieffermann, 1967; Servant, 1973; Servant-Vildary, 1978; Maley, 1980; Durand and Mathieu, 1980; Durand and Lang, 1986; Durand, 1995) allows a stratigraphic chronology to be established for the Late Quaternary.

The period from 26±1 to 14±1 ka cal BP (Late Pleistocene), termed Kanemian (Chad Basin; Servant and

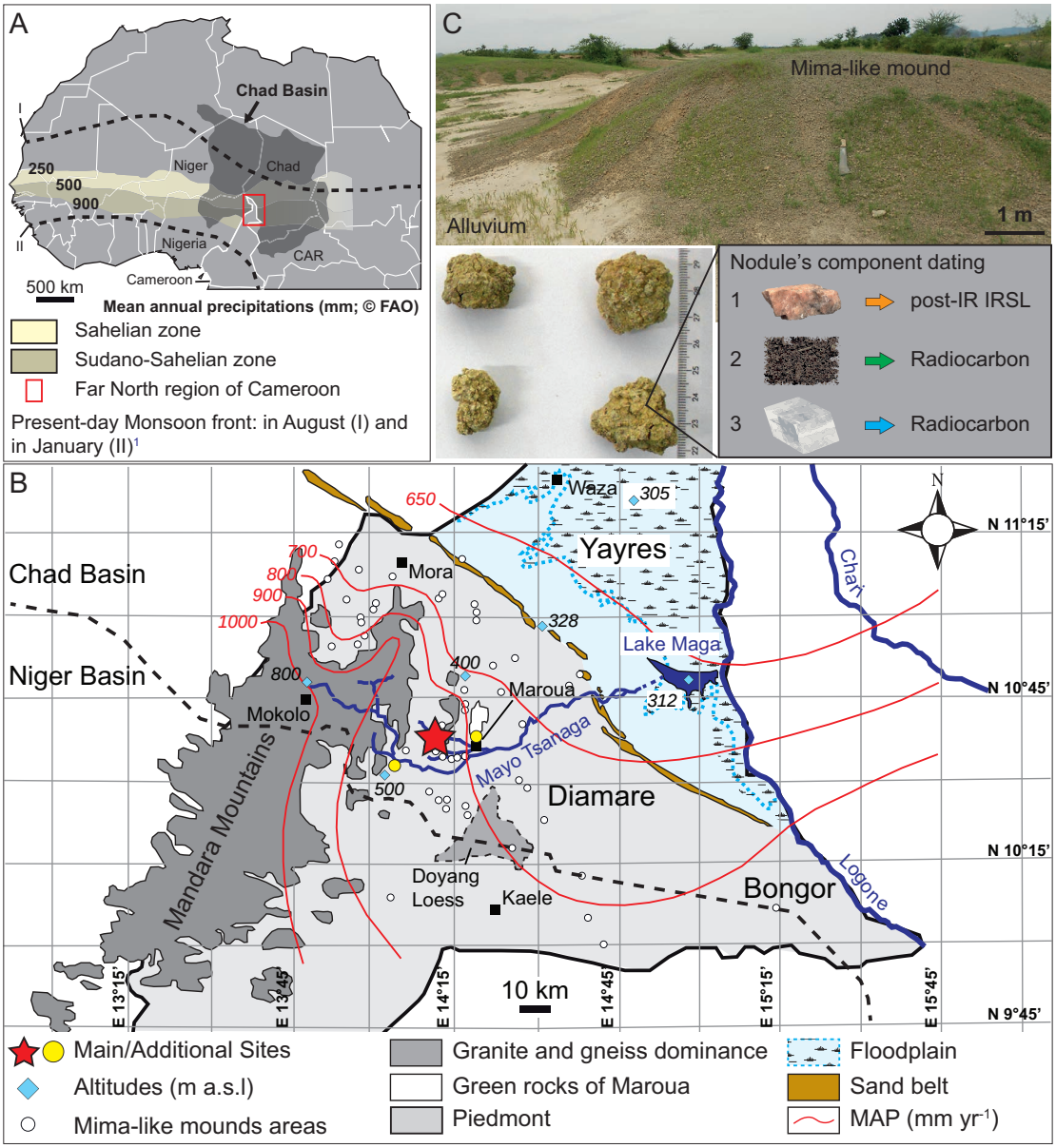

Figure 6.1 – A) Mean annual precipitations for the Sudano-Sahelian and the Sahelian belts and Far North region of Cameroon location belonging to the Chad Basin. Dashed lines are the mean ITCZ position during August and January (Nicholson, 2009[1]). B) Location of the main and additional study sites in the Diamare piedmont along the Mayo Tsanaga. Mima-like mounds occurrences are observed with Google Earth images and are reported with white dots. Red lines are the mean annual precipitation (MAP; mm yr^{-1}) which decrease gradually from the Mandara Mountains to the Yayres (L'Hôte, 1998). C) Mima-like mound and associated carbonate nodules, i.e. main study site of the pedo-sedimentary geosystem. Three compounds from the nodules collected at different depths in the mounds were extracted and dated; 1. K-feldspars dated using post-IR IRSL technique, 2. organic matter dated using radiocarbon technique, and 3. calcite dated using radiocarbon technique.

Servant-Vildary, 1970) or Bossoumian (Northern Cameroon; Hervieu, 1970), is drier than the previous period of the Ghazalian (44±1 to 26±1 cal kBP). The Kanemian can be divided into two parts (Durand, 1995), the Early Kanemian from 26±1 to 21±1 ka cal BP, corresponding to an arid maximum during

the LGM, and the Late Kanemian from 21±1 to 14±1 ka cal BP, coinciding with the Heinrich Stadial 1 (HS1) characterized by global warming conditions and the deglaciations in high latitudes (Servant, 1973; Durand, 1995). The Kanemian is thus characterized by the increase of aeolian activity, however, alluvial activity in the North and in the South of the basin, and lacustrine activity in the South, did not completely stopped, showing that this period was not extremely dry. Since c. 14 ka cal BP, a wetter period, called the Nigero-Chadian and characterized by the occurrence of lacustrine deposits in the whole basin, followed the Kanemian (Servant, 1973). The first part of the Nigero-Chadian, termed L1 (14 to 10 cal kBP; Servant, 1973), is characterized, in the oriental Kanem, by thin interdunal diatomite-rich sediments, associated with shallow lakes (Servant-Vildary, 1978) and overlaid by aeolian sediments (Maley, 1980). Both concomitant shallow lakes disappearance and aeolian onset event suggest the return of drier conditions and this coincides with the Younger Dryas (YD, 12.9 to 11.7 ka). Servant (1973) recognized then the L2 Nigero-Chadian period, beginning at 10±0.5 ka cal BP (MIS1, Holocene) and characterized by lacustrine sediments found in the whole basin. In the region of Lake Chad, the lacustrine sedimentation was never interrupted since the Late Pleistocene. Consequently, the present-day period still belongs to the L2 Nigero-Chadian period (Servant, 1973). At the African scale, this wet phase is well known as the African Humid Period (AHP) usually agreed to persist from 14.8 ka to 5.5 ka (deMenocal et al., 2000, Chase et al., 2010).

In this study, we demonstrate that, as a soil-sediment functional continuum, multi-dating of different components of a pedo-sedimentary geosystem located in the southwestern border of the Chad Basin was able to record environmental changes of the region since the LGM. Vertisol relics, i.e. degraded Vertisols, were investigated in the far North Region of Cameroon in the southwestern part of Chad Basin (Diaz et al., 2016a). They are (i) clay-rich / smectitic-rich, (ii) enriched in pedogenic carbonate nodules, and (iii) display mound morphologies within stream networks termed mima-like mounds (Fig. 5.2C). These features can be approached as pedo-sedimentary geosystems resulting from a four-step (S) succession of sedimentary and pedogenic processes: S1) the soil parent material deposition, being a mix between aeolian and saprolite compounds (Diaz et al., 2016a; Dietrich et al., 2017), S2) soil development and organic matter integration, S3) pedogenic carbonate precipitation, and S4) erosion, leading to the present-day mima-like mound landscape (Diaz et al., 2016a). This relative four-step chronological succession must be related to changes in environmental conditions, which in turn are driven by climate variations. Nevertheless, even if this scenario is well constrained by pedo-sedimentary proxies, the various phases of formation have not been attributed to absolute dating. In order to tackle this, three different compounds of carbonate nodules are dated performing different methods. The K-feldspars trapped within the nodules constitute a residual fraction of the host soil (Diaz et al., 2016b). Post-Infra-Red Infra-Red Stimulated Luminescence (post-IR IRSL) dating technic was applied on these minerals to assess the deposition age of the soil parent material (S1). Radiocarbon dating was performed on the organic and inorganic carbon fractions of nodules, in order to date the soil organic matter (S2) and the carbonate nodule (S3), respectively. Finally, the erosion event (S4) was not dated, but started likely after step S3. This study demonstrates the potential of a carbonate pedo-sedimentary geosystem to act as a continental palaeo-environmental archive in semi-arid areas from West Africa.

6.2 Study site and sampling

The Far North Region of Cameroon belongs to the Sudano-Sahelian belt of West Africa (Fig. 6.1A). The study site is located in the Diamare piedmont near Maroua, in the southwesten part of Lake Chad Basin (Fig. 6.1B). The piedmont lies between the Mandara Mountains, mainly granitic and gneissic (Brabant

and Gavaud, 1985), and the Yayres floodplain related to Logone River. The precipitation distribution is gradual (Fig. 6.1B) from the Mandara Mountains in Mokolo (1000 mm/yr), to Maroua (800 mm/yr) and to Waza (600 mm/yr). Mima-like mound areas are widespread in all the piedmont (Fig. 6.1B) and are associated to clay-rich sediments (Diaz et al., 2016a) intercalated, from the Mandara Mountains to the Yayres floodplain, in a general evolution of granitic sand, to colluvium and alluvium.

The grain size distribution in mima-like mounds is characterized, in average, by 32% ±12.8% (n=186) of a clay fraction (< 2μm), with maxima reaching 67% (Diaz et al., 2016a). High proportions of smectite are also present, with 34% ±7% (n=25) average values. The soil structure is prismatic to massive, with localized vertical cracks and secondary minerals, such as carbonate nodules and Fe-Mn micro-nodules, found in abundance at the surface but also at various depths. These characteristics point to Vertisol properties (Wieder and Yaalon, 1974; Wilding, 2004; Southard et al., 2011), but mima-like mounds are rather truncated Vertisols. They are essentially mineral, with an organic content <1%. Moreover, as stipulated above, carbonate nodules and Fe-Mn micro-nodules are found in high proportions at the surface and interpreted as a remnant part of a former deeper Bk horizon, i.e. calcic horizon (Diaz et al., 2016a). As they are occurring at the surface, mima-like mounds are interpreted as Vertisol relics, i.e. soil in disequilibrium with present environmental conditions (Retallack, 1991). Finally, thin section observations of carbonate nodules show that they are composed by a residual soil fraction cemented by calcite (Diaz et al., 2016b). Primary minerals, clays, and little organic matter compose this trapped soil fraction.

Therefore, nine nodules were selected at different depth, from 0 to 130 cm, in a mima-like mound located in the main study site (Fig. 6.1B). For each nodule, aliquots were kept for luminescence dating (OSL) and for radiocarbon dating on the inorganic carbon fraction ($^{14}C_{inorg}$). Due to the lack of sample material, radiocarbon dating on the organic carbon fraction ($^{14}C_{org}$) was performed on only five aliquots of this sample set (Table 6.1).

6.3 Methods

6.3.1 Sample preparation and measurements

Optically stimulated luminescence

The nodules were sawed to isolate the cores from the borders to select the minerals less or not affected by sunlight exposure (Diaz et al., 2016b). The carbonate and the organic matter were removed using HCl (10%) and H_2O_2 (15%), respectively. The residual minerals were sieved at different sizes and separated according to their density, using the Sodium Polytungstate liquid (SPT). Because of the abundance of this mineral fraction, it was decided to work on unetched (Duller, 1992) K-feldspars (K-f, <2.58 gcm^{-3} fraction) ranging between 90-180 μm. All these steps were done under red light conditions. The minerals were then mounted as small aliquots (diameter = 1 mm) on aluminium disks (n = 12), resulting of approximately 100 grains per disk. The D_e values from K-f were measured using the post-IR IRSL protocol (Buylaert et al., 2009) performed by a Risø TL/OSL-DA-20 reader (dose rate ≈ 0.1 Gy s^{-1}) at the Institute of Earth Surface Dynamics (University of Lausanne, Switzerland). The conditions of the measurements are the same than those described in Diaz et al (2016b). The measurement protocol was validated using a dose-recovery test (Murray and Wintle, 2003). The anomalous fading was assessed according to the method developed by Huntley and Lamothe (2001). The D_e values were determined using Analyst v.4.31.7 (Duller, 2015) according to the following acceptance criteria: recycling ratios of unity, maximum test dose, palaeodose error and maximum recuperation <5% of the

natural luminescence signal. The luminescence package (Kreutzer et al., 2012) in RStudio (v.0.98.1087) was used to determine the D_e value for age calculations performing either the central age model (Galbraith et al., 1999) or the maximum age model (Olley et al., 2006) according to the D_e distribution. The fading correction was also done in RStudio. Chemical values and description of $\dot{D}$ calculations are given in Diaz et al. (2016b). All results concerning the D_e values, the recovery test, the anomalous fading values, the resulted $\dot{D}$ and the age calculations for this study are given in the Appendix H. However, the OSL ages are given in Table 6.1.

Radiocarbon

An aliquot of each nodule was kept in order to perform radiocarbon on the inorganic carbon fraction. This aliquot was crushed with an agate mortar and fragments representing the most internal part were selected. They were washed with deionized water, dried under ambient air and finally crushed in fine powders. Aliquots of five sample powders were treated with HCl (32%) to remove the carbonate and then washed three times with deionized water, in order to get only the organic carbon fraction. Sample treatment and measurements for radiocarbon dating were performed at the Ion Beam Lab at the ETHZ (Zurich, Switzerland). Sample treatment procedure for organic and inorganic radiocarbon dating, are referred in Hajdas et al. (2007) and Hajdas (2008), respectively. The measurements were performed with an accelerator mass spectrometer (AMS). The fractionation of carbon isotopes ($^{14}C/^{13}C$ and $^{13}C/^{12}C$) is also measured in order to take into account the natural fractionation of the sample and the fractionation due to sample treatment (Table 1). The mass fractionation is used to correct the ^{14}C activity of the sample ($F^{14}C$). The radiocarbon age (T) is given by (Stuvier and Polach, 1977):

$$C^{14}Age = -8033 ln(F^{14}C) \tag{6.1}$$

Finally, the radiocarbon ages need to be calibrated due to the atmospheric ^{14}C content variability through time. The IntCal13 calibration curve (Reimer et al., 2013) in the program OxCal (version 4.2) (Ramsey, 2009) was used to obtain calibrated ages at 95% confidence.

6.4 Results

Details related to the results of the pIR IRSL technic, the dose rate calculations and the interpretations are given in the supplementary materials. Final luminescence ages and radiocarbon ages are given in Figure 6.2 and Table 6.1. The results show three distinct age ranges. The luminescence ages are variable depending on the signal, IR_{50} or $pIRIR_{225}$, and the correction or not by anomalous fading (Fig. 6.2). This variability is also discussed in the supplementary materials. However, within uncertainties, the luminescence ages for samples below 60 cm correspond to the Late Kanemian stratigraphic period (21 to 14 ka cal BP) and those above 60 cm to the first part of the Nigero-Chadian (L1, 14 to 10 ka cal BP). These two periods of time correspond to the Late Pleistocene. Moreover, the trend of the luminescence ages changes at 60 cm, i.e. c. 15 ka, and the slope becomes steeper to the surface. The slope can be an indicator of the vertical accretion rate (resulting thickness per period of time), which results from sediment deposition minus erosion. To assess the duration time, the difference between minimum and maximum ages below and above 60 cm were calculated for each signal, i.e. corrected IR_{50}, uncorrected $pIRIR_{225}$ and corrected $pIRIR_{225}$. The thickness was then divided by these duration times giving the

Table 6.1 – Anomalous fading values, fading-corrected IR_{50}, uncorrected (A) and fading-corrected (B) $pIRIR_{225}$ ages, inorganic and organic calibrated radiocarbon ages. The isotopic compositions of dated samples are used for the mass fractionation correction. All values are given at $\pm 1\sigma$ uncertainty.

		IR_{50}		$pIRIR_{225}$			**Radiocarbon**			
	Depth (cm)	g_{2days} (%/dec)	Age_{corr} (ka)	g_{2days} (%/dec)	Age_{uncorr} (ka)	Age_{corr} (ka)	Inorganic (cal kBP)	$\delta^{13}C$ ‰	Organic (cal kBP)	$\delta^{13}C$ ‰
M1	0	6.0±1.6	18.1±4.2	1.9±1.3	16.75±1.4	18.9±2.4	7.13±0.17	-8.2±1.0	nd	nd
M1	0	3.6±0.4	7.6±1.7	1.6±0.5	10.6±1.1	11.7±1.3	6.34±0.06	-8.8±1.0	nd	nd
M1	23.5	4.0±1.1	11.5±1.7	1.1±0.8	12.2±1.0	13.0±1.2	6.24±0.05	-8.8±1.0	8.83±0.24	-42.1±1.0
M1	43	3.9±1.0	13.4±1.9	1.6±0.6	14.4±1.1	15.9±1.4	6.45±0.06	-12.3±1.0	nd	nd
M1	71	4.9±1.1	16.0±2.5	2.9±0.2	16.2±1.3	19.7±1.5	6.34±0.06	-20.1±1.0	10.39±0.17	-23.7±1.0
M1	81	4.2±0.4	13.9±1.8	3.1±0.9	15.3±1.2	18.8±2.0	5.12±0.16	-6.2±1.0	9.52±0.04	-23.3±1.0
M1	101	5.9±1.0	17.4±2.9	2.3±1.6	17.0±1.4	19.8±3.0	5.19±0.13	-9.9±1.0	nd	nd
M1	105	4.9±2.0	14.7±3.9	1.2±0.3	16.6±1.3	17.9±1.4	5.04±0.17	-12.8±1.0	nd	nd
M1	111	4.2±0.8	15.9±2.2	0.6±0.5	17.5±1.3	18.2v1.5	6.54±0.09	-8.0±1.0	11.05±0.24	-31.±1.03
M1	125	4.3±0.5	15.8±1.9	0.7±0.8	17.2±1.3	17.9±1.6	5.83?0.08	-9.9±1.0	8.18±0.19	-23.6±1.0
Tri1	90	nd	nd	nd	nd	nd	6.59±0.11	-13.0±1.0	nd	nd
Tri2	90	nd	nd	nd	nd	nd	6.56±0.11	-15.1±1.0	nd	nd
Tri3	90	nd	nd	nd	nd	nd	6.54±0.14	-14.5±1.0	nd	nd
M2	0	nd	nd	nd	nd	nd	6.05±0.18	-7.5±1.0	nd	nd
M2	30	nd	nd	nd	nd	nd	7.06±0.10	-13.5±1.0	9.30±0.20	-19.1±1.0
M2	60	nd	nd	nd	nd	nd	0.30±0.14	-5.2±1.0	nd	nd
M3	0	nd	nd	nd	nd	nd	7.13±0.17	-8.2±1.0	nd	nd
M3	0	nd	nd	nd	nd	nd	6.06±0.12	-12.2±1.0	nd	nd
M3	30	nd	nd	nd	nd	nd	0.87±0.07	-8.3±1.0	nd	nd
M3	40	nd	nd	nd	nd	nd	2.54±0.05	-7.4±1.0	nd	nd
M3	55	nd	nd	nd	nd	nd	17.89±0.16	-4.9±1.0	nd	nd
M3	70	nd	nd	nd	nd	nd	8.79±0.19	-4.9±1.0	nd	nd
M3	95	nd	nd	nd	nd	nd	5.67±0.06	-11.1±1.0	nd	nd
M3	100	nd	nd	nd	nd	nd	10.05±0.15	-0.5±1.0	13.57±0.16	-15.9±1.0
M3	115	nd	nd	nd	nd	nd	17.42±0.18	-2.1±1.0	nd	nd
V1	0	nd	nd	nd	nd	nd	6.10±0.12	-6.8±1.0	nd	nd
V2	30	nd	nd	nd	nd	nd	4.41±0.11	-7.7±1.0	nd	nd
V3	60	nd	nd	nd	nd	nd	3.34±0.10	-8.2±1.0	8.51±0.10	-17±1.0
Quart. 25%		-	13.5	-	14.6	16.4	5.15	-	8.75	-
Median		-	15.3	-	16.4	18	6.21	-	9.41	-
Quart. 75%		-	16	-	17	18.9	6.74	-	10.56	-
Mean		-	14.4	-	15.4	17.2	6.52	-	9.92	-
Std. Dev.		-	3.1	-	2.3	2.8	3.73	-	1.75	-

accretion rates. In average, the accretion rate below 60 cm is 0.23±0.13 mm a^{-1} at $\pm 2\sigma$ uncertainty, and above 60 cm it is 0.10±0.04 mm a^{-1} at $\pm 2\sigma$ uncertainty. Radiocarbon ages on the organic matter fraction ($^{14}C_{org}$) trapped within the nodules range between 11.1 and 8 ka cal BP without any particular pattern with depth. These ages correspond to the second part of the Nigero-Chadian (L2, since 10 ka cal BP) or more precisely to the beginning of the Holocene. Finally, radiocarbon ages on the inorganic carbon ($^{14}C_{inorg}$) composing the nodules range between 6.6 and 5 ka cal BP without any pattern with depth either. They correspond to the mid-Holocene period.

Carbonate nodule samples were collected in other study sites (Fig. 6.1B) and the $^{14}C_{inorg}$ results are given in Table 6.1. Luminescence ages are not available for these samples, but $^{14}C_{org}$ dating was performed on three aliquots (Table 6.1). The aim was to look at the variability of the ages between different study sites. Results show a variability in $^{14}C_{inorg}$ ages ranging between 17 to 0.1 ka cal BP. However, the majority of the ages, i.e. between quartile 25% and 75% (50% of the data), are between 5.15 and 6.74 ka cal BP, (Table 6.1). Finally, to highlight a possible variability within a sample, a triplicate analysis was performed on one nodule sample (Table 6.1, Tri) and the $^{14}C_{inorg}$ results are very close, ranging from 5.54 to 5.59 ka cal BP. For the $^{14}C_{org}$ ages, 50% (i.e. between quartile 25% and 75%) of the data range between 8.75 and 10.56 ka cal BP, and the oldest age is 13.57±0.16 ka cal BP. The luminescence age quartiles were also calculated (Table 6.1). Corrected IR_{50} ages range between 13.5

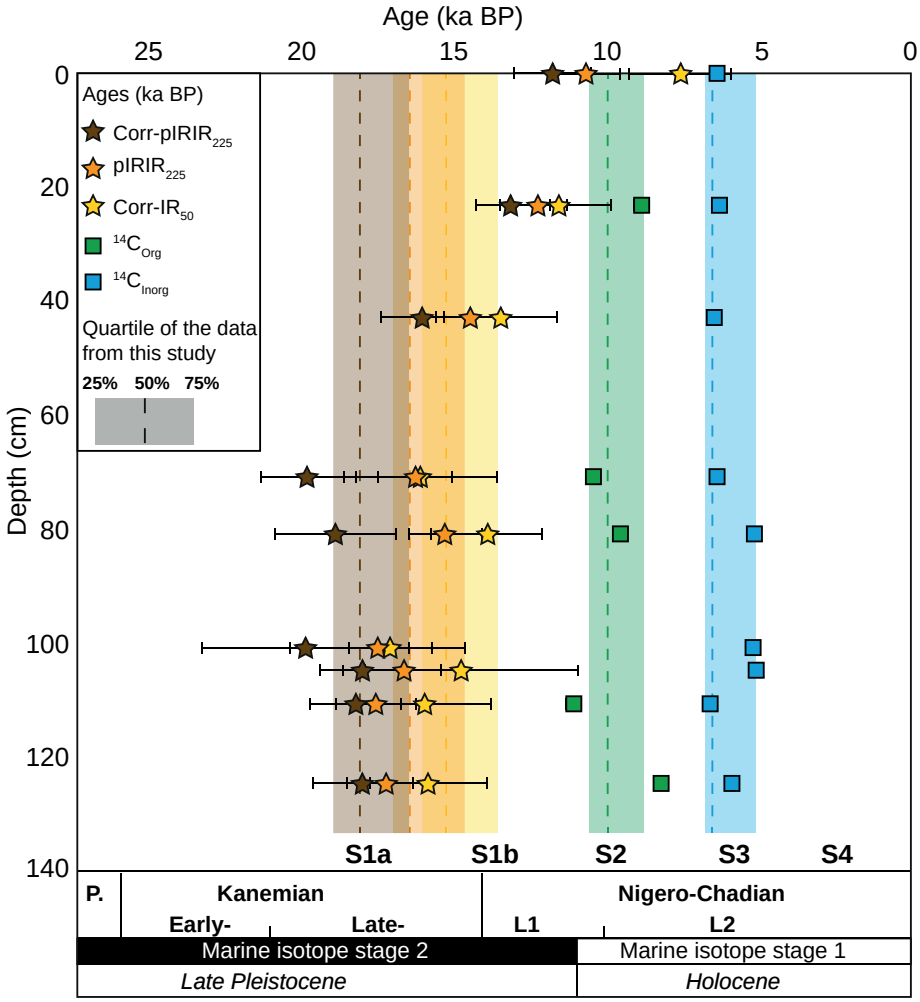

Figure 6.2 – Ages recorded in the pedo-sedimentary geosystem. Luminescence ages of K-feldspars (stars) for fading-corrected IR_{50}, uncorrected $pIRIR_{225}$ and fading-corrected $pIRIR_{225}$, calibrated organic matter radiocarbon ages (green squares) and calibrated inorganic radiocarbon ages (blue squares). Results recorded four steps: S1) soil parent material deposition, with a first phase (S1a) having a higher accretion rate than a second phase (S1b), S2) pedogenesis and organic matter integration in soil, S3) carbonate nodule formation, S4) erosion (not dated but post-AHP). The color bands represent the age data between quartiles 0.25 and 0.75, the dashed lines are the median (i.e. 0.5 quartile).

and 16.0 ka, i.e. between quartile 25% and 75%. Uncorrected $pIRIR_{225}$ ages range between 14.6 and 17.0 ka, and corrected $pIRIR_{225}$ ages range between 16.4 and 18.9 ka (Fig. 6.2).

To summarize, dating results of the different compounds (i.e., feldspars, organic matter and carbonates) from the nodules revealed three distinguished time ranges and show that the Vertisol relics are inherited from the Late Quaternary. The soil parental deposited during Late Pleistocene (S1), the soils developed during Early Holocene (S2), and the pedogenic carbonate precipitated during Mid-Holocene (S3). The erosion event (S4) was not dated but should last after S3 and thus likely during Late Holocene. Comparing these ranges, represented by the quartiles (color bands), with other records, they also correspond to specific past climate periods occurring in the last 20 ka (Fig. 6.3). For luminescence ages, the results from the $pIRIR_{225}$ signal uncorrected by anomalous fading are taken in the comparisons

(orange band). They were found to be the most representative of the true age of the soil parent material deposition (Appendix H; Diaz et al., 2016b).

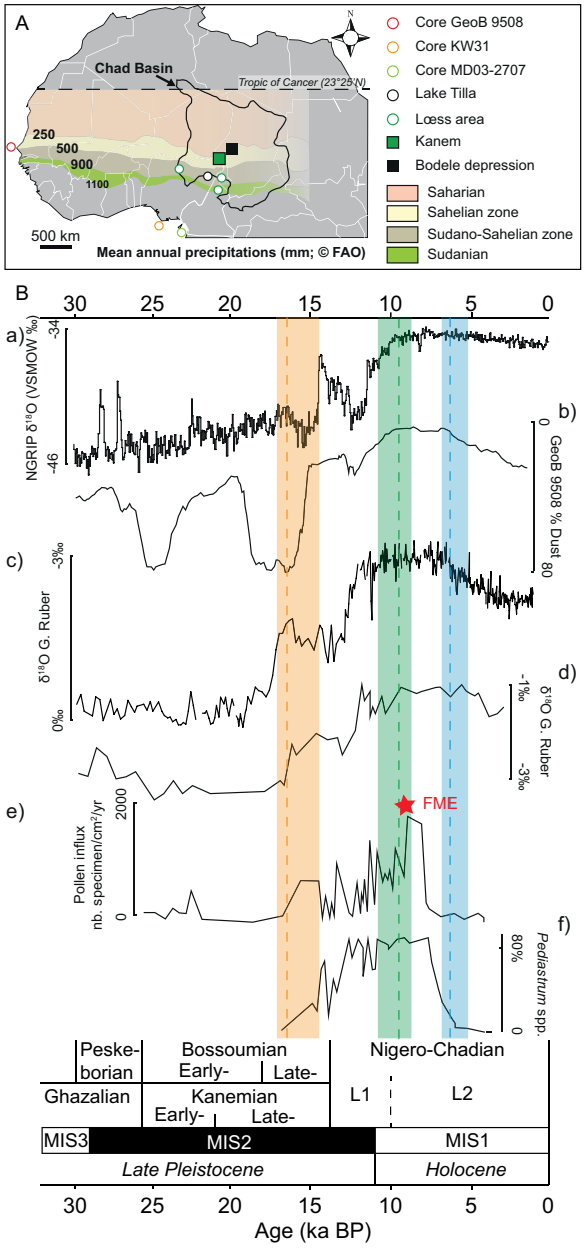

Figure 6.3 – Comparison of the pedo-sedimentary geosystem ages (color bands are the quartiles see Table 6.1) with other archives. A) Location of the records. B) $\delta^{18}O$ of North Greenland Ice Core (a, NGRIP members, 2004), dust record off Senegal Coasts (b, Collins et al., 2013), $\delta^{18}O$ of planktonic foraminifera (G. ruber) in marine core MD03-2707 (c, Gulf of Guinea, Weldeab et al., 2007), $\delta^{18}O$ of planktonic foraminifera (*G. ruber*) in Niger River delta marine core KW31 (d, Pastouret et al., 1978); pollen influx in marine core KW31 (e, Lézine and Cazet, 2005), Pediastrum green algae influx in marine core KW31 (f, Lézine and Cazet, 2005). FME for Forest Maximum Extension estimated at c. 8.5 ka (Lézine and Cazet, 2005).

6.5 Discussion

In order to give a synthesis of the climate and the environmental evolution (Fig. 6.3), the results and interpretations of stratigraphic studies performed within the Chad Basin (Servant, 1973; Servant-Vildary, 1978; Maley, 1980; Durand and Mathieu, 1980; Durand, 1995) were compared to a lacustrine core from Lake Tilla, located in the Biu plateau of Nigeria (Fig. 6.3A; Salzmann et al., 2002) and to three marine cores: (i) the MD03-2707 core (Gulf of Guinea, Weldeab et al., 2007), (ii) the KW31 core (Niger River Delta; Pastouret et al., 1978; Lézine and Cazet, 2005), and (iii) the GeoB9508 core (Senegal coast; Collins et al., 2013). Finally, they are also compared to oxygen isotopes of ice core located in Greenland (NGRIP: North Greenland Ice Core Project; NGRIP members, 2004) reflecting the northern hemisphere climatic changes (Dansgaard et al., 1969).

6.5.1 Comparison of pedo-sedimentary archives with other records

The soil parent material is a mix between a dust component and the local saprolite (Dietrich et al., 2017). Its deposition (S1) is mainly recorded when dust influx off Senegal coasts is decreasing (Fig. 6.3b; Collins et al., 2013) and when freshwater influx, i.e. heavier $\delta^{18}O$ values of planktonic foraminifera, in the Niger River delta and Gulf of Guinea areas are increasing (Fig. 6.3c, 6.3d; Pastouret et al., 1978; Weldeab et al., 2007). The decrease of dust influx can be explained by a change in the wind directions (Chase, 2009) and/or a decrease of dust production, due to an increase of the soil moisture and vegetation cover, protecting the sedimentary material against wind erosion (Pye and Tsoar, 1987; Snelder and Bryan, 1995). As freshwater influx in the ocean is increasing concomitantly (Fig. 6.3c, 6.3d; Pastouret et al., 1978; Weldeab et al., 2007), the second explanation seems to prevail. Consequently, due to moisture increase, dust is stabilized in the continent, and this event is recorded by luminescence ages of the pedo-sedimentary geosystem from 18 ka to 12 ka (Late Pleistocene). Interestingly, these results also correlate with other lœss deposits located in the Diamare piedmont and termed “lœss of Doyang” (Fig. 6.1B, Sieffermann, 1967; Mpeck, 1994). In the Benoue valley (southern part of Far North Cameroon) and even further in the South, in the Adamaoua piedmont (Fig. 6.3A; North Region of Cameroon), Maley (1980) also interpreted sedimentary sequences as “lœss of Doyang” analogues. Carbonate nodules were found in these lœss and radiocarbon dating gave ages ranging from 19 ka to 7 ka cal BP (Marilac, 1973; Maley, 1980). These resulting ages cannot precisely refer to the lœss deposition event, as emphasized in the present study (see below), but at least, they give a terminus post quem of the deposition, and this range of ages covers the Late Pleistocene. Finally, lœss deposits were also described in Nigeria (Bennett, 1980; Mac Tainsh, 1984) and sedimentary stratigraphy interpretations led also to attribute them to the Kanemian (26 to 14 ka cal BP) and thus the Late Pleistocene. Farther in the North within Chad Basin, aeolian activity is recognized with the occurrence of dunes in Kanem (Servant, 1973), recently dated between 18 ka and 15 ka (Armitage et al., 2015), i.e. Late Kanemian (21 ka to 14 ka cal BP). The same range of ages was found for sand deposits under the diatomite located in the Bodele depression (Armitage et al., 2015). Consequently, it can be suggested that, during the Late Pleistocene, lœss deposits were forming in the region corresponding today to the Sudano-Sahelian zone, whereas dune systems were forming at the time in the area covered by the present-day Sahelo-Saharian zone. The occurrence of dust stabilization along the Sudano-Sahelian belt during the Late Pleistocene suggests that the environmental conditions were moderately dry. This is strengthened by lacustrine record of Lake Tilla (Fig. 6.3A; Salzmann et al., 2002), which shows fluctuating water levels between 21 ka and 14 cal kBP and organic matter $\delta^{13}C$ values indicating a grass savannah vegetation (Salzmann et al., 2002). Finally, the luminescence ages suggest a decrease of the accretion rate by a factor of two around 15 ka. This change is concomitant with the beginning of the Nigero-Chadian or the AHP (c. 15-14 ka cal

BP; Servant, 1973; deMenocal et al., 2000). This evolution in the accretion rate can thus result from a decrease of aeolian input and/or the increase of erosion due to the onset of wetter climatic conditions.

The incorporation of organic matter in the soil is a process related to biological organic production and soil development (S2), which are related to favourable wet climatic conditions. This event is recorded during the L2 Nigero-Chadian (since 10 ka cal BP; Servant, 1973), corresponding to the climatic optimum (Early Holocene). This period, marked by an important increase of precipitations over West Africa, is linked to the northern migration of the monsoon system until latitude 31°N, mainly from 9.5 to 7 ka cal BP (Tierney et al., 2017). The maximal extension of the forest in West Africa is thus recognized at that time and assessed at 8.5 cal kBP (Fig. 6.3, FME; Lézine and Cazet, 2005). High freshwater influxes are recorded off Niger River delta and in Gulf of Guinea (Fig. 6.3c, 6.3d; Weldeab et al., 2007; Pastouret et al., 1978), as well as low dust influx off Senegal coasts (Fig. 6.3b; Collins et al., 2013). The pollen and green algae influx with freshwater show also high levels, meaning that the vegetation production and the soils were well developed at this time on continent (Fig. 6.3e, 6.3f; Lézine and Cazet, 2005). Data from Lake Tilla recorded a Sudano-Guinean tree taxa from 11.5±0.5 ka to 4±0.5 ka cal BP (Salzmann et al., 2002). Therefore, the $^{14}C_{org}$ ages suggest that the organic matter trapped within the carbonate nodules is inherited from this climatic optimum of West Africa occurring during the Early Holocene.

The precipitation of carbonate nodules is mainly recorded when freshwater influx in Gulf of Guinea and Niger River delta begin to decrease and when dust inputs off Senegal coasts are increasing again (Fig. 6.3c, 6.3d, 6.3b, respectively; Pastouret et al., 1978; Weldeab et al., 2007; Collins et al., 2013) around 6 ka cal BP. In lake Tilla, Salzmann et al. (2002) noted a shift from a wet Sudano-Guinean savannah to a drier Sudano-Guinean savannah around 8±1 cal kBP. Maley (1980) and Servant (1973) suggested major rainfall changes within the Chad Basin at this period as well. Interestingly, this period around 8.5-8 ka cal BP coincides with the global 8.2 ka cal BP cooling event, characterized by an oxygen anomaly in the NGRIP (Fig. 6.3a; NGRIP members, 2004). This event, half of the amplitude of the YD (Alley et al., 1997), is generally correlated to drier conditions in tropical regions related to monsoon system dynamics (Alley and Agùstsdòttir, 2005; Rholing and Pälike, 2005). Indeed, Tierney et al. (2017) highlighted a pause in the Green Sahara event around 8 ka cal BP. The decrease of the forest extension is followed by a drop of Pediastrum green algae at 7.1 ka cal BP (Fig. 6.3f; Lézine and Cazet, 2005), reflecting the decrease of highly productive and eutrophic water system, fed by rivers flowing through rich organic soils. Ecosystems on the continent are thus changing and this is marked by the precipitation and/or the preservation of pedogenic carbonate nodules. The $^{14}C_{inorg}$ ages along the soil profile are close to one another, which can be explained by some dissolution-recrystallization processes (Williams and Polach, 1971) However, three different aliquots from one nodule were dated and resulting ages are very close (6.59 ka cal BP, 6.56 ka cal BP and 6.54 ka cal BP), pointing to a possible fairly short period of time (c. 2 ka) conducive to carbonate nodule precipitation. When grouping all $^{14}C_{inorg}$ ages (Table 6.1), the carbonate nodules mainly precipitated from 7 ka to 5 cal kBP, with a main period of formation from 7 to 6 ka cal BP. It seems thus that the carbonate nodule event is linked to a global environmental shift toward drier conditions.

The erosion event (S4), whose intensity remains also unknown, is not dated but must have occurred after the precipitation of carbonate nodules and thus during Late Holocene. This is consistent with the hypothesis that erosion might have increased following a decrease of the vegetation cover (Diaz et al., 2016a). After 4±0.5 ka, the conditions shifted definitively toward drier conditions and the vegetation reconstruction in Lake Tilla showed an open Sudanian savannah with woody taxa from the Sahelian zone (Salzmann et al., 2002). This shift characterized by a vegetation from more open landscapes, is recorded in many places in Africa but not synchronously and is rather site dependant. Nevertheless,

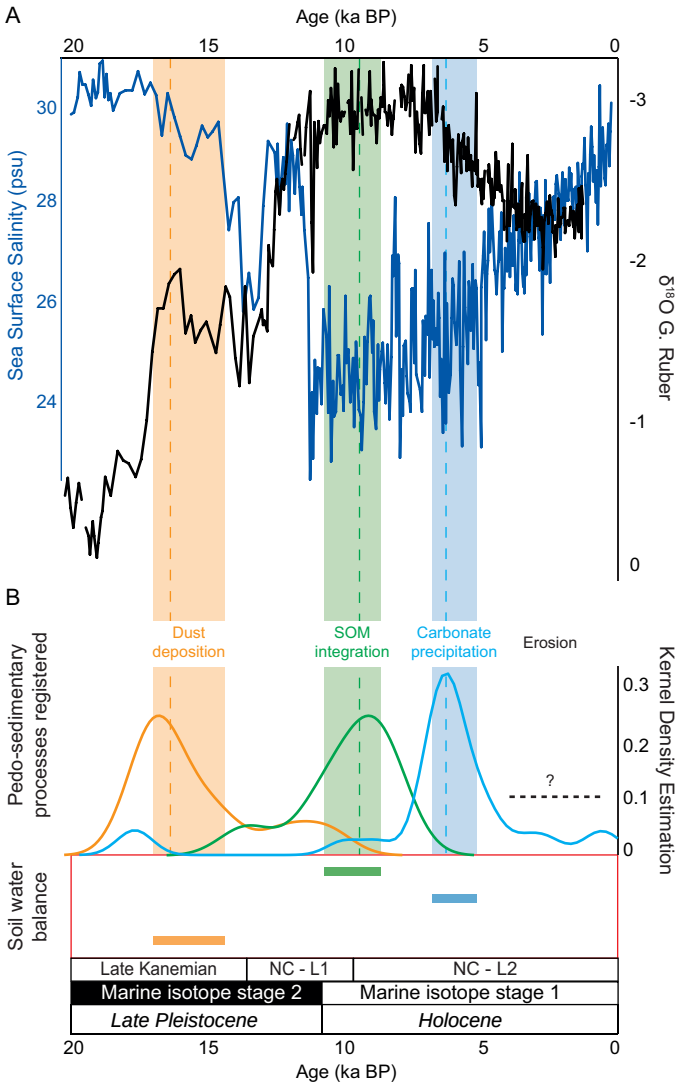

Figure 6.4 – A) Sea Surface Salinity reconstruction in the Gulf of Guinea estimated by Ba/Ca and $\delta^{18}O$ of planktonic foraminifera (*G. ruber*) (marine core MD03-2707, Weldeab et al., 2007) linked to freshwater influx in the ocean. B) Kernel density estimation of the multi-dating ages and associated process registered corresponding likely to an optimal soil water balance. The color bands represent the age data between quartiles 0.25 and 0.75, the dashed lines are the median (i.e. 0.5 quartile).

when grouping all studies, a shifting peak is recorded between 3 and 2 ka BP (Lézine and Cazet, 2005). At 5.5 ka cal BP, inputs of Pediastrum green algae disappeared and modern conditions of the Niger River took place around 3.5 ka BP (Lézine and Cazet, 2005). The decrease of the vegetation cover could thus be triggered by the onset of drier climate conditions. However, the role of anthropic activities should not be excluded. Indeed, archaeological studies in the sub-Saharian area of West Africa show the first traces of pearl millet domestication c. 3 ka BP (Manning et al., 2011). The oldest traces of metallurgy in the Diamare are c. 2 ka BP (Delneuf, 1998). These activities could cause important deforestation. Recently, a study in Lake Barombi Mbo (Southern Cameroon) showed that the abrupt retreat of the humid tropical forest c. 3 ka BP, i.e. the forest crisis (Ngomanda, 2009), could be due to anthropic activities (Garcin et al., *in prep*). Consequently, the erosion event (or events) is likely due to the decrease

of the vegetation cover, however the causes for this retreat can either be climatic, anthropic or both. But the timing of this event suggests that anthropic activities in the region could have had a significant role.

6.5.2 The nature of pedo-sedimentary geosystem archives

Each type of palaeo-environmental archive responds differently to an environmental change. The results of this study show that the dating of the different compounds of the pedo-sedimentary sequence allow to distinct and date different pedo-sedimentary processes in a continuum through time. It is suggested that the obtained time ranges are related to optimal environmental conditions for the registering of each process. The highest age density is thus not related to a strict time range for the occurrence of the process, but to the highest probability to record it. The process can occur before and/or after the time range but it may not be preserved and thus cannot be registered. Processes like erosion, organic matter consumption and carbonate dissolution may have affected the record of S1, S2 and S3, respectively. The question now is related to which one of the parameters was driving the record efficiency. Using the Kernel Density Estimation (KDE) to illustrate age densities for each process (Fig. 6.4), the highest probability density is well related to the records of the sea surface salinity and $\delta^{18}O$ of planktonic foraminifera reconstructions in the Gulf of Guinea (Weldeab et al., 2007). These two parameters represent the freshwater influx in the ocean and are thus proxies of the hydrology at the continent surface. Many soil and sedimentary processes are related to water, such as weathering, particle mobilisation and transfers, and/or secondary mineral formation (e.g. Lin, 2010). The soil water balance (e.g. Farmer et al., 2003) is characterized by water inputs (rainfalls, soil retention capacity, soil percolation, etc.) and water outputs (evaporation, transpiration, runoff, etc.). If the climatic parameters, e.g. rainfall or temperature, are determinant to explain the soil water balance, the soil characteristics, e.g. grain-size distributions or soil structure, play also an important role. Here it is suggested that the dominance of a process is linked to an optimal soil water balance for its occurrence and its preservation. The shift from the dominance of soil parent material deposition process, toward soil organic matter integration process, toward pedogenic carbonate precipitation and/or preservation process and toward erosion process, are thus proxies of soil water balance changes through time.

6.5.3 Occurrence at the Western African scale

The data set obtained in this study demonstrated that using multi-component dating, it was possible to assess the occurrence of a four pedo-sedimentary events continuum through time. They are suggested to be proxies of different soil water balance conditions. However, such a geosystem has always a local significance, and thus, is not necessarily relevant for regional palaeo-environmental reconstructions. Nevertheless, satellite image observations with Google Earth and field work in four of these areas, suggest that this type of carbonate pedo-sedimentary geosystem is present all along the Sudano-Sahelian belt (Fig. 6.5). Mima-like mound areas seem to be observable from Senegal coasts to Sudan. More investigation should be conducted in these areas but the first $^{14}C_{inorg}$ ages of carbonate nodules collected in four different areas (Fig. 6.5, yellow) gave ages in the same range than those from this study. The carbonate pedo-sedimentary geosystem may thus be much more informative than expected and thus of major importance for continental palaeo-environmental reconstructions of semi-arid areas at the African scale.

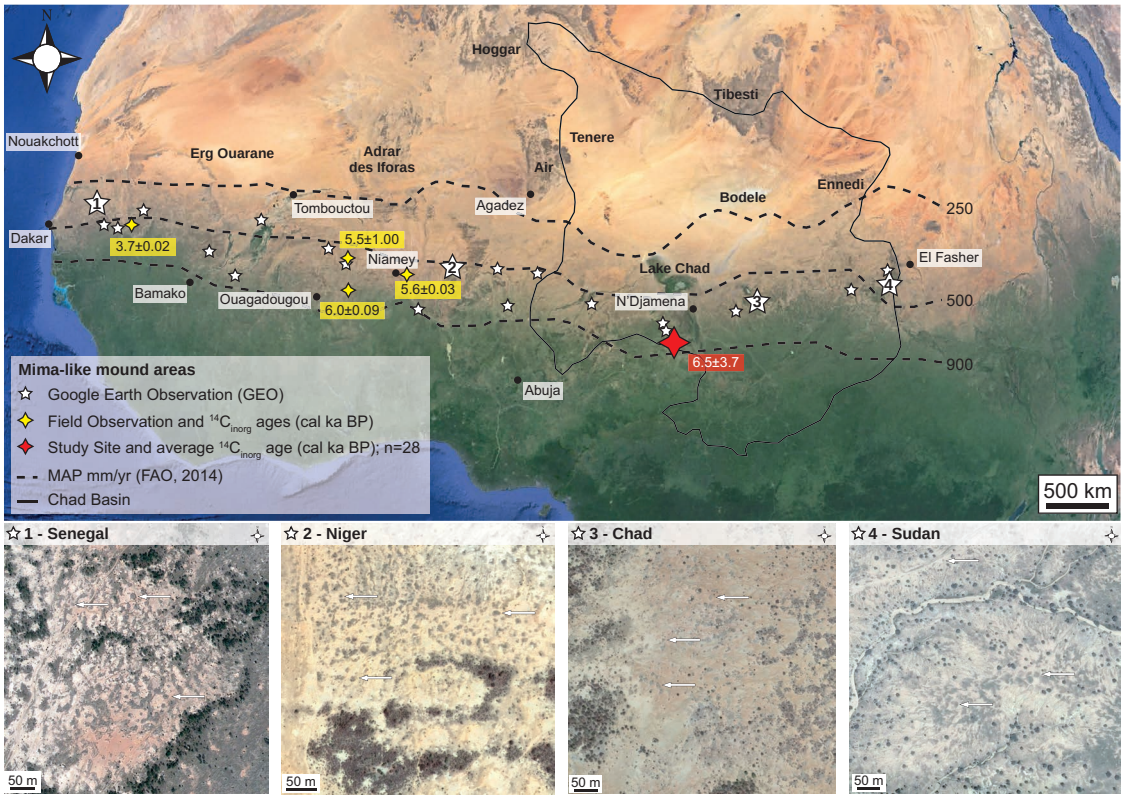

Figure 6.5 – Mima-like mound areas seem to be observable all along the Sudano-Sahelian belt (white stars, with four examples). Some areas were observed in the field (yellow stars) and inorganic radiocarbon ages of nodules collected in those sites are in the same order of magnitude than samples from the Far North Cameroon (red, average $\pm 1\sigma$).

6.6 Conclusion

Vertisol relics observed in Far North Cameroon can be seen as carbonate pedo-sedimentary sequences. It was suggested that they were formed by a four-step event succession. The multi-dating of the pedo-sedimentary sequence components showed that they occurred in the last 20 ka and that they are related to climate change. The soil parent material deposited (S1) during the Late Pleistocene between 18 and 12 ka BP. This period is marked by a generalized dust stabilization along the present-day Sudano-Sahelian belt suggesting moderately dry environmental conditions on the continent favourable for dust stabilization. The soil organic matter conserved in the pedo-sedimentary geosystem has ages ranging from 10 to 8 ka cal BP. It is thus inherited from the climatic optimum in the Early Holocene. During this period, the latitudinal vegetation extension is at its maximum and soils are developing in the continent (S2). The carbonate nodule precipitation (S3) is recorded mainly during the mid-Holocene, from 7 to 5 ka cal BP. This period is marked by the onset of drier environmental conditions. Finally, the erosion event (S4) occurred at some point during the Late Holocene and seems to be related to the decrease of the vegetation cover triggered by drier climatic conditions and/or anthropic activity in the region. The carbonate pedo-sedimentary geosystem studied in Far North Cameroon is a valuable palaeo-environmental archive recording distinct pedo-sedimentary processes linked to the evolution of continental hydrological conditions. They are suggested to be a proxy of the soil water balance, which changes through time in response to climate. This kind of geosystem might be extended all

along the Sudano-Sahelian belt making it promising for future palaeo-environmental reconstructions in this semi-arid area of West Africa.

Synthesis Part V

Terrestrial carbonate nodules from the Diamare piedmont (Far North Cameroon, Chad Basin) are associated with soils having mound morphologies observed within stream networks. These Ca-rich terrestrial carbonates are paradoxically occurring in Ca-poor granitic watersheds. In the present-day, they are in sedimentary disequilibrium and are dismantling, emphasizing their past heritage nature. The aim of this work was to understand the ***origin*** of these formations and more precisely to identify (i) their nature, i.e. by answering what can be these types of formations and in under what geomorphological and sedimentary conditions they developed? (ii) by answering through which processes they formed and how the palaeoenvironment evolved, and finally, (iii) their chronology, i.e. by answering what are the different steps of their formation and when did they occur? Linking sedimentology, pedology, geomorphology, geochronology and geochemistry, it was possible to recognize the nature of the geosystem hosting these terrestrial carbonates, and to propose a chronological framework of the palaeoenvironment and their associated processes.

In the present-day landscape, carbonate nodules are associated with clay-rich, smectitic-rich, and $Fe-Mn$-rich soils. These soils can have mound morphologies, termed ***mima-like mounds*** due to their regular overdispersion within stream networks (Diaz et al., 2016a). These mima-like mound areas were shown to be widespread in the whole Diamare piedmont. The mounds can also be flattened, have whaleback morphologies, or be buried under a reddish pediment, identified as a fersiallitic pedolith, i.e. a reworked soil sediment. These different geomorphic features emphasize the role of erosion in their genesis. Carbonate nodules are found as a layer at the soil surface, and within the soil matrix at different depths. Sparse vegetation is associated with these soils due to their high compaction and alkaline pH ($8 < pH_{H2O} < 10$). Soil scientists defined these soils as degraded Planosols (Brabant and Gavaud, 1985). The degraded nature is locally termed *hardé* and suggests that, in the past, the soils were not degraded and possibly different. The present-day soil properties were shown to be close to vertic characteristics, i.e. clay-rich, smectitic-rich, with $Fe-Mn$ and carbonate nodule occurrences, slickenside structure, and vertical crack developments. However, as already stated, the soils are qualified as Planosols and not Vertisols, because they lack of the needed horizon sequence to be defined as such (Coulombe et al., 1996a). The main argument is the occurrence of carbonate nodules and $Fe-Mn$ micro-nodules at the soil surface, whereas in Vertisols they should occur in deep horizons. The idea, as a consequence, is that, in the past, present-day *hardé* Planosols were Vertisols and these Vertisols were, at some point, affected by erosion processes. Therefore, the mima-like mounds can be seen as ***Vertisol relics***. To explain this specific morphology, it was proposed that, during a period favourable to their formation, a gilgai micro-relief, characterized by micro-lows and micro-highs (Mermut et al., 1996), was associated with Vertisol genesis. The increase of erosion would have emphasized this micro-relief, leading to mima-like mound formations of various amplitudes depending on the erosion intensity, and bringing at the surface carbonate and $Fe-Mn$ nodules originally formed deeper in the profile. Vertisol genesis and former erosion are thus linked to environmental changes and can be related to the Bio-Rhexistasy theory, i.e. the succession of stable and unstable environmental periods, developed by Erhart (1967). In the present-day, Vertisols are still developing but in the lower parts of the landscape, i.e. in waterlogged areas. It was thus proposed that these waterlogged areas could have been more extended in the past, and with them, the associated Vertisols.

Interestingly, the climate in Far North Cameroon would have been wetter during the African Humid Period (AHP, 14.8 to 5.5 ka; deMenocal et al., 2000), due to the northern migration of the African monsoon system (Tierney et al., 2017), and waterlogged areas would have been much more widespread (Lézine et al., 2011). Moreover, the end of the AHP is characterized by drier conditions, due to the southern migration of the African monsoon, these conditions becoming more intense until the present-day. Vertisol genesis and associated gilgai micro-relief, carbonate nodules, and Fe-Mn micro-nodules

were thus proposed to be inherited from the AHP. Nodules concentrated at the surface when the soil matrix have been eroded during the post-AHP period. In addition, the fersiallitic soils were likely also formed during the AHP but at higher elevations of the landscape, where weathering (hydrolysis) was more intense. These soils were then affected by erosion as well, explaining why, in the present-day, they can overlay and bury the mima-like mounds, and consequently, termed ***fersiallitic pedoliths***. Finally, grain size distributions demonstrated the presence of an aeolian component in the mima-like mounds. Before the AHP, the climatic conditions would have been favourable to aeolian stabilization. It was thus concluded that mima-like mounds from the Diamare piedmont could be ***sedimentary records*** of Late Quaternary climatic changes that occurred in the Southern part of Chad Basin.

Mima-like mound from Far North Cameroon resulted from a four-steps events succession: S1) the soil parent material deposition during a drier period, S2) the soil formation and later S3) pedogenic carbonate nodules and gilgai micro-relief formation, occurring during a wetter period, and finally, S4) the erosion. Mima-like mounds thus evolved as pedo-sedimentary geosystems. However, the processes explaining the way they formed is still missing. Parallel to this work, a second study has been devoted to the geochemistry of terrestrial carbonates, more precisely on the origin and dynamics of calcium (Ca). This research demonstrated that the Ca sources for pedogenic carbonate nodules were mainly plagioclases from the granitic bedrock (Dietrich et al., 2017). However, this bedrock is Ca-poor (1.65 wt-%) and the carbonate nodules are Ca-rich (45 wt-%). To explain this paradox, it was proposed that the Ca should have been preserved and accumulated in the surrounding environment. Two possible pools able to significantly trap Ca could have been smectitic clay minerals and organic matter (Dietrich et al., *in prep*). Nonetheless, an important issue is still pending: carbonate nodules are mainly composed of calcite, and this mineral needs ***alkaline conditions*** to precipitate, i.e. soil $pH \approx 8.4$ in surficial settings. As rare earth elements demonstrated that carbonate nodules precipitated in oxic conditions, how did pH rise in such conditions? The petrology of carbonate nodules emphasized a pedogenic environment affected by water-table fluctuations, which strengthens the Vertisol genesis hypothesis. However, $Fe-Mn$ oxides were mainly formed before carbonate nodules, as they are trapped within them. If both minerals can occur in oxic conditions, the pH for their occurrence is different (Krumbein and Garrels, 1952; Ashley et al., 2013, Appendix D). Consequently, at some point, the soil pH varied toward alkaline conditions, leading to the transition from an environment favourable to $Fe-Mn$ oxides to an environment favourable to calcitic carbonate nodules. Carbonate nodules were found to trap calcium oxalate as small needles in the micro-porosity. Processes leading to its presence are unclear (trapping, diagenesis?). Nevertheless, its solely presence suggests that calcium oxalate and/or oxalic acid were present in the environment. Interestingly, a large panel of vegetation and fungi produces oxalate (Franceschi and Nakata, 2005; Gadd et al., 2014). Stable C and O isotopes on carbonate nodules suggested the presence of an open forest dominated by C3 plants. However, with time they suggest that ecosystems changed and these changed are marked by an increase of C4 plants proportion and drier hydric conditions within the soil. Is dryness involved in pH increase? Oxalate could likely have been produced within the forest ecosystem. It is also a nutrient for oxalotrophic bacteria (Martin et al., 2012). It was demonstrated that the oxidation of oxalate by bacteria induced the alkalinisation of soil conditions, and led to secondary carbonate formation (Verrecchia et al., 2006). This process is known as the ***Oxalate-Carbonate Pathway (OCP)***. The convergence of the need for alkalinity and the presence of both oxalate and carbonate nodules points to the hypothesis that, drier conditions led some decrease of the forest (or change in its structure), liberating oxalate inside the soil, activating and/or accelerating the OCP. This chain of events would have induced an increase in pH (kinetic?) and the precipitation of calcitic nodules, as soon as favourable conditions were reached. Moreover, drier conditions also mean that carbonate nodules are preserved. Stable C isotopic compositions showed that C originates from soil organic matter and Ca was also proposed to be stocked in organic matter (as

calcium oxalate as well?). Consequently, it is likely that *C* and the *Ca* were transferred from an organic pool to an inorganic pool, i.e. carbonate nodules. Obviously, at some point, the system had to end because the organic pool is disappearing, while it is transformed into the inorganic pool. This concept can also be applied to aluminium, magnesium, iron and manganese, which were ***recycled*** into smectite and oxides. The soil parent material was showed to be a mixed between an aeolian dust componant and local saprolite. Dust stabilization implied moderately dry conditions to explain dust production and stabilization (≥400 mm/yr, Mc Tanish, 1984). These climatic conditions are alos favourable for smectite formation in a granitic watershed (Barshad, 1966; Appendix E). Consequently, smectite would have been stable during S1, S2 and S3 formation steps, due to moderately dry conditions (S1), to waterlogged conditions (S2 and S3), also found to be favourable for plagioclases hydrolysis into montmorillonite (Meilhac and Tardy, 1970). Consequently, the elements never left, or only very partially, the system. Finally, it is not clear if the last erosion event (or several of them?) is linked to climatic pejoration and/or anthropic activities. However, the step has definitely fossilized the geosystem, leading to the present-day mima-like mound landscape. Finally, a question remains: is such a geosystem evolution extendable to the West Africa? Nodules from this large area were also investigated and results show similar petrographic and geochemical characteristics than the nodules from Cameroon, strengthening the hypothesis of a genetic relationship and an extension of the processes at the African scale.

This reconstruction of the palaeoenvironment is based on a relative chronology of events and not of absolute numerical ages. By combining luminescence and radiocarbon dating, it was possible to constrain the four-steps succession through time (Diaz et al., 2016b; Diaz et al., *in prep*). The numerical age results well integrate in the Chad Basin regional, and even in the global West African, palaeo-climatic context, and confirmed that pedo-sedimentary processes forming Vertisol relics are inherited from Late Quaternary. The soil parent material deposited from 18 ka to 12 ka (S1). The dates were obtained with optically stimulated luminescence (OSL) on K-feldspars trapped within the carbonate nodules. This period of deposition corresponds to Late Kanemian (21 to 12 ka cal BP, Servant, 1973), which was demonstrated to be favourable to aeolian stabilization, and thus, moderately dry (precipitations ≥400 mm/yr). It seems that aeolian stabilization was not only occurring in the Diamare piedmont at that time, but was also extended to the present-day Sudano-Sahelian zone with aeolian deposits observed in Nigeria (Bennett, 1980; Mc Tainsh, 1984), in the southern part of the Diamare piedmont (Marliac, 1973; Maley, 1981) and more in the South of Cameroon near the Adamaoua region (Maley, 1981). More northward, in the region of present-day Lake Chad and in the Bodele Depression, dune systems were stabilized at the same period (Armitage et al., 2015), suggesting precipitations ≈ 150 mm/yr (in Durand, 1995). The major impact of vegetation and life on the pedogenesis was showed to occur between 11.5 to 8 ka cal BP, dates obtained using radiocarbon dating of the organic matter trapped within the carbonate nodules. Since the climatic optimum (Early Holocene), at 11.5 ka cal BP, the conditions became wetter and the vegetation migrated to the North (at the central and northern African scale), with a maximal extension around 8.5 ka cal BP (Lézine and Cazet, 2005). During this period, soils are actively developing and, in the Diamare piedmont, waterlogged areas likely extended leading to more widespread Vertisol areas than in the present-day. In this context, the soil systems and potentially the organic pool, showed to be an open forest with C3 plant dominance, can stock the elements such as *Ca* and *C*. Moreover, it is highly possible that this ecosystem is producing oxalate. The carbonate nodule precipitation would have occurred between 7 and 5 ka cal BP, a timespan obtained with radiocarbon dating of the inorganic phase of carbonate nodules. Interestingly, by grouping radiocarbon dating ages (n=53) of the carbonate nodules measured on various sites in the Diamare and those found in studies conducted in the region (North Cameroon, Chad, Niger), it can be shown that carbonate nodules were mainly precipitating between 7 and 5 ka cal BP (50%). Stable *C* and *O* isotopes on the carbonate phase showed vegetation and hydrological changes, suggesting a shift

toward drier conditions at the time of pedogenic carbonate nodules formation. Since c. 8 v, different palaeo-climatic and sedimentary archives demonstrated that the climate was becoming drier and the vegetation was retreating Southward, evolving from a wet Sudano-Sahelian savannah to a dry Sudano-Sahelian savannah (Salzmann et al., 2002). This event could possibly be linked to a global cooling observed in the northern hemisphere, known as the 8.2 ka anomaly (Alley et al., 1997). It seems that there was a sort of a "carbonate nodule event" that corresponded to a shift toward drier conditions, this peak agreeing with the period just before the end of the AHP at the African scale (c. 5.5 ka, deMenocal et al., 2000). Finally 4) the erosion (in several phases?) of the inherited AHP landscape, leading to its fossilization, is not precisely dated, but probably occurred after the formation of the last carbonate nodules, thus after 5-4 ka cal BP. Salzmann et al. (2002) indeed demonstrated that the conditions shifted definitely toward drier conditions at 4 ka cal BP. However, is the erosion event linked solely to climatic parameters or is it also linked to anthropic activities, that were showed to be present around 3 ka?

The pedogenic carbonate nodules were thus used as time archives to constrain the relative chronology of mima-like mound formation. The idea is that these events, i.e. the soil parent material deposition, pedogenesis, carbonate nodule formation, and final erosion, point to a succession of sedimentary and pedogenic processes through time. This specific geosystem can be seen as a true ***pedo-sedimentary continuum***. The succession of events is related to specific soil water balance conditions, in turn related to climate variations due to the ITCZ shift in the West Africa during the Late Quaternary. This history might be extended to the whole West Africa, as areas displaying mima-like mounds were detected with Google Earth images all along the Sudano-Sahelian belt. Carbonate nodules were observed and collected in four of these localities, in Mali, northern and southern Burkina Faso, and Niger. Radiocarbon dating of the carbonate phase resulted in the same range of ages than those from Far North Cameroon, i.e. between 5 ka and 3 ka cal BP. It was already proposed that these formations were genetically related and now results suggest that the timing would also concord.

Terrestrial carbonate nodules from Far North Cameroon were showed to be pedogenic and related to past Vertisol genesis, within areas affected by water-table fluctuations. The genesis of these formations began at least 18 ka years ago and led to a chronology of four main events, all related to soil water balance changes due to the migrations of the ITCZ. The trigger for the precipitation of carbonate nodules was the shift toward drier conditions, leading to a forest retreat/clearance and the decrease of the water-table fluctuation frequency. The increase of organic matter, probably oxalate-rich, input to the soil triggered the OCP. The increase of soil pH related to the oxidation of this organic component led to the precipitation of secondary calcitic nodules. The observation of similar features along the Sudano-Sahelian belt raises the question of a potential extension of this particular geosystem at the West African scale. Oxalogenic vegetation and oxalotrophic bacteria are ubiquitous, so their occurrence in the whole continent is perfectly plausible.

These conclusions fit well with the whole palaeoclimatic reconstructions at the West African scale, although they bring questions concerning the hypothesis of the occurrence of a Mega-Lake Chad. This 350'000 km^2 lake would have last occurred during a 5.3 to 4.4 cal kBP timespan and is interpreted as the result of Mid-Holocene wetter conditions (Gasse, 2000; Schuster et al., 2005; Sepulchre et al., 2008). However, it was showed that hydric conditions were already becoming drier since c. 8 ka cal BP in the southern part of the Basin (Far North Cameroon), which is in agreement with other proxies at the African scale. It seems thus that there is a disagreement between climatic conditions in the Chad Basin at the time of the occurrence of a Mega-Lake. However, it is important to keep in mind that a lake is an hydrological system. It is linked to climate but not solely. Gap could exist between the responses of a climatic system and an hydrological system to a change. For example, the *inertia*

effect implies that a water-table responds slowly than climate (Durand and Lang, 1986). Lake Chad is an interesting hydrological system as it is mainly fed by the Chari-Logone rivers coming from the humid tropics (Sudano-Guinean belt). Consequenty, even if the Chad Basin region is becoming drier, waters are still coming from the southern wetter latitudes. However, assuming that the system was the same during Mid-Holocene, since c. 8 ka cal BP climatic conditions in the Chad Basin are becoming drier, implying more evapotranspiration and less rainfall, thus less water for Lake Chad. Intuitively, a Mega-Lake should thus occur before 8 ka cal BP. Could there be another explanation for an occurrence after 8 ka cal BP? There might be a hydrological answer. As just said, the main rivers fedding Lake Chad are the Chari and the Logone. However, the Logone would not have always been the tributary of the Chari and would have been captured by the Mayo Kebi during the Pleistocene (in Durand et al., 2011). Its present-day flow would have been definitive around 4.5 ka cal BP, the same period of the last Mega-Lake Chad occurrence. Indeed, its waters represent 40% of inputs in the lake (Gac, 1980), so adding this amount should not be neglected. Could this hydrological event be sufficient to explain the paradox of a Mega-lake occurring when climate is becoming drier?

The monsoon system is global and affects both tropical hemispheres. Vertisols are mainly found in the tropical zones (Southard, 2011); is it therefore possible that they were extended in the whole tropical belt during the past? Carbonate nodules were observed and studied in India (Violette et al., 2010) and in North America (Nordt and Driese, 2010), were they also related to the same type of geosystem? There is always a thought that pedogenic carbonates are related to dry conditions (e.g. Durand et al., 2007; Violette et al., 2010; Zamanian et al., 2016). It is true that they are mainly found in arid and semi-arid areas (USDA-NRCS, 2000), but is this occurrence really related to genetic reasons? Could not it be an occurrence related to a specific type of preservation for such carbonate? Are these areas particular places where a past organic carbon has been converted into an inorganic carbon after a climatic shift and possibly through an alkalinization of the environment by the OCP? As already stated, oxalate and oxalogenic bacteria are ubiquitous, they can certainly be found along the whole tropics. Maybe the OCP is more widespread than thought and could be massively involved in terrestrial carbonate formation as its alkaline engine.

Nevertheless, palaeoenvironmental archives are sparse within the semi-arid tropics in both hemispheres (Chase, 2009; Duller, 2016) due to lack of sedimentary preservation (i.e. few organic matter, erosion inducing hiatus). However, understand past changes in those regions is important as they are very sensitive (Pastouret et al., 1978). The study of terrestrial carbonates associated to pedo-sedimentary geosystems might help to fill the gap as they were showed to be valuable palaeoenvironmental archives, registering processes and their evolution through time.

General conclusion and perspectives Part VI

The aim of this research was to give new clues on the origin of the terrestrial carbonate formation from Far North Cameroon. A study site located along the Mayo Tsanaga in the Diamare piedmont was investigated. Parallel to this work, another PhD study was dedicated to the geochemistry of terrestrial carbonate formations. Crossing the conclustions, it was possible to propose hypotheses concerning the nature of terrestrial carbonate formations, the processes and the palaeoenvironment of formation, and the timing for their genesis.

Terrestrial carbonates formations were found to be Vertisol relics resulting form succession of pedo-sedimentary processes linked to the monsoon system variation during Late Pleistocene-Holocene. Vertisol relics registered palaeoenvironmental events, such as: 1) the deposition of the soil parent material being a mixed between dust and local regolith, 2) the pedogenesis linked to forested wetlands, 3) the precipitation of carbonate nodules related to alkalinization and dryness of the soil environment, and 4) the erosion of the system due to climate and/or anthropic activities. These phases were dated and could be correlated to regional and African palaeoclimatic context. The deposition occurred since 18 to 12 ka, during a moderately dry period corresponding to Late Kanemian and Nigero-Chadian L1. The forested wetlands to which Vertisol genesis is associated occurred mainly during the climatic optimum, between 11 and 8 ka cal BP. The carbonate nodule genesis were found to be linked to a shift of climatic conditions leading to vegetation and hydrological changes, since 8 ka cal BP. Finally, the erosion events should occur after nodule formation, since 5-4 ka cal BP. The processes recorded are thus not overlapping and correspond to climatic variations, the geosystem responding through succession of pedo-sedimentary processes. It was demonstrated that the elements were transferred from one compartment to another according to these pedo-sedimentary processes. Living forms were showed to have an important role in the accumulation of elements and soil chemical changes.

If the whole geosystem is generally well understood, the processes leading to the formation of pedogenic carbonate as nodules are still unclear. The nodular form is the most common pedogenic carbonate morphology found in soils. However, the reasons and processes explaining this ubiquitous morphology are still unclear (Zamanian et al., 2016). Why is secondary carbonate precipitating as a nodule? Answer this question is not simple and beyond the scope of this present work. However, the occurrence of this particular morphology is not hazardous and should be related to palaeoenvironmental conditions. The hardness of carbonate nodules is often interpreted as the result of diagenesis, the original carbonate being rather soft (e.g. Kovda et a., 2003; Zhou and Chafetz, 2009). Seeing hard nodules as advanced stage of evolution, Zhou and Chafetz, (2009) proposed that diagenesis was probably related to palustrine environments with water-table fluctuations. Even if this is not a generality, nodular carbonate horizons are frequently described in sedimentary facies attributed to palustrine environments, being affected by pedogenesis when the environment is exposed to sub-aerial conditions (Freytet and Verrecchia, 2002; Alonso-Zarsa, 2003; Verrecchia 2002). Even if clear reasons explaining the nodular morphology are never really handled, it seems that there is a link between nodular morphologies and areas frequently waterlogged, and thus affected by pedogenesis when conditions are drained. The precipitation of secondary carbonate appears thus to be linked to soil hydric changes. Is the precipitation related to simple evaporation processes linked to the water-table fluctuation? In this case, the secondary carbonate should rather have laminar morphology, or at least being continuously, i.e. homogeneously, precipitated? Concentric morphologies suggest that the nodules grow from a central point to the outside. Each nodule represents thus a point favourable for calcite nucleation, which thus emphasizes rather a heterogeneous environment. As this environment is a soil, are these nucleation points related to living forms, such as bacterial hot spots and/or root systems? Pias (1968) described hydromorphic soils in Chad Basin, in the Chari-Logone region, and showed that secondary carbonate nodules were associated to these soils. This is interesting in two aspects. First, there is a similar context in the

present-day, corresponding to the palaeoenvironment reconstructed. Second, the aim of this work was not to explain the occurrence of these nodules, however, the author noted the strangeness of their presence. He reported his colleague suggestion (H. Erhart) proposing that the carbonate nodules were probably linked to root systems. However, this topic was never deeper investigated and in further studies in the region, the carbonate nodules were just reported and described by soil scientists and/or geomorphologists (Brabant and Gavaud, 1985; Morin, 2000) or used as chronometers by Quaternary scientists (Hervieu, 1967; Marillac, 1973; Maley, 1981). Nevertheless, already at that time, biota was suspected to play a role in nodule genesis. Looking at a greater scale, carbonate precipitates mainly as micritic phases and fibrous calcite. Both types of crystals suggest a thermodynamic disequilibrium. Is it induced by life? It is well known that life changes its surrounding environment due to various chemical excretions, such as root acids, hydrated extracellular polymeric substances (EPS) biofilms, etc., and thus influencing the kinetic of chemical reactions (Sposito, 1994). To form micrite, Pouguet and Rambaud (1980) showed that the solution should be supersaturated in $CaCO_3$ to induce fast precipitation from numerous nucleous. Furthermore, Loisy et al. (1999) showed that micrite can be related to organic matter and they demonstrated that the role of bacteria in pedogenic carbonate precipitation should not be neglected. Looking at another environment, micrite cements in stromatolite are related to cyanobacteria. It was demonstrated that micrite formed via dead cyanobacteria calcifications and/or precipitated directly on cyanobacteria filaments by bacterial mediation (Chafetz and Buczynski, 1992). Moreover, in mats, exopolysaccharides are known to fix high amounts of Ca and Mg, which are released during degradation and leading to $CaCO_3$ precipitation (Kazmierczak et al., 2015). Clearly the context in Far North Cameroon is very different (i.e terrestrial and not marine), however, these examples show the important involvement of microorganisms in secondary carbonate precipitation during OM degradation. The main component of a soil after the mineral fraction is organic matter (OM). Its composition is complex but it is a source of nutrient for soil microorganisms. Bacteria communities live in EPS biofilms, which represent the dominant reduced-carbon fraction in soils (Flemming and Wingender, 2010). These highly hydrated EPS developing physic-chemical gradients are similar microenvironments to microbial mats, and could likely be involved in the soil micritic cementation, such as mats are in stromatolite ecosystems. Are the carbonate nodules the expression of the degradation of pedogenic EPS biofilms, which are, after having liberated cations, further calcified? Finally, Aassoumi et al., (1992) worked on pedogenic carbonate nodules and suggested that cone-in-cone structures (similar to Fc cement) were linked to specific root-bacteria systems. Calcified roots and fine needles (fungal filaments? Appendix C) were observed at the carbonate nodule-soil interface. Are these structures also relics of the palaeo-environment? Are they more recent? This is hard to answer these questions, nevertheless it seems that roots, fungi and bacteria have a role in secondary carbonate nodule precipitation, potentially in both the nodular morphology (hot spots, root systems) and cement facies. The questions are related to the precise role of all these actors in carbonate nodule precipitation and the answers could lead to the elaboration of a model, which is lacking.

Finally, the question on the smectitic clay formation is still pending. The great thickness accumulated in the Diamare piedmont already intrigated soil scientists and geomorphologists working in this region (Morin, 2000). They proposed an aeolian, palustrine or lacustrine origin. Are these clay minerals authigenous? The question remains open as the mineral fraction was not studied in details. However, it was demonstrated that the climatic conditions were favourable for their genesis since 26 ka cal BP, due to low mean annual precipitation (Durand, 1995) favourable for smectite formation (Annexe F), and then to waterlogged environmental settings, also favourable for smectite formation and stability (Aoudjit et al., 1995). This long time period favourable for smectite could thus explain its accumulation in the watershed. However, more work is definitely needed on this topic.

Appendix Part VII

A Mima-like mounds GPS locations

Table A.1 – GPS data of the mima-like mound areas observed with Google Earth.

Region	Latitude	Longitude	Altitude (m)
Nigeria	11°6’38.99"N	13°51’6.42"E	428
	11°9’49.98"N	13°52’23.70"E	399
	11°12’52.48"N	13°53’10.66"E	377
Mora	11°8’19.22"N	13°56’50.21"E	381
	11°2’56.33"N	13°54’36.73"E	426
	10°54’35.33"N	13°51’56.61"E	494
	10°54’54.24"N	13°56’41.31"E	473
	10°56’27.72"N	13°57’57.36"E	459
	10°58’45.44"N	13°57’19.21"E	435
	10°59’45.84"N	13°57’10.38"E	428
	11°1’7.41"N	13°59’29.10"E	418
	11°2’17.55"N	13°59’59.59"E	410
	11°7’1.09"N	14°2’59.79"E	372
	11°3’4.58"N	14°11’26.62"E	388
	11°3’50.53"N	14°12’8.60"E	377
	11°10’8.99"N	14°15’43.26"E	319
	11°1’57.80"N	14°17’56.74"E	353
	11°0’35.32"N	14°18’19.24"E	358
	10°59’8.59"N	14°18’16.32"E	364
Tchéré	10°52’18.25"N	14°25’17.36"E	353
	10°51’4.09"N	14°21’18.72"E	369
	10°46’17.97"N	14°22’43.04"E	377
	10°46’42.53"N	14°16’4.87"E	412
	10°44’14.15"N	14°16’17.89"E	421
	10°43’5.97"N	14°16’8.35"E	428
Maroua	10°40’24.75"N	14°12’0.16"E	480
	10°37’19.54"N	14°11’9.64"E	451
	10°36’39.65"N	14°11’10.83"E	445
	10°34’53.51"N	14°12’6.72"E	431
	10°34’27.01"N	14°13’45.57"E	426
	10°34’39.92"N	14°14’47.14"E	418
	10°34’58.27"N	14°16’10.83"E	416
	10°40’36.29"N	14°26’34.23"E	369

	10°47’18.79"N	14°35’1.73"E	340
	10°49’22.72"N	1°37’2.50"E	335
Salak	10°28’39.03"N	14°9’38.27"E	452
	10°27’11.71"N	14°11’23.62"E	441
	10°27’5.84"N	14°12’55.59"E	433
	10°25’35.74"N	14°12’41.66"E	430
	10°26’5.76"N	14°16’11.68"E	420
	10°24’27.83"N	14°16’31.59"E	422
	10°30’38.72"N	14°25’50.87"E	382
	10°29’14.52"N	14°27’25.34"E	393
	10°23’31.55"N	14°30’20.99"E	395
	10°18’38.07"N	14°24’36.21"E	416
Kaele	10°9’59.83"N	14°2’38.61"E	409
	10°13’40.83"N	14°37’7.45"E	402
	10°6’18.77"N	14°38’13.75"E	402
	10°1’32.69"N	14°40’56.42"E	377
Yagoua	10°7’42.48"N	15°12’4.83"E	327
N’Djamena	11°44’25.06"N	15°3’3.32"E	302
	11°47’26.53"N	15°3’47.50"E	298
	11°53’54.53"N	15°1’21.58"E	301
	12°14’14.66"N	15°2’52.21"E	296
Senegal	15°56’5.98"N	14° 7’40.54"O	63
Senegal	14°55’32.58"N	13°27’58.53"O	44
Senegal	14°48’49.06"N	12°33’42.65"O	63
Mauritania	15°42’51.04"N	11° 5’18.78"O	259
Mali	15° 0’14.63"N	11°43’2.03"O	77
Mali	14° 3’34.73"N	7° 6’36.10"O	290
Mali	13° 7’1.88"N	5°36’51.25"O	282
Mali	15°35’32.46"N	4°31’11.09"O	269
Burkina Faso	14°24’52.87"N	1° 5’14.13"O	290
Burkina Faso	14° 0’56.19"N	0° 7’50.54"O	287
Burkina Faso	13°48’30.53"N	0°14’5.71"O	301
Burkina Faso	12°40’41.34"N	0° 4’11.44"O	297
Niger	13°30’38.84"N	2°31’26.81"E	264
Niger	13°29’47.44"N	2°31’58.57"E	236
Niger	13°23’47.98"N	2°32’56.16"E	260
Niger	13°24’20.65"N	2°33’59.41"E	260
Niger	13°25’20.47"N	2°38’3.12"E	260
Niger	13°53’18.10"N	4°35’52.67"E	279
Niger	13°46’13.32"N	6°36’4.70"E	358
Niger	13°35’36.42"N	8°19’30.62"E	445
Benin	12° 0’0.41"N	3° 5’52.38"E	179
Benin	11°56’28.78"N	3°10’35.79"E	172
Nigeria	12°21’15.91"N	10°41’2.54"E	356
Nigeria	12°12’54.10"N	7° 2’46.06"E	464
Nigeria	11°32’19.98"N	13°51’47.49"E	316
Nigeria	11°27’28.65"N	13°42’1.78"E	939
Nigeria	11° 9’56.84"N	13°52’22.17"E	396
Nigeria	11° 6’41.19"N	13°50’59.78"E	428
Cameroon	10°37’57.30"N	14°11’20.40"E	451
Chad	12°17’23.47"N	17°54’53.17"E	363
Chad	11°54’22.34"N	16°54’11.54"E	321

Chad	12°40’50.79"N	22°11’24.53"E	667
Chad	12°38’5.60"N	22°17’28.27"E	649
Chad	12°35’50.78"N	22°17’5.96"E	628
Sudan	13°23’21.97"N	24° 1’15.92"E	1162
Sudan	12°48’9.93"N	24° 3’22.31"E	1174

$$r_A = \frac{\sum r}{n} \tag{A.1}$$

$$r_E = \frac{1}{2\sqrt{\rho}} \tag{A.2}$$

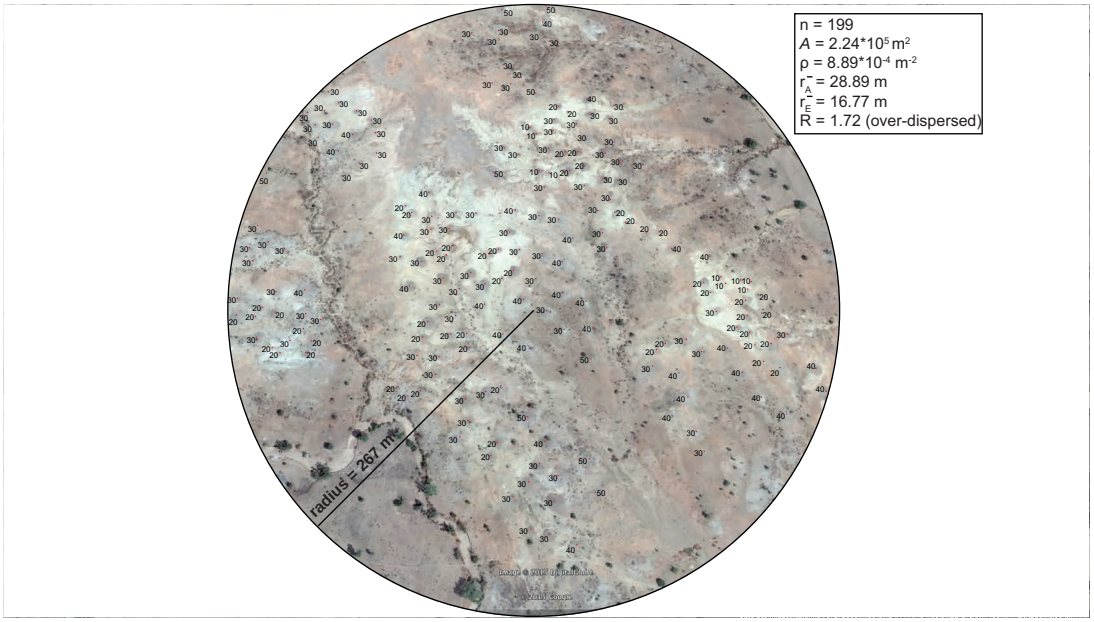

Figure A.1 – Investigated area for the spatial relationship analysis of mima-like mounds according to their distance to their nearest neighbour (Clark and Evans, 1954). Each point (red) represents a mima-like mound (n=199) and is characterized by the observed distance (r) of its nearest neighbour. A is the area, ρ is the density of points in the area, r_A is the observed mean distance (Eq. A.1) and rE is the expected mean distance if mima-like mounds were randomly distributed (Eq. A.2). R is the ratio between r_A and r_E and assesses the degree to which the observed distribution approaches or departs from random distribution. If the spatial distribution is random, then R=1, if the aggregation is maximal (where the nearest neighbour distance is 0), then R=0, if R > 1, then there is an over-dispersion.

B Carbon and Calcium amounts in mima-like mounds

Table B.1 – Parameters used to calculate amount of C and Ca in mima-like mounds

Density soil	**Density nodule**	**Soil carbonate** mean (n=25)	**Nodule carbonate** mean (n=5)	**Skeleton** mean (n=25)	**Surface nodule** mean (n=12)
gcm^{-3}	gcm^{-3}	$mgkg^{-1}$	$mgkg^{-1}$	%-nodule	kgm^{-2}
1800	2.7	0.041±0.003	$7.2*10^5$ $\pm 3.3*10^4$	7.53±4.99	11.17±3.3

Table B.2 – C and Ca amount in mima-like mounds

Volume m^3	1
Soil mass kg	1800
Nodule mass kg	136
Soil carbonate mg	75
Nodule carbonate mg	97592744
Total carbonate kgm^{-3}	97.6
Total carbonate kgm^{-3}	97.6±30
Total carbon kgm^{-3}	19.5±6
Total calcium kgm^{-3}	65±20
Total carbon $kmolm^{-3}$	1.6±0.5
Total carbon $molm^{-3}$	1625±498
Ton per hectar	
Total carbon tC/ha (20 cm prof)	39±12
Total carbon tC/ha (1 cm prof)	2±0.6

C Picture boards

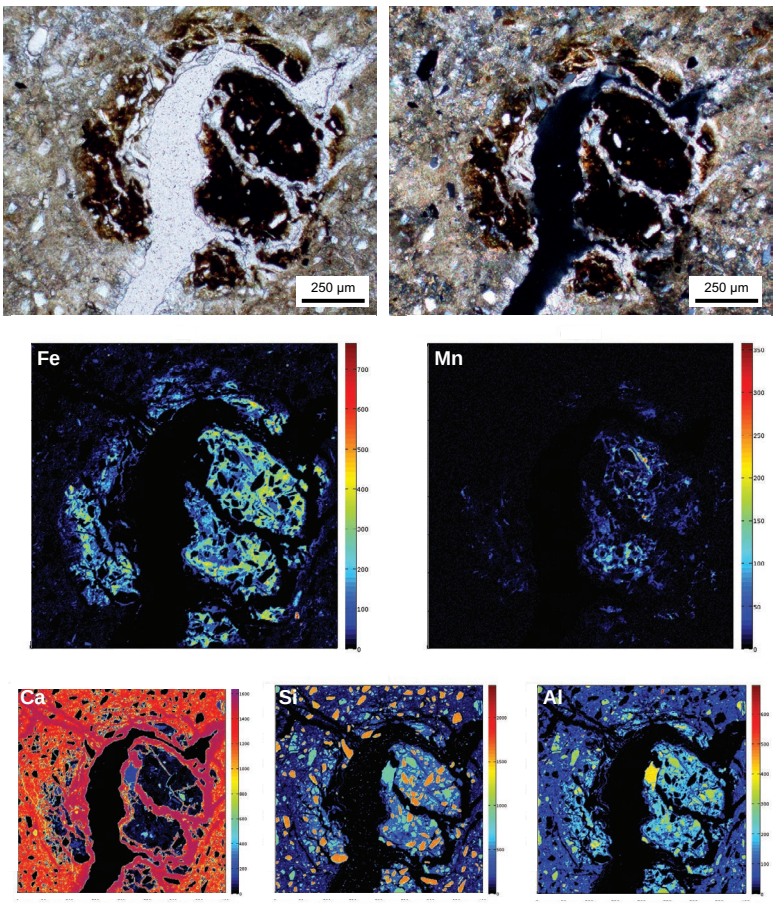

Figure C.1 – The main component of trapped oxide is Fe

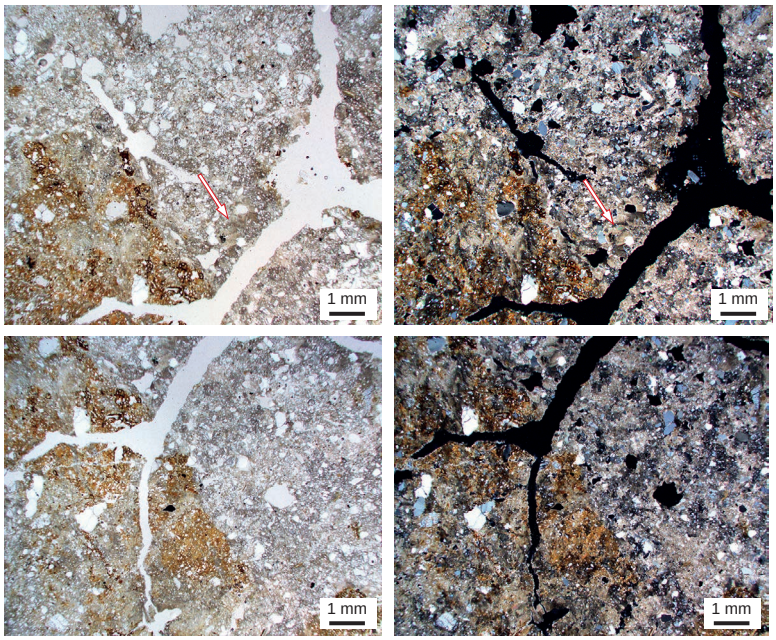

Figure C.2 – Thin section of a *secondary* carbonate nodule.

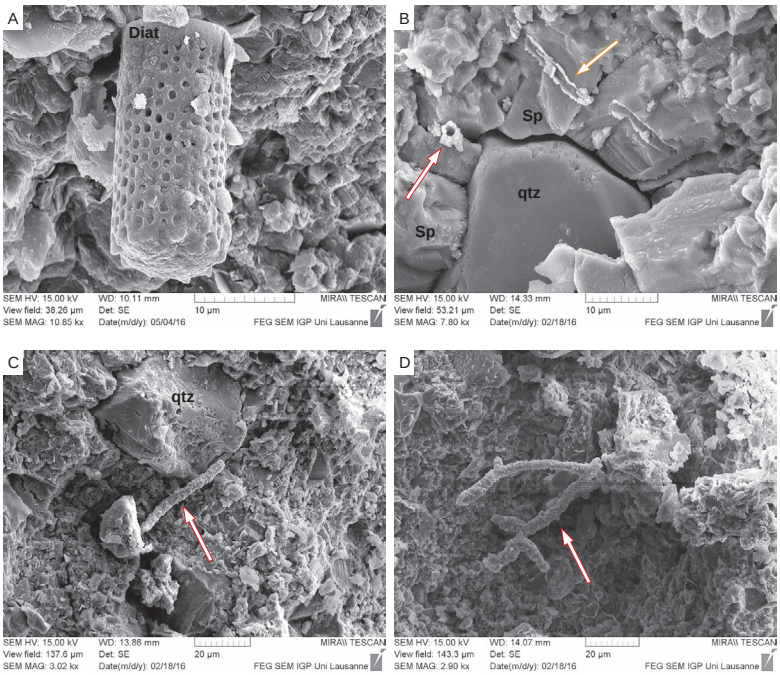

Figure C.3 – At the interface of soil-carbonate nodules, living features are observable, such as, skeleton of diatom (wind input?), calcified hyphae.

D Stable C and O isotopes

Table D.1 – Stable C and O isotopic data.

Country	Code sample	Type	Sampling	Depth (cm)	$\delta^{13}C_{inorg}$ VPDB	int. Err	$\delta^{18}O_{inorg}$ VPDB	int. Err.	TOC (%)	$\delta^{13}Corg$ (VPDB)	C_{inorg} Age cal ka BP	err	$Corg$ Age cal ka BP	err
Cameroon	Cn 073-pi	Nodule	subsample	-20	-7.93	0.05	-6.88	0.05	nd	nd	nd	nd	nd	nd
Cameroon	Cn 073-gg	Nodule	subsample	-20	-8.42	0.03	-7.28	0.03	nd	nd	nd	nd	nd	nd
Cameroon	Cn 080	Nodule	subsample	-10	-9.13	0.04	-8.01	0.04	nd	nd	nd	nd	nd	nd
Cameroon	Kalliao-pi	Nodule	subsample	0	-8.91	0.05	-8.20	0.03	nd	nd	nd	nd	nd	nd
Cameroon	Kalliao-gg	Nodule	subsample	0	-7.98	0.06	-7.58	0.03	nd	nd	nd	nd	nd	nd
Cameroon	Kalliao	Nodule	Bulk	0	-8.91		-4.82		0.12	-22.93	nd	nd	nd	nd
Cameroon	CaK04-pi	Nodule	subsample	0	-7.50	0.06	-6.88	0.05	nd	nd	nd	nd	nd	nd
Cameroon	CaK04-gg	Nodule	subsample	0	-7.61	0.09	-7.03	0.07	nd	nd	nd	nd	nd	nd
Cameroun	Ca005-no	Nodule	Bulk		nd	nd	nd	nd	0.13	-20.90	nd	nd	nd	nd
Cameroon	S1-so	Soil	Bulk	-2.5	-6.56	0.06	-5.66	0.07	nd	nd	nd	nd	nd	nd
Cameroun	S5-so	Soil	Bulk	-20	-6.99	0.06	-5.74	0.05	nd	nd	nd	nd	nd	nd
Cameroon	S20-so	Soil	Bulk	-60	-5.91	0.05	-6.14	0.05	nd	nd	nd	nd	nd	nd
Cameroun	Ca0023-so	Soil	Bulk		nd	nd	nd	nd	0.18	-21.65	nd	nd	nd	nd
Cameroon	E1 p1	Nodule	Sparite	-115	-6.13	0.09	-6.54	0.05	nd	nd	nd	nd	nd	nd
Cameroon	E1 p2	Nodule	Reddish	-115	-8.71	0.05	-8.47	0.04	nd	nd	nd	nd	nd	nd
Cameroon	E1 p3	Nodule	Dark-grey	-115	-0.48	0.03	-6.66	0.04	nd	nd	nd	nd	nd	nd
Cameroon	E1-P3	Nodule	subsample	-115	-0.33	0.04	-6.59	0.06	nd	nd	nd	nd	nd	nd
Cameroon	E1 p4	Nodule	Grey	-115	-7.72	0.06	-7.49	0.03	nd	nd	nd	nd	nd	nd
Cameroon	E5-P1	Nodule	subsample	-10	-8.67	0.14	-7.05	0.11	nd	nd	nd	nd	nd	nd
Cameroon	A1 p1	Nodule	Sparite	-5	-6.37	0.06	-4.38	0.08	nd	nd	nd	nd	nd	nd
Cameroon	A1 p2	Nodule	Aggr	-5	-5.00	0.11	-7.21	0.07	nd	nd	nd	nd	nd	nd
Cameroon	A1 p3	Nodule	Grey	-5	-4.15	0.11	-7.59	0.04	nd	nd	nd	nd	nd	nd
Cameroon	A2-2-P1	Nodule	subsample	-50	-4.44	0.15	-5.30	0.14	nd	nd	nd	nd	nd	nd
Cameroon	A2-2-P2	Nodule	subsample	-50	-5.27	0.12	-6.18	0.07	nd	nd	nd	nd	nd	nd
Cameroon	A2-2-P3	Nodule	subsample	-50	-4.87	0.12	-6.42	0.07	nd	nd	nd	nd	nd	nd
Cameroon	A3-P1	Nodule	subsample	-100	-9.41	0.06	-8.66	0.12	nd	nd	nd	nd	nd	nd
Cameroon	A3-P2a	Nodule	subsample	-100	-9.23	0.03	-8.80	0.07	nd	nd	nd	nd	nd	nd
Cameroon	A3-P2b	Nodule	subsample	-100	-9.34	0.02	-8.82	0.06	nd	nd	nd	nd	nd	nd
Cameroon	A3-P2c	Nodule	subsample	-100	-9.42	0.04	-8.92	0.06	nd	nd	nd	nd	nd	nd
Cameroon	V-no	Nodule	subsample		nd	nd	nd	nd	0.31	-19.19	nd	nd	nd	nd
Cameroon	B2 p1	Nodule	Grey	-10	-9.58	0.05	-8.33	0.09	nd	nd	nd	nd	nd	nd
Cameroon	B2 p2	Nodule	External	-10	-6.24	0.04	-5.33	0.05	nd	nd	nd	nd	nd	nd
Cameroon	B2 p3	Nodule	Grey	-10	-9.52	0.08	-8.00	0.07	nd	nd	nd	nd	nd	nd
Cameroon	B4 p1	Nodule	Grey	-60	-9.66	0.07	-8.40	0.06	nd	nd	nd	nd	nd	nd
Cameroon	B4 p2	Nodule	Reddish	-60	-9.73	0.05	-8.43	0.05	nd	nd	nd	nd	nd	nd
Cameroon	B4 p3	Nodule	External	-60	-10.17	0.04	-7.34	0.07	nd	nd	nd	nd	nd	nd
Cameroon	B6-b-P1	Nodule	subsample	-125	-7.36	0.15	-7.42	0.13	nd	nd	nd	nd	nd	nd
Cameroon	B6-b-P2	Nodule	subsample	-125	-6.72	0.05	-7.23	0.07	nd	nd	nd	nd	nd	nd
Cameroon	C2 p1	Nodule	Reddish	-7.5	-4.73	0.04	-6.09	0.07	nd	nd	nd	nd	nd	nd
Cameroon	C2 p2	Nodule	Grey	-7.5	-6.69	0.04	-5.88	0.05	nd	nd	nd	nd	nd	nd
Cameroon	C3-P1	Nodule	subsample	-30	-9.20	0.13	-8.60	0.15	nd	nd	nd	nd	nd	nd
Cameroon	C3-P2	Nodule	subsample	-30	-9.69	0.04	-9.02	0.07	nd	nd	nd	nd	nd	nd
Cameroon	C3-P3	Nodule	subsample	-30	-9.39	0.02	-8.75	0.04	nd	nd	nd	nd	nd	nd
Cameroon	D3a-P1	Nodule	subsample	0	-5.26	0.04	-5.86	0.04	nd	nd	nd	nd	nd	nd
Cameroon	D3a-P2	Nodule	subsample	0	-5.78	0.03	-5.54	0.03	nd	nd	nd	nd	nd	nd
Cameroon	D3a-P3	Nodule	subsample	0	-5.86	0.03	-5.37	0.04	nd	nd	nd	nd	nd	nd
Cameroon	C1	Nodule	Bulk	0	-8.30	0.08	-8.14	0.04	0.13	-21.59	7.13	0.12	nd	nd
Cameroon	C2	Nodule	Bulk	0	-7.55	0.11	-7.79	0.05	0.20	-20.06	6.34	0.06	nd	nd
Cameroon	C3	Nodule	Bulk	-7.5	-8.85	0.06	-7.54	0.03	0.20	-20.48	6.24	0.05	8.83	0.24
Cameroon	C4	Nodule	Bulk	-35	-9.31	0.09	-7.90	0.05	0.14	-20.37	6.45	0.06	nd	nd
Cameroon	C5	Nodule	Bulk	-45	-8.30	0.15	-7.60	0.09	0.10	-22.28	6.34	0.06	10.39	0.17
Cameroon	C6	Nodule	Bulk	-65	-6.84	0.09	-7.24	0.05	0.12	-23.32	5.12	0.16	9.52	0.04
Cameroon	C7	Nodule	Bulk	-85	-7.09	0.08	-7.49	0.04	0.09	-21.17	5.19	0.13	nd	nd
Cameroon	C8	Nodule	Bulk	-95	-9.36	0.13	-8.03	0.06	0.08	-23.05	6.55	0.09	11.05	0.24
Cameroon	C9	Nodule	Bulk	-105	-6.82	0.13	-7.23	0.05	0.17	-25.74	5.04	0.17	nd	nd
Cameroon	C10	Nodule	Bulk	-125	-8.11	0.13	-7.79	0.08	0.16	-24.22	5.83	0.08	8.18	0.19
Cameroon	TCF1-no	Nodule	Bulk		nd	nd	nd	nd	0.19	-21.22	nd	nd	nd	nd
Cameroon	TCF2-no	Nodule	Bulk		nd	nd	nd	nd	0.26	-21.70	nd	nd	nd	nd

Cameroon	F1-so	Soil	Bulk	-2.5	-6.50	0.04	-5.68	0.07	nd	nd	nd	nd	nd	nd
Cameroon	F4-so	Soil	Bulk	-20	-7.29	0.06	-5.73	0.08	nd	nd	nd	nd	nd	nd
Cameroon	F8-so	Soil	Bulk	-60	-8.03	0.16	-7.85	0.09	nd	nd	nd	nd	nd	nd
Cameroon	N1-so	Soil	Bulk	-2.5	-5.46	0.12	-3.99	0.11	0.10	-19.26	nd	nd	nd	nd
Cameroon	N4-so	Soil	Bulk	-20	-6.01	0.07	-3.30	0.09	nd	nd	nd	nd	nd	nd
Cameroon	N8-so	Soil	Bulk	-60	-6.53	0.13	-5.32	0.11	nd	nd	nd	nd	nd	nd
Cameroon	V1-so	Soil	Bulk	-2.5	-10.51	0.14	-4.95	0.16	0.49	-16.02	nd	nd	nd	nd
Cameroon	V4-so	Soil	Bulk	-20	-10.59	0.25	-5.09	0.23	nd	nd	nd	nd	nd	nd
Cameroon	V8-so	Soil	Bulk	-60	-9.94	0.18	-5.08	0.13	nd	nd	nd	nd	nd	nd
Cameroon	H1-so	Soil	Bulk	-2.5	nd	nd	nd	nd	0.12	-18.10	nd	nd	nd	nd
Burkina Faso	BF 69BE-to	Nodule	subsample	0	-12.87	0.04	-8.83	0.05	nd	nd	nd	nd	nd	nd
Burkina Faso	BF 69BE-to2	Nodule	subsample	0	-11.27	0.05	-8.23	0.05	nd	nd	nd	nd	nd	nd
Burkina Faso	BF 71-tob	Nodule	subsample	0	-9.98	0.09	-5.91	0.05	nd	nd	nd	nd	nd	nd
Burkina Faso	BF 71-ton	Nodule	subsample	0	-9.32	0.05	-7.99	0.05	nd	nd	nd	nd	nd	nd
Burkina Faso	BF 70	Nodule	subsample	0	-7.18	0.05	-7.04	0.02	nd	nd	nd	nd	nd	nd
Burkina Faso	BF 70-tob	Nodule	subsample	0	-8.71	0.10	-6.20	0.06	nd	nd	nd	nd	nd	nd
Burkina Faso	BF70-2-P1	Nodule	subsample	0	-6.64	0.15	-7.61	0.14	nd	nd	nd	nd	nd	nd
Burkina Faso	BF70-2-P2	Nodule	subsample	0	-8.14	0.11	-8.34	0.11	nd	nd	nd	nd	nd	nd
Burkina Faso	GPS70-bulk	Nodule	Bulk	0	-6.53	0.09	-7.59	0.13	nd	nd	4.85	0.02	nd	nd
Burkina Faso	BF72-1-P1	Nodule	subsample	0	-7.19	0.03	-7.22	0.07	nd	nd	nd	nd	nd	nd
Burkina Faso	BF72-1-P2	Nodule	subsample	0	-6.79	0.02	-7.27	0.04	nd	nd	nd	nd	nd	nd
Burkina Faso	BF72-2-P1	Nodule	subsample	0	-8.13	0.10	-7.89	0.11	nd	nd	nd	nd	nd	nd
Burkina Faso	GPS72-bulk	Nodule	Bulk	0	-7.07	0.10	-7.97	0.08	nd	nd	nd	nd	nd	nd
Burkina Faso	GPS72-bulk	Nodule	Bulk	0	-7.12	0.04	-8.28	0.06	nd	nd	6.25	0.04	nd	nd
Burkina Faso	BF C7-pi	Nodule	subsample	0	-9.07	0.07	-7.42	0.08	nd	nd	nd	nd	nd	nd
Burkina Faso	BF C7-gg	Nodule	subsample	0	-7.55	0.07	-5.42	0.06	nd	nd	nd	nd	nd	nd
Burkina Faso	GPS33-2-P1	Nodule	subsample	0	-7.97	0.02	-6.61	0.03	nd	nd	nd	nd	nd	nd
Burkina Faso	GPS33-bulk	Nodule	Bulk	0	-8.25	0.07	-7.13	0.10	nd	nd	nd	nd	nd	nd
Burkina Faso	GPS33-bulk	Nodule	Bulk	0	-7.87	0.05	-6.76	0.05	nd	nd	5.95	0.04	nd	nd
Burkina Faso	GPS-31	Nodule	Bulk	0	-5.51		-2.87		0.24	-20.81	nd	nd	nd	nd
Burkina Faso	GPS-31	Nodule	Bulk	0	-7.92		-2.86		0.11	-20.05	nd	nd	nd	nd
Niger	NG 01	Nodule	subsample	0	-10.80	0.06	-6.81	0.06	nd	nd	nd	nd	nd	nd
Niger	NG3-P1	Nodule	subsample	0	-11.28	0.06	-6.73	0.06	nd	nd	nd	nd	nd	nd
Niger	NG3-P2	Nodule	subsample	0	-11.41	0.02	-7.17	0.03	nd	nd	nd	nd	nd	nd
Niger	NG4-P1	Nodule	subsample	0	-11.26	0.03	-7.04	0.02	nd	nd	nd	nd	nd	nd
Niger	NG4-P2	Nodule	subsample	0	-11.48	0.04	-7.35	0.06	nd	nd	nd	nd	nd	nd
Niger	NG-bulk	Nodule	Bulk	0	-11.83	0.05	-7.83	0.10	nd	nd	5.56	0.01	nd	nd
Niger	NG-bulk	Nodule	Bulk	0	-11.63	0.03	-7.72	0.04	nd	nd	nd	nd	nd	nd
Niger	Niger	Nodule	Bulk	0	-10.80		-3.43		0.07	-23.25	nd	nd	nd	nd
Mali	ML1-P1	Nodule	subsample	0	-5.99	0.03	-6.54	0.05	nd	nd	nd	nd	nd	nd
Mali	ML1-P2	Nodule	subsample	0	-3.26	0.02	-7.28	0.04	nd	nd	nd	nd	nd	nd
Mali	ML-bulk	Nodule	Bulk	0	-3.71	0.02	-7.39	0.06	nd	nd	3.67	0.01	nd	nd
Mali	ML-bulk	Nodule	Bulk	0	-3.69	0.04	-7.27	0.06	nd	nd	nd	nd	nd	nd

E Eh-pH conditions in wetlands

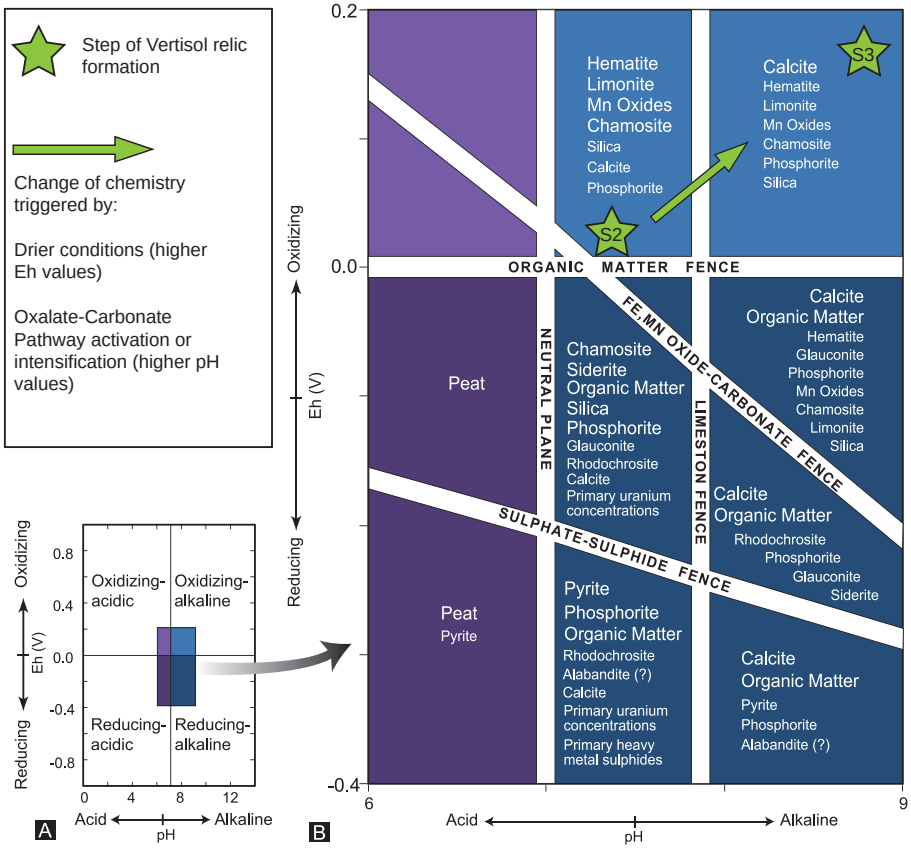

Figure E.1 – A) Ranges of Eh-pH conditions in wetlands (Asheley et al., 2013). B) Eh-pH conditions found in wetlands and related to organo-mineral stabilities. It is hypothesized that during Step 2 of Vertisol relic formation, the Eh-pH conditions were within the Hematite-Mn-oxide box, while the Eh-pH conditions during Step 3 were within the Calcite box. The reasons for a shift from Step 2 to Step 3 were a shift toward drier conditions triggering more oxidizing conditions (higher Eh) and activating the Oxalate-Carbonate Pathway (higher pH).

F Weathering and clay mineral stability

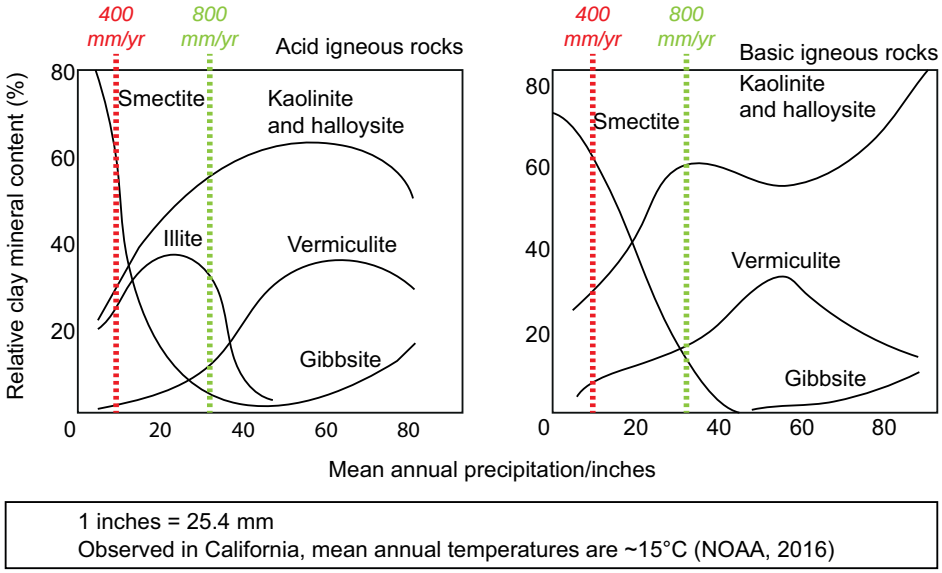

Figure F.1 – Domain of clay mineral stabilities according to mean annual precipitation and primary rock chemistry. These observations have been made by Barshad (1966) in California, where mean annual temperatures are ~15°C. For mean annual precipitation of 400 mm/yr (red), the amount favourable for dust stabilization (Kanemian), smectite is largely dominant (> 60%), and for mean annual precipitation of 800 mm/yr (green), the amount in the Diamare piedmont in the present-day, kaolinite-halloysite are favoured.

G OSL methodology

Table G.1 – Energies (MeV/Bq s^{-1}) emitted by alpha, beta and gamma events for the ^{238}U-series, ^{235}U-series and ^{232}Th-series (Guérin et al., 2011). The total of the energies are used in the calculations if the series are assumed to be in secular equilibrium. Otherwise, if daughter products are absent, their energies are removed from the total energy calculation and their loss accounted for in calculation of the k factor.

Energy (MeV/Bq s^{-1})			
Radiation event	α	β	γ
^{238}U	4.193	0.007	0.001
^{234}Th	-	0.059	0.008
^{234}Pam	-	0.81	0.016
^{234}Pa	-	0.001	0.001
^{234}U	4.759	0.012	0.001
^{230}Th	4.664	0.013	0.001
^{226}Ra	4.775	0.004	0.007
^{222}Rn	5.489	-	0
^{218}Po	6.001	-	-
^{214}Pb	-	0.291	0.239
^{214}Bi	0.001	0.654	1.475
^{214}Po	7.687	-	0
^{210}Pb	-	0.033	0.005
^{210}Bi	-	0.389	-
^{210}Po	5.304	0	0
Total	42.873	2.273	1.754

Energy (MeV/Bq s^{-1})			
Radiation event	α	β	γ
^{235}U	4.114	0.029	0.164
^{231}Th	-	0.146	0.023
^{231}Pa	4.924	0.032	0.04
^{227}Ac	0.07	0.012	0.001
^{227}Th	5.808	0.05	0.154
^{223}Fr	0.005	0	0.001
^{223}Ra	5.664	0.068	0.135
^{219}Rn	6.753	0.007	0.058
^{215}Po	7.392	-	-
^{211}Pb	-	0.45	0.064
^{211}Bi	6.549	0.013	0.047
^{211}Po	0.021	-	-
^{207}Tl	-	0.495	0.002
Total	41.3	1.302	0.689

Energy (MeV/Bq s^{-1})			
Radiation event	α	β	γ
^{232}Th	4.003	0.0113	0.0011
^{228}Ra	-	0.0092	0.0004
^{228}Ac	-	0.4171	0.8602
^{228}Th	5.406	0.0195	0.0031
^{224}Ra	5.673	0.0023	0.0104
^{220}Rn	6.288	-	0.0006
^{216}Po	6.778	-	0
^{212}Pb	-	0.1721	0.1437
^{212}Bi	2.175	0.5034	0.1039
^{212}Po	5.631	-	-
^{208}Tl	-	0.214	1.2136
Total	35.954	1.3489	2.337

Table G.2 – Energies E_x (MeV/Bq s^{-1}) and calculated k_x factors for decay chains of the element x, either considering equilibrium (black) or disequilibrium (i.e. assuming loss of daughters; grey) scenarios.

	Decay-event	E_x (MeV/Bq s^{-1})	k factor
^{238}U	α	42.87	0.036
	β	2.27	0.01
	γ	1.75	0.009
^{238}U	α	4.19	0.003
	β	0.88	0.004
	γ	0.03	0.0001
^{234}U	α	4.76	0.004
	β	0.01	0.0001
	γ	0.001	0.00001
^{235}U	α	41.3	0.0003
	β	1.3	0.00004
	γ	0.69	0.00002
^{232}Th	α	35.95	0.035
	β	1.35	0.006
	γ	2.34	0.012

Table G.3 – Attenuated dose rates for each component and scenario. The effectiveness of α-radiation is corrected using an a-value of 0.11±0.03 according to Balescu and Lamothe (1993). The water content is estimated to be 10±2%. A ($^{234}U/^{238}U$) activity ratio of 1.31 is used (Violette et al., 2010) for the disequilibrium scenario.

	State	Element	Radiation event	Attenuated dose rate (Gy ka^{-1})
Soil	Equilibrium	U	α	0.23
			β	0.55
			γ	0.48
		Th	α	0.34
			β	0.47
			γ	0.98
		K	β	2
			γ	0.65
		Rb	β	0.02
Nodule	Equilibrium	U	α	0.29
			β	0.68
			γ	0.59
		Th	α	0.1
			β	0.14
			γ	0.29
		K	β	0.5
			γ	0.16
		Rb	β	0.01
	24% Equilibrium	U	α	0.07
			β	0.16
			γ	0.14
	76% Disequilibrium	U	α	0.06
			β	0.02
			γ	0.002

Table G.4 – Luminescence data for nodules NO1 and NO2 and calculated OSL ages for the two scenarios (1 = equilibrium and 2 = disequilibrium) for different T_2 durations (ka). The maximum carbonate nodule age (T_2 = Max) is equal to the OSL age depending on the scenario. An activity ratio ($^{234}U/^{238}U$) of 1.31 was chosen according to the study of Violette et al. (2010). $pIRIR_{225}$ ages are not corrected for fading.

Sample	t_2 (ka BP)	D_e	Scenario 1			Scenario 2		
			$D_{e,no}$ (Gy)	$D_{e,so}$ (Gy)	Age (ka)	$D_{e,no}$ (Gy)	$D_{e,so}$ (Gy)	Age (ka)
NO1	Max	88.44±0.99	88.44	0	22.6±1.5	88.44	0	27.2±1.8
	15		58.73	29.70	20.1±1.4	48.75	39.68	21.8±1.5
	14		54.82	33.62	19.8±1.3	45.50	42.93	21.4±1.4
	13		50.90	37.53	9.5±1.3	42.25	46.18	20.90±1.4
	12		46.98	41.45	19.1±1.3	39.00	49.43	20.5±1.4
	11		43.07	45.36	18.8±1.3	35.75	52.6	20.1±1.4
	10		39.15	49.28	18.5±1.2	32.50	55.9	19.6±1.3
	9		35.24	53.20	18.2±1.2	29.25	59.18	19.2±1.3
	8		31.32	57.11	17.8±1.2	26.00	62.43	18.7±1.3
	7		27.40	61.03	17.5±1.2	22.75	65.68	18.3±1.2
	6		23.49	64.94	17.2±1.2	19.50	68.93	17.9±1.2
	5		19.57	68.86	16.8±1.1	16.25	72.18	17.4±1.2
	4		15.66	72.77	16.5±1.1	13.00	75.43	17.0±1.1
	3		11.74	76.69	16.2±1.1	9.75	78.68	16.5±1.1
	2		7.83	80.60	15.9±1.1	6.50	81.93	16.1±1.1
	1		3.91	84.52	15.5±1.1	3.25	85.18	15.7±1.1
	0		0	88.44	15.2±1.0	0	88.44	15.2±1.0
NO2	Max	90.46±1.07	90.46	0	22.8±1.5	90.46	0	27.0±1.8
	15		59.39	31.06	20.4±1.4	50.19	40.26	22.0±1.5
	14		55.43	35.02	20.1±1.4	46.85	43.60	21.6±1.5
	13		51.47	38.98	19.8±1.3	43.50	46.95	21.2±1.4
	12		47.51	42.94	19.5±1.3	40.15	50.30	20.8±1.4
	11		43.55	46.90	19.2±1.3	36.81	53.64	20.4±1.4
	10		39.59	50.86	18.9±1.3	33.46	56.99	19.9±1.3
	9		35.63	54.82	18.6±1.3	30.11	60.34	19.5±1.3
	8		31.67	58.78	18.3±1.2	26.77	63.68	19.1±1.3
	7		27.71	62.74	17.9±1.2	23.42	67.03	18.7±1.3
	6		23.75	66.70	17.6±1.2	20.07	70.38	18.3±1.2
	5		19.79	70.66	17.3±1.2	16.73	73.72	17.9±1.2
	4		15.83	74.62	17.0±1.1	13.38	77.07	17.4±1.2
	3		11.87	78.58	16.7±1.1	10.03	80.42	17.0±1.1
	2		7.91	82.54	16.4±1.1	6.69	83.76	16.6±1.1
	1		3.95	86.50	16.1±1.1	3.34	87.11	16.2±1.1
	0		0	90.46	15.8±1.1	0	90.46	15.8±1.1

H OSL results from carbonate nodules

H.1 Luminescence data

The natural luminescence signal of K-feldspar is bright and typical decay curves for paired measurements at 50°C and 225°C and associated dose response curves are showed in Figure H.1A and H.1B, respectively (sample H6). For each sample, 12 to 24 small aliquots were measured to emphasize the variability within a sample, assessed by the overdispersion (OD). The natural equivalent dose (s) of an aliquot is assessed with the dose response curve. This value is then multiplied by the dose rate of the Risø reader (≈ 0.1 Gy s^{-1}) to obtain the final D_e value. According to the overdispersion (OD) of the D_e of a sample, the central age model (OD <20%) or the maximum age model (OD >20%) was applied. The results are showed in Table H.1. For all samples and both signals, the OD values are below 20% except for the IR_{50} signal of sample H0. The D_e value for this sample was thus also assessed with the maximum age model (H0b). A general trend is observable for both signals showing an increase of the D_e values with depth, from 23.4 Gy to 56.6 Gy (IR_{50}) and from 50.4 Gy to 88.1 Gy ($pIRIR_{225}$). The increase is weaker since sample H6, ~10 Gy above H6 and ~2 Gy below. Samples H8 and G12 are out of the trend with slightly lower values. The $IR_{50}/pIRIR_{225}$ ratio values range from 0.66 and 0.67 for samples H2, E5 and H6. They are lower for samples H8, H10, H11 and G14, and range from 0.62 to 0.64. The ratio value for sample G12 is 0.59, and finally, for sample H0, the value is 0.40 or 0.46 according to the D_e values calculated, i.e. with central age model and maximum age model respectively. These values are illustrated in Figure H.1C, and generally, the samples are distributed along the 0.6 line except for sample H0 falling between the 0.6 and 0.4 lines. To validate the SAR protocol used, the residual doses after 6 hours of sunlight exposure are in average 0.62±0.30 Gy for the IR_{50} signal and 1.88±0.49 Gy for the $pIRIR_{225}$ signal. The recovery ratio values are 1.0±0.01 and 0.98±0.02 for the IR_{50} and the $pIRIR_{225}$ signals, respectively. The g_{2days} values for the IR_{50} signal range from 3 to 4 %/dec for samples H0, H2 and E5, from 4 to 5 %/dec for samples H6, H8, G12, H11 and G14, and is up to 5.9±1.0 %/dec for sample H10. For the $pIRIR_{225}$ signal, g_{2days} values are <1 %/dec for samples H11 and G14, are from 1 to 2 %/dec for samples H0, H2, E5 and G12, and are >2 %/dec for samples H6 (2.9±0.2 %/dec), H8 (3.1±0.9 %/dec) and H10 (2.3±1.6 %/dec).

The environmental dose rate ($\dot{D}$Ãá) around primary minerals evolved through time, due to chemical changes induced by carbonate nodule formation. The effect of these changes was studied in detail and is explained in Diaz et al., 2016b. It is thus necessary to distinguish the soil external dose rate (i.e $\dot{D}_{ext1}$ during T_1) from the carbonate nodule external dose rate (i.e $\dot{D}_{ext2}$ during T_2). The first is the same for all samples but the second one is proper to each sample, as it takes into account the γ-rays emitted

by radionuclides composing the soil, and this is related to the nodule diameter (Aitken, 1985, Diaz et al., 2016b). Finally, the $\dot{D}_{int}$ is similar for each sample as well. The sum of the $\dot{D}_{ext1}$ during T_1 and the $\dot{D}_{int}$ represents the $\dot{D}_{so}$, and sum of $\dot{D}_{ext2}$ during T_2 and the $\dot{D}_{int}$ represents the $\dot{D}_{no}$. The $\dot{D}_{int}$ value is 0.45±0.09 Gy ka^{-1}, the soil $\dot{D}_{ext1}$ is 5.11±0.34 Gy ka^{-1} and the nodule $\dot{D}_{ext2}$ ranges from 3.33 to 3.36 Gy ka^{-1}.

Table H.2 shows the results from Equ. 5.16-5.17 (chapter 5), the resulted OSL ages are still uncorrected by anomalous fading. The $D_{e,so}$ of sample H0 for the IR_{50} signal is negative (-2.1 Gy). The ages range from 6.0 ka to 11.9 ka BP (IR_{50}) and from 10.6 to 17.5 ka BP ($pIRIR_{225}$). Fading-corrected IR_{50} ages range from 7.6 ka to 17.4 ka. Younger ages are at the surface for H0, H2 and E5 with ages <14.0 ka. From sample H6, the ages are >14 ka except for sample H8 (13.9 ka). The fading-uncorrected and fading-corrected $pIRIR_{225}$ ages are older than fading-corrected IR_{50} ages, except for sample H10, whose fading-uncorrected $pIRIR_{225}$ age is 0.5 ka younger. Although for fading-uncorrected $pIRIR_{225}$ ages the deviation from fading-corrected IR_{50} ages is within 10% (Fig. H.1D). The deviation is >10% for fading-corrected $pIRIR_{225}$ ages. For uncorrected $pIRIR_{225}$ ages, the trend with depth follows IR_{50} ages, however they range from 10.6 ka to 17.5 ka. Corrected $pIRIR_{225}$ ages range from 11.7 ka to 19.8 ka, with ages <17 ka from H0 to E5 and >17 ka until sample H6.

H.2 Adequate luminescence age used in the interpretations

OSL ages are challenging to assessed in the carbonate nodule context, as showed by the large variability when using the IR_{50} or the $pIRIR_{225}$ signal (Fig. H.1D). However, the $IR_{50}/pIRIR_{225}$ ratio values of the samples are distributed on the same line (0.6) suggesting that the difference between both signals is induced by different anomalous fading, rather than partial bleaching (Fig. H.1C). This is confirmed by OD values, which are <15% (Table H.1). The exception is sample H0. The higher OD and lower $IR_{50}/pIRIR_{225}$ ratio suggest that the sample is affected by post-depositional partial bleaching. This explanation is supported by the results obtained for the experiment comparing the luminescence signals from the minerals located in the border (external) and in the centre (internal) of a nodule (Diaz et al., 2016b). The OD and $IR_{50}/pIRIR_{225}$ ratio of sample H0 are similar to values measured for external minerals. On the contrary, the values of the others samples are close to those measured for internal minerals. Sample H0 was brought at the soil surface by later erosion processes, and thus was longer exposed to sunlight than other samples. Even the minerals from the core are affected by post-depositional partial bleaching and thus the maximum age model was used to calculate the D_e value (Olley et al., 1996). However, the calculation of H0 IR_{50} $D_{e,so}$ giving a negative value (-2.1 Gy) suggests that in addition to fading loss, a part of the signal is still lost by post-deposition partial bleaching. This effect is less important for the $pIRIR_{225}$ signal. Consequently, the OSL ages of H0 are underestimated, but this underestimation is higher for the IR_{50} age than the $pIRIR_{225}$ age. Finally, the fading correction of the IR_{50} ages gets them closer to the $pIRIR_{225}$ ages at 10% within uncertainties, but fading-corrected $pIRIR_{225}$ ages deviate > 10% from the fading-corrected IR_{50} ages (Fig. H.1D). We discussed above that we should not have an issue with post-deposition partial bleaching, except for H0, thus this should not explain the difference between IR_{50} and $pIRIR_{225}$ ages. The anomalous fading is very difficult to assess in the laboratory (Wallinga et al., 2007), it is thus possible that this deviation is related to the poor accuracy of g_{2days} values measurement. Nevertheless, beyond these uncertainties and the reasons behind these disagreements, all ages are related to the stratigraphic period of the Kanemian. Consequently, a numerical chronology for mima-like mound formation can still be proposed and according to the discussion above, fading-uncorrected $pIRIR_{225}$ ages are used for the palaeo-environmental interpretations.

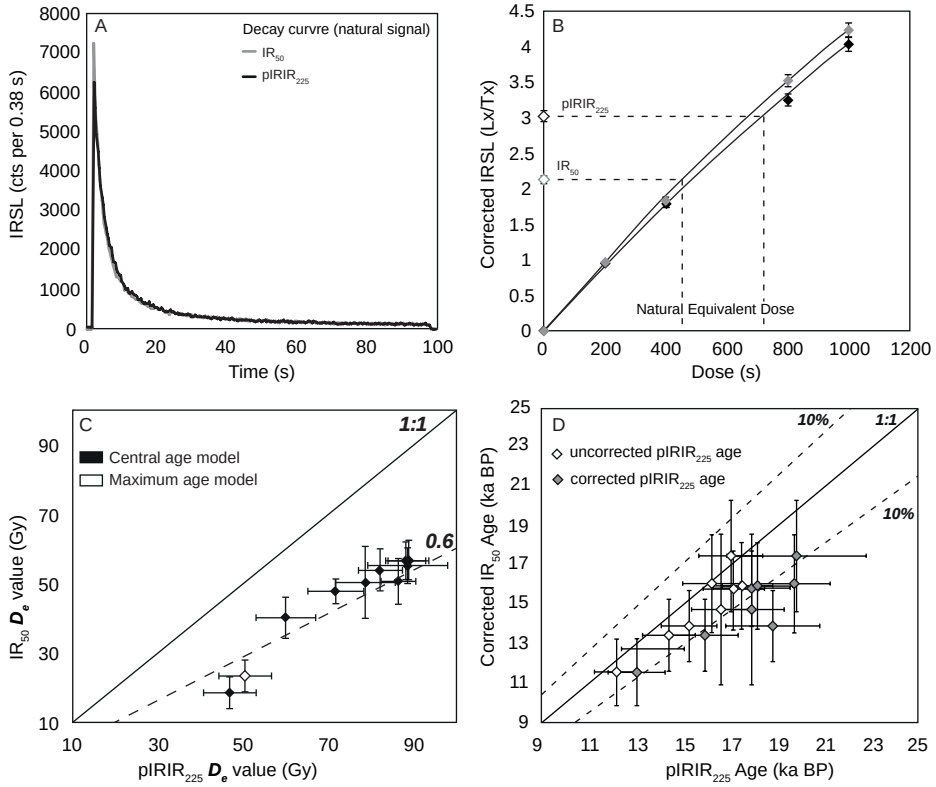

Figure H.1 – A) Typical curve response dose for a sample, B) Typical calibration curve (black diamonds) and natural equivalent dose of a sample (white diamond), C) IR_{50} D_e values as a function of the $pIRIR_{225}$ D_e values, the dashed line represents the $IR_{50}/pIRIR_{225}$ ratio value of 0.6, D) comparison of fading-corrected IR_{50} ages with $pIRIR_{225}$ ages not fading-corrected (white diamonds) and with fading-corrected (grey diamonds). The dashed lines represent the 10% error margins.

Table H.1 – Luminescence data for the nodules.

		IR_{50}		$pIRIR_{225}$		
	Depth (cm)	D_e (Gy)	OD (%)	D_e (Gy)	OD (%)	$IR_{50}/pIRIR_{225}$
H0a	0	18.5±4.5	23±1	46.8±6.1	11±0.7	0.4
H0b	0	23.4±4.5	23±1	50.4v6.1	11±0.7	0.46
H2	23.5	40.2±5.9	14±0.4	59.9±7.0	9±0.3	0.67
E5	43	47.8±3.6	6±0.5	71.7±6.5	7±0.6	0.67
H6	71	54.0±5.9	10±0.7	82.1±5.1	3±0.6	0.66
H8	81	50.4±10.2	16±1	78.6±6.7	7±0.6	0.64
H10	101	55.2±5.0	7±0.6	88.6±9.2	9±0.7	0.62
G12	105	50.7±6.5	11±0.7	86.4±4.4	0	0.59
H11	111	56.6±5.8	9±0.6	88.8±4.7	2±0.8	0.64
G14	125	56.6±5.3	7±0.6	88.1±4.6	0	0.64

Table H.2 – OSL Ages calculated for the equilibrium scenario

	Environmental dose rate			IR_{50}			$pIRIR_{225}$		
	$\dot{D}_{int}$ (Gy ka^{-1})	$\dot{D}_{ext1}$ (Gy ka^{-1})	$\dot{D}_{ext2}$ (Gy ka^{-1})	$D_{e,no}$ (Gy)	$D_{e,so}$ (Gy)	Age (ka)	$D_{e,no}$ (Gy)	$D_{e,so}$ (Gy)	Age (ka)
H0b	0.45±0.09	5.11±0.34	3.33±0.34	25.6	-2.1	6.0±1.3	25.6	24.8	10.6±1.1
H2	0.45±0.09	5.11±0.34	3.35±0.34	25.4	14.8	8.8±1.0	25.4	34.6	12.2±0.9
E5	0.45±0.09	5.11±0.34	3.33±0.34	25.8	22	10.3±1.1	25.8	45.9	14.4±1.1
H6	0.45±0.09	5.11±0.34	3.33±0.34	25.2	28.7	11.3±1.3	25.2	56.9	16.2±1.2
H8	0.45±0.09	5.11±0.34	3.33±0.34	20.3	30.1	10.4±1.3	20.3	58.3	15.3±1.2
H10	0.45±0.09	5.11±0.34	3.33±0.34	20.6	34.7	11.2±1.3	20.6	68	17.0±1.4
G12	0.45±0.09	5.11±0.34	3.36±0.34	20.1	30.6	10.4±1.4	20.1	66.3	16.6±1.2
H11	0.45±0.09	5.11±0.34	3.33±0.34	25.9	30.6	11.9±1.4	25.9	62.9	17.5±1.3
G14	0.45±0.09	5.11±0.34	3.36±0.34	23.2	33.4	11.7±1.3	23.2	64.9	17.2±1.3

I Radiocarbon Ages

Table I.1 – Radiocarbon ages obtained in this study.

	Profile	Type	Depth cm	C^{14} age BP	$\pm 1\sigma$	cal BC from	to	%	cal BP from	to	%	cal BP mean	err	$\delta^{13}C$
C2	Site 2012	Carbonate	0	6029	33	5014	4835	95.4	6964	6785	95.4	6874.5	126.6	-9.5
X0	Big nodule	Carbonate	0	6220	31	5301	5060	95.4	7251	7010	95.4	7130.5	170.4	-8.2
G0	H	Carbonate	0	5521	30	4450	4330	95.4	6400	6280	95.4	6340	84.9	-8.8
H2	H	Carbonate	-7.5	5434	30	4345	4240	95.4	6295	6190	95.4	6242.5	74.2	-8.8
H2	H	Organic Matter	-7.5	7971	32	7045	6708	95.4	8995	8658	95.4	8826.5	238.3	-42.1
E5	E	Carbonate	-35	5662	31	4560	4440	92.1	6510	6390	92.1	6450	84.85	-12.3
H6	H	Carbonate	-45	5527	32	4450	4330	95.4	6400	6280	95.4	6340	84.9	-20.1
H6	H	Organic Matter	-45	9236	35	8562	8322	95.4	10512	10272	95.4	10392	169.7	-23.7
H8	H	Carbonate	-65	4447	29	3332	3010	93.8	5282	4960	93.8	5121	227.7	-6.2
H8	H	Organic Matter	-65	8554	34	7601	7541	95.4	9551	9491	95.4	9521	42.4	-23.3
H10	H	Carbonate	-85	4557	29	3371	3107	94.4	5321	5057	94.4	5189	186.6	-9.9
H11	H	Carbonate	-95	5747	30	4690	4504	95.4	6640	6454	95.4	6547	131.5	-12.8
H11	H	Organic Matter	-95	9706	36	9272	8937	95.4	11222	10887	95.4	11054.5	236.9	-31.3
G12	G	Carbonate	-105	4420	29	3266	2921	93.2	5216	4871	93.2	5043.5	244.0	-8
G14	G	Carbonate	-125	5106	30	3968	3800	95.4	5918	5750	95.4	5834	118.8	-9.9
G14	G	Organic Matter	-125	7362	33	6361	6094	95.4	8311	8044	95.4	8177.5	188.8	-23.6
Artemis 2.2	N	Carbonate	-30	6150	30	5210	5009	95.4	7160	6959	95.4	7059.5	100.5	-13.5
Artemis 2.2	N	Organic Matter	-30	8330	80	7551	7143	95.4	9501	9093	95.4	9297	204	-19.1
Artemis 2.3	N	Carbonate	-60	275	30	1514	1789	95.4	436	161	95.4	298.5	137.5	-5.2
Artemis 3.1	Site 2012	Carbonate	0	5265	30	4230	3987	95.4	6180	5937	95.4	6058.5	121.5	-12.2
Artemis 3.2	Site 2012	Carbonate	-30	975	30	1013	1155	95.4	937	795	95.4	866	71	-8.3
Artemis 3.3	Site 2012	Carbonate	-100	8915	45	8251	7951	95.4	10201	9901	95.4	10051	150	-0.5
Artemis 3.3	Site 2012	Organic Matter	-100	11700	70	11776	11456	95.4	13726	13406	95.4	13566	160	-15.9
Artemis 4.1	Vertisol	Carbonate	0	5285	30	4232	4000	95.4	6182	5950	95.4	6066	116	-6.7
Artemis 4.2	Vertisol	Carbonate	-30	3965	30	2573	2348	95.4	4523	4298	95.4	4410.5	112	-7.7
Artemis 4.3	Vertisol	Carbonate	-60	3125	30	1492	1297	95.4	3442	3247	95.4	3344.5	97	-8.12
Artemis 4.3	Vertisol	Organic Matter	-60	7725	45	6640	6473	95.4	8590	8423	95.4	8506.5	83	-17
N1	G	grey part	-90	5797	27	4717	4556	95.4	6667	6506	95.4	6586.5	113	-13
N2	G	external part	-90	5754	27	4690	4533	95.4	6640	6483	95.4	6561.5	111	-15.1
N3	G	reddish part	-90	5724	27	4682	4492	95.4	6632	6442	95.4	6537	134	-14.5

Table I.2 – Compilation of inorganic radiocarbon ages. The calibration was made with oxcal, IntCal13

Sample	Area	Age (BP)	Range Age cal BC		Range Age cal BP		Mean	Reference
Kosselilli	Chad	8570±210	8242	7145	10192	9095	9644±549	Bocquier (1973, p.263)
Kosselilli	Chad	2710±160	1263	416	3213	2366	2790±424	
Mindera	Chad	8665±240	8342	7143	10292	9093	9693±600	
Mindera	Chad	1780±95	22	528	1972	2478	2225±253	
Figuil	Cameroon	8400±110	7601	7141	9551	9091	9321±230	Marliac (1973, p.95)
Figuil	Cameroon	14720±200	16467	15498	18417	17448	17933±485	
Figuil	Cameroon	15320±210	17051	16121	19001	18071	18536±465	
Figuil	Cameroon	8690±110	8200	7548	10150	9498	9824±326	
Figuil	Cameroon	7030±100	6076	5718	8026	7668	7847±179	in Maley (1981, p.187)
Figuil	Cameroon	6450±90	5610	5227	7560	7177	7369±192	
Adoumri	Cameroon	10100±230	10601	9202	12551	11152	11852±700	
Koutoukalé	Niger	5780±60	4777	4496	6727	6446	6587±141	Taupin (2003)
Koutoukalé	Niger	6680±60	5707	5510	7657	7460	7559±99	
Koutoukalé	Niger	6535±80	5626	5344	7576	7294	7435±141	

Namardé G.	Niger	1750±50	-138	-394	1812	1556	1684±128	
Namardé G.	Niger	1910±70	85	-318	2035	1632	1834±202	
Km85	Niger	3610	70±2195	1767	4145	3717	3931±214	
Km85	Niger	3670	60±2206	1890	4156	3840	3998±158	
Km85	Niger	3770	70±2458	1984	4408	3934	4171±237	
Tillabéri	Niger	5940±70	5006	4619	6956	6569	6763±194	
Tillabéri	Niger	5470±80	4464	4057	6414	6007	6211±204	
Tillabéri	Niger	6000±100	5209	4691	7159	6641	6900±259	
Tillabéri	Niger	5320±120	4444	3813	6394	5763	6079±316	
Tillabéri	Niger	7550±200	7022	6017	8972	7967	8470±503	
Tillabéri	Niger	7100±90	6207	5773	8157	7723	7940±217	
C2	Cameroon	6029±33	4992	4782	6942	6732	6837±105	This study
X0	Cameroon	6220±31	5226	5001	7176	6951	7064±113	
G0	Cameroon	5521±30	4444	4250	6394	6200	6297±97	
H2	Cameroon	5434±30	4339	4071	6289	6021	6155±134	
E5	Cameroon	5662±31	4526	4361	6476	6311	6394±83	
H6	Cameroon	5527±32	4446	4257	6396	6207	6302±95	
H8	Cameroon	4447±29	3316	2911	5266	4861	5064±203	
H10	Cameroon	4557±29	3357	3097	5307	5047	5177±130	
H11	Cameroon	5747±30	4679	4457	6629	6407	6518±111	
G12	Cameroon	4420±29	3093	2908	5043	4858	4951±93	
G14	Cameroon	5106±30	3961	3775	5911	5725	5818±93	
U11	Cameroon	14709±39	16101	15782	18051	17732	17892±160	
S8	Cameroon	1496±23	536	635	2486	2585	2536±50	
W14	Cameroon	7908±28	7023	6653	8973	8603	8788±185	
S19	Cameroon	4950±25	3778	3660	5728	5610	5669±59	
S23	Cameroon	14305±38	15650	15292	17600	17242	17421±179	
Diaz/Dietrich 1.1	Cameroon	5710±30	4668	4461	6618	6411	6515±146	
Diaz/Dietrich 1.2	Cameroon	5465±30	4358	4260	6308	6210	6259±69	
Diaz/Dietrich 1.3	Cameroon	5880±30	4827	4692	6777	6642	6710±95	
Diaz/Dietrich2.1	Cameroon	5250±30	4229	3977	6179	5927	6053±178	
Diaz/Dietrich 2.2	Cameroon	6150±30	5210	5009	7160	6959	7060±142	
Diaz/Dietrich 2.3	Cameroon	275±30	1514	1789	436	161	299±194	
Diaz/Dietrich 3.1	Cameroon	5265±30	4230	3987	6180	5937	6059±172	
Diaz/Dietrich 3.2	Cameroon	975±30	1013	1155	937	795	866±100	
Diaz/Dietrich 3.3	Cameroon	8915±45	8251	7951	10201	9901	10051±212	
Diaz/Dietrich 4.1	Cameroon	5285±30	4232	4000	6182	5950	6066±164	
Diaz/Dietrich 4.2	Cameroon	3965±30	2573	2348	4523	4298	4411±159	
Diaz/Dietrich 4.3	Cameroon	3125±30	1492	1297	3442	3247	3345±138	

J Luminescence ages compilation for Chad Basin

Table J.1 – Compilation of luminescence ages from different sediments within the Chad Basin.

Area	Site	Code sample	Longitude	Latitude	Depth (m)	Dating Methode	Age (ka)	Error (ka)	Remarks	Source	Sample Type
Nigeria	Manga Grasslands	970/1	11°01'E	13°18'N	1.5	OSL	4.34	0.41	Barchanoid dune	Holmes et al 1999	Dune
		970/1A	11°01'E	13°18'N	1.3	OSL	5.3	0.26	Barchanoid dune		Dune
		970/2	11°01'E	13°18'N	4.5	OSL	6.51	0.8	Barchanoid dune		Dune
		970/3	11°01'E	13°18'N	7	OSL	4.95	0.41	Barchanoid dune		Dune
		971/1	11°01'E	13°22'N	1.5	OSL	5.51	0.36	Sandy interdune depression		Dune
		973/1	10°55'E	13°15'N	5	OSL	6.65	0.37	Barchanoid ridge		Dune
		973/2	10°55'E	13°15'N	2	OSL	9.98	0.45	Barchanoid ridge		Dune
		974/3	10°55'E	13°16'N	1.5	OSL	6.8	0.4	Playa sand sheet		Dune
		974/3	10°55'E	13°16'N	1	OSL	0.21	0.09	Playa sand sheet		Dune
		975/1	10°55'E	13°16'N	2	OSL	1.27	0.15	Barchan dune		Dune
		975/2	10°55'E	13°16'N	1	OSL	0.17	0.03	Barchan dune		Dune
		976/1	10°55'E	13°17'N	1.8	OSL	1.7	0.12	Transverse duneform		Dune
		978/1	11°49'E	13°02'N	2.2	OSL	2.2	0.2	Barchanoid dune		Dune
		980/1	10°40'E	13°20'N	1.4	OSL	5.25	0.31	Deflating barchanoid		Dune
		981/1	10°40'E	13°18'N	1.6	OSL	3.24	0.21	Proto-linear dune		Dune
Nigeria	Damasak NW	Dk NW-1	12°21'25.97"E	13° 0'56.03"N	2.25	OSL	2.9	0.2	alluvium	Gunmio and Preusser 2007	Alluvium
	Damasak NW	Dk NW-2	12°21'25.97"E	13° 0'56.03"N	3.25	OSL	2.7	0.1	alluvium		Alluvium
	Damasak W	Dk W-1	12°20'55.28"E	13° 1'48.58"N	1.25	OSL	4.8	0.4	alluvium		Alluvium
	Damasak W	Dk W-2	12°20'55.28"E	13° 1'48.58"N	2.25	OSL	11.8	0.9	alluvium		Alluvium
	Damasak W	Dk W-3	12°20'55.28"E	13° 1'48.58"N	3.25	OSL	11.7	1.1	alluvium		Alluvium
	Damasak W	Dk W-4	12°20'55.28"E	13° 1'48.58"N	4.25	OSL	9.4	0.3	alluvium		Alluvium
	Damasak W	Dk W-5	12°20'55.28"E	13° 1'48.58"N	5.25	OSL	11.8	0.6	alluvium		Alluvium
	Geidam S	G S-1	11°54'24.09"E	12°50'43.12"N	0.85	OSL	5.7	0.3	alluvium		Alluvium
	Geidam S	G S-2	11°54'24.09"E	12°50'43.12"N	1.85	OSL	6	0.3	alluvium		Alluvium
	Geidam S	G S-3	11°54'24.09"E	12°50'43.12"N	2.85	OSL	5.8	0.4	alluvium		Alluvium
	Gumsa NE	Gu NE-1	11°50'40.80"E	12°38'20.86"N	3.5	OSL	17.4	1	alluvium		Alluvium
	Gumsa NE	Gu NE-1g	11°50'40.80"E	12°38'20.86"N	3.5	OSL	10.8	0.3	alluvium		Alluvium
	Geidam SW	G SW-1	11°49'36.51"E	12°51'4.55"N	0.85	OSL	8.6	0.5	alluvium		Alluvium
	Geidam SW	G SW-2	11°49'36.51"E	12°51'4.55"N	1.85	OSL	11.2	0.5	alluvium		Alluvium
	Geidam SW	G SW-3	11°49'36.51"E	12°51'4.55"N	2.85	OSL	1.7	0.1	alluvium		Alluvium
	Geidam SW	G SW-4	11°49'36.51"E	12°51'4.55"N	3.85	OSL	7.8	0.8	alluvium		Alluvium
	Geidam SW	G SW-5	11°49'36.51"E	12°51'4.55"N	4.85	OSL	12.5	0.6	alluvium		Alluvium
	Geidam W n	G W-1	11°55'5.35"E	12°53'17.39"N	2.3	OSL	5.9	0.2	alluvium		Alluvium
	Geidam W s	G W-1g	11°55'5.35"E	12°53'17.39"N	2.3	OSL	6.3	0.2	alluvium		Alluvium
	Geidam W s	G W-2	11°55'5.35"E	12°53'17.39"N	2.3	OSL	6.2	0.4	alluvium		Alluvium
	Geidam W s	G W-2g	11°55'5.35"E	12°53'17.39"N	3.5	OSL	7.5	0.2	alluvium		Alluvium
	Geidam W n	G W-3	11°55'5.35"E	12°53'17.39"N	3.5	OSL	12.6	0.7	alluvium		Alluvium
	Geidam W n	G W-4	11°55'5.35"E	12°53'17.39"N	4.5	OSL	21.5	2	alluvium		Alluvium
	Geidam W n	G W-4g	11°55'5.35"E	12°53'17.39"N	9	OSL	12.9	1.2	alluvium		Alluvium
Nigeria	Bama Ridge	BR5B	13° 9'0.89"E	11°50'4.53"N	16.5	OSL	26.4	9.3	Medium sand	Abafoni et al 2014	Sand Ridge
		BRSC	13° 9'0.89"E	11°50'4.53"N	15.3	OSL	24.8	7.3	very coarse sand		Sand Ridge
		BR5D	13° 9'0.89"E	11°50'4.53"N	14	OSL	21.8	3.1	granule		Sand Ridge
		BR5E	13° 9'0.89"E	11°50'4.53"N	13.4	OSL	35.2	3.4	very coarse sand		Sand Ridge
		BR5F	13° 9'0.89"E	11°50'4.53"N	12.1	OSL	29.8	3.4	fine sand		Sand Ridge
		BR5G	13° 9'0.89"E	11°50'4.53"N	10.4	OSL	18.4	1.5	very fine sand		Sand Ridge
		BR5H	13° 9'0.89"E	11°50'4.53"N	8	OSL	7.2	0.63	fine sand		Sand Ridge
		BR5I	13° 9'0.89"E	11°50'4.53"N	6	OSL	9.6	0.7	Medium sand		Sand Ridge
		BR5J	13° 9'0.89"E	11°50'4.53"N	5.4	OSL	6.1	0.54	fine sand		Sand Ridge
		BR5	13° 9'0.89"E	11°50'4.53"N	5	OSL	6.3	0.56	fine sand		Sand Ridge
		BR3	13° 9'0.89"E	11°50'4.53"N	4	OSL	4.1	0.37	fine sand		Sand Ridge
		IBRK	13° 9'0.89"E	11°50'4.53"N	4.6	OSL	6.6	0.64			Sand Ridge
		2BRK	13° 9'0.89"E	11°50'4.53"N	9.5	OSL	9.3	0.58			Sand Ridge
		IBRM	13° 9'0.89"E	11°50'4.53"N	2	OSL	3.3	0.31			Sand Ridge
		2BRM	13° 9'0.89"E	11°50'4.53"N	4.4	OSL	7.1	0.5			Sand Ridge
		CFRM7	13° 9'0.89"E	11°50'4.53"N	4.4	OSL	17.8	2.1			Sand Ridge
		CFRM8	13° 9'0.89"E	11°50'4.53"N	1.2	OSL	4.6	0.8			Sand Ridge

		CFRM11	13° 9'0.89"E	11°50'4.53"N	4.9	OSL	38.2	5.2			Sand Ridge
		CFRM10A	13° 9'0.89"E	11°50'4.53"N	5	OSL	38	4.7			Sand Ridge
		CFRM10B	13° 9'0.89"E	11°50'4.53"N	4.1	OSL	35.9	7.5	Note GPS is for Maiduguri		Sand Ridge
Nigeria	Paleo-Bama Ridge	NG22?	12°23'40.19"E	12°19'29.83"N nd		OSL	125	nd	Drake et al 2011	Sand Ridge	
	Paleo-Bama Ridge	NG24	12°27'46.34"E	12°21'23.16"N	nd	OSL	114	nd			Sand Ridge
Nigeria	Bama Ridge	NG12	12°49'5.60"E	12° 8'0.90"N	5	OSL	8.6	0.7	Beach ridge fluvial sediment	Armitage et al 2015	Alluvium
		NG11	13° 1'3.70"E	11°56'24.80"N	5	OSL	9.4	0.9	Beach Ridge sands		Sand Ridge
		NG10	13° 2'11.50"	11°55'33.90"N	3.4	OSL	5.7	0.4	Beach Ridge sands		Sand Ridge
		NG9	13° 2'13.40"E	11°55'32.70"N	3.5	OSL	5.4	0.5	Beach Ridge sands		Sand Ridge
		NG39	13°12'50.90"E	11°47'1.50"N	2.2	OSL	6	0.6	Beach Ridge sands		Sand Ridge
		NG40	13°12'45.90"E	11°46'55.00"N	1.7	OSL	8.1	0.7	Beach Ridge sands		Sand Ridge
		NG41	13°12'42.70"E	11°46'48.00"N	2.3	OSL	19	2	Beach Ridge sands		Sand Ridge
		NG38	13°13'19.50"E	11°46'32.00"N	1.8	OSL	6.5	0.6	Beach Ridge sands		Sand Ridge
		NG6	13°13'57.80"E	11°45'54.30"N	8.5	OSL	10.4	0.8	Fluvial sands		Alluvium
		NG7	13°13'57.80"E	11°45'54.30"N	7.5	OSL	10.9	0.8	Fluvial sands		Alluvium
		NG8	13°13'57.80"E	11°45'54.30"N	3.5	OSL	8.2	0.6	Fluvial sands		Alluvium
	Ngelewa Ridge	NG31	13°36'42.90"E	13° 4'45.70"N	2.95	OSL	3.2	0.2	Beach Ridge sands		Sand Ridge
		NG32	13°36'42.90"E	13° 4'45.70"N	1.75	OSL	3	0.2	Beach Ridge sands		Sand Ridge
		NG29	13°38'55.50"E	13° 0'2.60"N	2.25	OSL	2.8	0.2	Beach Ridge sands		Sand Ridge
	Lake Chad	NG35	13°48'43.30"E	13ƒÑ24'21.40"N	nd	OSL	19	2.3	Dune sand from Lake Chad island		Dune
		NG34	13°48'43.30"E	13°24'21.40"N	nd	OSL	18.7	2.2	Dune sand from Lake Chad island		Dune
		NG36	13°50'8.50"E	13°22'5.90"N	nd	OSL	16.4	2	Dune sand from Lake Chad island		Dune
		NG33	13°52'57.50"E	13°50'8.50"E	nd	OSL	15.6	1.9	Dune sand from Lake Chad island		Dune
Chad	Bodélé Depression	CH51	17°42'57.10"E	16°42'17.50"N	nd	OSL	17	2	Sand from barchan dune beneath diatomite		Dune
		CH16	18°32'38.20"E	16°52'48.50"N	nd	OSL	15	1.8	Sand from barchan dune beneath diatomite		Dune
		CH22	18°17'57.50"E	16°46'45.60"N	nd	OSL	15	1.8	Sand from barchan dune beneath diatomite		Dune
		CH62(3)	18° 1'42.00"E	16°41'3.20"N	0.5	OSL	2.4	0.1	Sand overlaid by 30 of clay (Bahr el Ghazal)		Dune
	Angamma Delta	CH46	17°49'51.40"E	17°34'0.00"N	0.5	OSL	6	0.3	Beach Ridge sands		Sand Ridge
		CH44	17°39'41.50"E	17°35'14.20"N	0.5	OSL	5.7	0.3	Beach Ridge sands with pebbles		Sand Ridge
	Goz Keri	CH74	18°42'57.40"E	15°50'17.20"N	0.5	OSL	11.5	0.9	Beach Ridge sands		Sand Ridge
		CH73	18°43'18.80"E	15°51'30.80"N	0.5	OSL	6.6	0.4	Beach Ridge sands		Sand Ridge
Chad	Erg Djourab	BN197	19° 5'23.00"E	17°54'22.00"N	1.4	OSL	4.7	0.2	Dune sand	Mauz and Felix-Henningsen 2005	Dune
		BN199	18°36'59.00"E	16°23'25.00"N	0.4	OSL	4.7	0.3	Dune sand		Dune
	Bahr el Ghazal	BN200	17°42'4.00"E	15° 6'50.00"N	0.3	OSL	3.9	0.4	Gleyic cambic arenosol (bBwg)		Dune
		BN201	17°15'28.00"E	14°50'41.00"N	0.7	OSL	3.4	0.2	Gleyic cambic arenosol (bBw)		Dune
		BN202	16°28'43.00"E	13°50'31.00"N	0.4	OSL	3.1	0.2	Dune sand		Dune
		BN203	16°11'52.00"E	13°37'56.00"N	0.2	OSL	1.3	0.1	Dune sand (in krotovinas)		Dune
Nigeria	Kala-balge	Bidelli 1	14°24'0.47"E	12° 2'0.26"N	0.9	OSL	10.4	0.84	Loamy sand	Adderley et al. 2004	Soil
		Bidelli 2	14°24'0.47"E	12° 2'0.26"N	0.83	OSL	8.17	0.7	sandy silt loam		Soil
		Tiwa 1	14°21'0.52"E	11°59'0.33"N	0.45	OSL	10.4	0.61	loamy sand		Soil
		Tiwa 2	14°21'0.52"E	11°59'0.33"N	0.1	OSL	0.35	0.06	Loamy sand		Soil
		Tiwa 2	14°21'0.52"E	11°59'0.33"N	0.4	OSL	1.22	0.11	silty clay loam		Soil
		Tiwa 2	14°21'0.52"E	11°59'0.33"N	1.25	OSL	3.02	0.27	silty clay loam		Soil
		Tiwa 2	14°21'0.52"E	11°59'0.33"N	1.75	OSL	3.97	0.3	silty clay loam		Soil
		Tiwa 2	14°21'0.52"E	11°59'0.33"N	2.15	OSL	8.27	0.76	loamy sand		Soil

K Water flows near Bongor

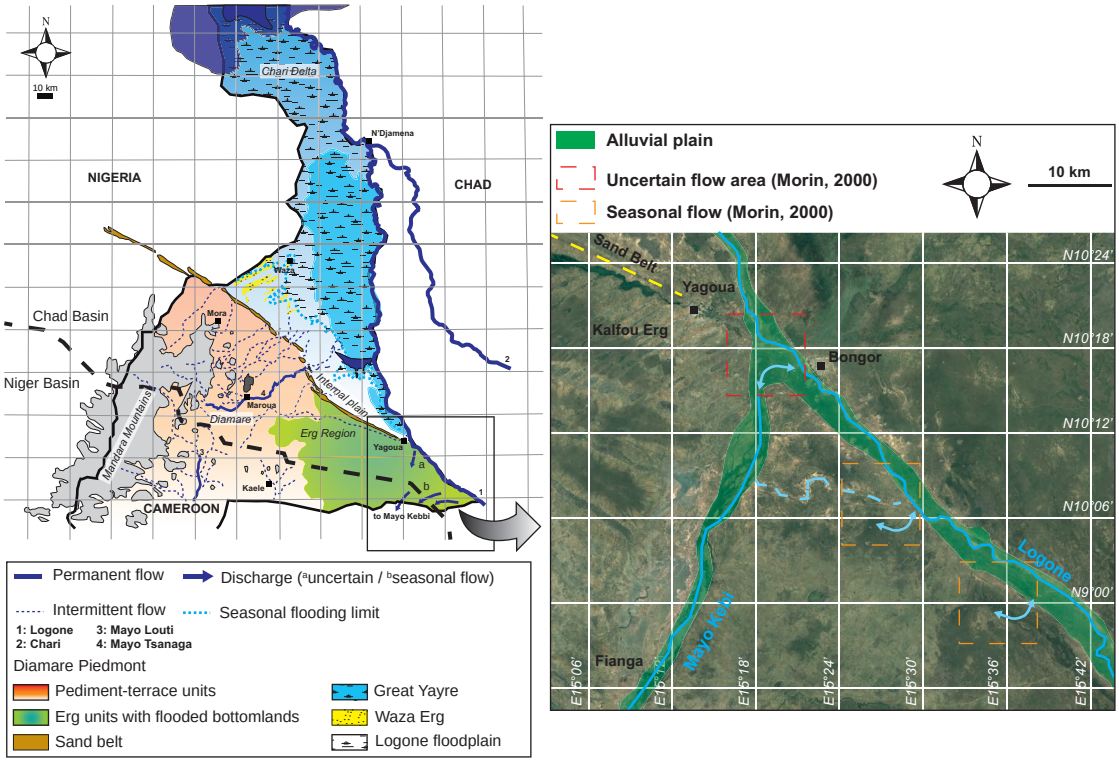

Figure K.1 – In the Bongor area, the Logone flows toward Chad Basin and the Mayo Kebi toward the Niger Basin. However, the waters from the Logone have seasonal and/or uncertain flows toward Mayo Kebi. This behaviour could be inherited by past Logone flow recognized to belong to the Niger Basin (in Durand et al., 2011). Present-day flow into the Chari could be ~4500 cal BP (in Durand, 1995).

L Publications

Geomorphology 261 (2016) 41–56

Contents lists available at ScienceDirect

Geomorphology

journal homepage: www.elsevier.com/locate/geomorph

Can mima-like mounds be Vertisol relics (Far North Region of Cameroon, Chad Basin)?

Nathalie Diaz [a,*], Fabienne Dietrich [a], Guillaume Cailleau [a], David Sebag [b], Benjamin Ngounou Ngatcha [c], Eric P. Verrecchia [a]

[a] Institute of Earth Surface Dynamics, Faculty of Geosciences and the Environment, University of Lausanne, Geopolis, 1015 Lausanne, Switzerland
[b] Laboratoire HydroSciences Montpellier, UMR CNRS/IRD 5569, University of Ngaoundéré, Cameroon, and Laboratoire de Morphodynamique Continentale et Côtière, UMR 6143 CNRS, University of Rouen, 76821 Mont Saint Aignan Cedex, France
[c] University of Ngaoundéré, Faculty of Sciences, Department of Earth Sciences, BP 454 Ngaoundéré, Cameroon

ARTICLE INFO

Article history:
Received 1 July 2015
Received in revised form 5 January 2016
Accepted 20 February 2016
Available online 23 February 2016

Keywords:
Erosion
Vertisol genesis
Gilgai
Late Pleistocene-Holocene

ABSTRACT

Non-anthropogenic earth mounds, defined as mima-like mounds in this study, have recently been observed in non-carbonate watersheds along the Sudano-Sahelian belt in the Chad Basin. In the Diamare piedmont (northern Cameroon) they are particularly well developed within stream networks. In less eroded areas, they occur as whaleback, flattened morphologies, or even as buried features. All these shapes are composed of clay-rich sediment associated with high proportions of secondary carbonate nodules and Fe—Mn micro-nodules. Their soil structure is prismatic to massive and vertical cracks are observed locally. Grain-size distributions emphasize the clay-rich nature of the sediment, with average clay contents of 32% ± 12.8% (n = 186), which is significantly higher than the clay content in the adjacent sediments in the landscape (mean = 10% ± 4%, n = 21). Moreover, high proportions of smectite characterize the soil, with average contents of 34 ± 7% (n = 25). At the micro-scale, the groundmass has a cross-striated b-fabric, with embedded smooth subangular quartz and feldspar grains of the silt-size fraction. All the characteristics point to altered vertic properties in the clay-rich sediment composing the mima-like mounds. Mima-like mounds are thus interpreted as degraded Vertisols. Compared to present-day Vertisols occurring in the piedmont, mima-like mounds are located upstream. It is thus proposed that the Vertisol areas were more extensive during a former and wetter period than the present-day. Subsequent changing climatic conditions increased erosion, revealing the gilgai micro-relief by preferential erosion in micro-lows rather than in micro-highs. Mima-like mounds of the Chad Basin might thus result from pedogenesis combined with later erosion. These local processes can be inherited from regional climatic variations during the Late Pleistocene-Holocene and likely be related to the African Humid Period.

© 2016 Elsevier B.V. All rights reserved.

1. Introduction

Non-anthropogenic earth mounds occur in many parts of the world and the questions related to their origin make them exciting features (Cramer et al., 2012). The debate is generally centred upon the discussion of their abiotic or biotic origin. For example, earth mounds observed in South Africa (locally termed *heuweltjies*; Moore and Picker, 1991; Francis et al., 2012) and Brazil (Funch, 2015) are attributed to termite activity, but others provide some evidence they can result from differential erosion (Cramer et al., 2012). In North America, the geomyid pocket gopher may be involved in the mound (or mima mound) formation (e.g. Cox, 1984), but the debate on their real capability to produce them is still open (e.g. Butler, 1995). Silva et al. (2010) proposed that erosive processes combined with vegetation patterns are the cause of earth mounds (*campos de murundus*) observed in Brazil instead of resulting from termite activity. The origin of earth mounds changes from one region to another, but they have some common features, such as their regular spatial distribution or their size (Cramer et al., 2012). It was recently proposed that many of these different earth mounds, termed mima-like mounds, can be explained by the combination of erosion and/or aeolian processes with vegetation patterns (Cramer and Barger, 2014; Cramer and Midgley, 2015).

All along the Sudano-Sahelian belt, carbonate nodules have been observed in non-carbonate watersheds (Fig. 1A). In northern Cameroon (Fig. 1B), these nodules are associated with non-anthropogenic earth mounds (Fig. 2). These new features have not been studied up until now. In the Far North region of Cameroon (Chad Basin) they are frequently observed in the Diamare piedmont (Fig. 1B), and are particularly well developed within stream networks (10 m < diameter < 30 m and height up to 1 m). On Google Earth images (Fig. 1C), they are distributed in eroded areas as regularly spaced (i.e. over-dispersed) round features. They can be defined as mima-like mounds due to their size and their spatial distribution. However, vegetation patterns do not play a main

* Corresponding author.
E-mail address: nathalie.diaz@unil.ch (N. Diaz).

http://dx.doi.org/10.1016/j.geomorph.2016.02.021
0169-555X/© 2016 Elsevier B.V. All rights reserved.

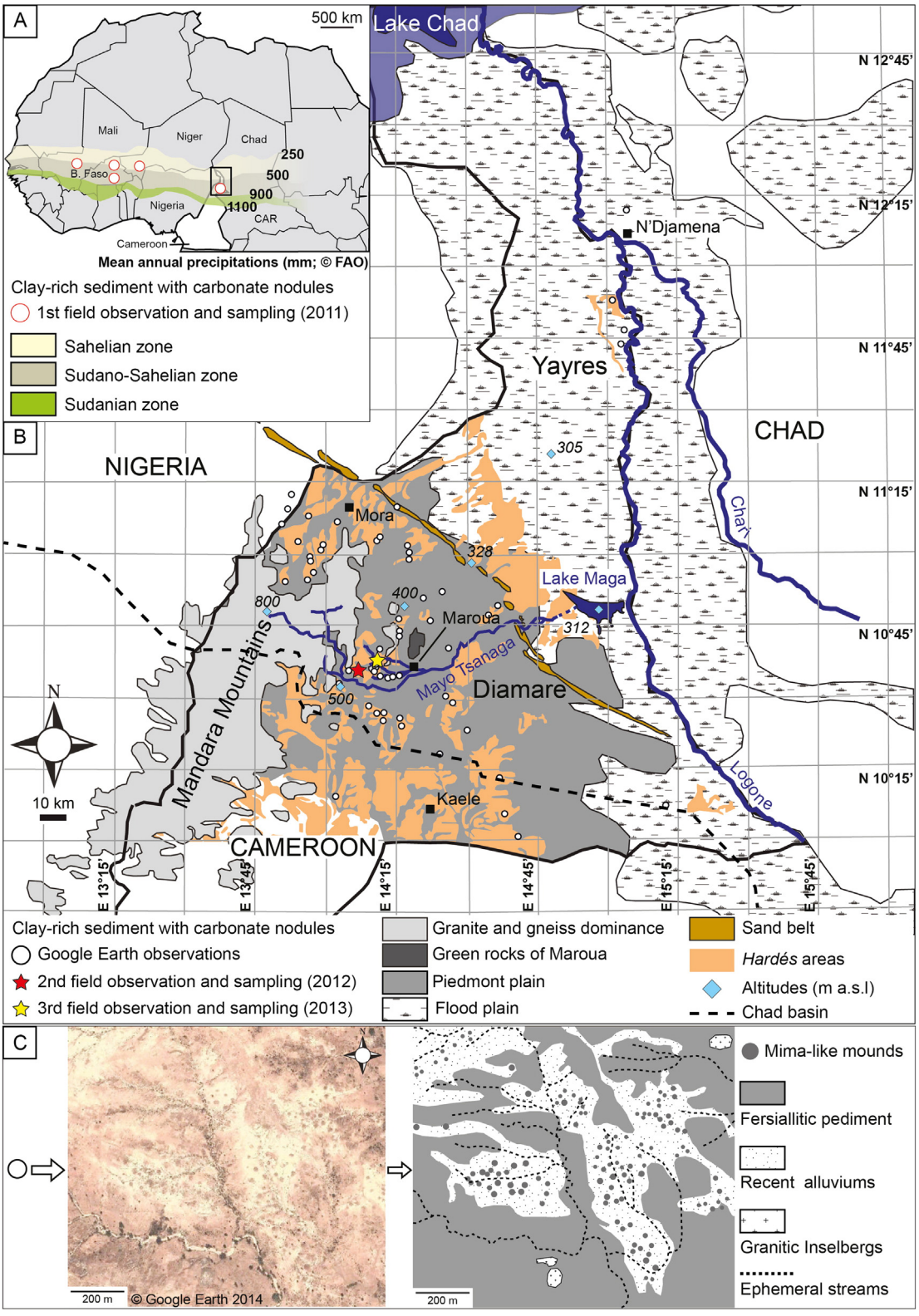

Fig. 1. Location and settings of study sites. A) Location of observed sediments associated with carbonate nodules (circles) along the Sudano-Sahelian belt (MAP 900–500 mm/yr; FAO/GIEWS, 2004); mean annual precipitation ranges are given for the three climatic zones. The black rectangle refers to the location of the Far North region of Cameroon. B) Far North region of Cameroon map showing, from SW to NE, the Mandara Mountains, the Diamare piedmont, separated from the Yayres floodplain by a sand belt, and finally, Lake Chad. The stars represent the study sites. They are located in the Mayo Tsanaga watershed, which belongs to the Chad Basin (large dashed-line; Olivry et al., 1996). Circles indicate the location of the clay-rich sediment outcropping as mima-like mounds within stream networks (Google Earth observations, see Appendix Table A.1) and generally found in *hardés* areas or degraded soil areas reported by Brabant and Gavaud (1985). C) Example of a Google Earth view (10°37′12.08″N, 14°11′13.55″E) showing regularly spaced (R = 1.72, over-dispersion, Clark and Evans, 1954, see appendix Fig. A.1) mima-like mounds outcropping in eroded areas between ephemeral streams. A beige alluvium surrounds them and less eroded areas display a reddish pediment interpreted as a fersiallitic pedolith (Retallack, 2001). Some granitic inselbergs outcrop as well.

role in their formation, whereas erosion processes do. Generally, mima-like mounds are associated with sparse vegetation or none at all (Figs. 2A, 3). Consequently, the conditions under which they form still remain unclear.

The clay- and carbonate-rich association composing the mima-like mound sediments was already described in the Diamare piedmont (Martin, 1961; Sieffermann, 1963; Brabant and Gavaud, 1985; Morin, 2000) and also farther away in the Chad Basin (Erhart, 1954; Pias, 1962; Bocquier, 1973). Compilation of former and new field observations raises questions on the potential links that could exist between these multiple locations. The clay-rich sediment, enriched in carbonate nodules, can be interpreted as a layer (or multi-layer?) forming residual mima-like mounds in highly eroded areas. Regarding the soils developing from this clay-rich parent material, there are mainly Planosol, Solontez and Vertisol (Brabant and Gavaud, 1985). However, these soils are often described and mapped as degraded soils (Brabant and Gavaud, 1985). Interestingly, mima-like mounds are typically observed in these degraded zones. This is consistent with their presence in eroded areas. However, could pedogenesis have a specific role in their genesis?

The aim of this study is to characterize sedimentological and geomorphological settings of mima-like mounds from the Far North region of Cameroon and to propose a possible origin of their formation. To achieve this goal, a multiple scale approach is used compiling (1) field observations, (2) grain-size distribution and clay mineralogy data at the mound scale, and (3) thin-section observations. Roles of pedogenesis and later erosion in the formation of mima-like mounds are investigated. Two main hypotheses are proposed: (i) mima-like mounds observed in northern Cameroon are relics of Vertisols associated with a gilgai micro-relief; and (ii) they result from abiotic processes related to the succession of pedogenesis and erosion-deposition phases associated to Late Quaternary regional climatic changes. They may also be useful as paleo-environmental records for the Late Pleistocene-Holocene period in the Chad Basin.

2. General settings

Mima-like mounds are observed in the Diamare piedmont, spreading between the Mandara Mountains and the Yayres floodplain (Fig. 1B). The Mandara Mountains are mainly composed of granite and gneiss. Metamorphic rocks (greenschist facies), known as *the green rocks of Maroua*, constitute only a minor part of the massif around Maroua (Brabant and Gavaud, 1985). The transition from the Mandara Mountains to the Diamare piedmont is abrupt, with a decreasing slope from about 10% to 2%, which is a typical dryland landform associated with slopes and called pediment (Morin, 2000; Goudie, 2013). The pediment infilling is heterogeneous and related to multiple pediment generations resulting from Quaternary climatic variations (Morin, 2000). From the foot of the Mandara Mountains to the Yayres floodplain, the pediment evolves from a thin cover of weathered granitic sand, to a colluvium, and finally to an alluvium with a grain-size distribution skewed to finer sizes. However, these settings are complicated by evidence of lateral changes, such as a clay-rich intercalation pediment, possibly of palustrine origin, and in sand lenses resulting from changes in the Mayo riverbed (Morin, 2000). The clay-rich pediment, with which carbonate nodules are often associated, outcrops along the southern bank of the Mayo Tsanaga, or is overlain by either alluvium (for example near Mora) or various generations of fersiallitic pediments starting from the foot of granitic inselbergs, as observed around Maroua and in the region of Kaele (Sieffermann, 1967; Morin, 2000). The clay-rich and carbonate-rich nature of mima-like mounds (Fig. 2) suggests that they are associated to this clay-rich pediment.

Planosol is the main type of soil found in the Diamare piedmont (Brabant and Gavaud, 1985). These soils are generally associated with Solonetz and Vertisol depending on the topography, the latter being favoured by hydromorphic conditions and developing in lower areas. The particularity of these soils is that they are often mapped as degraded soils. The local term used to emphasize soil degradation is *hardé*. This term characterizes soils that are very compact, with low permeability, and alkaline. These conditions make these lands sterile and only sparse vegetation can grow on them. These areas are extensive and cover 886,500 ha (Brabant and Gavaud, 1985). The other soils found in the region and not termed as *hardé*, are Cambisol, Ferralsol mainly located east of Kaele, and Lithosol (Brabant and Gavaud, 1985). Interestingly, the *hardé* characteristics listed above are also typical of mima-like mounds (Fig. 2, Table 1). The *hardé* areas are not automatically associated with mima-like mounds but the latter are almost always found in these specific areas (Fig. 1B).

According to the Köppen-Geiger climate classification (Peel et al., 2007), the Far North region of Cameroon belongs to the hot (h = mean annual temperature ≥ 18 °C), steppic (S = mean annual precipitation ≥5*$P_{threshold}$[1]), arid (B) climate type (BSh). Summers are generally hot and there is a short well-marked wet season regulated by the monsoon. The weather station located in Salak (Fig. 1B) records an average annual rainfall of 800 mm and an average annual temperature of 27.6 °C (L'Hôte, 1998). The potential evapotranspiration is 2193 mm and the dry season lasts for seven months with five months without any rainfall (Mahop et al., 1995). From January to April, the region is also marked by dry NE trade winds, called the Harmattan (L'Hôte, 1998). Under these climatic conditions, streams are mainly ephemeral and have a WSW-ENE-flow direction through the Diamare piedmont from the Mandara Mountains to the Yayres floodplain. They belong to the endorheic Chad Basin watershed, whose hydrological limits reach the south of Maroua (Fig. 1B).

3. Material and methods

3.1. Sampling

Soil profiles are described according to the guidelines provided by the Food and Agricultural Organization of the United Nations (FAO, 2006). Depth, percentage and components of the skeleton (>2 mm), structure, relative abundance of carbonate (tested with 10% hydrochloric acid) and colour (determined in the field with a Munsell colour chart) are given in Table 1. Samples were collected at two main sites (Fig. 1B, stars). Trenches were opened through selected mounds. Soil profiles were described each meter along the trench. The site investigated in 2013 is located along an affluent stream of the Mayo Tsanaga (Fig. 1B). A trench 12 m long and 1.30 m deep was opened through a well-developed mima-like mound (M1, Fig. 2B, C). Twelve soil profiles (A to L, Table 1) were described and sampled at 5-cm intervals in the first 10 cm from the top, and then every 10 cm. A second trench, 5 m long and 1.30 m deep, was opened through a less well developed and flattened mima-like mound partially buried by a coarse-grained alluvium interfingering with the clay-rich sediment (M2, Fig. 4B). Five soil profiles (N to R, Table 1) were described and sampled the same way as in mound M1. A last profile (T, Table 1) was described in a fersiallitic terrace (P, Fig. 4A) overlying the clay-rich sediment and sampled as in mounds M1 and M2. The site investigated in 2012 is located along the Mayo Tsanaga (Fig. 1B). A trench 7 m long and 1.30 m deep was opened in a mima-like mound from centre to perimeter (M3). Seven soil profiles (S, U to AB, Table 1) made at 1 m intervals were sampled every 5 cm. This second site was investigated during a different fieldwork campaign and soil descriptions are not as complete as at the first site (Table 1, nd = no data). All samples were dried at 45 °C and sieved at 2 mm (fine earth fraction). A part of this fraction was crushed to a powder with an agate mortar (grain-size <10 μm). Carbonate nodules were collected as well, at various depths; some of them were crushed with an agate mortar in order to have both small pieces and powders.

[1] $P_{threshold}$ = 2 * Mean annual temperature (Peel et al., 2007).

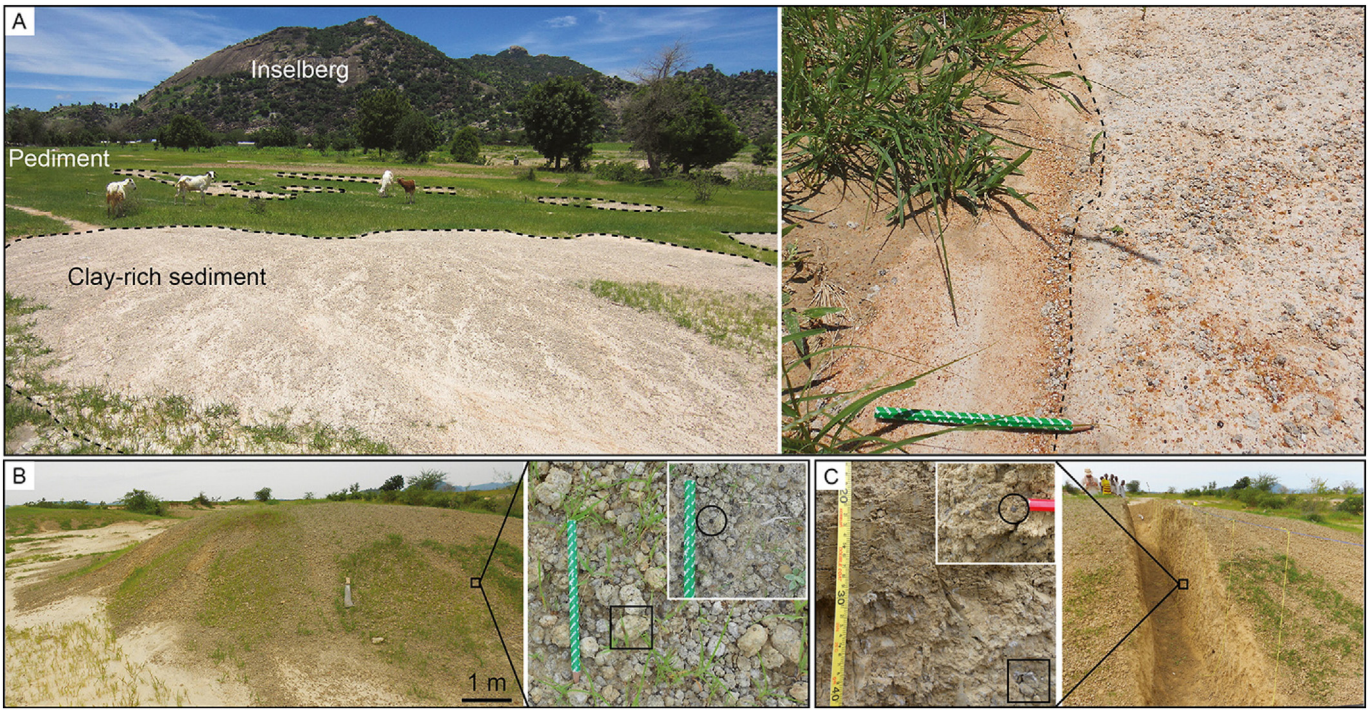

Fig. 2. A) Relationships between mima-like mounds and vegetation patterns. Generally, the clay-rich sediment is devoid of vegetation compared to surrounding sediments, and shows sharp limits (dashed line), which makes it easily recognizable in the landscape. B) Mima-like mound M1 located along the Mayo* Tsanaga watershed (Fig. 1B, 2013 field observation) surrounded by a fine alluvium and covered by carbonate nodules and Fe—Mn micro-nodules. C) Trench through the mima-like mound M1 composed by a yellowish-grey, clay-rich and massive soil matrix. A few carbonate nodules (black square) and Fe—Mn micro-nodules (black circle) are also observed in the soil skeleton (>2 mm). Pictures taken in September 2013. *A *term used to designate a stream in the Foulfoulde language. Nowadays, it is a local scientific term used as a synonym for ephemeral stream.*

Soil samples were put in metallic boxes (8 × 8 × 4 cm) to make thin sections (thickness = 30 μm). They were collected from mounds M1, M2, and profile P at specific depths (Table 1). Samples were wedged in the best possible manner to keep the original soil structure.

3.2. Analytical methods

Measurement of pH_{H2O} was performed on the 2-mm sieved soil fraction. The soil was agitated in deionized water with a 1:25 soil to water ratio during 2 h. The pH in the solution was then measured with a lab pH meter (Metrohm SA).

Grain-size distributions were performed with the laser diffraction method (Malvern™ Mastersizer 2000). Carbonate and organic fractions were removed from the dried <2 mm soil fraction, using 10% hydrochloric acid (HCl) and 15–35% hydrogen peroxide (H_2O_2), respectively. Finally, mineral particles were dispersed with Na-hexametaphosphate (40 g/L). Samples are put in water suspension during the analysis (Hydro 2000S module). Due to their compositional nature, a centred log-ratio (clr) transformation was applied to the data:

$$x_n = \ln \frac{x_i}{G(x_i)}$$

where, x_n is the transformed data, x_i is the original data, and G the geometric mean of the x_i variable. Data resulting from the clr transformation were used to build a cluster tree by performing hierarchical cluster analysis (CA). The groups were obtained using the Euclidian distance between samples and the Ward algorithm for clustering. To compare the dissolution silicate residue trapped in carbonate nodules with the embedding soil matrix, this specific fraction was taken as a

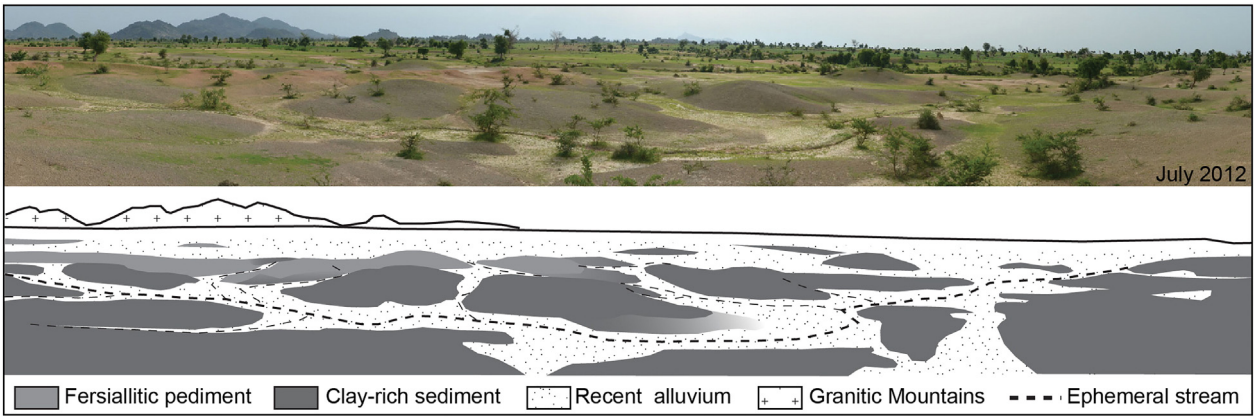

Fig. 3. Mima-like mounds in the landscape. The clay-rich sediment outcrops as dark mima-like mounds at various stage in their development. Beige alluvium associated with ephemeral stream systems surround them. The fersiallitic pediment is always observed overlaying the clay-rich sediment.

Table 1
Soil profile descriptions according to FAO's (2006) descriptive codes for mima-like mound M1 (A to L), M2 (N to R), M3 (S to AB) and the fersiallitic pediment (T). Horizons marked in bold represent the locations where samples were collected to make thin sections. The pH_{H2O} was measured in the lab with a pH meter.

Mima-like mound	Horizons	Depth (cm)	Structure[a]	Skeleton (%)[b]	Skeleton composition[c]	Munsell colour (moist)	$CaCO_3$%[d]	pH_{H2O}
M1	**AH1**	0–9	SG + AB	0	–	2.5Y5/6	2–10	8.9
	AH2	9–24	AB + MA	1	Ox/Cnod	2.5Y6/4	2–10	8.9
	AH3	24–44	AB + MA	1	Ox/Cnod	2.5Y6/4	0–2	8.8
	AH4	44–59	MA	0	–	2.5Y5/6	0–2	8.9
	BH1	0–5	AS + SG	0	–	2.5Y5/6	2–10	8.6
	BH2	5–24	MA	0	–	2.5Y5/4	10–25	9.0
	BH3	24–64	MA	1	Cnod	2.5Y6/6	0–2	8.9
	CH1	0–1	AS	1	Ox	2.5Y5/4	>25	8.8
	CH2	1–9	AS + MA	5	Cnod>Sil/ox	2.5Y6/4	0–2	8.9
	CH3	9–29	MA	1	Cnod	2.5Y5/4	10–25	9.1
	CH4	29–76	MA	1	Sil	2.5Y6/4	0–2	9.0
	DH1	0–3	AB	1	Cnod	2.5Y5/4	10–25	9.1
	DH2	3–24	MA	1	Ox/Cnod	2.5Y5/4	0–2	9.1
	DH3	24–60	MA	1	Cnod	2.5Y5/4	0–2	9.1
	DH4	60–100	MA + SG	1	Cnod	2.5Y6/4	nd	8.8
	EH1	0–5	AS	5	Ox/Cnod	2.5Y4/4	>25	8.9
	EH2	5–34	MA	10	Ox/Cnod	2.5Y6/4	0–2	9.1
	EH3	34–114	MA	15	Ox/Cnod	2.5Y6/4	0–2	8.9
	FH1	0–10	AS	3	Cnod > Ox	2.5Y5/4	10–25	8.7
	FH2	10–37	MA	2	Cnod	2.5Y6/3	0–2	9.1
	FH3	37–54	MA	15	Cnod	2.5Y5/4	0–2	9.6
	FH4	54–100	MA	20	Cnod	2.5Y5/4	0–2	9.1
	FH5	100–120	MA	5	Cnod	2.5Y5/4	0–2	8.7
	GH1	0–7	AS	2	Ox	2.5Y6/3	10–25	8.6
	GH2	7–32	MA	2	Ox	2.5Y6/3	10–25	9.2
	GH3	32–112	MA	15	Cnod	2.5Y5/4	2–10	9.1
	GH4	112–128	MA	1	Cnod	2.5Y6/3	0–2	8.9
	HH1	0–7	AS + MA	2	Ox	2.5Y5/4	10–25	9.1
	HH2	7–96	MA	10	Cnod	2.5Y5/3	2–10	9.2
	HH3	96–120	MA + AS	5	Cnod	2.5Y5/4	0–2	9.0
	IH1	0–20	MA	5	Ox/Cnod	2.5Y6/4	0–2	8.5
	IH2	20–100	MA	0	–	2.5Y6/5	0	9.0
	JH1	0–17	MA	0	–	2.5Y6/3	0	8.7
	JH2	17–69	MA	1	Cnod	2.5Y6/3	0	9.0
	KH1	0–5	AS	1	Cnod	2.5Y5/4	2–10	8.5
	KH2	5–35	MA	0	–	2.5Y6/2	0	8.3
	LH1	0–35	MA	0	–	2.5Y6/2	0	8.5
M2	NH1	0–8	AS	3	Cnod	2.5Y6/3	0–2	9.3
	NH2	8–41	MA	2	Cnod	2.5Y6/4	0–2	9.5
	NH3	41–115	MA	10	Cnod	nd	0–2	9.5
	OH1	0–7	AS	5	Ox/Cnod	2.5Y6/4	0–2	9.2
	OH2	7–39	MA	15	Cnod	2.5Y5/3	10–25	9.2
	OH3	39–110	MA	15	Cnod	2.5Y5/4	0–2	9.4
	PH1	0–13	AB + SG	2	Cnod	2.5Y6/4	>25	8.1
	PH2	13–45	SG	70	Mix	2.5Y6/4	0–2	9.1
	PH3	45–100	MA	5	Ox/Cnod	2.5Y6/4	>25	9.2
	QH1	0–3	SG + AS	70	Mix	10YR4/3	0	8.0
	QH2	3–50	SG	70	Mix	10YR4/4	0	8.1
	QH3	50–70	MA	2	Ox/Cnod	2.5Y6/4	0–2	7.9
	QH4	70–100	MA	1	Ox/Cnod	2.5Y6/3	2–10	8.5
	RH1	0–2	SG	70	Mix	7.5YR3/3	0	7.5
	RH2	2–34	SG	70	Mix > Sil	10YR5/6	0	7.8
	RH3	34–67	SG	70	Mix > Sil	10YR4/4	0	8.3
	RH4	67–83	AS	50	Mix	2.5Y6/4	0–2	8.5
	RH5	83–95	MA	70	Mix	2.5Y5/4	0–2	8.2
	RH6	95–100	MA	2	Ox/Cnod	2.5Y5/4	0–2	8.2
P	TH1	0–6	SG	0	–	10YR4/6	0	7.2
	TH2	6–21	AS	1	Sil	10YR4/4	0	7.4
	TH3	21–42	AS	2	Sil/Ox	10YR4/6	0	7.7
	TH4	42–54	AS	3	Ox	10YR4/6	0	7.8
	TH5	54–105	MA	3	Ox	2.5Y5/6	0–2	8.0
M3	SH1	0–10	SG + AB	nd	nd	nd	10–25	9.3
	SH2	10–70	AB + PR	nd	nd	nd	0–2	9.2
	SH3	70–100	AB + MA	nd	nd	nd	2–10	9.3
	SH4	100–120	AB + MA	nd	nd	nd	0–2	9.3
	UH1	0–16	SG + AB	nd	nd	nd	>25	9.2
	UH2	16–50	AB + PR	nd	nd	nd	10–25	9.3
	UH3	50–110	AB + MA	nd	nd	nd	10–25	9.3
	WH1	0–4	SG + AB	nd	nd	nd	10–25	9.3
	WH2	4–80	AB + PR	nd	nd	nd	2–10	9.3
	WH3	80–100	AB + MA	nd	nd	nd	2–10	9.3
	XH1	0–10	SG + AB	nd	nd	nd	>25	9.1
	XH2	20–40	AB + PR	nd	nd	nd	10–25	9.3

(continued on next page)

Table 1 (*continued*)

Mima-like mound	Horizons	Depth (cm)	Structure[a]	Skeleton (%)[b]	Skeleton composition[c]	Munsell colour (moist)	$CaCO_3$%[d]	pH_{H2O}
	XH3	40–70	AB + MA	nd	nd	nd	10–25	9.4
	YH1	0–10	AB	nd	nd	nd	>25	9.3
	YH2	10–30	AB + PR	nd	nd	nd	2–10	9.4
	YH3	30–60	AB + PR	nd	nd	nd	10–25	9.4
	ZH1	0–20	SG + AB	nd	nd	nd	2–10	9.4
	ZH2	20–58	AB + PR	nd	nd	nd	>25	9.4
	ABH1	0–14	SG + AB	nd	nd	nd	2–10	9.5
	ABH2	15–50	AB + PR	nd	nd	nd	2–10	9.5

nd = no data.
[a] SG = single grained, AB = angular blocky, AS = angular and subangular blocky, MA = massive, SAB = sub-angular blocky, PR = prismatic.
[b] Soil fraction >2 mm.
[c] Ox = Fe–Mn oxide, Cnod = carbonate nodule, Sil = silicate, Mix = mixed composition (Ox, Cnod and Sil).
[d] Carbonate reaction to HCl 10%, estimation of carbonate content.

group without going through clr and CA processing. Each cluster is represented by its median and standard error of its median (σ_{median}):

$$\sigma_{median} = 1.253\frac{\sigma}{\sqrt{n}}$$

where, σ is the standard deviation of samples composing a cluster and n the number of samples composing each cluster. For graphical reasons, the data are logarithmically transformed into phi (Φ) values using the expression proposed by Krumbein in 1934 (Blott and Pye, 2001):

$$\phi = -\log_2 d$$

where, d is the grain-size in millimetres. Clay percentage interpolation (n = 89) was performed using a cubic interpolation with Matlab (R2014a 8.3.0.532).

X-ray Diffraction (XRD) analyses were performed with both <2 μm and 2–16 μm fractions. Carbonate was removed from dried 2 mm-sieved soil samples with 10% HCl in an ultra-sonic bath for 3 min. The residual fraction was washed in order to remove the excess HCl. Separation of the <2 μm and 2–16 μm fractions was performed by centrifugation and deposited on separate glass plates. Five samples per cluster resulting from the CA analysis were selected and prepared for XRD analyses, which were performed using an ARL Xtra diffractometer (Thermo). Clay minerals were identified according to their diffraction properties, i.e. the spacing (d) between rows of atoms and the angle of incidence (θ), defined by Bragg's law:

$$2d\sin\theta = n\lambda$$

where, $n\lambda$ is the number of wavelengths (Moore and Reynolds, 1997). The software PeakFit™ (Systat Software Inc.) was used to deconvolve two parts of the diffractograms in order to discriminate between the different components combined in the signal (Velde and Meunier, 2008). The first part ranges from 4°2θ to 11°2θ and refers to smectite, illite and interlayered illite-smectite. The second part ranges from 23°2θ to 26°2θ and refers to the second peak of kaolinite and the fourth peak of the chlorite, which are overlapping. Kaolinite and chlorite were calculated as follows:

$$\text{Kaolinite (cps)} = CK001 * \left(\frac{K002}{K002 + C004}\right)$$

$$\text{Chlorite (cps)} = CK001 * \left(\frac{C004}{K002 + C004}\right)$$

where, $CK001$ is the first peak of the kaolinite overlapping the second peak of chlorite occurring at about 12.5°2θ, $K002$ is the second peak of the kaolinite occurring at about 24.2°2θ, and $C004$ is the fourth peak of chlorite occurring at about 25.1°2θ (Moore and Reynolds, 1997).

The signals were first smoothed and deconvolved with the residue method using the Pearson VII operator. Relative percentages were calculated for smectite, illite, chlorite and kaolinite. However, only the results for smectite and kaolinite clay minerals are presented in this study.

3.3. Thin section descriptions

Thin section observations are used to identify pedogenic processes involved in the mima-like mound formation and to highlight the differences between sediments observed in the landscape. Thin section descriptions are performed according to the guidelines given in Stoops (2003). Particular attention is paid to the groundmass and the identification of pedofeatures, as they indicate lithology and weathering processes, as well as past and present pedogenic processes, respectively (Stoops, 2003). The characterization of the b-fabric, which is based on the patterns of orientation and distribution of interference colours in the soil micro-mass, is the main descriptor of groundmass, whereas, coatings, infillings, and nodules are mainly considered as pedofeatures (Stoops, 2003). Descriptors such as size, abundance, boundary, sorting, shape, sphericity, roughness, roundness, orientation, mineralogy, and colour, are used to differentiate the fabric units and patterns. The c/f related distribution, which is the ratio between individual fabric units, small fabric units, and associated pores (Stoops and Jongerius, 1975), is used to describe the relationships between coarse and fine elements of the fabric.

4. Results

4.1. Field and soil descriptions

The studied mima-like mounds are located in the Mayo Tsanaga granitic watershed (Fig. 1B). They are distributed within stream networks and are regularly spaced (Fig. 1C) with R = 1.72 (see Appendix, Fig. A.1) meaning over-dispersion (Clark and Evans, 1954). They are easily identified because of their sparse vegetation cover (Fig. 2A) and their darker colour (Fig. 3). The size of the mounds is up to 10 m in diameter and up to 1 m in height (Fig. 2B). Their nature can be referred to as the clay-rich pediment layer described by Sieffermann (1967) and Morin (2000), to which carbonate nodules are often associated (see Section 2).

Field observations showed that mima-like mounds have various heights; some are flattened, whereas others have whaleback morphologies (Fig. 4A, B). A fine beige alluvium surrounds all the various types of mima-like mounds (Figs. 3, 4C). In less eroded and well-preserved areas, a red-brown fersiallitic pediment, described by Sieffermann (1967) and Morin (2000), overlies them (Figs. 3, 4A). Some flattened mima-like mounds are also partially buried by a coarse alluvium interfingering with the clay-rich sediment (Fig. 4B). The various observed morphologies are undoubtedly related to the intensity of erosion processes (Fig. 4). The peculiarity of mima-like mounds is that their surface is completely covered by carbonate nodules (2 cm < diameter < 10 cm) and Fe—Mn micro-nodules (Fig. 2B). These nodules can also be found in deeper horizons (Fig. 2C, Table 1).

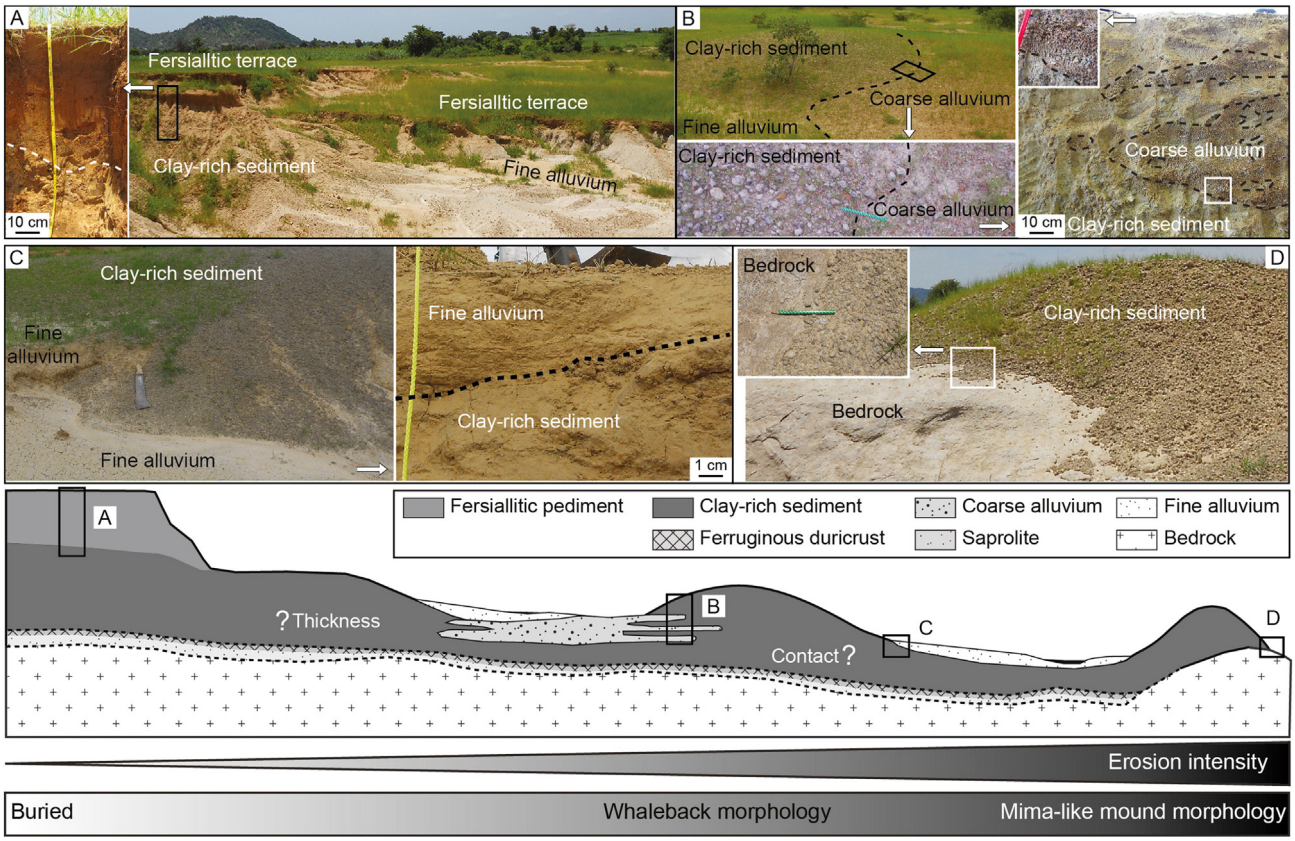

Fig. 4. Field relationships between clay-rich sediment morphologies and erosion intensity. The drawing represents a cross-section of the various sediments observed in the landscape and the relationships to each other. The pictures illustrate four different situations represented in the drawing (black rectangles). A) Detail of the fersiallitic pediment overlaying the clay-rich sediment (profile P). B) Example of a flattened mima-like mound (M2) in contact with a coarse alluvium interfingering the clay-rich sediment. C) Detail of the contact between the fine alluvium and the mima-like mound M1. D) Clear contact between a mima-like mound and the granitic bedrock. The thickness of the clay-rich sediment and its contact with a deep ferruginous duricrust described in the literature and/or the bedrock saprolite were not observed during the fieldwork. The clay-rich sediment outcrops as flattened mima-like mounds, whaleback morphologies, or mima-like mounds depending on the intensity of erosion. A fersiallitic pediment buries mounds in less eroded parts of the landscape.

In the studied areas, the thickness of the clay-rich sediment composing mima-like mounds is still unknown, as its base could not be reached. However, according to Morin (2000), it can be up to several meters (about 6 m) in the northwestern area of Mora. Nevertheless, field observations suggest that this clay-rich sediment has no genetic relationship with the granitic bedrock. Morin (2000) reported the following sedimentary and lithological succession in the region, from top to bottom: (i) clays with sand lenses, corresponding to the sediment composing the mima-like mounds, on (ii) a ferruginous duricrust, overlaying (iii) a saprolite directly developed from the cratonic rocks. However, the clay-rich sediment seems genetically related neither to the ferruginous duricrust nor the granitic bedrock. A mima-like mound deposited directly with a sharp unconformity on granitic inselbergs emphasizes the lack of any kind of causal relationship (Fig. 4D). However, more arguments are needed to strengthen this assumption.

Twenty-seven soil profiles were described along the trenches and descriptions are given in Table 1. The soils contain a very small amount of organic matter (<1%) and are essentially mineral (Fig. 5). The structure is single grain to angular blocky in the surficial horizons, becoming angular blocky to prismatic or massive with depth. Some vertical cracks are visible in mound M3 below 10 cm (Fig. 5A, B, arrows). Mound M1 shows some preferentially orientated cracks, such as in profile D (Fig. 5C, top, arrows). However, the structure of M1 is angular blocky to massive in depth (Fig. 5C top, ped), and vertical cracks are locally visible but to a lesser extent compared to M3 (Fig. 5C, bottom, arrow). Carbonate nodules (Fig. 5, white squares) and Fe—Mn oxides compose the skeleton; soil colour is yellowish-grey and pH_{H2O} is alkaline ($8 < pH_{H2O} < 10$). The fine earth reacts to HCl indicating the presence of diffuse carbonate (Table 1). However, the coarse alluvium interfingering the clay-rich sediment in mound M2 has a single grained structure with a skeleton composed of silicate minerals, mainly quartz and feldspars, and a dark yellowish brown soil colour. The fine earth does not, or only weakly, react to HCl and pH_{H2O} is $7 < pH_{H2O} < 8$. The dark brown fersiallitic pediment has a sub-angular blocky structure with a skeleton composed of silicate minerals. The fine earth does not react to HCl, and pH_{H2O} is around 7. However, the lower part of the fersiallitic pediment displays the same properties as the mima-like mound soils, with a massive structure, a yellowish-grey soil colour, a $pH_{H2O} > 8$ and a fine earth weakly reacting to HCl.

4.2. Grain-size distribution

Cluster analysis of grain-size distributions of all sediment samples (Fig. 6) generates seven clusters (with a cophenetic correlation coefficient of 0.54, $n = 207$). Each cluster is represented by its median (Fig. 6, black lines) and its associated standard error (Fig. 6, grey-shaded areas). The median and its error are plotted as an independent cluster ($n = 10$, no clr and no CA processing) for the silicate residue trapped within the carbonate nodules, for comparison with other sediments. Six main modal classes (mc_i) have been recognized (Fig. 6): mc_1) coarse-medium sands, mc_2) medium-fine sands, mc_3) very fine sands-coarse silts, corresponding to the desertic loess window (Crouvi et al., 2010), mc_4) fine silts, mc_5) coarse clays, and, finally, mc_6) fine clays. These modal classes display various relative amplitudes and are used to characterize each cluster type.

The samples belonging to mound M3, especially those found on the lower edge of the mound, are in the first cluster ($n = 18$). Cluster 1 is characterized by five modal classes, listed from higher to lower

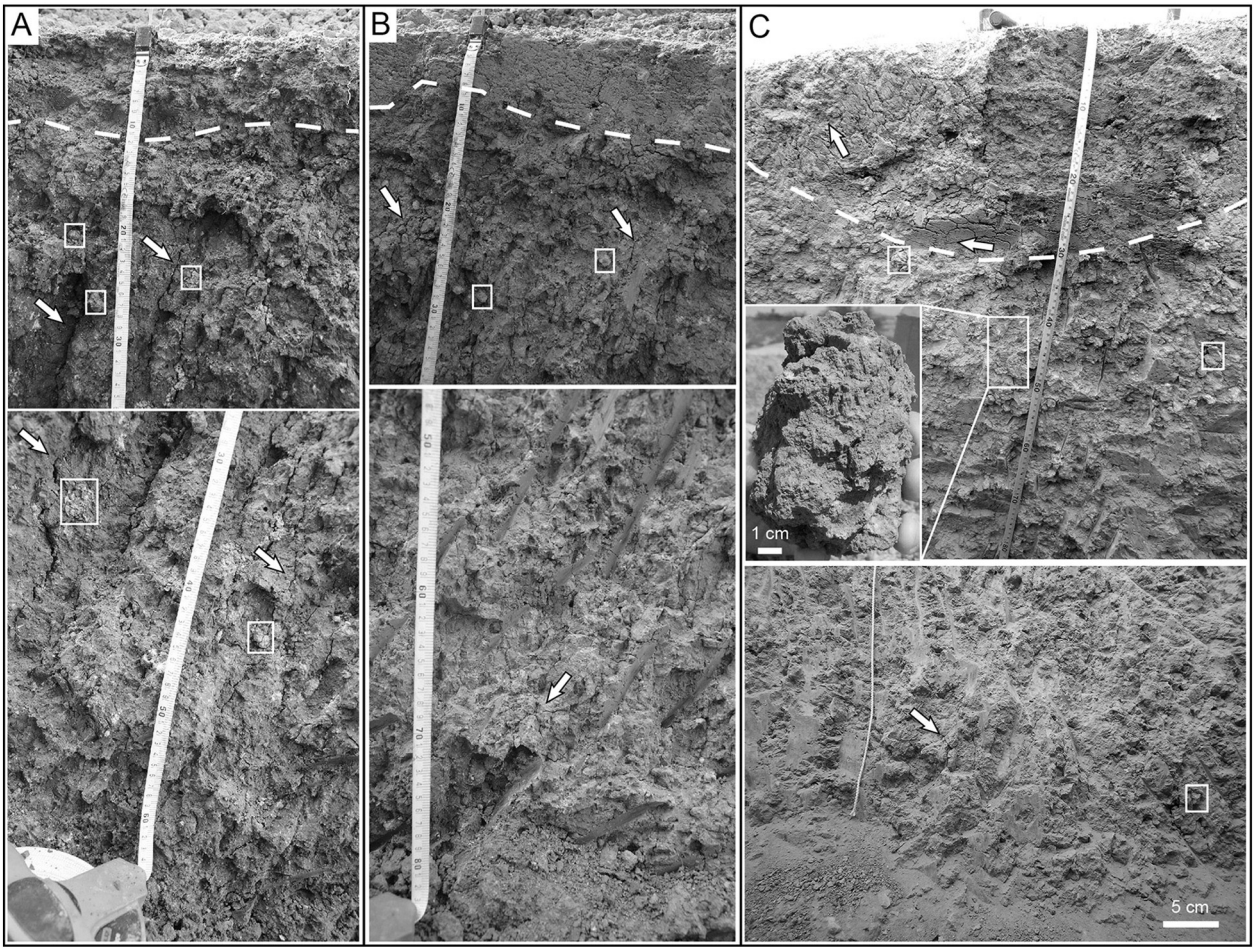

Fig. 5. Soils observed in mima-like mounds. White squares highlight some carbonate nodules inside the soil profiles. A) Soil profile Y in mima-like mound M3. The structure is angular blocky from surface to 10 cm deep and angular blocky to prismatic below 10 cm (dashed line limit). Below 10 cm, slickensides are well developed and associated with vertical cracks (arrows). B) Soil profile W in mima-like M3. The structure is single-grained to angular blocky in the first 10 cm and angular blocky to prismatic below. Slickensides are also visible with vertical cracks (arrows). C) Top photo: soil profile D in mound M1. The structure is angular blocky in the first 30 cm and some preferentially oriented cracks are visible (arrows). The structure is massive below 30 cm and peds are blocky, although cracks are less visible. Bottom photo: soil profile J in mound M1. The structure is massive. Cracks, visible in the lower part of the profile, are not well developed (arrows). Pictures of mound M3 were taken in July 2012 and mound M1 in September 2013.

amplitudes: $mc_5 > mc_3 > mc_1 > mc_4 > mc_6$. The second cluster (n = 21) is fairly similar to cluster 1, with the same five modal classes characterized by similar amplitudes, except mc_1, which is shifted toward the coarse sands. It groups samples from the upper edge of mound M3 and from both convex sides of mound M1. Cluster 3 (n = 41) groups samples from the surface of mound M1 and five modal classes are identified: $mc_5 \approx mc_3 > mc_1 > mc_4 > mc_6$. The alluvium deposited on the sides of mounds M1, M2, M3, and the transitional part between the fersiallitic pediment and the clay-rich sediment in P, are represented by cluster 4 (n = 16). This cluster is characterized by four modal classes: $mc_1 > mc_3 > mc_5 > mc_4$. Samples from the core of mounds M1, M2, and the deeper part of P are grouped in cluster 5 (n = 54). This cluster is characterized by five modal classes: $mc_3 > mc_5 > mc_4 > mc_1 > mc_6$. Cluster 6 (n = 52) is fairly similar to cluster 5, except that mc_1 mode is shifted toward very coarse sand. Samples from the core of M3 are found in this cluster. Finally, surficial horizons from the fersiallitic pediment P are displayed in cluster 7 (n = 5), with the following mode amplitudes: $mc_3 > mc_2 > mc_4 > mc_5$. The carbonate nodule residue group (n = 10) is characterized by the following 4 modes listed from higher to lower amplitudes: $mc_3 > mc_5 > mc_4 > mc_1$.

Table 2 summarizes the mean, the minimal and maximal values of the clay, silt and sand contents (%) for each cluster and for the silicate residue trapped inside the nodules. The maximal clay proportions in the clay-rich sediment are >30% and can reach 67% (e.g. in cluster 2). However, the clay content can also be fairly low, e.g. in clusters 3, 5, and 6. In clusters 5 and 6, mean values are close to 20%. As expected, alluvium and fersiallitic pediment have high proportions of sand, i.e. 47.6 ± 6% and 63.2 ± 10.1% in average, respectively. The silt-fraction is high, between 30 and 55% in all the clusters. The silicate residue trapped inside the nodules has a high silt fraction content (52.2 ± 3.5%) and displays a maximal clay value of 39.2%. The sand proportion is around 20%.

At the mound scale, highest proportions in the clay fraction (50–70%) are found in both convex sides and in the deepest layers of mound M1 (Fig. 7, mound M1 see Fig. 2B). The lowest values of clay content (<20%) are concentrated in a belt located in the middle part of the mound and at both extremities.

4.3. Clay mineralogy

Smectite and kaolinite are the main clay minerals composing the clay-rich sediment, the alluvium, and the silicate residue trapped in the carbonate nodules, whereas kaolinite is clearly dominant in the fersiallitic pediment (represented by cluster 7; Table 2). Regarding the smectite/kaolinite ratio (S/K) of samples belonging to each grain-size cluster and carbonate nodule residues (Table 2), their mean values are above 1 in clusters 1, 6 and for carbonate nodule residues. They range from 0.5 to 1 in clusters 2, 5, and 4, and are <0.5 in clusters 3 and 7. In terms of absolute values, the lowest S/K is about 0.04 in the fersiallitic pediment. High ratio values are <1 in clusters 3 and 7, between 1 and

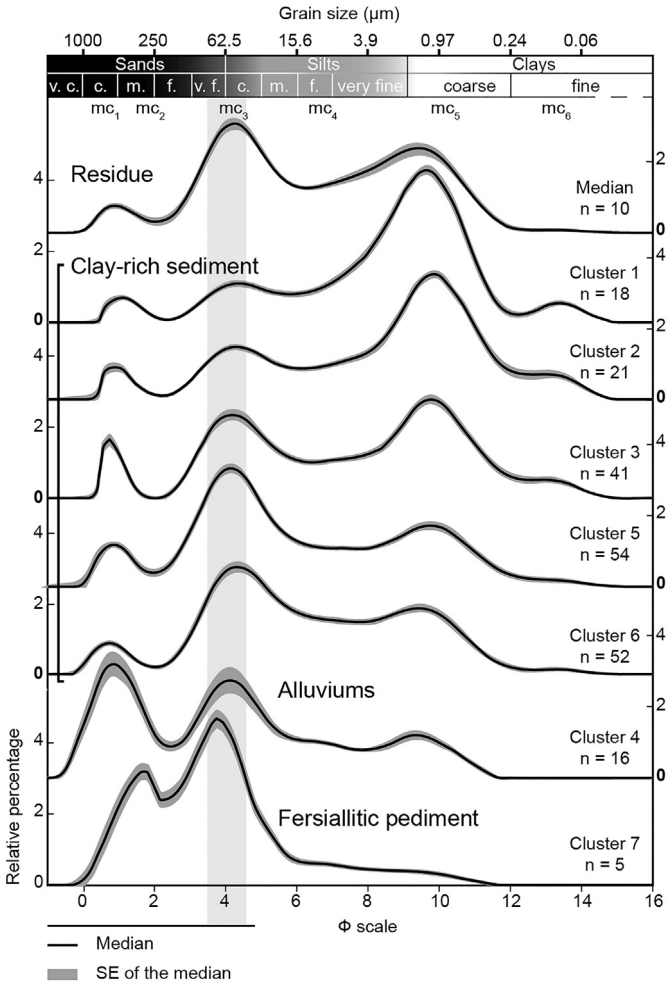

Fig. 6. Grain-size distributions grouped in seven clusters represented by their median (black line) and its associated standard error (grey-shaded areas). The clusters were processed according to the Euclidian distance between the samples (n = 207) using the Ward agglomeration algorithm (with a cophenetic correlation coefficient of 0.54). Data were previously transformed using the centred log-ratio method. Six modal classes (mc_i) are identified. Their respective presence and amplitudes are used to characterize each cluster. The dark rectangle around 4 Φ represents the desertic lœss window (20–80 µm) according to Crouvi et al. (2010). The cluster representing the silicate residue of carbonate nodules (n = 10) has not been included in the hierarchical clustering analysis in order to directly compare this particular group with other sediments from the landscape. In order to provide a maximum of information, the descriptive terminology used for sands and silts is adapted from the GRADISTAT program (Blott and Pye, 2001) and the one for the clays from the United States Department of Agriculture. Abbreviations: *v* for very, *c* for coarse, *m* for medium and *f* for fine.

1.5 in clusters 2, 5, 6, and 4, and finally <2 in cluster 1 and in carbonate nodule residues.

4.4. Soil micromorphology

Soil thin sections from mound M1 were sampled between 10 and 18 cm and 90–98 cm, respectively (Fig. 8A, B). Thin sections were also made in coarse and fine alluvium sediments (Fig. 8C, D, respectively), and the fersiallitic pediment (Fig. 8E, F).

The aggregate microstructure of the soil composing the mima-like mound (Fig. 8A) is angular blocky, with long horizontal and vertical channel voids between aggregates. The groundmass is composed of a very fine and unrecognizable clay fraction, with a pale yellow and striated b-fabric (Fig. 8A, white arrows). The cross-striated nature of the b-fabric is better observed at higher magnification (Fig. 8B, white and grey arrows). The groundmass also includes a coarse silt fraction: the grains are essentially composed of quartz and sparse epidote, feldspar, and biotite. The grains display a weakly weathered pattern, with a high sphericity, smooth edges, but an angular roundness. The two major pedofeatures are Fe—Mn oxyhydroxide nodules and carbonate nodules. They both are disorthic nodules, enclosing skeleton grains of similar nature to their surrounding matrix, but with sharp boundaries.

The coarse alluvium partially burying the flattened mound M2 was sampled between 23 and 30 cm for thin sections (Fig. 8C). Peds are subangular blocky. The groundmass is yellowish-brown, displayed as coatings around mineral grains but also as broken coatings floating between the grains (Fig. 8CII). The coarse material is sandy and composed of microcline, quartz, epidote, biotite, and feldspars. The only pedofeature is an anorthic Fe—Mn oxyhrydroxide nodule. Finally, the c/f related distribution is chitonic.

The structure of the fine-grained alluvium surrounding mound M1 (2–10 cm) is horizontal and laminated (Fig. 8D). The coarse fraction (mainly silt-sized) in the groundmass is well sorted and composed of quartz, feldspars, epidote, and biotite. There is no fine material in the groundmass, except that associated with some rare relic peds (yellowish-brown b-fabric). Anorthic Fe—Mn oxyhydroxide nodules and fibrous organic components are the only observed pedofeatures. Finally, the c/f-related distribution is coarse monic.

The structure of the peds in the fersiallitic pediment (40–48 cm) is angular blocky (Fig. 8E). The colour of the groundmass varies from pale yellow to yellowish-red. It is granostriated and porostriated, and coatings are randomly orientated. Two classes of grain-sizes are observed, one in the fine silt fraction and another in the fine sand fraction. Grains are mainly quartz and feldspars (weakly weathered), with a smooth angular shape. Epidote and biotite are also present as accessory minerals.

The b-fabric of the groundmass in the fersiallitic pediment (between 14 and 20 cm) is granostriated and its colour varies from yellow to red (Fig. 8F). There are two major grain-sizes, a fine silt and a fine sand fraction. In the silt fraction, angular quartz and feldspar grains are mainly smooth. The sand fraction displays the same mineralogy, with smooth- and subangular-shaped grains. Both fractions are weakly weathered.

5. Discussion

The presence of mima-like mounds in eroded areas from the landscape supports that erosion processes are involved in their morphology. Field observations show that vegetation patterns do not have a role in mound formation (Figs. 2A, 3). The question of another biotic factor (termite activity?) may be involved is not totally ruled out, especially as the over-dispersion spacing of the mounds may support a biotic origin (Cramer and Midgley, 2015). Nevertheless, up until now, observations pointed to an abiotic origin for mima-like mounds from northern Cameroon. Interestingly, the clay- and carbonate-rich sediment composing mima-like mounds has already been described. It was observed (i) at various depths in all the Diamare piedmont (i.e. in the Mora and Kaele plains), (ii) outcropping on the southern bank of the Mayo Tsanaga (Sieffermann, 1967; Brabant and Gavaud, 1985; Morin, 2000), and (iii) was even observed farther away in the Chad Basin between the Logone and Chari rivers (Erhart, 1954; Pias, 1962; Bocquier, 1973). Consequently, these repeated occurrences have led this sediment to be interpreted as an extended layer, possibly associated to a specific regional deposition event (aeolian, palustrine?). But how can mound morphologies be explained? Another interesting point is that mima-like mounds systematically occur in areas described as *hardés* or degraded soil (Fig. 1B), questioning the role of pedogenesis in their formation.

5.1. Mima-like mounds as Vertisol relics

Vertisols are clay-rich soils with a content ≥30% in the <2 µm size fraction (Wilding, 2004; Southard et al., 2011; FAO, 2014). The smectitic

Table 2
Mean percentages, standard errors of the mean (SEM), minimum (min) and maximum (max) clay, silt, and sand contents (relative %), smectite, and kaolinite contents (relative %), and ratios of smectite/kaolinite (S/K) in each cluster and silicate residue of carbonate nodules.

		Clay-rich sediment					Alluvium	Fersiallitic pediment	Residue
		Cluster 1	Cluster 2	Cluster 3	Cluster 5	Cluster 6	Cluster 4	Cluster 7	–
n		18	21	41	52	54	16	5	10
Clay (%)	**Mean**	**49.5**	**52.4**	**39.2**	**23.9**	**22.8**	**12.0**	**4.5**	**26.2**
	SEM	*2.2*	*2.2*	*1.4*	*1.0*	*1.0*	*1.0*	*0.8*	*2.8*
	Min value	36.7	45.5	28.1	14.0	9.1	7.6	3.3	22.1
	Max value	56.2	67.0	48.6	35.0	33.0	16.4	6.3	39.2
Silt (%)	**Mean**	**40.6**	**34.3**	**42.1**	**46.0**	**55.0**	**40.4**	**32.3**	**52.2**
	SEM	*1.9*	*1.4*	*1.3*	*0.8*	*1.1*	*3.0*	*3.9*	*3.5*
	Min value	34.5	26.0	35.3	40.2	48.0	32.3	25.7	29.3
	Max value	53.0	39.7	51.4	52.8	68.4	55.3	39.5	47.9
Sand (%)	**Mean**	**9.8**	**13.3**	**18.7**	**30.1**	**22.2**	**47.6**	**63.2**	**21.6**
	SEM	*0.8*	*1.2*	*1.0*	*1.4*	*0.9*	*6.0*	*10.1*	*3.0*
	Min value	7.1	7.1	14.2	22.1	16.0	37.1	54.2	10.6
	Max value	14.9	17.0	22.4	41.6	29.4	53.7	70.9	20.4
n		5	5	5	5	5	5	3	12
Smectite (%)	**Mean**	**42.9**	**30.4**	**25.1**	**29.8**	**40.7**	**33.8**	**12.2**	**46.0**
	SEM	*8.9*	*3.6*	*2.8*	*7.3*	*2.8*	*4.6*	*0.8*	*4.2*
	Min value	15.8	20.2	14.1	4.5	35.0	23.8	10.2	24.1
	Max value	70.1	42.4	29.1	47.9	48.4	49.4	13.1	71.5
Kaolinite (%)	**Mean**	**37.4**	**45.4**	**48.1**	**46.7**	**40.2**	**46.1**	**54.1**	**30.6**
	SEM	*4.6*	*1.9*	*1.9*	*4.1*	*2.1*	*2.9*	*3.1*	*2.3*
	Min value	21.4	40.5	43.1	35.5	35.9	34.9	48.9	16.2
	Max value	46.8	49.2	53.5	60.4	46.7	50.4	60.9	44.1
S/K	**Mean**	**1.4**	**0.7**	**0.5**	**0.7**	**1.0**	**0.8**	**0.2**	**1.8**
	SEM	*0.4*	*0.1*	*0.1*	*0.2*	*0.1*	*0.1*	*0.1*	*0.2*
	Min value	0.4	0.4	0.3	0.5	0.8	0.4	0.0	0.7
	Max value	2.9	1.0	0.6	1.3	1.3	1.2	0.3	3.8

group of swelling clays (e.g. montmorillonite) represents the main soil clay mineralogy. Consequently, soils swell and shrink when they undergo marked changes in their soil moisture content (Hubble, 1984; Dudal and Eswaran, 1988; Mermut et al., 1996; Southard et al., 2011). Swell-shrink processes induce important volume variations in the soil (Southard et al., 2011). They can shape the ground surface with an alternation of knolls and depressions, known as gilgai micro-relief (Prescott, 1931; Oakes and Thorp, 1950; Hallsworth et al., 1955; Mermut et al., 1996). They also lead to characteristic macro-features in the solum, such as vertical cracks, slickensides (or grooved shear planes), and cyclic horizons, organized in micro-low, micro-high, and intermediate parts at all depths (Wilding and Tessier, 1988; Eswaran et al., 1988; Wilding et al., 1990). The presence of a vertic horizon characterized by these macro-features is needed to define a soil as a Vertisol (FAO, 2014). According to Wilding et al. (1990), micro-lows have deep A and Bss horizons, while micro-highs have a thin A horizon, without any Bss horizons. When present, a Bk horizon in the micro-highs is characterized by a higher content in hard secondary carbonate than in micro-lows.

Today, climatic conditions in northern Cameroon (see Section 2) are favourable for Vertisol genesis. In terms of their global distribution, about 60% are found in the Tropics (Wilding, 2004). Brabant and Gavaud (1985) described and mapped some Vertisols in the Diamare, but most of them are in the south bank of the Mayo Tsanaga, near Kaele, or downstream near the sand belt. In the studied sites where mima-like mounds are observed, Planosol, associated with Solonetz, is generally the soil type. However, independently of the nature of soil, the striking feature is that mima-like mounds are observed in degraded areas (*hardés*). Soil descriptions, grain-size distributions, clay mineralogy, and thin-section observations suggest that mima-like mounds can be interpreted as degraded Vertisols or Vertisol relics, which could possibly have evolved toward Planosol or Solonetz.

Soil observations demonstrate that cycling and vertical cracks are present in some parts of the mima-like mounds (Fig. 5). Vertical cracks are observable in the mound M3 (Fig. 5A, B). In soil profile D (M1), what can be interpreted as a Bss horizon seems to have been truncated (Fig. 5C, top). Interestingly, the clay content in micro-lows can be slightly higher than in micro-highs (Yule and Ritchie, 1980; Mermut et al., 1996). The truncated Bss horizon is located on the perimeter of the mound M1, where the clay fraction reaches 67% (Profile D, Fig. 7). It may thus be interpreted as an ancient micro-low. Cracks are less visible in the profile J (Fig. 3C, down) compared to what is seen in M3. This could be due to the season in which the pictures were taken. In M3, they were taken during the dry season of July 2012 and in mound M1 in September 2013, during the wet season. The cracks generally occur during the dry season; it is likely that they were less visible in September. Nevertheless, the soil structure observed in mima-like mounds is typical of swell-shrink processes. Fe—Mn oxides and carbonate nodules are significant components of mima-like mounds (Fig. 2B, C) and they are

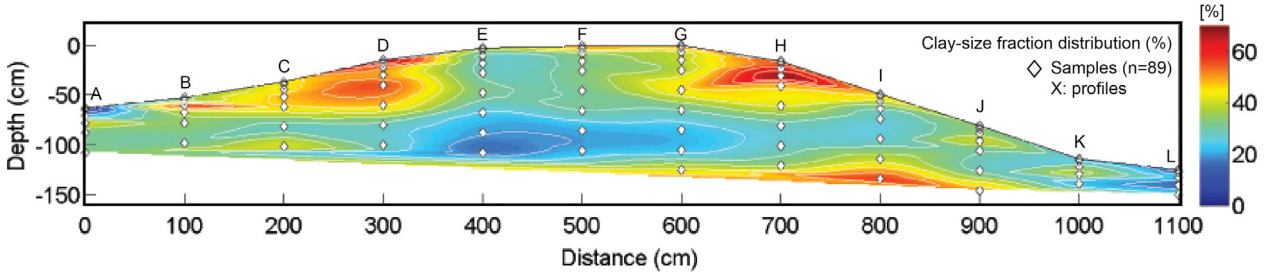

Fig. 7. Distribution of the clay-size fraction (%) in mima-like mound M1 according to a cubic interpolation (n = 89). Capital letters refer to profile names.

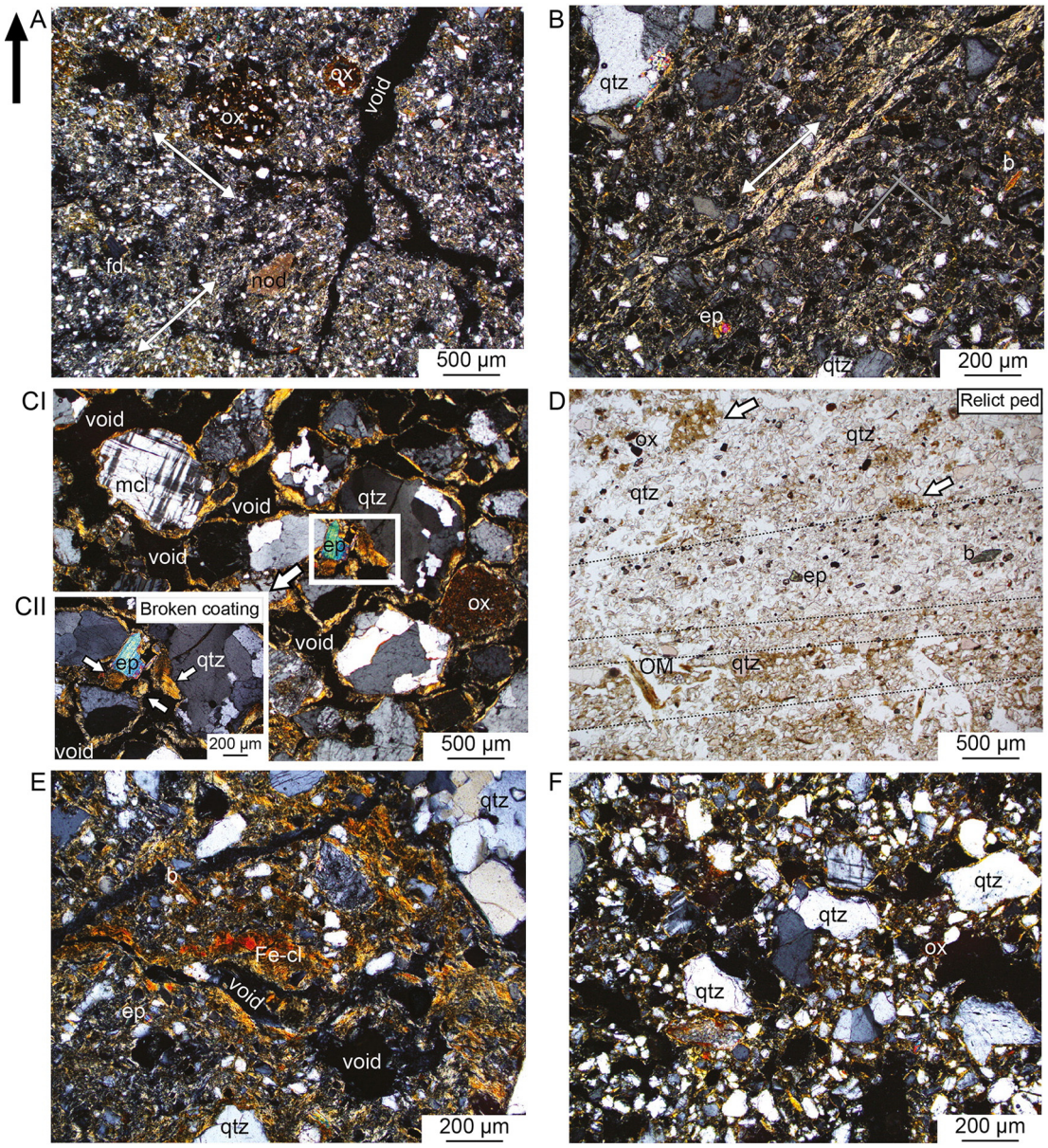

Fig. 8. Illustrations of soil thin sections from the various sediments composing the landscape. The black arrow refers to the top. Following abbreviations are used: *ox* for Fe—Mn oxide nodule, *nod* for carbonate nodule, *fd* for feldspar, *mcl* for microcline, *qtz* for quartz, *ep* for epidote, *b* for biotite, *OM* for organic matter and *Fe-cl* for iron-clay coating. A) Mima-like mound (M1) between 10 and 18 cm: the groundmass is pale yellow and has a striated b-fabric, whose orientation is illustrated by the white arrows (cross-polarized light). B) Mima-like mound (M1) between 90 and 98 cm: the grey and white arrows show the cross-striated and striated orientation of the groundmass, respectively (cross-polarized light). The striated and cross-striated nature of the b-fabric in the mima-like mounds (A and B) can be referred to as slickensides, which are typical features resulting from shrink-swell processes. C) Coarse alluvium interfingering the clay-rich sediment in M2 (23–31 cm): a broken coating is shown in a white box (cross polarized light); the c/f related distribution is chitonic with a fine yellow birefringence layer surrounding all minerals. D) Fine alluvium (2–10 cm) surrounding M1: several horizontal deposits are shown and highlighted by black dashed-lines; relict peds (shown by white arrows) show a c/f single-spaced porphyric, (plane-polarized light) and are found in a c/f coarse monic material. E) Fersiallitic pedolith between 40 and 48 cm (cross-polarized light): the groundmass varies from yellow to yellowish-red and coatings are randomly orientated. F) Fersiallitic pedolith between 14 and 21 cm (cross-polarized light): the groundmass is yellow to yellowish-red and displays a granostriated b-fabric. (For interpretation of the references to colour in this figure legend, the reader is referred to the web version of this article.)

known to be common features in Vertisols (Wieder and Yaalon, 1974; Ahmad, 1983). Regarding grain-size distributions and clay mineralogy of the soil residue trapped in carbonate nodules, it is similar to the surrounding soil (Fig. 6, Table 2). Consequently, these nodules are secondary pedogenic carbonate nodules precipitated inside the mima-like mound soil matrix. However, in Vertisols, secondary carbonate nodules are generally observed in the Bk horizon, which occur at about 20 cm deep in micro-highs, or about 100 cm deep in micro-lows (Wilding et al., 1990; Kovda et al., 2003, 2006). In mima-like mounds, even if some nodules are observed in deep horizons, they accumulate in large amounts at the surface, forming a cover (Fig. 2B, C). It is likely that the erosion of the surficial horizons, leaving only the Bk horizon at the surface, explains this surficial nodule accumulation.

Regarding the grain-size distributions and the clay mineralogy in mima-like mounds, they are similar to what is generally expected in Vertisols. The clay content in mima-like mounds is high, with an average proportion of 32% (standard error of the mean = 0.935, n = 186) and with maximum values reaching 67% (Table 2). In addition, they contain a high proportion of smectite (Table 2), which is significantly higher than in the overlaying fersiallitic pediment (mean S/K ratio = 0.2 ± 0.1). However, even if these components seem to be key features of the sediment forming mima-like mounds, they do not strictly

correspond to Vertisol characteristics. First of all, in some cases, the clay content can be <30% (Table 2). The grain-size distribution shows that coarse clays are more abundant that fine clays, which is generally the opposite in Vertisols well-structured (McGarry, 1996). Moreover, kaolinite can be the main clay mineral composing the clay-size fractions, which is often the case at the mound surface (cluster 3, Table 2). But a potential and progressive denaturation of smectite or an exogenic and aeolian contribution can explain this. Regardless of the reasons why kaolinite is dominant, these observations show that smectite is not always the main clay mineral in the clay-rich sediment, whereas it should be in Vertisol (Coulombe et al., 1996a). At the microscale, the b-fabric is striated to cross-striated (Fig. 8A, B), which is common in clay-rich soils subject to shrink-swell processes (Dalrymple and Jim, 1984; Jim, 1990). These features are particularly observed in mima-like mounds and absent in the alluvium or the fersiallitic pediment. All these observations point to Vertisols, but not exclusively. Consequently, mima-like mounds from the Diamare piedmont are interpreted as "degraded Vertisols" or "Vertisol relics".

5.2. From gilgai micro-relief to present-day mima-like mounds

The mima-like mounds from the Diamare piedmont may thus be interpreted as Vertisol relics. Vertisol degradation implies that there was a phase during which the Vertisols developed and another phase when they were degraded and eroded. The *Bio-Rhexistasy* theory, proposed by Erhart (1967), illustrates this conjecture. He described two major environmental phases: (i) *Biostasy* phases are stable periods characterized by dense vegetation cover, high soil development and biogeochemical weathering, during which leaching processes, and biogeochemical deposits prevail. In contrast, (ii) *Rhexistasy* phases are characterized by instable periods due to drastic changes in ecosystems. The decrease of vegetation cover and the destabilization of soils due to hydric changes favour erosion and detrital sedimentary deposits. It is demonstrated that there is a critical threshold of 55% vegetation cover, below which erosion rates increase rapidly (Snelder and Bryan, 1995). At the regional scale, Vertisols are perfectly adapted to present-day climatic conditions and can easily develop in the Diamare piedmont because of the presence of clay-rich sediment. However, Vertisols are located at lower altitudes compared to mima-like mounds (Martin, 1961; Sieffermann, 1967; Bocquier, 1973; Brabant and Gavaud, 1985). It can be hypothesized that the topography plays an important role for Vertisol genesis in this region. This is explained by their chemical properties. Vertisols must have a high content of clay with high surface area and usually be highly alkaline (Coulombe et al., 1996a). The cation exchange capacity in Vertisols is typically high, saturated with Ca^{2+}, Mg^{2+}, and Na^{+}, depending on the clay mineralogy and the parent material. Moreover, the pH is often neutral to alkaline. These conditions, and a high silica activity, favour the stability and the formation of smectite (Eswaran and Wong, 1978). On the contrary, leaching processes and acidic conditions induce the denaturation of smectite and the formation of kaolinite, leading to the development of other types of soils (Eswaran et al., 1988). The mima-like mounds are presently located in eroded and degraded areas (*hardés*), but it is possible that these areas were not always degraded. Consequently, it is proposed that the extent of the area favourable to Vertisol genesis varied through time and reached mima-like mound locations under different climatic conditions.

To explain the link between Vertisol genesis and mound formation, it is interesting to note that the diameter of mima-like mounds, which can reach up to 10 m, is consistent with what is commonly observed in a gilgai landscape. The common distance from the micro-high to the micro-low, or the radius, ranges from 2 to 5 m (Miller and Bragg, 2007). Consequently, Vertisol genesis could have been associated with a gilgai micro-relief, during a period when Vertisol areas were extensive. This period of widespread occurrence can be defined as a *Biostasy* phase (Fig. 9). Precipitation of secondary pedogenic carbonate nodules and Fe—Mn micro-nodules are linked to Vertisol genesis, and thus, to this phase as well. Then, a *Rhexistasy* phase occurred as a response to climatic changes, inducing a decrease in favourable areas for Vertisol genesis, and an increase in erosion processes (Fig. 9). The gilgai micro-relief might have favoured preferential runoff in micro-lows rather than in micro-highs, inducing pejoration of landscape irregularities. Consequently, mima-like mounds observed in the present-day landscape are interpreted as residual micro-highs and micro-lows inherited from the gilgai micro-relief and resulting from differential erosion (Fig. 9). Furthermore, the wind has probably played a determinant role as an erosion agent. The Sahel of West Africa is a place for high-velocity winds produced by intense baroclinal gradients. In these subhumid to arid areas, wind erosion is important and creates a large panel of morphologies such as inverted relief or yardangs, for example, which are the result of wind deflation erosion (Goudie, 2013). The mima-like mounds might be the result of contemporary interactions of both aeolian and fluvial erosion systems. This erosion association is highly discussed (Goudie, 2013) but seems to be effective particularly under short-term climate changes (Bullard and Livingstone, 2002). Independently of the type of erosion agent, erosion of fine fractions from surficial horizons can explain the relative accumulation, or pavement, of secondary carbonate nodules and Fe—Mn micro-nodules, normally found in a deeper Bk horizon, as a layer at the mima-like mound surface (Fig. 2B). It also explains the high clay content in both sides of the mounds (Fig. 7), which are the remaining parts of ancient micro-lows (Fig. 9).

5.3. Sediments adjacent to mima-like mounds and landscape changes

Analyses of sediments adjacent to mima-like mounds provide evidence of landscape geomorphogenesis. The grain-size distributions in the alluvium (both fine and coarse) and in the fersiallitic pediment are represented in clusters 4 and 7, respectively (Fig. 6). These two clusters lack a clay fraction (Fig. 6, mc_6). They are also different from each other with the presence of mc_2 in cluster 7 and a significant higher amplitude of mc_5 in cluster 4. These variations can be explained by different sources of sediments and/or transportation parameters (Vandenberghe, 2013). From their mineralogy observed in thin sections (Fig. 8), they definitely differ in terms of transportation parameters rather than sources of sediment.

Coarse alluvium includes some broken clay coatings and a fine yellow birefringence rim surrounds all mineral grains (Fig. 8C). This type of chitonic c/f related distribution corresponds to periods of high energy (coarse fraction) followed by slow water flow, which resulted in impregnations by fine material (Mücher et al., 2010). Field observations showed that the coarse alluvium was interfingering the clay-rich sediment of mound M2 (Fig. 4B), suggesting contemporaneous deposition. In the fine alluvium (Fig. 8D), the fine fraction is only present as relic peds, demonstrating the contribution of some reworked soils. Moreover, the S/K ratio in the alluvium varies between 0.45 and 1.23, which is close to the values observed in the clay-rich sediment, emphasizing the reworking of this proximal sediment. The fersiallitic pediment shows a complete disorganization of the clay-Fe coatings in the deepest horizon (Fig. 8E), while they are poorly marked in the surficial horizon (Fig. 8F). This disorganization indicates that fersiallitic pedofeatures are probably inherited and the soil material reworked. Therefore, the fersiallitic pediment may instead be a fersiallitic pedolith (Retallack, 2001). In the landscape, this pedolith is always found above the clay- and carbonate-rich sediment (Figs. 3, 4). This suggests they were reworked at the same time as the Vertisol surficial horizons, during gilgai micro-relief erosion. This means that the fersiallitic soil developed during the same period as Vertisols, but upstream. These interpretations strengthen hypotheses of high erosion events (*Rhexistasy* phase) occurring in northern Cameroon after a phase favourable for soil development (*Biostasy* phase). Moreover, they emphasize the complexity of erosion-deposition processes in such terrestrial environments.

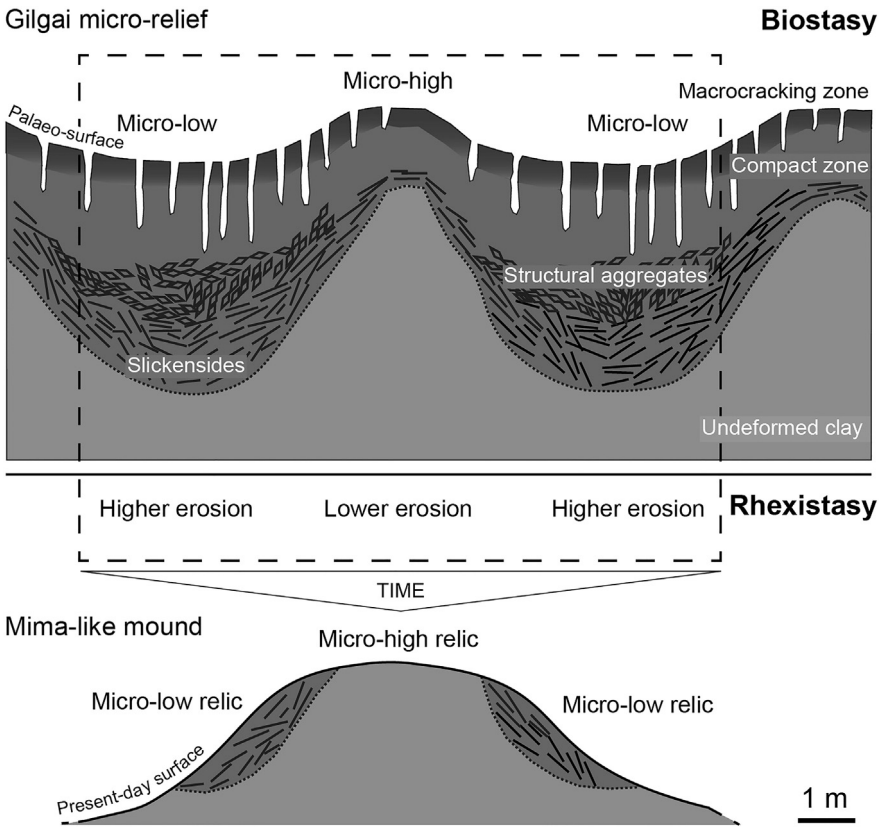

Fig. 9. Hypothetical erosion scenario leading to mima-like mound formation. Top: this figure is modified from Coulombe et al. (1996b) and shows Vertisol genesis associated with a gilgai micro-relief characterized by alternations of micro-highs and micro-lows. Secondary carbonate nodules form during Vertisol genesis in a Bk horizon, developing at 20 cm in micro-highs and at 100 cm in micro-lows. Bottom: mima-like mound, or residual gilgai micro-relief, after a phase of erosion and composed by relics of micro-lows and micro-highs (compare with Fig. 7). Vertisol genesis at mima-like mound locations may occur during a *Biostasy* phase, characterized by wetter conditions than in present-day; onset of erosion may correspond to a *Rhexistasy* phase, characterized by drastic changes in climatic conditions.

Finally, grain-size distributions (Fig. 6) for all the sediments, including the clay-rich sediment, show a common modal class belonging to the desertic lœss window (20–80 μm) defined by Crouvi et al. (2010). At the micro-scale, well-sorted, smooth, and angular quartz, feldspars, and a few epidote grains characterize this fraction (Fig. 8). These observations raise questions about a possible aeolian contribution to the sediments. Maley (1981) already proposed an allochtonous contribution of sediments to explain the wide extent of the clay-rich sediment layer in the Far North region of Cameroon. Later, Mpeck (1994) studied the *formation of Doyang*, located in the south bank of the Mayo Tsanaga, between Maroua and Kaele, a formation already studied by Sieffermann in 1967. Mpeck (1994) proved the aeolian origin for this silty clay-rich deposit and emphasized its probable reworking after deposition. As previously demonstrated, field observations suggest the absence of a genetic relationship between the granite bedrock and the clay-rich sediment (Fig. 4D), making its origin as a simple result of granite bedrock weathering unlikely. Nevertheless, more investigations are needed to strengthen the hypothesis of an aeolian contribution to the mima-like mound area.

5.4. Are mima-like mounds inherited from Late Pleistocene-Holocene climatic changes?

Two main phases can thus explain mima-like mounds (Fig. 9); (i) during *Biostasy*, the Vertisol area was extended, and (ii) during *Rhexistasy* erosion increased, leading to Vertisol degradation in areas corresponding to the present-day mima-like mound locations. The shift from one phase to another probably results from regional climatic forcing. It is proposed that the extent of Vertisol areas was related to wetter conditions than nowadays. An increase in erosion, and thus the formation of mima-like mounds, can result from a serious decrease in the vegetation cover induced by climate change from wetter toward drier conditions. With these two environmental constraints, it is possible to discuss the potential role of Quaternary climatic changes in the Chad Basin area.

During the Quaternary (Fig. 10), the main climatic changes in the African tropics are related to the intensity and the latitudinal position of the monsoon front (or ITCZ - Inter-Tropical Convergence Zone), which is a thermodynamic heat response to orbital forcing (deMenocal et al., 2000; Mayewski et al., 2004; Wanner et al., 2008; Lézine et al., 2011; Shanahan et al., 2015). From ca. 14.8 to 5.5 ka BP, a strengthening and a northward expansion of the African monsoon system, due to a gradual increase of the Northern Hemisphere summer insolation, led to a climatic optimum, known as the African Humid Period (AHP; deMenocal et al., 2000; deMenocal and Tierney, 2012; Shanahan et al., 2015). This period is characterized by a higher rainfall rate and a general northward displacement of the vegetation zonation by 400–500 km, in conjunction with the monsoon system shift (Lézine, 1989; Hély et al., 2009). However, the climatic conditions during Holocene were unstable and marked by hydrological variations (Mayewski et al., 2004). Several studies showed differences between Early Holocene (9.5–8 ka BP) and mid-Holocene (6.5–5 ka BP; Maley, 1983, 2010; Gasse, 2000; Lézine et al., 2011). Lézine et al. (2011) examined more than 1500 paleohydrological records collected between 10 and 28°N in the Sahara and the Sahel in Africa and demonstrated that a reduced and fragmented geographical extent of lakes and wetlands occurred during the Early Holocene (9.5–8 ka BP) compared to mid-Holocene (6.5–5 ka BP). The widespread extent of humid sectors in the mid-Holocene can be attributed to high groundwater levels, which might have been filled during Early Holocene, when maximum rainfall was recorded. In these conditions, the

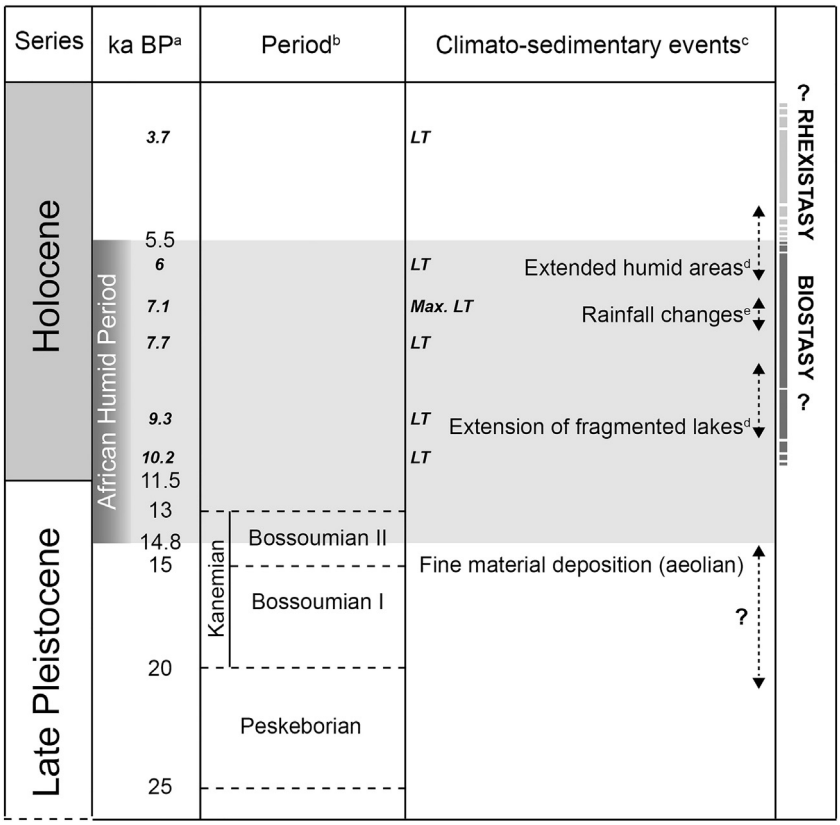

Fig. 10. Summary of the main events that occurred in the Chad Basin during the Late Pleistocene-Holocene period and relationships with mima-like mound formation ([a]DeMenocal et al., 2000; [b]Hervieu, 1969, Brabant and Gavaud, 1985; [c]Hervieu, 1970; Maley, 1981, 2004; Morin, 2000; [d]Lézine et al., 2011; [e]Servant, 1983). Abbreviations: *LT* for lacustrine transgression; *Max* for maximum. The African Humid Period lasted from 14.8 ka to 5.5 ka BP; the extent of Vertisol areas in the Diamare piedmont is hypothesized to have varied during this period in concomitance with different climatic events (e.g. lake-level changes, extent of humid areas) and may have been larger than in the present-day. This period can be referred to as a *Biostasy* phase. A climate change, inducing an increase of erosional processes characterized the end of the AHP. Vertisol erosion in a gilgai micro-relief is likely at the origin of the present-day mima-like mound landscape. This period can be referred to as a *Rhexistasy* phase. The time limits of all these phases are uncertain and illustrated by dashed lines and arrows.

humid areas might have been widespread during the mid-Holocene, even if rainfall decreased (Lézine et al., 2011). Therefore, it is likely that the extent of Vertisol areas associated with a gilgai micro-relief has varied in the Diamare piedmont during the AHP. These variations may be concomitant with humid sector variations. Vertisol genesis in the Diamare piedmont might therefore be related to palustrine areas.

The contemporaneous deposition of the coarse alluvium and the clay-rich sediment implies changes in transportation energy. As demonstrated above, climate was not stable during the AHP. Servant (1983) already identified rainfall changes around 7 ka BP, due to the slight migration of the monsoon front position toward the south (Fig. 10). The rainfall regime is directly associated with this front. Dhonneur (1974) demonstrated that cumulonimbus clouds are dominant preceding the monsoon front and associated with big raindrops (>2 mm); on the other hand, stratus clouds are dominant behind the front, and their associated raindrops are smaller (<2 mm). Consequently, before 7 ka BP, fine sedimentary deposits are favoured, whereas after 7 ka BP, coarse-grained sediments are dominant (Maley, 1983; Servant, 1983). Another process can be related to variations in the Lake Chad water level, which is the base level of rivers draining into the Chad Basin, such as the Mayo Tsanaga (Fig. 1B). Leopold and Bull (1978) defined the base level of a river as the elevation below which a stream cannot flow. The base level changes would have caused disequilibrium in river profiles: if it rises, the whole profile will tend to be raised by increasing accommodation space and then favouring deposition processes and fine material production; if it lowers, the profile will tend to be lowered by increasing erosion and coarse material production (Davis, 1902). Several studies showed that the lake level would have varied several times during the Holocene (Durand, 1982, 1995; Ghienne et al., 2002; Maley, 2004; Bouchette et al., 2010). Both runoff change processes due to rainfall and/or base level changes might have induced transportation energy changes able to explain the coarse alluvium/clay-rich sediment interfingering.

The AHP ended around 5.5 ka BP (Fig. 10), mainly because of the weakening and the southward migration of the monsoon front (Kröpelin et al., 2008; deMenocal and Tierney, 2012; Shanahan et al., 2015). Even if it is known that another humid phase occurred between 3.5 and 2.5 ka BP (Lézine et al., 2011), it never reached the same maximum of rainfall. Nevertheless, efficient Vertisol genesis cannot be excluded during this period as well, and another erosion period might have been initiated again at the end of this second wet phase. However, it is likely that erosion might have increased with drier conditions and a decrease in vegetation cover. Consequently, it is probable that the *Rhexistasy* phase might be related to the end of the AHP.

Finally, the question remains of the potential aeolian origin of the material composing all the sediments. It was demonstrated that aeolian sediments are generally mobilized under dry conditions and stabilized during wet conditions, due to the increase of vegetation cover and soil moisture (Kocurek, 1998; Swezey, 2001; Vandenberghe, 2013). McTainsh (1984) showed that the isohyet of 400 mm/yr is the minimum for dust stabilization. It is recognized that during the climato-sedimentary event, known as the Bossoumian II (from 15 ka to 13 ka BP; Hervieu, 1969, 1970; Maley, 1981; Brabant and Gavaud, 1985; Morin, 2000), fine aeolian deposits were favoured (Fig. 10). However, Durand (1995) showed that aeolian stabilization might have already been possible since 20 ka BP (Kanemian climato-sedimentary event). He demonstrated that the ergs observed in northern Cameroon and northeastern Nigeria, which represent the maximal extent of the

Sahara, were probably formed before 28 ka BP and thus much older than the Kanemian. Consequently, the Kanemian was not as dry as was previously thought, and it is not excluded that the 400 mm/y isohyet might have been effective since 20 ka BP, leading to the possible stabilization of aeolian material.

In summary, the following chronological succession is proposed: (i) a pre-AHP period, during which aeolian material is deposited and probably reworked and mixed with the local material along the slopes, (ii) an AHP period, during which Vertisol developed, associated to gilgai micro-relief and secondary mineral precipitation; the extent of Vertisol was larger than nowadays, and during this period, fersiallitic soils were developing upstream Vertisols; and finally, (iii) a post-AHP period, during which erosion increased, forming the present-day mima-like mounds and reworking the fersiallitic soil above the clay-rich sediment. However, dating constraints are needed to support and improve the proposed chronology. Nevertheless, mima-like mounds and their adjacent sediments offer a great potential for the sedimentary record of the Chad Basin.

6. Conclusions

Investigations on newly observed earth mounds in the Chad Basin led to an original interpretation of their formation. According to their size and spatial distribution, they can be defined as mima-like mounds (Cramer and Barger, 2014). Recently it was postulated that mima-like mound shapes result from the combination of erosion and/or aeolian and vegetation patterns. Mima-like mounds observed in northern Cameroon are strongly linked to erosion, and there is no evidence that vegetation patterns play or played any particular role. Field observations and analytical results, such as grain-size distribution, clay mineralogy, and thin section observations show mima-like mounds to be degraded Vertisols or Vertisol relics developed in a former gilgai micro-relief. Erosional processes induced the stripping of surficial horizons of Vertisols and the accentuation of the gilgai micro-relief. They also induced the formation of a large accumulation of pedogenic nodules at the mound surface, remains of a former Bk horizon. In addition, a fersiallitic pedolith (e.g. reworked soil) buries them at some places in the landscape and this highly supports the occurrence of erosion events at some points. Present-day climatic conditions in the region of northern Cameroon are favourable to Vertisol genesis. But locally, climatic changes in the region during the Quaternary may have modified the extent of the Vertisol area. Larger areas of Vertisol can be related to widespread humid fields during the second part of the AHP during the Mid-Holocene (*Biostasy* phase). At the end of the AHP, climatic conditions became drier, inducing a decrease in vegetation cover and an increase in erosional processes (*Rhexistasy* phase). Moreover, water level fluctuations of Lake Chad and/or changes in the rainfall regime also occurred during the AHP, which might have influenced transportation-deposition processes in the Diamare piedmont. These changes would explain the occurrence of coarse alluvium interfingering the clay-rich sediment in a mima-like mound, which indicates a concomitant formation. Some questions are still pending regarding the origin of some fractions in the sediments from this landscape: all of them include a modal class corresponding to an aeolian component. Therefore, the possibility of a substantial aeolian contribution occurring before the AHP is proposed but this hypothesis remains open. Finally, the mima-like mounds from the Chad Basin have a significant potential as a regional sedimentary record.

Acknowledgements

The authors want to thank Dr. Jean-Louis Rajot and the other members of the Hydraride program (2011), who drew our attention to the mounds of the Sudano-Sahelian belt and collected the first samples from Niger and Burkina Faso. They also made the first observations in Northern Cameroon. The PEERS MORDRED insured the logistical aspects during the initial fieldwork in 2012. The LMI PICASS'EAU from the IRD and the members of Water and Environmental Sciences lab from the University of Ngaoundéré brought their help for logistic and technical support for fieldwork in 2013. Dr. Thierry Adatte (ISTE, University of Lausanne) performed XRD analyses. The authors also want to thank Aurélie Rubin and Yohan Ancey for pH measurements and sample preparation for clay mineralogy analyses. The authors appreciated substantial improving remarks given by Prof. Dr. Alain Durand and Karin Verrecchia on a first version of the manuscript. The authors would like to thank the two anonymous reviewers who provide extremely useful comments. The Swiss National Science Foundation supported this work (grant no. 200021-147038).

Map. KMZ file containing the Google map of the most important area described in this article.

Appendix A. Supplementary data

Supplementary data associated with this article can be found in the online version, at: http://dx.doi.org/10.1016/j.geomorph.2016.02.021. These data include the Google map of the most important area described in this article.

References

Ahmad, N., 1983. Vertisols. In: Wilding, L.P., et al. (Eds.), Pedogenesis and Soil TaxonomyThe Soil Orders vol. II. Elsevier Science, New York, USA, pp. 91–123.
Blott, S.J., Pye, K., 2001. GRADISTAT: a grain-size distribution and statistics package for the analysis of unconsolidated sediments. Earth Surf. Process. Landf. 26, 1237–1248.
Bocquier, G., 1973. Genèse et Evolution de Deux Toposéquences de Sols Tropicaux du Tchad. Interprétation Biogéodynamique. Mémoires de l'ORSTOM, Paris, France, p. 327.
Bouchette, F., Schuster, M., Ghienne, J.-F., Denamiel, C., Roquin, C., Moussa, A., Marsaleix, P., Duringer, P., 2010. Hydrodynamics in Holocene Lake Mega-Chad. Quat. Res. 73 (2), 226–236. http://dx.doi.org/10.1016/j.yqres.2009.10.010.
Brabant, P., Gavaud, M., 1985. Les Sols et les Ressources en Terres du Nord-Cameroun. ORSTOM, Paris, France (369 pp.).
Bullard, J., Livingstone, I., 2002. Interactions between Aeolian and fluvial systems in dryland environments. Area 34, 8–16.
Butler, D.R., 1995. Zoogeomorphology: Animals as Geomorphic Agents. Cambridge University Press, Cambridge, UK.
Clark, P.J., Evans, F.C., 1954. Distance to nearest neighbor as a measure of spatial relationships in populations. Ecology 35 (4), 445–453.
Coulombe, C.E., Dixon, J.B., Wilding, L.P., 1996a. Mineralogy and chemistry of Vertisols. In: Ahmad, N., Mermut, A.R. (Eds.), Vertisols and Technologies for their Management. Elservier Science, Amsterdam, The Netherlands, pp. 115–188.
Coulombe, C.E., Wilding, L.P., Dixon, J.B., 1996b. Overview of Vertisols: characteristics and impacts on society. Adv. Agron. 57, 289–357.
Cox, G.W., 1984. The distribution and origin of mima mounds grasslands in San Diego County. California, Ecology 65, 1397–1405.
Cramer, M.D., Barger, N.N., 2014. Are mima-like mounds the consequence of long-term stability of vegetation spatial patterning? Palaeogeogr. Palaeoclimatol. Palaeoecol. 409, 72–83http://dx.doi.org/10.1016/j.palaeo.2014.04.026.
Cramer, M.D., Midgley, J.J., 2015. The distribution and spatial patterning of mima-like mounds in South Africa suggests genesis through vegetation induced aeolian sediment deposition. J. Arid Environ. 119, 16–26.
Cramer, M.D., Innes, S.N., Midgley, J.J., 2012. Hard evidence that heuweltjie earth mounds are relictual features produced by differential erosion. Palaeogeogr. Palaeoclimatol. Palaeoecol. 350-352, 189–197.
Crouvi, O., Amit, R., Enzel, Y., Gillespie, A.R., 2010. Active sand seas and the formation of desert lœss. Quat. Sci. Rev. 29 (17–18), 2087–2098. http://dx.doi.org/10.1016/j.quascirev.2010.04.026.
Dalrymple, J.B., Jim, C.Y., 1984. Experimental study of soil microfabrics induced by isotropic stresses of wetting and drying. Geoderma 34, 43–68.
Davis, W.M., 1902. Basel-level, grade and peneplain. J. Geol. 10, 77–111.
DeMenocal, P.B., Tierney, E.J., 2012. Green Sahara: African humid periods paced by Earth's orbital changes. Nat. Educ. 3 (10) (12 pp.).
DeMenocal, P.B., Ortiz, J., Guilderson, T., Adkins, J., Sarnthein, M., Baker, L., Yarusinsky, M., 2000. Abrupt onset and termination of the African humid period: rapid climate responses to gradual insolation forcing. Quat. Sci. Rev. 19, 347–361.
Dhonneur, G., 1974. Nouvelle Approche des Réalités Météorologiques de l'Afrique Occidentale et Centrale (Thèse Doctorale Ing.) Université de Dakar, ASECNA, Dakar.
Dudal, R., Eswaran, H., 1988. Distribution, properties and classification of Vertisols. In: Wilding, L.P., Puentes, R. (Eds.), Vertisols: Their Distribution, Properties, Classification and Management. SMSS-Texas AandM University, pp. 1–22.
Durand, A., 1982. Oscillations of Lake Chad over the past 50,000 years: new data and new hypothesis. Palaeogeogr. Palaeoclimatol. Palaeoecol. 39, 37–53.
Durand, A., 1995. Quaternary sediments and climates in the Central Sahel. Afr. Geosci. Rev. 2 (3–4), 323–614.
Erhart, M.H., 1954. Bassin du Moyen Logone. Commission Scientifique du Logone et du Tchad, Etude Pédologique du Bassin Alluvionnaire du Logone-Chari. ORSTOM, Paris, France, pp. 17–107.

Erhart, M.H., 1967. La Genèse des Sols en Tant que Phénomène Géologique. Esquisse d'une Théorie Géologique et Géochimique. Biostasie et Rhexistasie. Masson et Cie. second ed. Paris Vie, France.
Eswaran, H., Wong, C.B., 1978. A study of a deep weathering profile on granite in peninsular Malaysia: I. Physico-chemical and micromorphological properties. Soil Sci. Soc. Am. J. 42, 144–148.
Eswaran, H., Kimble, J., Cook, T., 1988. Properties, genesis and classification of Vertisols. Workshop Swell-Shrink Soils, October 24–28, National Bureau of Soil Survey and Land Use Plannign, Nagpur India. Oxford and IBH Publ. Co, New Delhi, India.
FAO, 2006. Guidelines for Soil Description. Food and Agriculture Organization of the United Nations (FAO), Rome, Italy.
FAO, 2014. World reference base for soil resources 2014. International Soil Classification System for Naming Soils and Creating Legends for Soil Maps. World Soil Resources Reports 106, Rome, Italy.
FAO/GIEWS, 2004. Sahel weather and crop situation report. The rainy season has started against a backdrop of worrying desert locust situation. Sahel report, 1. http://www.fao.org/docrep/006/J2517e/J2517e00.htm#carte.
Francis, M.L., Ellis, F., Lambrechts, J.J.N., Poch, R.M., 2012. A micromorphological view through a Namaqualand termitaria (heuweltjie, a mima-like mound). Catena 100, 57–73.
Funch, R.R., 2015. Termite mounds as dominant land forms in semiarid northeastern Brazil. J. Arid Environ. 122, 27–29.
Gasse, F., 2000. Hydrological changes in the African tropics since the last glacial maximum. Quat. Sci. Rev. 19, 189–211.
Ghienne, J.-F., Schuster, M., Bernard, A., Duringer, P., Brunet, M., 2002. The Holocene Giant Lake Chad revealed by digital elevation models. Quat. Int. 87, 81–85.
Goudie, A.S., 2013. Arid and Semi-Arid Geomorphology. Cambridge University Press, New York, USA.
Hallsworth, E.G., Robertson, G.K., Gibbson, F.R., 1955. Studies in pedogenesis in New South Wales. VII. The gilgai soils. J. Soil Sci. 6, 1–31.
Hély, C., Braconnot, P., Watrin, J., Zheng, W., 2009. Climate and vegetation: simulating the African humid period. Compt. Rendus Geosci. 341 (8–9), 671–688. http://dx.doi.org/10.1016/j.crte.2009.07.002.
Hervieu, J., 1969. Le Quaternaire du Nord-Cameroun Schéma d'Evolution Géomorphologique et Relations avec la Pédogenèse. ORSTOM, Paris, France (38 pp.).
Hervieu, J., 1970. Influence des Changements des Climats Quaternaires sur le Relief et les Sols du Nord-Cameroun. Bull. Ass. Sénég. Quatern. Ouest Afr. 25, 97–105.
Hubble, G.D., 1984. The cracking clay soils: definition, distribution, nature, genesis and use. In: McGarity, J.W., Hoult, E.H., So, H.B. (Eds.), The Properties and Utilization of Cracking Clay Soils, Review in Rural Science University of New England, Armidale, Australia 5, pp. 3–13.
Jim, C.Y., 1990. Stress, shear deformation and micromorphological clay orientation: a synthesis of various concepts. Catena 17, 431–447.
Kocurek, G., 1998. Aeolian system response to external forcing factors. In: Alsharhan, A., Glennie, K., Whittle, G., Kendall, C. (Eds.), Quaternary Deserts and Climatic Change. Balkema, Rotterdam, The Netherlands, pp. 327–337.
Kovda, I.V., Wilding, L.P., Drees, L.R., 2003. Micromorphology, submicroscopy and microprobe study of carbonate pedofeatures in a Vertisol gilgai soil complex, South Russia. Catena 54 (3), 457–476. http://dx.doi.org/10.1016/S0341-8162(03)00121-8.
Kovda, I., Mora, C.I., Wilding, L.P., 2006. Stable isotope compositions of pedogenic carbonates and soil organic matter in a temperate climate Vertisol with gilgai, Southern Russia. Geoderma 136 (1–2), 423–435. http://dx.doi.org/10.1016/j.geoderma.2006.04.016.
Kröpelin, S., Verschuren, D., Lézine, A.-M., Eggermont, H., Cocquiyt, C., Francus, P., Cazet, J.-P., Fagot, M., Rumes, B., Russell, J.M., Darius, F., Conley, D.J., Schuster, M., Von Suchodoletz, H., Engstrom, D.R., 2008. Climate-driven ecosystem succession in the Sahara: the past 6000 years. Science 320, 765–768.
Leopold, L.B., Bull, W.B., 1978. Base level, aggradation, and grade. Proc. Am. Philos. Soc. 123 (3), 168–202.
Lézine, A.-M., 1989. Late Quaternary vegetation and climate of the Sahel. Quat. Res. 32, 317–334.
Lézine, A.-M., Hély, C., Grenier, C., Braconnot, P., Krinner, G., 2011. Sahara and Sahel vulnerability to climate changes, lessons from Holocene hydrological data. Quat. Sci. Rev. 30 (21—22), 3001–3012. http://dx.doi.org/10.1016/j.quascirev.2011.07.006.
L'Hôte, Y., 1998. Climatologie et Agroclimatologie de la Province Extrême-North (P. E. N.) du Cameroun. ORSTOM, Paris, France.
Mahop, F., Van Ranst, E., Boukar, S., 1995. Influence de l'aménagement des sols sur l'efficacité des pluies au Nord-Cameroun. Etud. Gest. Sols 2 (2), 105–117.
Maley, J., 1981. Etudes Paylnologiques dans le Bassin du Tchad et Paléoclimatologie de l'Afrique Nord-Tropicale de 30000 ans à l'Epoque Actuelle. Palaeoecol. Afr. 13, 45–52.
Maley, J., 1983. Histoire de la Végétation et du Climat de l'Afrique Nord-Tropicale au Quaternaire Récent. Bothalia 14 (3–4), 377–389.
Maley, J., 2004. Le Bassin du Tchad au Quaternaire Récent: Formations Sédimentaires, Paléoenvironnements et Préhistoire. La Question des Paléotchads. In: Sémah, A.-M., Renault-Miskovsky, J. (Eds.), Guide de la Préhistoire mondiale. Artcom' – Errance, Paris, France, pp. 179–217.
Maley, J., 2010. Climate and palaeoenvironment evolution in North Tropical Africa from the end of the Tertiary to the Upper Quaternary. Palaeoecol. Afr. 30, 227–278.
Martin, D., 1961. Carte Pédologique du Nord-Cameroun au 1/100.00e feuille de Mora. ORSTOM-IRCAM, Yaoundé, Cameroun.
Mayewski, P.A., Rohling, E.E., Curt Stager, J., Karlén, W., Maasch, K.A., David Meeker, L., Meyerson, E.A., Gasse, F., van Kreveld, S., Holmgren, K., Lee-Thorp, J., Rosqvist, G., Rack, F., Staubwasser, M., Schneider, R.R., Steig, E.J., 2004. Holocene climate variability. Quat. Res. 62 (3), 243–255. http://dx.doi.org/10.1016/j.yqres.2004.07.001.
McGarry, D., 1996. The structure and grain-size distribution of Vertisols. In: Ahmad, N., Mermut, A.R. (Eds.), Vertisols and Technologies for Their Management. Elservier Science, Amsterdam, The Netherlands, pp. 231–259.
McTainsh, G., 1984. The nature and origin of the Aeolian mantles of Central Northern Nigeria. Geoderma 33, 13–37.
Mermut, A.R., Padmanabham, E., Eswaran, H., Dasog, G.S., 1996. Pedogenesis. In: A. N., Mermut, A.R. (Eds.), Vertisols and Technologies for Their Management. Elsevier Science B. V., Amsterdam, The Netherlands, pp. 43–58.
Miller, W.L., Bragg, A.L., 2007. Soil Characterization and Hydrological Monitoring Project, Brazoria County, Texas, Bottomland Hardwood Vertisols. The United States Department of Agriculture (USDA), Washington, D. C., USA, p. 333.
Moore, J.M., Picker, M.D., 1991. Heuweltjies (earth mounds) in the Clanwilliam District, Cape Province, South Africa: 4000-year-old termite nests. Oecologia 86, 424–432.
Moore, D.M., Reynolds, R.C., 1997. X-Ray Diffraction and the Identification and Analysis of Clay Minerals. Oxford University Press, New York, USA.
Morin, S., 2000. Géomorphologie. In: Seignobos, C., Iyébi-Mandjek, O. (Eds.), Atlas de la Province Extrême-Nord Cameroun. Ministère de la Recherche Scientifique et Technique Institut National de Cartographie, Institut de Recherche pour le Développement, Cameroun, Paris, France.
Mpeck, E., 1994. Contribution des Poussières Sahariennes à la Sédimentation du Pléistocène Supérieur au Nord Cameroun: La Formation de Doyang (Thèse de Doctorat) Terre, Océan et Espace, Université Paris 6, Paris, France, p. 303.
Mücher, H., Van Steijn, H., Kwaad, F., 2010. Colluvial and mass wasting deposits. In: Stoops, G., Marcelino, V., Mees, F. (Eds.), Interpretation of Micromorphological Features of Soils and Regoliths. Elsevier Science, Amsterdam, The Netherlands, pp. 37–48.
Oakes, H., Thorp, J., 1950. Dark clay soils of warm regions of variously called rendzina black cotton soils, regurs and tirs. Soil Sci. Soc. Am. Proc. 15, 347–354.
Olivry, J.-C., Chouret, A., Vuillaume, G., Lemoalle, J., Bricquet, J.-P., 1996. Hydrologie du Lac Tchad. ORSTOM, Paris, France (301 pp.).
Peel, M.C., Finlayson, B.L., McMahon, T.A., 2007. Updated world map of the Köppen-Geiger climate classification. Hygrol. Earth Syst. Sci. 11, 1633–1644.
Pias, J., 1962. Les Sols du Moyen et Bas Logone, du Bas Chari, des Régions Riveraines du Lac Tchad et du Bahr El Ghazal. Mémoires ORSTOM, Paris, France (434 pp).
Prescott, J.A., 1931. The soils of Australia in relation to climate. The Commonwealth Scientific and Industrial Research Organisation (CSIRO). Aust. Bull. 52, 65–67.
Retallack, G.J., 2001. Soils of the past. An Introduction to Paleopedology. Blackwell Science Ltd, Oxford, United Kingdom.
Servant, M., 1983. Séquences Continentales et Variations Climatiques: Evolution du Bassin du Tchad au Cenozoïque supérieur. Travaux et Documents de l'ORSTOM, Paris, France, pp. 1–567.
Shanahan, T.M., McKay, N.P., Hugen, K.A., Overpeck, J.T., Otto-Bliesner, B., Heil, C.W., King, J., Scholz, C.A., Peck, J., 2015. The time-transgressive termination of the African humid period. Nat. Geosci. 8, 140–144.
Sieffermann, G., 1963. Carte Pédologique du Nord-Cameroun au 1/100.000e, feuille de Kalfou. ORSTOM-IRCAM, Yaoundé, Cameroun.
Sieffermann, G., 1967. Variations Climatiques au Quaternaire dans le Sud-Ouest de la Cuvette Tchadienne. C. R. 92e Congr. Nat. Soc. Sav., Strasbourg, Colmar, France, pp. 485–494.
Silva, L.C.R., Vale, G.D., Haidar, R.F., da S.L. Sternberg, L., 2010. Deciphering earth mound origins in Central Brazil. Plant Soil 336, 3–14.
Snelder, D.J., Bryan, R.B., 1995. The use of rainfall simulation tests to assess the influence of vegetation density on soil loss on degraded rangelands in the Baringo District. Kenya. Catena 25, 105–116.
Southard, R.J., Driese, S.G., Nordt, L.C., 2011. Vertisols. In: Huang, P.M., Li, Y., Sumner, M.E. (Eds.), Handbook of Soil Sciences Properties and Processes. CRC Press Taylor and Francis Group, USA, pp. 33–82.
Stoops, G., 2003. Guidelines for Analysis and Description of Soil and Regolith Thin Sections. Soil Science Society of America, Wisconsin, USA (184 pp.).
Stoops, G., Jongerius, A., 1975. Proposal for a micromorphological classification of soil materials. I. A classification of the related distribution of coarse and fine particles. A reply. Geoderma 19, 247–249.
Swezey, C., 2001. Eolian sediment responses to late quaternary climate changes: temporal and spatial patterns in the Sahara. Palaeogeogr. Palaeoclimatol. Palaeoecol. 167, 119–155.
Vandenberghe, J., 2013. Grain-size of fine-grained windblown sediment: a powerful proxy for process identification. Earth Sci. Rev. 121, 18–30http://dx.doi.org/10.1016/j.earscirev.2013.03.001.
Velde, B., Meunier, A., 2008. The Origin of Clay Minerals in Soils and Weathered Rocks. Springer, Berlin, Germany.
Wanner, H., Beer, J., Bütikofer, J., Crowley, T.J., Cubasch, U., Flückiger, J., Goosse, H., Grosjean, M., Joos, F., Kaplan, J.O., Küttel, M., Müller, S.A., Prentice, I.C., Solomina, O., Stocker, T.F., Tarasov, P., Wagner, M., Widmann, M., 2008. Mid- to Late Holocene climate change: an overview. Quat. Sci. Rev. 27 (19–20), 1791–1828. http://dx.doi.org/10.1016/j.quascirev.2008.06.013.
Wieder, M., Yaalon, D.H., 1974. Effect of matric composition on carbonate nodule crystallisation. Geoderma 11, 95–121.
Wilding, L.P., 2004. Advancement in the knowledge base of vertisols genesis, classification, distribution and management. Rev. Ciênc. Agron. 8 (1), 45–54.
Wilding, L.P., Tessier, D., 1988. Genesis of Vertisols: shrink-swell phenomena. In: Wilding, L.P., Puentes, R. (Eds.), Vertisols: Their Distribution, Properties, Classification and Management. SMSS-Texas AandM University, pp. 55–82.
Wilding, L.P., Williams, D., Miller, W., Cook, T., Eswaran, H., 1990. Close interval spatial variability of Vertisols: a case study in Texas. In: Kimble, J.M. (Ed.), Proc. Sixth Int. Soil Correlation Meeting (ISCOM)Characterization, Classification and Utilization of Cold Aridisols and Vertisols. USDA, Soil Conservation Service, National Soil Survey Center, Lincoln, USA, pp. 232–247.
Yule, D.F., Ritchie, J.T., 1980. Soil shrinkage relationships of Texas vertisols, I: small cores. Soil Sci. Soc. Am. J. 44, 1285–1291.

Quaternary Geochronology 36 (2016) 120–133

Contents lists available at ScienceDirect

Quaternary Geochronology

journal homepage: www.elsevier.com/locate/quageo

Research paper

Pedogenic carbonate nodules as soil time archives: Challenges and investigations related to OSL dating

Nathalie Diaz [a, *], Georgina E. King [a, b], Pierre G. Valla [a], Frédéric Herman [a], Eric P. Verrecchia [a]

[a] Institute of Earth Surface Dynamics, Faculty of Geosciences and the Environment, University of Lausanne, Geopolis, 1015 Lausanne, Switzerland
[b] Institute of Geography, University of Cologne, Germany

ARTICLE INFO

Article history:
Received 4 February 2016
Received in revised form
7 August 2016
Accepted 16 August 2016
Available online 21 August 2016

Keywords:
Partial bleaching
U-series disequilibrium
Environmental dose rate
African humid period
Northern Cameroon

ABSTRACT

Pedogenic carbonate nodules have been observed in the Far North region of Cameroon. They have been interpreted as Vertisol relic components inherited from the African Humid Period (AHP), however their processes of formation remain poorly constrained. Here we explore the possibility of targeting the minerals trapped within such nodules, which represent a residual soil fraction, to date the deposition time of the soil parent material using optically stimulated luminescence (OSL). As the trapped minerals have a complex history, related to pedogenesis and sedimentary processes since their deposition, it was necessary to identify a suitable mineral population. To achieve this, a nodule collected at the surface was investigated in order to compare the OSL signals from feldspar minerals from within its external and internal parts. The resultant luminescence data were then compared with minerals trapped in a buried nodule, with the scatter in OSL signals between the different populations indicating potential partial bleaching of grains and/or pedoturbation processes. Our results show that the minerals from the internal part of the nodule are appropriate for OSL dating. Furthermore, the environmental dose rate has changed through time following carbonate precipitation and the radionuclide decay series may be in disequilibrium. Because of its solubility, the ^{238}U-series is particularly affected, and when a complete absence of ^{234}U daughters is assumed, our calculations show a maximum and significant decrease of 20% in the environmental dose rate compared to secular equilibrium. Finally, changing the time of carbonate nodule precipitation results in a maximum OSL age range of 12 ka (from 15 to 27 ka) for the deposition of the soil parent material. Despite this relatively high uncertainty, these ages suggest that the deposition occurred before the AHP. Consequently, if their formation time is well constrained from independent methods, the pedogenic carbonate nodules can be exploited as valuable time archives, providing temporal information on soil parent material deposition and thus a maximum age for the onset of pedogenesis.

© 2016 Elsevier B.V. All rights reserved.

1. Introduction

Pedogenic carbonates comprise $CaCO_3$ accumulations in soil horizons (Lal and Kimble, 2000; Tanner, 2010), which can have various morphologies such as nodular, laminar, tubular, and also different strengths (e.g. Durand et al., 2007). They are widespread and their geochemical properties (e.g. stable carbon and oxygen isotopic composition) can be used as proxies for reconstructing palaeo-climatic conditions (e.g. Dworkin et al., 2005; Retallack, 2005; Yang et al., 2014), palaeo-elevations (Quade et al., 1989, 2007) and also for assessing palaeo-vegetation (Cerling, 1984; Ding and Yang, 2000). The occurrence of pedogenic carbonate is generally observed in soils where there is enough water to provide ions in solution (e.g. Ca^{2+}) and, at the same time, where the moisture regime can be sufficiently xeric (i.e. dry) to reach calcite supersaturation and lead to secondary carbonate precipitation and accumulation (Deocampo, 2010; Gocke et al., 2012; Zamanian et al., 2016). Consequently, pedogenic carbonates are characteristic soil features of arid to sub-humid climatic conditions or where soil moisture conditions alternate strongly (Cerling, 1984; Gocke et al., 2012). Pedogenic carbonates also comprise an important part of the global soil carbon budget (around 30–40% of the global soil carbon inventory is soil inorganic carbon; Eswaran et al., 2000), and, in addition to understanding the processes of their formation, it is also

* Corresponding author.
E-mail address: nathalie.diaz@unil.ch (N. Diaz).

http://dx.doi.org/10.1016/j.quageo.2016.08.008
1871-1014/© 2016 Elsevier B.V. All rights reserved.

important to constrain the time scale of carbonate precipitation. Numerical dating is possible with methods such as U/Th dating (e.g. Durand et al., 2007; Violette et al., 2010) and radiocarbon dating (e.g. Williams and Polach, 1971; Achyuthan et al., 2010). Furthermore, pedogenic carbonates may also contain a substantial non-carbonate fraction and we show here that this fraction can give important temporal constraints for sedimentary processes and soil formation.

In the Far North Region of Cameroon (Fig. 1A), pedogenic carbonate nodules formed in clay-rich soils have been investigated in granitic watersheds belonging to the Chad Basin. These soils are highly eroded and degraded (Fig. 1B), and have been interpreted as Vertisol relics (Diaz et al., 2016) likely inherited from the African Humid Period (AHP), which lasted from c. 15 ka to c. 5 ka (DeMenocal et al., 2000). Consequently, the carbonate nodules may be important continental palaeo-environmental archives for this region (Alonso-Zarza and Tanner, 2010), where major precipitation variations occurred in relation to the northern migration of the monsoon front (DeMenocal et al., 2000; DeMenocal and Tierney, 2012; Shanahan et al., 2015). The aim of this study is to explore the potential of the carbonate nodules as time archives using the mineral fraction trapped within them. The nodules are pedogenic in origin (Diaz et al., 2016), i.e. were formed *in situ* in the host soil, meaning that primary minerals trapped within them represent a residual soil fraction (Fig. 1C). Singhvi et al. (1996) previously explored this trapped mineral fraction in carbonate nodules using thermoluminescence (TL) dating, to assess the age of carbonate precipitation. Here we aim to use this trapped mineral fraction for dating the deposition time of the soil parent material, i.e. the sediment from which Vertisols and then carbonate nodules formed, through the measurement of optically stimulated luminescence (OSL). The trapped minerals have a complex post-deposition history linked to pedogenesis (i.e. Vertisol genesis) and subsequent geomorphological processes (i.e. erosion; Diaz et al., 2016). This needs to be carefully addressed for accurate interpretation of the luminescence measurements and OSL age calculations.

Luminescence dating is a useful method for establishing absolute Quaternary chronologies in continental sedimentary sequences. It is widely used to determine the time that has elapsed since buried sediments were last exposed to sunlight. During burial, trapped electrons accumulate in the minerals in response to environmental radiation (α-, β-particles and γ-rays) emitted by the decay of radiogenic elements present in the host sediment and by cosmic rays. These electrons recombine when the minerals are exposed to light or heat, resulting in the emission of light (luminescence), and can thus be used to date the deposition time of the

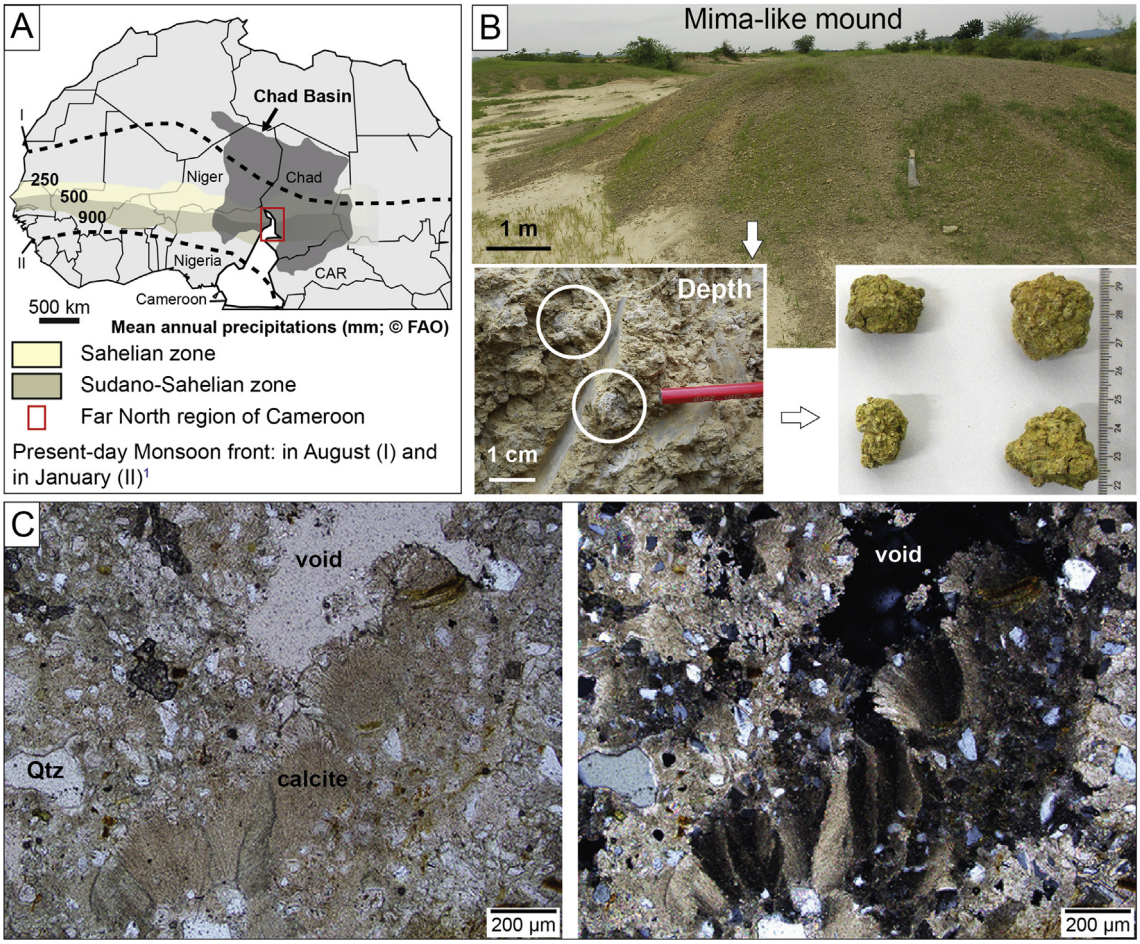

Fig. 1. General setting and samples. A) Location of investigated samples along the Sudano-Sahelian belt in the Chad Basin (Far North region of Cameroon, red square). Dashed lines represent the present-day average latitudinal position of the ITCZ in August (I) and January (II) ([1]Nicholson, 2009), which regulates wet and dry season occurrences during the year. B) Clay-rich soils forming mima-like mounds and covered by large amounts of carbonate nodules (up to 11 kg m^{-2}). Insets show nodules found within the soil and representative nodules. C) Thin section of a pedogenic carbonate nodule in polarized light (left) and cross-polarized light (right). The calcite precipitated around soil components, such as primary minerals (e.g. quartz, feldspars), secondary minerals (clays, oxides) and organic matter. (For interpretation of the references to colour in this figure legend, the reader is referred to the web version of this article.)

sediment (Aitken, 1998). In luminescence dating, an age (ka) is derived from:

$$Age = \frac{D_e}{\dot{D}} \quad (1)$$

where, D_e is the equivalent dose (Gy) and relates to the natural dose received by the mineral, and $\dot{D}$ is the environmental dose rate (Gy ka^{-1}).

Successful OSL dating of trapped minerals within pedogenic carbonate nodule requires two main challenges to be addressed. First, the D_e value of the sample needs to be carefully determined, as some nodules were brought at the surface following erosion processes and were thus exposed to light. Consequently, there is a risk that the OSL signal of the trapped minerals has been partially reset, which would result in an underestimation of the sediment depositional age. Moreover, the investigated soils are Vertisol relics. Vertisols are clay-rich, smectitic-rich soils and are affected by swelling-shrinking processes due to soil moisture changes (Wilding, 2004; Southard et al., 2011). These processes induce vertical crack structures leading to the input of surficial soil material in deeper horizons (Food and Agriculture Organization, 2014). Consequently, these pedoturbation processes can potentially cause a mixing between younger and older sedimentary grains. Both partial bleaching, due to erosion, and sediment mixing, due to pedoturbation, are expected to induce some variability in the D_e distribution (Bateman et al., 2003). The second challenge is to accurately characterize the environmental dose rate ($\dot{D}$). Carbonate accumulation must have led to chemical changes in the soil environment. The concentration of radionuclides surrounding the trapped minerals has thus changed since carbonate precipitation, affecting the $\dot{D}$ (Aitken, 1998). Environmental radiation is mainly emitted following the decay of the uranium (U) and thorium (Th) series and the simple decay of potassium (K) and rubidium (Rb), as well as an additional cosmic dose component. In luminescence dating, the decay series are generally assumed to be in secular equilibrium, implying that the dose rate is constant through time (Olley et al., 1996; Aitken, 1998). However, in the case of carbonate nodules, it is likely that disequilibrium has occurred due to the precipitation of carbonate (Ferronsky and Polyakov, 2012). Finally, as relic soils have been subsequently eroded, the contribution from cosmic rays may have also changed through time, which should also be assessed.

To summarize, two main questions are investigated in this study: (1) is there a suitable population of trapped minerals within the pedogenic carbonate nodules for luminescence dating, and (2) can the $\dot{D}$ changes through time and potential disequilibrium effects be adequately accounted for? Overcoming both challenges would enable the minerals trapped within the carbonate nodules to be used to date the deposition time of the soil parent material. This would also set a maximum age for the onset of pedogenesis, constraining the carbonate nodule genesis that related to the formation and evolution of the Vertisols. As such, pedogenic carbonate nodules can be used as sedimentary archives in a multi-proxy approach using not only the carbonate fraction but also the silicate fraction, which is the objective of this study.

2. Material and methods

2.1. General settings and sample preparation

The pedogenic carbonate nodules were collected from soils located in the Diamare piedmont (Far North region of Cameroon) where they form mima-like mounds in eroded areas (Fig. 1B; Diaz et al., 2016). This specific soil morphology was recently attributed to pedogenesis and later erosion processes. The mounds were defined as Vertisol relics, i.e. degraded Vertisols, and the precipitation of carbonate nodules is related to Vertisol genesis (Diaz et al., 2016). In the present-day, non-degraded Vertisols occur downstream in piedmont waterlogged areas (Brabant and Gavaud, 1985). This suggests that Vertisols were more extensive under past wetter climatic conditions, where humid areas were widespread (Diaz et al., 2016). Due to changes in the position of the monsoon front during the Quaternary, such expansion must have occurred during the AHP (Lézine et al., 2011; Armitage et al., 2015), as precipitation is strongly linked to the position of the monsoon front (Fig. 1A). The assessment of the time of soil parent material deposition is thus crucial for constraining the onset of Vertisol genesis and confirming their possible inheritance from the AHP.

For logistical reasons, soil samples were not collected under light-safe conditions and thus cannot be directly used for luminescence dating. Consequently, we propose to explore an alternative approach by using the trapped mineral fraction within the carbonate nodules to assess the time of soil parent material deposition. In the mima-like mound settings, the carbonate nodules are found both as a cover at the surface and within the soil matrix (Fig. 1B). Thin sections show that a significant fraction of the carbonate nodules comprises a residual soil component (Fig. 1C). X-ray diffraction measurements also confirm this observation, with averages ($n = 5$) of 57 ± 8% calcite ($CaCO_3$) and of 43 ± 8% other minerals (e.g. quartz, feldspars, phyllosilicates, oxides). These non-carbonate minerals have been shown to represent the surrounding host sediment mineralogy (Diaz et al., 2016). However, in such settings, this trapped mineral fraction has experienced a complex history from grain deposition to sampling for OSL analysis. Several steps can describe the trapped mineral history (Fig. 2). First, the mineral grains are deposited and buried to constitute a sediment sequence (step I). From this sediment deposit, soils (e.g. Vertisols) have then developed during step II. Vertisol genesis induced favourable conditions for secondary carbonate accumulation (Wieder and Yaalon, 1974; Ahmad, 1983) with pedogenic carbonate nodule precipitation that trapped a host soil fraction (step III). Note that there are unknown time gaps between steps I and II, and between steps II and III. Finally, erosion affected the Vertisols leading to the present-day mima-like mound Vertisol relics with some nodules brought to the surface (step IV). As already stated, this complex history has direct implications for the equivalent dose data and for the dose rate assessment.

To investigate the possibility of using trapped minerals for OSL dating despite the complex setting, two carbonate nodules were selected. One nodule was collected at the surface (NO1, diameter (Ø) = 10 cm) and a second nodule was collected at 100 cm depth in a mima-like mound (NO2, Ø = 4 cm). Due to its surficial position, sample NO1 was exposed to light for an unknown duration. To assess the influence of sunlight exposure on the luminescence signal, the outer most layer of sample NO1 ($NO1_{Ext}$, 2–3 cm thick) was removed under red light conditions using a diamond saw and isolated from the central part ($NO1_{Int}$). The luminescence properties of grains from both NO1 subsamples and the buried sample NO2 were then compared. A non-light-safe mineral population should exhibit partial bleaching, following sample exposure to sunlight after carbonate precipitation, and thus a scatter in the equivalent dose (D_e) distribution should be expected. Consequently, a scatter in the equivalent dose distributions could be induced by pedoturbation processes (Bateman et al., 2003), affecting $NO1_{Ext}$, $NO1_{Int}$, and NO2, while we expect sunlight exposure to preferentially affect $NO1_{Ext}$.

The nodules were treated with HCl (35%) to remove carbonates and with H_2O_2 (20 vols) to remove any organic material. Samples were then sieved to isolate the 90–180 μm fraction, which was

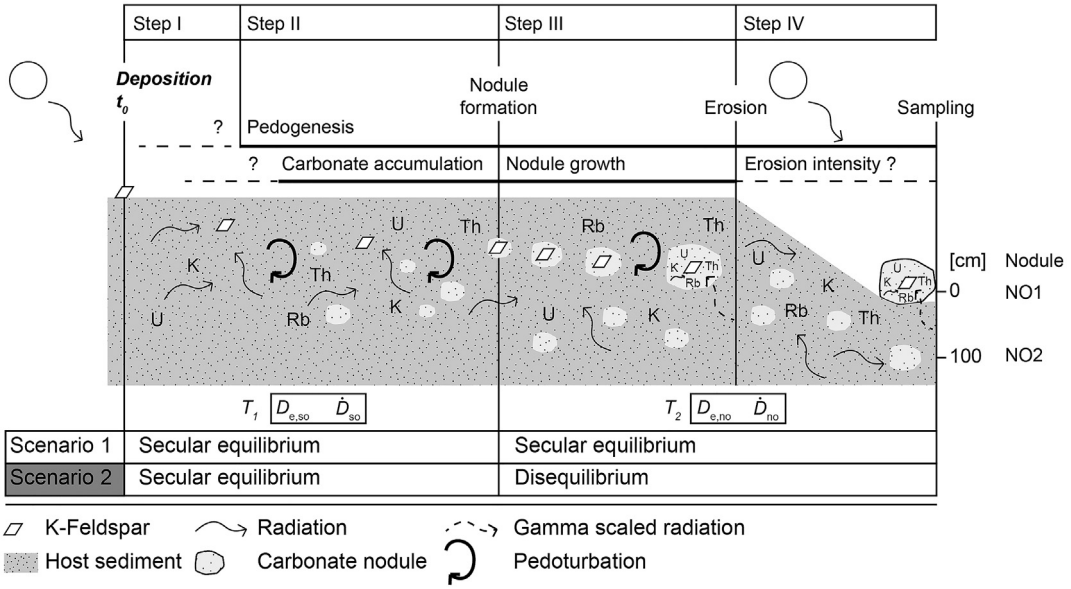

Fig. 2. Schematic illustration of proposed scenarios for environmental dose rate changes through time. After deposition (t_0), K-feldspars are buried in the sediment (step I), from which the soil will form during period of time T_1 (step II). The luminescence signal ($D_{e,\,so}$) results from the environmental dose rate ($\dot{D}_{so}$), to which the decay of radionuclides (U, Th, K, Rb) composing the sediment contributes. After carbonate nodule precipitation (step III), the K-feldspars are trapped, and the luminescence signal ($D_{e,\,no}$) results from the environmental dose rate during time T_2 ($\dot{D}_{no}$), to which the decay of radionuclides composing the nodule and the sediment contribute (γ-dose rate is scaled). Finally, erosion brought some nodules (e.g. NO1) to the surface leading to their exposure to sunlight (step IV). Radionuclides are assumed to be in secular equilibrium during both T_1 and T_2 in scenario 1 (white). Some radionuclides are likely to be in disequilibrium since T_2 in scenario 2 (grey).

selected for further analysis because of the abundance of grains in this range. The minerals were then separated by density using sodium polytungstate to isolate quartz (2.7–2.62 g cm^{-3}), plagioclase (2.62–2.58 g cm^{-3}) and K-feldspar (<2.58 g cm^{-3}). A low abundance of quartz led us to the use the K-feldspar fraction, which was not etched (Duller, 1992; page 16). Each sample preparation step was performed under subdued red light conditions.

2.2. Luminescence measurements

Luminescence measurements were performed using a Risø TL/OSL-DA-20 reader (dose rate ≈ 0.1 Gy s^{-1}) at the Institute of Earth Surface Dynamics (University of Lausanne). To assess the D_e, a single-aliquot regenerative post-IR IRSL protocol was used to access a high temperature signal from feldspars, which is in theory less affected by anomalous fading (Thomsen et al., 2008; Buylaert et al., 2009). A pre-heat of 250 °C for 60 s was followed by an IR stimulation at 50 °C for 100 s (IR_{50}) and a post-IR IRSL stimulation at 225 °C for 100 s ($pIRIR_{225}$). This $pIRIR_{225}$ protocol was chosen instead of the $pIRIR_{290}$ protocol to limit high potential residual doses from partial resetting and thus age overestimations (Thiel et al., 2011; Roberts, 2012). The measured responses of the aliquot to a regenerative dose (L_x) and to a test dose (T_x) were integrated over 3 s, and the background signals were integrated over the last 10 s of stimulation. Measurements were done using small aliquots (SA, Ø = 1 mm, 100–150 grains measured per aliquot), mounted on stainless steel discs, and single grain measurements were done using aluminium discs (hole diameter Ø = 300 μm, 10–20 grains per hole). Due to a high number of grains in the single grain disks, we refer to these as pseudo-single grain (PSG) measurements. However, SA and PSG comparison still allow us to further investigate the possibility of partial bleaching through reducing the number of analysed grains by one order of magnitude (Duller, 2008). The measurement protocol was validated using a dose-recovery test (Murray and Wintle, 2003) and PSG measurements (n = 3 discs ≈ 120 measurements), whereby samples were exposed for 4 h to direct sunlight in Lausanne prior to measurement. Samples were given a dose approximately equal to the equivalent dose (~30 Gy) and dose recovery ratios were calculated following subtraction of measured residuals (n = 3 discs ≈ 120 measurements).

Although the post-IR IRSL protocol reduces the effects of anomalous fading, a fading test was done for both samples (n = 3 SA discs) following Huntley and Lamothe (2001). Previously measured aliquots were given a dose approximately equal to the equivalent dose (~30 Gy) and measured following increasing delays (n = 4) between 100 and 800 min. The resulting g-values (%/decade) were calculated following Auclair et al. (2003) and were normalised to 2 days (Huntley and Lamothe, 2001).

Finally, the D_e values were determined using Analyst v.4.31.7 (Duller, 2015) according to the following acceptance criteria: recycling ratios within 5 and 10% of unity for SA and PSG measurements respectively, maximum test dose and palaeodose error <10%, and maximum recuperation <10% of the natural luminescence signal. The D_e values of the samples were calculated using the central age model (CAM; Galbraith et al., 1999) and are cited at 1σ uncertainty. The sample residual doses and the dose recovery test D_e values are reported with standard error (SE) and 1σ uncertainties, respectively.

2.3. Environmental dose rate assessment

The external dose rate ($\dot{D}_{ext}$ in Gy ka^{-1}) is defined as:

$$\dot{D}_{ext} = \dot{D}_{\alpha} + \dot{D}_{\beta} + \dot{D}_{\gamma} + \dot{D}_{cos} \quad (2)$$

where, $\dot{D}_{\alpha}$, $\dot{D}_{\beta}$ and $\dot{D}_{\gamma}$ are the energy emitted by α-, β-particles and γ-rays, respectively, and $\dot{D}_{cos}$ is the cosmic ray dose rate. As K-feldspars are used in this study, it is also necessary to consider the contribution of the internal dose rate ($\dot{D}_{int}$) resulting from the internal K decay. The combination of the external and internal doses gives the environmental dose rate ($\dot{D}$). The soil and nodule U (ppm),

Th (ppm), K (%) and Rb (ppm) compositions were assessed by X-Ray fluorescence at the Institute of Earth Sciences (University of Lausanne) and by ICP-MS at Actlabs (Activation Laboratories, Ancaster). The internal K-content (%) was measured on individual feldspar grains (n = 187) with a JEOL 8200 Superprobe at the Institute of Earth Sciences (University of Lausanne). The calculations of $\dot{D}_{int}$ and $\dot{D}_{cos}$ were done with the online dose rate calculator DRAC v1.1 (Durcan et al., 2015). The beta grain size attenuation factors of Guérin et al. (2012) and alpha grain size attenuation factors of Bell (1980) were used. The cosmic ray dose rate contribution was assessed using the protocol outlined by Prescott and Hutton (1994) corrected for the geomagnetic latitude (11.789°N; F = 0.39, J = 0.55 and H = 4.35), and taking into account the cosmic-ray attenuation with depth (0 and 100 cm for nodules NO1 and NO2, respectively). We used the water content attenuation factors of 1.5 (α), 1.25 (β) and 1.14 (γ) following Zimmerman (1971) and Aitken and Xie (1990).

2.3.1. External dose rate changes through time

Due to carbonate precipitation, the chemical environment surrounding the minerals varied since the time of deposition (t_0), resulting in external dose rate ($\dot{D}_{ext}$) changes (Fig. 2). During the time period T_1, environmental radiation is solely derived from the radionuclides within the soil matrix and the cosmic dose rate ($\dot{D}_{ext1}$). However, following carbonate precipitation (i.e. during the time period T_2), the α- and β-contributions are derived from radionuclides composing the carbonate nodule, whilst the γ-dose is derived from both the surrounding soil and the carbonate nodule (Aitken, 1985). As nodule diameters are 10 cm (NO1) and 4 cm (NO2), the nodules cannot be seen as an infinite matrix, and γ-rays emitted by the host sediment have to be considered. The γ-dose contribution thus needs to be scaled by the nodule size. To summarize, the carbonate nodule formation results in a different external dose rate ($\dot{D}_{ext2}$). However, beyond this simple time frame, there are some potential complexities that still need to be investigated:

a. During the time period T_1, pedogenesis begins followed by potential carbonate accumulation, leading to a different soil chemical environment (step II). How does this affect the $\dot{D}_{ext1}$ assessment?
b. When the minerals become trapped in a nodule (step III), the nodule growth rate is unknown. The nodule size has most likely increased incrementally through time with different precipitation events, resulting in an uncertainty on the scaled γ-dose. This may also influence the β-dose, but only at the early onset of precipitation when the carbonate size was <3 mm (Aitken, 1985); we thus assume this effect to be negligible. Concerning the γ-dose, can the nodule growth rate affect the $\dot{D}_{ext2}$ assessment?
c. Has the cosmic ray contribution changed through time, due to late-stage erosion (step IV), which would then affect the $\dot{D}_{ext2}$?

These different points need to be addressed in the assessment of the environmental dose rate changes, and will be individually discussed in the next sections.

2.3.2. Decay chain disequilibrium

In typical silt/sand alluvium, the U and Th decay chains can contribute up to approximately 50% of the external dose rate $\dot{D}_{ext}$ (Olley et al., 1996). In most luminescence dating applications, the decay chains are assumed to be in secular equilibrium with $\dot{D}_{ext}$ constant over Quaternary timescales (Armitage, 2015). However, because some radionuclides are mobile, in surficial sediments the ^{238}U decay chain is likely to be in disequilibrium (e.g. Osmond et al., 1983; Short et al., 1989; Olley et al., 1996), and this disequilibrium is very common in environments where carbonates are present or where weathering processes occur (e.g. Guibert et al., 2009; Zander and Hilgers, 2013). Therefore, in the context of pedogenic carbonate nodules, the disequilibrium is linked to the incorporation of U within carbonate during nodule precipitation. In oxic environments, U exists mainly as uranyl species (UO_2^{2+}) and in waters it can form uranyl carbonates ($UO_2(CO_3)_2^{-2}$) (Chabaux et al., 2008). The disequilibrium of U is mainly caused by the α-recoil of ^{238}U in minerals, inducing the ejection of ^{234}Th at the mineral boundaries. This radionuclide will decay rapidly to ^{234}U, and due to high U solubility it will be leached in pore fluids (DePaolo et al., 2006; Dosseto et al., 2008). Another process is the preferential release of ^{234}U from crystal lattices that are damaged by α-recoil (e.g. Andersen et al., 2009). Consequently, natural surficial waters are generally enriched in ^{234}U compared to ^{238}U.

As secondary carbonate precipitates from a supersaturated soil solution, the U incorporated in the secondary mineral has similar disequilibrium; because U is a heavy element, further fractionation can be assumed to be negligible. In most natural river waters the (^{234}U/^{238}U) activity ratio is close to unity when chemical weathering processes are dominant (Chabaux et al., 2003), higher than unity (up to 4) when physical erosion processes are dominant (e.g. Vigier et al., 2001; Andersen et al., 2009) or when groundwaters are contributing to surficial waters (Andersen et al., 2009; Chkir et al., 2009), and lower than unity if there is no renewal of sediment and thus a strong depletion in ^{234}U (Israelson et al., 1997; Riotte and Chabaux, 1999). In this study, low material availability prevented high-resolution gamma spectrometry to directly determine the degree of U-series disequilibrium. Consequently, following the literature summarized above, different (^{234}U/^{238}U) activity ratios between 0.5 and 3 have been investigated. Moreover, in order to illustrate the effect of the most extreme disequilibrium scenario on the environmental dose rate, we have assumed that all the daughter radioisotopes of ^{234}U are absent following carbonate precipitation.

As a carbonate nodule precipitates within a soil, U is also derived from minerals within the residual soil fraction trapped in the nodule. This fraction of U is assumed to be in secular equilibrium, unlike the U included as $UO_2(CO_3)_2^{-2}$. In contrast to U, as chemical processes, such as ion leaching and secondary mineral formation, have no or very little effect on Th, this radionuclide should not accumulate in secondary minerals as a soluble phase (Ferronsky and Polyakov, 2012). A comparison of the granite, the soil and the carbonate nodule chemistry (Table 1), shows that Th is four to five times more abundant than U in the granite and soil, whereas the Th and U contents are approximately equal in the carbonate nodule. Uranium is thus in excess in the carbonate nodules, which is a

Table 1
Thorium and Uranium composition (XRF and ICP-MS) of the granite bedrock, soil and carbonate ($CaCO_3$) nodule. n is the number of measurements.

	n	K (%)	Rb (ppm)	Th (ppm)	U (ppm)	Ratio Th/U
Granite	1	5.0 ± 0.07	215.8 ± 1	12.0 ± 2	3.4 ± 1	4/1
Soil	35	2.7 ± 0.03	126.6 ± 1.2	20.1 ± 0.3	4.3 ± 0.1	5/1
$CaCO_3$ nodule	12	0.7 ± 0.03	36.1 ± 0.9	6.1 ± 0.1	5.4 ± 0.2	6/5

consequence of U inclusion as $UO_2(CO_3)_2^{-2}$ during carbonate precipitation; whereas all Th within the carbonate nodule is a component of the trapped residual soil fraction. Consequently, considering the Th/U ratios of the soil $\left(\frac{Th}{U}\right)_{so}$ and nodule $\left(\frac{Th}{U}\right)_{no}$ given in Table 1, it is possible to distinguish the proportion of U derived from the residual soil fraction (f_{so}) included in the nodule, as follows:

$$\left(\frac{Th}{U}\right)_{no} = \left[\left(\frac{Th}{U}\right)_{so} * f_{so}\right] + \left[\left(\frac{Th}{U}\right)_{w} * f_{w}\right] \quad (3)$$

where f_{so} is the U fraction of the residual soil fraction trapped within the nodule, and f_w is the U fraction composed in water as $UO_2(CO_3)_2^{-2}$, and,

$$f_{so} + f_w = 1 \quad (4)$$

$$\left(\frac{Th}{U}\right)_{w} = 0 \quad (5)$$

so,

$$f_{so} = \frac{\left(\frac{Th}{U}\right)_{no}}{\left(\frac{Th}{U}\right)_{so}} \quad (6)$$

The sum of the two fractions represents the total U in the nodule (Eqn. (4)) and as all Th within the nodule is derived from the trapped residual soil fraction, the second term of Eqn. (3) is equal to zero (Eqn. (5)). The fraction of U included in the nodule as a soil detrital fraction, and thus assumed to be in secular equilibrium, can thus be calculated according to Eqn. (6).

For the nodule samples and hypothesizing that the carbonate precipitation event is the main factor affecting disequilibrium, we can assume that only the ^{238}U-series is in disequilibrium. Concerning the ^{235}U-series, it comprises only 0.07% of total natural U. Its contribution to the total U dose rate is relatively small: c. 4% (α-decay), ~2% (β-decay) and ~1% (γ-decay) (Guérin et al., 2011). Consequently, we assumed this decay chain to be in secular equilibrium, while a potential disequilibrium (if present) would be negligible relative to the total U dose rate. Finally, as all Th is derived from the trapped residual soil fraction, i.e. not to the carbonate precipitation event, the ^{232}Th-series is also assumed to be in secular equilibrium.

2.3.3. Proposed burial scenarios

To assess the effect of disequilibrium from carbonate precipitation on the $\dot{D}$ (Gy ka^{-1}) and thus on the resulting OSL ages, two end-member scenarios have been considered (Fig. 2): (1) the surrounding environment of the minerals has changed through time but radionuclides have remained in secular equilibrium during both time periods T_1 and T_2; and (2) the surrounding environment of the minerals has changed through time, and, in addition, carbonate precipitation induced disequilibrium of the ^{238}U-series during time period T_2. The relationships between the measured equivalent doses, the dose rates, and the time periods are as follow:

$$D_e = D_{e,\,so} + D_{e,no} = T_1 * \dot{D}_{so} + T_2 * \dot{D}_{no} \quad (7)$$

and,

$$\dot{D}_{so} = \dot{D}_{int} + \dot{D}_{ext1} \quad (8.1)$$

$$\dot{D}_{no} = \dot{D}_{int} + \dot{D}_{ext2} \quad (8.2)$$

where, D_e (Gy) is the equivalent dose, $D_{e,\,so}$ (Gy) is the dose received during the time period time T_1 which thus results from $\dot{D}_{so}$; and $D_{e,no}$ (Gy) is the equivalent dose received during the time period T_2 which thus results from $\dot{D}_{no}$. The internal dose rate ($\dot{D}_{int}$) does not change through time whereas the external dose rate is different during time T_1 ($\dot{D}_{ext1}$) and time T_2 ($\dot{D}_{ext2}$) as explained above. During T_1, the soil environment also varied through time as carbonate progressively accumulated. In the present-day soil, the proportion of carbonate nodules is 7% maximum. To assess this potential influence on the dose rate, the external dose rate for $\dot{D}_{so}$ was also calculated as mixture of a 7% $\dot{D}_{ext2}$ and 93% $\dot{D}_{ext1}$. Moreover, during time T_2, the cosmic ray contribution varied following late-stage erosion (step IV). As the intensity and the timing of the erosion event are unknown, a mean $\dot{D}_{cos}$ was calculated assuming erosional removal of 30 cm of soil during approximately 30% of the total time period, i.e $T_1 + T_2$ (see section 3.2). Finally, the nodule growth rate during time T_2 remains unconstrained. As the nodule size is expected to increase incrementally through time, this would result in an uncertainty on the scaled γ-dose ($\dot{D}_\gamma$), which was calculated with varying nodule diameters from 0.5 to 10 cm.

2.4. Calculations

2.4.1. External dose rate

To assess the relative contributions of the different decay series to the external dose rate ($\dot{D}_{ext}$, Gy ka^{-1}), the method outlined by Stokes et al. (2003) and later applied by Armitage (2015) was used. It is possible to calculate the external dose rate for both time periods T_1 and T_2 (i.e. $\dot{D}_{ext1}$ and $\dot{D}_{ext2}$, respectively), either assuming secular equilibrium (scenario 1) or taking into account various degrees of ^{238}U-series disequilibrium during T_2 (^{234}U/^{238}U ratios from 0.5 to 3, scenario 2). The resulting environmental dose rates calculated for scenarios 1 and 2 will then be compared to highlight the potential effect of disequilibrium on calculated environmental dose rates and OSL ages.

In the following section, each step leading to the calculation of the α, β and γ-event contributions to the $\dot{D}_{ext}$ are detailed. For the simple decay of K and Rb, the β and γ-dose contributions are calculated according to the conversion factors reported by Guérin et al. (2011). However, for the ^{238}U-series, the radioisotope specific activity (k) needs to be calculated for each radiation event in order to account for potential disequilibrium.

The following calculations must be done for the α-, β- and γ-decays of each radioisotope. Here we detail a representative example for the α-decay contribution (k_α) of a radioisotope x ($k_{x\alpha}$):

$$k_{x\alpha} = \left(\sum_{parent}^{n\ daughters} E_{x\alpha}\right) * a * b * c_\alpha \quad (9)$$

where, $E_{x\alpha}$ is the decay energy (MeV/Bq s^{-1}) of a radioisotope x and for an α-decay (Table A.1), a is the number of seconds per ka, b is the number of joules (J) per MeV and c_α is the grain size attenuation factor for α-radiation (e.g. Bell, 1980). The k factor is thus expressed in J/Bq ka^{-1}. As U comprises two decay chains with different abundances in nature (99.29% for ^{238}U and 0.07% for ^{235}U), the k factors for each decay event (α, β and γ) must be adjusted by their relative abundance. The k factor for a given decay chain varies with the number of daughter radioisotopes that are considered, i.e. for a decay chain in secular equilibrium, all daughters will be considered

in $E_{x\alpha}$ (i.e. the total energy of all α-particles for a given parent, listed in Table A.1).

As a result, the attenuated radiation (Gy ka^{-1}) for an α-decay event of an element X is calculated as follows:

$$X_\alpha = [X]*A_x*\ k_{x\alpha} \tag{10}$$

where, [X] is the element concentration in ppm (or in % for K), A_x is the isotopic activity of the radioisotope x in Bq/kg ppm (i.e. the number of decays occurring in a given time for a specific number of atoms), and $k_{x\alpha}$ is the specific activity of radioisotope x for an α-decay event (Eqn. (9)).

Both ^{238}U and ^{235}U radionuclides have to be added and scaled by their respective activities (A) and k factors for a given U content [U] (Eqn. (11)). Finally, for α-decay events, it is necessary to take into account the effectiveness of the α-particles (Aitken, 1985, 1998) and thus to multiply the outcome of Eqn. (8) by the a-value (a_{val}). Balescu and Lamothe (1993) measured the alpha efficiency of 150–250 μm K-feldspar grains for their samples, estimating an a_{val} of 0.11 ± 0.03, which we use in this study. The final equation to assess the energy of the U α-decay event (Gy ka^{-1}) is:

$$U_\alpha = ((A_{238U}*k_{238U\alpha}*[U]) + (A_{235U}*k_{235U\alpha}*[U]))*a_{val} \tag{11}$$

This calculation is valid for U series in secular equilibrium. However, for scenario 2 the ^{238}U-series is in disequilibrium; we can assume that all daughter radioisotopes below ^{234}U are absent, and that ^{234}U may be in excess or in deficit. Consequently, only the parent radioisotopes are considered in the calculation of E_x (Eqn. (9)), and [U] is scaled by its (^{daughter}X/^{parent}X) activity ratio μ, which represents the excess or lack of ^{daughter}X compared to ^{parent}X. Consequently, the U α-decay dose rate, where ^{234}U is in disequilibrium with ^{238}U, is:

$$U_\alpha = ((A_{238U}*k_{238U\alpha}*[U]) + (A_{234U}*k_{234U\alpha}*[U]*\mu) + (A_{235U}*k_{235U\alpha}*[U]))*a_{val} \tag{12}$$

Furthermore even in scenario 2, not all U within the nodule can be considered to be in disequilibrium because some is derived from the residual soil fraction (Eqn. (6)). Consequently, the U_α dose rate needs to be calculated for both equilibrium and disequilibrium, and the U concentrations [U] must be multiplied by the relative proportions calculated in Eqn. (6).

After the calculation of the contribution for each element, the same decay events' contribution must be added together and corrected for water attenuation using the appropriate factor (here for $\alpha = 1.49$; Aitken and Xie, 1990). The following equation shows an example for the total α-dose rate contribution ($\dot{D}_\alpha$):

$$\dot{D}_\alpha = \frac{U_\alpha + Th_\alpha}{\left(1 + 1.49*\frac{WF}{100}\right)} \tag{13}$$

where, U_α and Th_α are the attenuated doses calculated in Eqns (11) or (12), depending on the scenario (1 or 2), and WF is the water content (%) of the sample (estimated here to be 10 ± 2%).

Finally, the γ-dose rate ($\dot{D}_\gamma$) needs to be scaled during the time period T_2. Because the nodule diameter is < 30 cm, a nodule cannot be considered as an infinite matrix (Fig. 2). The final $\dot{D}_\gamma$ then accounts for the self-dose from the nodule and a contribution from the host sediment (Aitken, 1985):

$$\dot{D}_\gamma = \frac{p}{100}\dot{D}_\gamma^i + \left(1 - \frac{p}{100}\right)\dot{D}_\gamma^{ex} \tag{14}$$

where, the self-dose p (%) is calculated by multiplying the diameter of the nodule (cm) by its density (2.7 g cm^{-3}, as estimated for the nodules (n = 5)), $\dot{D}_\gamma^i$ is the gamma dose emitted by the decay of radionuclides present in the carbonate nodule, and $\dot{D}_\gamma^{ex}$ is the gamma dose emitted by the decay of radionuclides present in the soil.

2.4.2. OSL ages

The OSL age (ka) of trapped minerals, reflecting the deposition time of the soil parent material (t_0), can be calculated as follows:

$$t_0 = T_1 + T_2 = \frac{D_{e,so}}{\dot{D}_{so}} + \frac{D_{e,no}}{\dot{D}_{no}} \tag{15}$$

so,

$$t_0 = \left(\frac{D_{e,so}}{\dot{D}_{so}}\right) + T_2 \tag{16}$$

The length of T_2, or the age of carbonate nodule formation, is thus important to assess. The objective here is to evaluate the effect of different T_2 durations on the OSL age (t_0) for both scenarios. As specified in section 2.1, the pedogenic carbonate nodules are expected to form in Vertisols inherited from the AHP from c. 15 to 5 ka BP; (DeMenocal et al., 2000). Moreover, it is not excluded that carbonate is still precipitating in the present-day, as the soil chemical conditions are still favourable (Diaz et al., 2016). Consequently, the two end-members, represented by the minimum and maximum deposition ages, are:

$$t_{min} = \frac{D_e}{\dot{D}_{so}} \tag{17}$$

$$t_{max} = \frac{D_e}{\dot{D}_{no}} \tag{18}$$

where, t_{min} considers that the carbonate nodule never precipitated, i.e $T_2 = 0$, and t_{max} considers that the carbonate nodule always existed, i.e $T_2 = t_0$. The true sediment age should lie between these two unlikely end-members, i.e. some residence time in the soil followed by a second phase trapped in the nodule (Eqns. (15) and (16)).

For the disequilibrium scenario, the OSL ages are first calculated with a (^{234}U/^{238}U) activity ratio of 1.31, assuming that the ^{234}U daughters are absent. This ratio value is used following the ^{234}U/^{238}U ratios measured for Holocene pedogenic carbonate nodules from a similar environment in India (Violette et al., 2010). Different activity ratio values are also tested in subsequent calculations in order to more specifically determine this effect on the OSL ages.

3. Results

3.1. Luminescence results

A summary of the luminescence results is given in Table 2 for nodules NO1 and NO2. The SA overdispersion values (OD) for subsample NO1$_{Ext}$ are much higher than for subsample NO1$_{Int}$ for both the IR$_{50}$ (19.4 ± 0.6% and 8.6 ± 0.3%, respectively) and pIRIR$_{225}$ (8.4 ± 0.3% and 1.1 ± 0.8%, respectively) signals. PSG measurements have higher OD values than SA measurements, but follow the same trends. The IR$_{50}$/pIRIR$_{225}$ ratios, which represent the relationship between the doses derived by the IR$_{50}$ and the pIRIR$_{225}$ signals, are 0.50 and 0.41 for PSG and SA respectively for NO1$_{Ext}$. For NO1$_{Int}$, they are 0.74 and 0.64, while for NO2 they are 0.66 and 0.60. This ratio is expected to be less than unity as the IR$_{50}$ signal is more

Table 2
Comparison of pseudo-single grain (PSG) and small aliquot (SA) measurements for samples $NO1_{Ext}$, $NO1_{Int}$ and NO2. The D_e values were calculated according to the central age model (CAM; Galbraith et al., 1999) with uncertainties expressed at ±1σ. The $IR_{50}/pIRIR_{225}$ ratio illustrates the difference between investigated signals. The PSG/SA ratio compares the two measurement approaches. n is the number of aliquots/grains measured.

	Signal	Pseudo-single grain (PSG)				Small aliquot (SA)				PSG/SA
		n	D_e (Gy)	$IR_{50}/pIRIR_{225}$	OD (%)	n	D_e (Gy)	$IR_{50}/pIRIR_{225}$	OD (%)	
$NO1_{Ext}$	IR_{50}	63	33.9 ± 15.2	0.50	38.1 ± 0.4	24	25.5 ± 6.3	0.40	19.4 ± 0.6	1.3
	$pIRIR_{225}$	25	67.3 ± 11.8		15.0 ± 0.5	24	63.1 ± 7.0		8.4 ± 0.3	1.1
$NO1_{Int}$	IR_{50}	125	57.3 ± 13.3	0.74	22.8 ± 0.1	24	56.4 ± 6.9	0.64	8.6 ± 0.3	1.0
	$pIRIR_{225}$	54	77.8 ± 10.4		11.3 ± 0.2	24	88.3 ± 5.2		1.1 ± 0.8	0.9
NO2	IR_{50}	148	52.2 ± 15.6	0.66	29.9 ± 0.2	24	53.6 ± 4.0	0.60	5.1 ± 0.3	1.0
	$pIRIR_{225}$	24	78.9 ± 16.8		23.1 ± 0.7	24	90.5 ± 5.5		2.2 ± 0.5	0.9

affected by anomalous fading (Thomsen et al., 2008). This is supported by the measured g_{2days} values (n = 3), which are 4.5 ± 0.9%/decade (NO1) and 5.0 ± 0.7%/decade (NO2) for the IR_{50} signals, and 1.7 ± 0.6%/decade (NO1) and 1.9 ± 0.6%/decade (NO2) for the $pIRIR_{225}$ signals. Moreover, the $pIRIR_{225}$ signal has been shown to bleach more slowly than the IR_{50} signal (Buylaert et al., 2012), supported for these samples by the residual doses measured after sunlight bleaching (~4 Gy for the IR_{50} signal and ~8 Gy for the $pIRIR_{225}$ signal, Table 3). The dose recovery ratios (measured dose - residual dose/given dose) measured using PSG for both samples show acceptable deviations from unity within 10% (Table 3). The OD values for the PSG dose recovery test range between 10 and 24% (Table 3).

The D_e values determined using the PSG and SA measurement approaches are within uncertainties for all samples, and only the $NO1_{Ext}$ IR_{50} signal has a ratio beyond 10% of unity, i.e. 1.3 (Table 2 and Fig. 3). The kernel density estimate (KDE) plots illustrate the SA D_e distribution for $NO1_{Ext}$ and $NO1_{Int}$, with both IR_{50} (Fig. 4A) and $pIRIR_{225}$ (Fig. 4B) signals. The difference between the two sample D_e values is smallest for the $pIRIR_{225}$ signal.

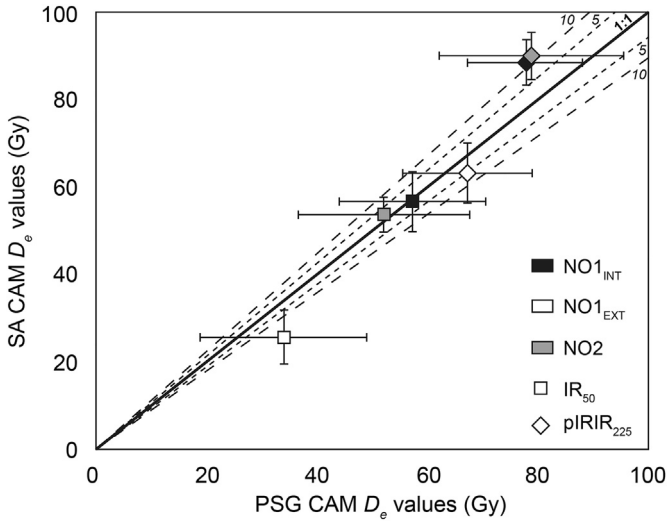

Fig. 3. Comparison of the pseudo- single grain (PSG) measurements with small aliquot (SA) measurements for sample $NO1_{Int}$ (black), $NO1_{Ext}$ (white) and NO2 (grey), showing both IR_{50} (square) and $pIRIR_{225}$ (diamond) signals. Dashed lines show the deviation percentage (5 and 10%) from the 1:1 line (bold). Uncertainties are shown at one standard deviation (±1σ).

3.2. Dose rate assessment

Electron microprobe micro-analysis on individual grains indicated that the <2.58 g cm^{-3} mineral extract comprises 30% K-poor plagioclases (Oligoclase, K-content <5%) and 70% K-rich feldspars (Orthoclase), resulting in a mean K-content of 12.65 ± 0.10% (±1σ) for the K-rich feldspar fraction. Assuming the K-rich feldspars contribute mostly to the measured signal, the calculated $\dot{D}_{int}$ is 0.45 ± 0.09 Gy ka^{-1} for both NO1 and NO2. The $\dot{D}_{cos}$ may have varied during T_2 following late-stage erosion (Step IV, Fig. 2). The extent of erosion is unknown but if we assume a total erosion of 30 cm, $\dot{D}_{cos}$ changes from ~0.21 Gy ka^{-1} (before erosion) to ~0.29 Gy ka^{-1} (after erosion) for NO1, and from ~0.17 to 0.18 Gy ka^{-1} for NO2. The other unconstrained parameter is the proportion of time affected by the change in the $\dot{D}_{cos}$, i.e. when the erosion event occurred. As proposed by Diaz et al. (2016), this event occurred after nodule formation and could therefore have been initiated towards the end of the African Humid Period. The proportion of time affected by the change in $\dot{D}_{cos}$ should then be ~30%. Consequently, $\dot{D}_{cos}$ values of 0.25 ± 0.03 Gy ka^{-1} and 0.17 ± 0.02 Gy ka^{-1} are obtained for NO1 and NO2, respectively, for the whole time period, i.e. $T_1 + T_2$.

Table 3
Residuals and dose recovery test results from pseudo-single grain (PSG) measurements. The residual D_e values were calculated according to the central age model (CAM; Galbraith et al., 1999) represented with uncertainties expressed at ±SE (standard error). The dose recovery ratio is calculated as the recovered dose - mean residual (D_{e-res}) divided by the given dose (D_{eg}) and are expressed at ±1σ.

	Signal	Residual dose		Recovery test		
		n	D_e ±SE (Gy)	n	$D_{e\text{-}res}/D_{eg}$±1σ	OD (%)
$NO1_{Ext}$	IR_{50}	98	3 ± 0.3	48	1.03 ± 0.30	22 ± 0.4
	$pIRIR_{225}$	59	8 ± 0.6	22	1.13 ± 0.25	10 ± 0.6
$NO1_{Int}$	IR_{50}	106	4 ± 0.4	149	1.03 ± 0.23	16 ± 0.1
	$pIRIR_{225}$	75	8 ± 1.0	81	0.97 ± 0.58	24 ± 0.2
NO2	IR_{50}	194	3 ± 0.2	211	0.93 ± 0.14	10 ± 0.1
	$pIRIR_{225}$	168	6 ± 0.3	96	0.94 ± 0.19	14 ± 0.1

The external dose rates in the nodule ($\dot{D}_{ext2}$) were calculated for both scenarios. Continuing with the example of α-decay as developed in sections 2.4, the energy values for an α-decay ($E_{x\alpha}$) of the ^{238}U-series in equilibrium is 42.87 MeV/Bq s^{-1}, whereas in disequilibrium, $E_{x\alpha}$ is reduced to 4.19 MeV/Bq s^{-1} (Table A.2). The resultant $k_{238U\alpha}$ factors (Eqn. (6)) are thus 0.036 and 0.003, for the equilibrium and the disequilibrium scenario, respectively. This represents a one order of magnitude reduction in $\dot{D}_{U\alpha}$ (Table A.3). All the attenuated radiation values, for each element and radiation type, in the soil and nodule and for both scenarios, are given in the supplementary material (Table A.3).

Following Eqns. (3)–(6) and geochemical measurements (Table 1), the calculation of the U fraction included in the carbonate nodule as a soil detrital fraction, and thus assumed to be in secular equilibrium, is 0.24 (i.e. 24%). This implies that 76% U was included as $UO_2(CO_3)_2^{-2}$ and can thus be assumed to be in disequilibrium. The resulting external dose rate during the time period T_1 ($\dot{D}_{ext1}$, i.e. from the soil and cosmic ray dose during step I), is 5.36 ± 0.34 Gy ka^{-1} and 5.28 ± 0.34 Gy ka^{-1} for NO1 and NO2

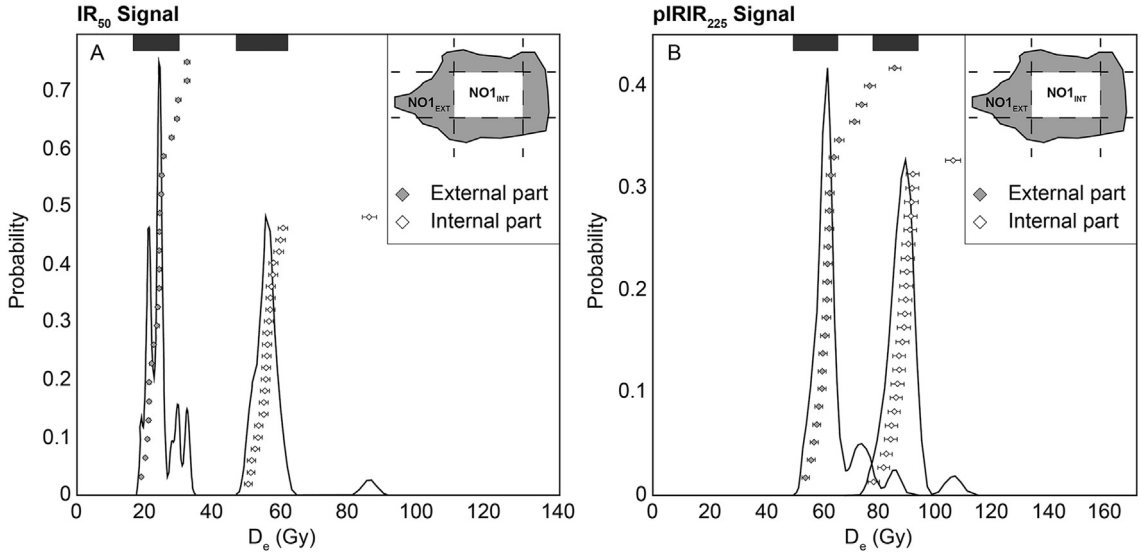

Fig. 4. Kernel Density Estimate (KDE) plots. Comparison of the SA equivalent dose (n = 24) for the external part of nodule NO1 ($NO1_{Ext}$) with its internal part ($NO1_{Int}$), for both IR_{50} (A) and $pIRIR_{225}$ (B) signals. The equivalent doses for both signals are significantly different between $NO1_{Ext}$ and $NO1_{Int}$. This difference is greater for the IR_{50} signal than the $pIRIR_{225}$ signal.

respectively. The external dose rate during the time period T_2 ($\dot{D}_{ext2}$, i.e. from the nodule and the soil), is 3.67 ± 0.34 Gy ka^{-1} and 3.79 ± 0.34 Gy ka^{-1} for NO1 and NO2, respectively, when assuming secular equilibrium (scenario 1). If disequilibrium is accounted for (scenario 2), the $\dot{D}_{ext2}$ is 3.00 ± 0.34 Gy ka^{-1} and 3.18 ± 0.34 Gy ka^{-1} for NO1 and NO2, respectively (Table 3).

The total environmental dose rate, i.e. taking into account the $\dot{D}_{int}$, for the time period T_1 ($\dot{D}_{so}$) is thus 5.81 ± 0.34 Gy ka^{-1} (NO1) and 5.73 ± 0.34 Gy ka^{-1} (NO2). For the time period T_2 ($\dot{D}_{no}$), when assuming secular equilibrium, it is 3.92 ± 0.34 Gy ka^{-1} (NO1) and 3.96 ± 0.34 Gy ka^{-1} (NO2), while it is reduced to 3.25 ± 0.34 Gy ka^{-1} (NO1) and 3.35 ± 0.34 Gy ka^{-1} (NO2) if disequilibrium is accounted for (Table 4).

The effect of different nodule diameters on the dose rate shows an increase of ~0.3 Gy between nodule diameters of 0.5 and 10 cm, which represent a maximum error of c. 8%. Moreover, different ($^{234}U/^{238}U$) activity ratio values, ranging from 0.5 to 3 assuming that ^{234}U daughters are absent, were explored in the calculation of $\dot{D}_{ext2}$. Resulting dose rates range from 3.04 to 3.10 Gy ka^{-1} inducing a maximum change of 0.06 Gy ka^{-1} (~2%). Finally, the potential accumulation of carbonate during T_1 induced a maximum change of 0.2 Gy ka^{-1} (~8%) if we consider a concentration of 7% carbonate nodules in the soil according to the present-day observations. Regarding the lack of real quantitative constrains of these factors and the negligible effect on the calculated dose rates, we did not consider them in the age calculations.

3.3. OSL ages

Fig. 5 illustrates the anomalous fading corrected and uncorrected ages for NO1. It shows the ages calculated for the secular equilibrium scenario (scenario 1) and between the end-members (Eqns. (16)–(18)). According to the g_{2days} values (%-dec), the correction is more important for the IR_{50} ages than the $pIRIR_{225}$ ages (Fig. 5A, B). The corrected IR_{50} ages are in good agreement, i.e. on the 1:1 line, with the uncorrected $pIRIR_{225}$ ages (Fig. 5C). Greater deviation between values is observed when comparing the corrected IR_{50} ages with the corrected $pIRIR_{225}$ ages (Fig. 5D). Even if the residual doses are subtracted from the $pIRIR_{225}$ D_e value and the IR_{50} D_e value, the corrected $pIRIR_{225}$ ages are ~25% greater than the corrected IR_{50} ages. The agreement between IR_{50} ages and $pIRIR_{225}$ ages is good when $pIRIR_{225}$ ages are uncorrected by anomalous fading.

Fig. 6 illustrates the equilibrium and disequilibrium OSL ages for samples NO1 and NO2, calculated with time period T_2 ranging from 0 to 15 ka. The represented ages are the uncorrected $pIRIR_{225}$ ages. The OSL age (t_0) ranges from 15 ka to 22 ka. The difference between the equilibrium and disequilibrium OSL ages is <5% if the carbonate nodule precipitation age is <7 ka, and between 5 and 10% if the nodule precipitation age is 7–15 ka. This is represented by the deviation from the 1:1 line, which increases with the carbonate nodule age. The OSL ages shown in Fig. 6 were calculated with a ($^{234}U/^{238}U$) activity ratio of 1.31 for scenario 2. However, if the effect of different ($^{234}U/^{238}U$) activity ratios (0.5–3), as a function of different T_2 durations, is added (Fig. 6, inset), this increases the difference between equilibrium and disequilibrium OSL ages by only 1%.

Fig. 7 shows the resulting OSL ages of sample NO1 and NO2 calculated as a function of the carbonate nodule age. The black bold line and grey bold line represent the disequilibrium and the secular equilibrium scenarios, respectively. The minimum OSL ages (white stars) are obtained for a carbonate nodule age of 0 ka, i.e. the

Table 4
Internal ($\dot{D}_{int}$), cosmic ($\dot{D}_{cos}$) and environmental dose rates ($\dot{D}$) for NO1 and NO2, for the equilibrium (1) and disequilibrium (2) scenarios.

	$\dot{D}_{int}$ Gy ka^{-1}	$\dot{D}_{ext1}$ Gy ka^{-1}	$\dot{D}_{so}$ Gy ka^{-1}	Scenario 1		Scenario 2	
				$\dot{D}_{ext2}$ Gy ka^{-1}	$\dot{D}_{no}$Gy ka^{-1}	$\dot{D}_{ext2}$ Gy ka^{-1}	$\dot{D}_{no}$ Gy ka^{-1}
NO1	0.45 ± 0.09	5.36 ± 0.34	5.81 ± 0.34	3.67 ± 0.34	3.92 ± 0.34	3.00 ± 0.34	3.25 ± 0.34
NO2	0.45 ± 0.09	5.28 ± 0.34	5.73 ± 0.34	3.79 ± 0.34	3.96 ± 0.34	3.18 ± 0.34	3.35 ± 0.34

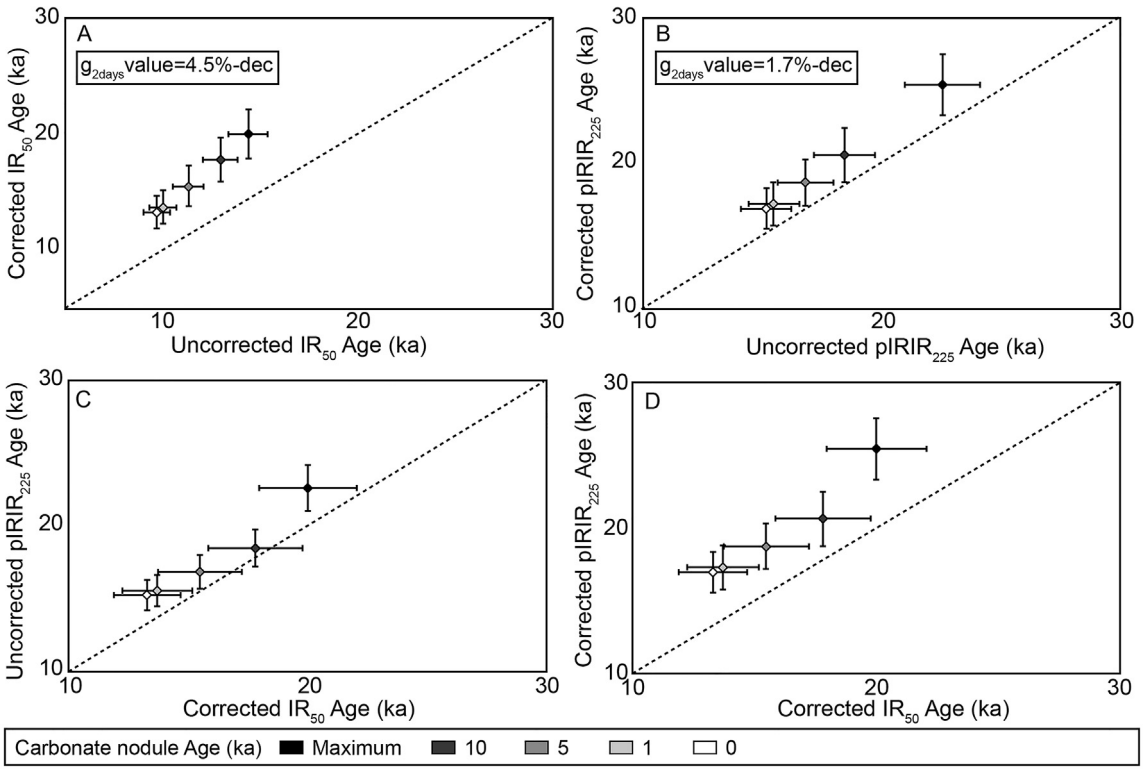

Fig. 5. Ages calculated for NO1, using different carbonate nodule ages (grey scale) and assuming secular equilibrium (scenario 1). A) Uncorrected IR_{50} age versus fading corrected IR_{50} age, B) Uncorrected $pIRIR_{225}$ age versus fading corrected $pIRIR_{225}$ age; the g-values are given in the boxes. C) Fading corrected IR_{50} age versus uncorrected $pIRIR_{225}$ age, D) Corrected IR_{50} age versus corrected $pIRIR_{225}$ age.

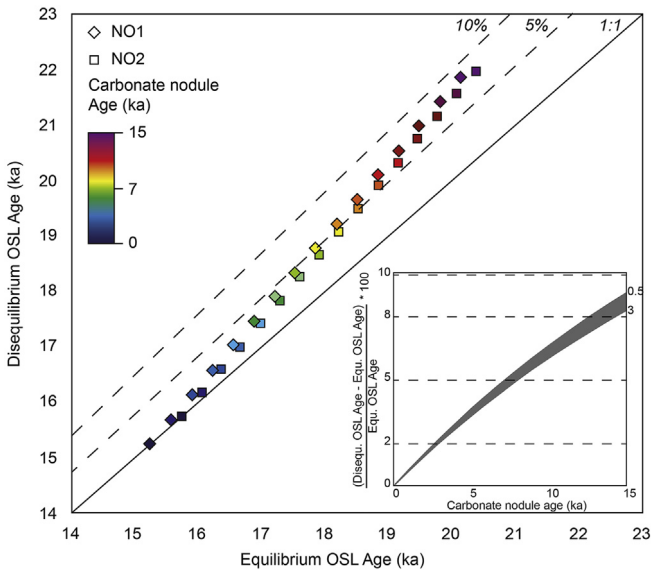

Fig. 6. Effect of nodule precipitation on calculated OSL ages. OSL ages were calculated for $NO1_{Int}$ (diamond) and NO2 (square) considering either an equilibrium or disequilibrium scenario. An activity ratio ($^{234}U/^{238}U$) of 1.31 was taken in the calculations. The difference between both scenarios increases with the carbonate nodule age (i.e. the duration of T_2). The inset shows the effect of changing the ($^{234}U/^{238}U$) activity ratio from 0.5 to 3 on OSL ages as a function of carbonate nodule age and duration of time T_2. Calculations were done taking the most extreme scenario, i.e. assuming that all ^{234}U daughters were lacking. The error is <10% irrespective of the ($^{234}U/^{238}U$) activity ratio if the nodule age is 15 ka. The error associated with different ($^{234}U/^{238}U$) activity ratios (ranging from 0.5 to 3, grey area) increases with the carbonate nodule age but is negligible compared to the effect of the absence of ^{234}U daughters. If these were present, the disequilibrium scenario would get closer to secular equilibrium.

carbonate nodule never precipitated (=no disequilibrium effect on the dose rate), and are 15.2 ka (NO1) and 15.8 ka (NO2). However, when the carbonate nodule precipitates, the $\dot{D}_{ext}$ will differ according to the different scenarios. This results in two different age-accumulation rates (Fig. 7), which deviate from one another with time, i.e. with increasing the carbonate nodule age. The slope of the lines assuming decay chain equilibrium for nodules NO1 and NO2 (~0.3) is lower than the disequilibrium lines (~0.4), which is a consequence of the greater $\dot{D}$. The maximum OSL ages (black stars) are c. 23 ka for scenario 1 and c. 27 ka for scenario 2, with a maximum deviation of 18%. These maximum ages imply that the OSL age is equal to the carbonate age (i.e. the carbonate nodule already existed at the deposition time). The grey area in Fig. 7 represents the African Humid Period (AHP, c. 5 ka to c. 15 ka); if we consider that the carbonate nodule formed during the AHP (Fig. 7, white arrow), giving plausible OSL age ranges between c. 16 to 22 ka.

4. Discussion

4.1. Suitable mineral population

In this study, we investigated the potential issue of partial bleaching using PSG instead of strict SG. The number of grains is ~10–20 but chemical measurements of the <2.58 gcm^{-3} fraction showed that 70% of the grains were K-rich feldspars and 30% K-poor feldspars. Consequently, as K-rich feldspars are brighter, the number of responding grains is ~7–14 for each PSG measurement. Except for the IR_{50} signal of $NO1_{Ext}$, the OD values are <30%. For PSG measurements, the high OD in the D_e values can be attributed to intrinsic factors, such as measurement uncertainties, thermal transfer, variable rates of fading and extrinsic factors, such as partial

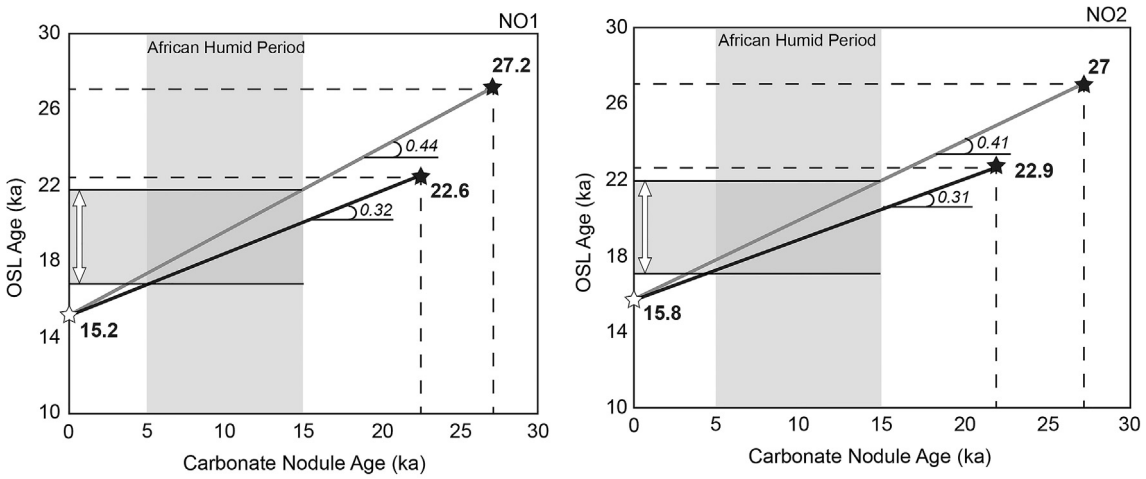

Fig. 7. OSL ages for NO1 (left) and NO2 (right) as a function of the carbonate nodule formation age. The bold black line represents the equilibrium scenario (1) and the bold grey line represents the disequilibrium scenario (2). The end-members calculated assuming that the nodule has always existed (maximum OSL age, black stars) and late, instantaneous nodule precipitation until a nodule age of 0 ka, i.e. carbonate nodule never existed (minimum OSL age, white stars), calculated with Eqns. (17) and (18). The plausible OSL ages should thus range between these two end-members. As carbonate nodules are expected to form during the African Humid Period (grey area), the most plausible OSL age should range between 16 and 22 ka (white arrows).

bleaching, post-depositional processes and potentially variable micro-dosimetry (e.g. Duller, 2008; Lamothe et al., 2012; Reimann et al., 2012; Mayya et al., 2006). As the grains might have been mixed by pedoturbation after deposition, and as the carbonate nodules were exposed to light after precipitation, scatter in the equivalent dose (D_e) distributions relating to partial bleaching, is anticipated.

Overdispersion from the dose recovery experiment should enable scatter caused by intrinsic factors only, to be characterised (Reimann et al., 2012), and for single-grain feldspar the OD values measured in other studies range from 6 to 22% (Neudorf et al., 2012; Reimann et al., 2012; Trauerstein et al., 2014; Smedley et al., 2015). The OD values of the dose recovery experiments for NO1 and NO2 (PSG) range between 10 and 24% (Table 3); which is significantly greater than the measured instrument reproducibility (<10% for PSG measurements). This could be explained by variability in rates of anomalous fading between grains from the same sample (Lamothe et al., 2012), or variations in the rate of signal bleaching (Buylaert et al., 2012; Smedley et al., 2015). When the OD values recorded for the natural measurements are contrasted with those from the dose-recovery measurements, it is apparent that most signals and samples contain some scatter attributed to extrinsic factors. Heterogeneous carbonate accumulations could result in micro-dosimetric variations that partly explain this apparent excess in dispersion. This would be true during step I (Fig. 2), however during step II, thin section analyses (Fig. 1C) indicate a near-homogeneous distribution of detrital minerals in the nodules. $NO1_{Ext}$ has the greatest OD and had the greatest degree of sunlight exposure (nodule surface, sampled from the surface of a mima-like mound), which suggests that partial bleaching may be a key cause of the overdispersion that we observe. This interpretation is supported by the $IR_{50}/pIRIR_{225}$ ratio, which is significantly smaller (~0.2) for $NO1_{Ext}$ (0.50) compared to $NO1_{Int}$ (0.74), indicative of greater reset of the fast-bleaching IR_{50} signal (e.g. Thiel et al., 2011; Buylaert et al., 2012). Furthermore pedoturbation processes, which are characteristic of Vertisols, may also have induced some of the observed scatter (Bateman et al., 2003). The OD value of NO2 is 29.9± 0.2% for the IR_{50} signal, but the NO2 $IR_{50}/pIRIR_{225}$ ratio is similar to $NO1_{Int}$ (0.66 and 0.74, respectively), suggesting that the luminescence signals have not been partially reset. Nevertheless, the OD values for both $NO1_{Int}$ and NO2 assessed by PSG measurements suggest that any partial bleaching is not significant (i.e OD values are ≤30%) and the minerals from the internal part of the nodule are considered suitable for luminescence dating.

Contrasting the PSG and SA measurements indicates that although some SA D_e values are higher than the PSG D_e values, they are within errors and the difference between both approaches is ≤ 10% (Fig. 3). The difference is greater (>10%) for the IR_{50} signal of $NO1_{Ext}$, emphasizing that post-deposition bleaching affects the exterior of surficial nodule NO1 and that the IR_{50} signal bleaches most rapidly. Consequently, as PSG measurements are time consuming and technically challenging (Duller, 2008; Trauerstein et al., 2014), and as they do not significantly change the D_e values determined for these samples, it is suggested that the SA approach is both sufficient and appropriate.

Finally, comparing the SA measurements for $NO1_{Ext}$ and $NO1_{Int}$ (Fig. 4), the difference in D_e values between the internal and external parts is significant for both the IR_{50} and $pIRIR_{225}$ signals, but is greatest for the IR_{50} signal. This may be explained by the slower bleaching of the $pIRIR_{225}$ signal in comparison to the IR_{50} signal (Buylaert et al., 2012), as also evidenced by our residual measurements (Table 3). Differences between the IR_{50} and $pIRIR_{225}$ D_e values are explained by anomalous fading (Thomsen et al., 2008; Buylaert et al., 2012). Fading corrections were done using the luminescence package (v.0.3.4) in RStudio (Kreutzer et al., 2012) following Huntley and Lamothe (2001). According to Fig. 5, the IR_{50} and $pIRIR_{225}$ ages are in good agreement when $pIRIR_{225}$ ages are uncorrected for anomalous fading (Fig. 5C). However, when $pIRIR_{225}$ ages are corrected for anomalous fading, they overestimate the age compared to corrected IR_{50} ages (Fig. 5D). Subtraction of the residual measured following 4 h of sunlight exposure in Lausanne cannot reduce the fading-corrected $pIRIR_{225}$ age overestimation, relative to the fading corrected IR_{50} ages. The g_{2days} values measured for the $pIRIR_{225}$ signal are close to 1.5%/decade within error, measuring such low fading rates accurately is difficult. Therefore, fading correction may not necessarily give more accurate ages (Wallinga et al., 2007; Roberts, 2012). Moreover, the residual dose was measured after sunlight exposure in Lausanne, which may be considerably different from the natural depositional environment in Cameroon. Finally, as discussed previously, our results suggest that the $pIRIR_{225}$ signals of $NO1_{Int}$ and NO2 were not affected by partial bleaching. Consequently, regarding (i) the

challenge of accurately constraining low rates of anomalous fading, (ii) the lack of an appropriate residual dose analogue, and (iii) the good agreement between fading-corrected IR_{50} ages and uncorrected $pIRIR_{225}$ ages, the latter are regarded as being the most representative of the true age (Fig. 5C).

4.2. Effect of carbonate nodule formation on the environmental dose rate

The carbonate nodule formation event induced two different effects: (1) a change in the radionuclide concentration, and (2) as assumed in this study, a disequilibrium in the ^{238}U-series. Consequently, the $\dot{D}$ is 50% lower during T_2 than during T_1, as the respective radionuclide concentrations also reduced. Moreover, if the ^{238}U-series is considered to be in disequilibrium (scenario 2) during T_2, the $\dot{D}$ is reduced by a further 19 ± 3% (~0.7 Gy ka^{-1}) than when secular equilibrium is assumed (scenario 1). This is a maximum estimate because we assume that all ^{234}U daughters are absent. However, this difference is significant and two times more important than the uncertainties induced by different (^{234}U/^{238}U) activity ratios or different carbonate nodule diameters, which exert maximum changes of 2% (0.07 Gy ka^{-1} between ^{234}U/^{238}U activity ratios of 0.5 and 3) and 8 ± 1% (0.3 Gy ka^{-1} between diameters of 0.5 and 10 cm), respectively. Finally, the progressive accumulation of carbonates during T_1 could induce a change in the infinite matrix dose rate. Calculating the dose rate assuming a maximum probable carbonate accumulation of 7% (as presently observed in the soil), results in maximum change of $\dot{D}$ during T_1 of 3% (0.2 Gy a^{-1}). Consequently, all combined, the maximum total uncertainty, without the disequilibrium effect, on the environmental dose rate may be ~10% (~0.5 Gy ka^{-1}).

4.3. Soil parent material deposition age

The significance of the disequilibrium effect depends directly on the age of the carbonate nodule, i.e. the duration of time period T_2. Thus whilst the environmental dose rate ($\dot{D}$) may change considerably, the effect on the OSL age may be relatively limited. The uncertainty induced by the disequilibrium is <10% for nodule ages ranging from 0 to 15 ka. As $\dot{D}_{no}$ is lower than $\dot{D}_{so}$, when the $\dot{D}_{no}$ contribution increases, i.e. T_2 increases, the OSL age becomes older (Fig. 6). This is also apparent within the disequilibrium scenario. The effect of different (^{234}U/^{238}U) activity ratios (0.5–3) on the OSL age (Fig. 6, inset), as a function of different T_2 durations, is even less significant (~1%) than the absence of ^{234}U daughters (<10%). If some ^{234}U daughters were present, the difference between the equilibrium and disequilibrium OSL ages would be smaller. Furthermore, regarding Fig. 7, it is possible to state that both minimum (c. 15 ka) and maximum (c. 23 or 27 ka) OSL ages are improbable: $T_2 = 0$ is impossible as the nodule exists, and $T_2 = t_0$ is unlikely as the carbonate nodule formed within the host soil. It is thus certain that the deposition event preceded carbonate accumulation (i.e. $T_2 < t_0$). The time of mineral deposition (t_0) should thus range between these two end-members (Fig. 7). Finally, the nodule growth rate is unknown but this effect on the final age would induce a maximum uncertainty of 5% (~2 ka). However, this is for t_{max}, if we look at OSL calculated ages between the expected T_2 range, the error would be less than 2% on the OSL age (<1 ka), which is considered negligible as it is within errors.

Consequently, the maximum difference between the two scenarios is 15.5 ± 1.5% on average for both samples (Fig. 7). As the carbonate nodules are expected to form during the AHP (Fig. 7; grey area), the uncertainty induced by disequilibrium should be less than 10%. Nevertheless, even in this range, the most probable OSL age ranges are 17–20 ka and 17–22 ka for the equilibrium and the disequilibrium scenarios, respectively. The OSL age uncertainty is thus still ~20%, which is significant. Consequently, it is crucial to independently assess the duration of T_2 to calculate accurate OSL ages. The uncertainty attributed to the carbonate nodule age is higher than the uncertainty attributed to the disequilibrium. Finally, the uncertainties related to other parameters, such as the nodule growth rate, the degree of disequilibrium or the progressive accumulation of carbonate during T_1, are even lower than the disequilibrium. Since these parameters have a negligible influence on the paleoenvironmental interpretation, they are not considered further.

4.4. Mineral fractions within pedogenic carbonate nodule as time archives

The minerals trapped in the pedogenic carbonate nodules can be used to assess the age of the soil parent material deposition. Despite the amount of uncertainty induced by the carbonate nodule age and the associated disequilibrium, calculated OSL ages show that the deposition of the soil parent material may have occurred before the AHP, i.e. before 15 ka. Such ages would suggest that the soil parent material was deposited during a drier period, termed the Bossoumian (Hervieu, 1970). This information is important and confirms the hypothesis that the soils may have been initiated during the AHP (Diaz et al., 2016) following the Bossoumian and thus the deposition of the soil parent material. However, to strengthen this statement the deposition ages need to be calculated more accurately, and in order to achieve this, the carbonate nodule precipitation ages must be determined independently with other methods (i.e. U/Th or radiocarbon dating). Nevertheless, pedogenic carbonate nodules are important time archives and can be used to get temporal information on the soil parent material deposition constraining the onset of pedogenesis, to which carbonate precipitation is related.

5. Conclusions

Carbonate nodules in soil relics can be used as time archives. As they are pedogenic in origin, the minerals trapped within them are representative of the soil parent material. Luminescence dating of these minerals can provide information on the deposition time of the sediments from which the soils developed. In this study, pedoturbation and post-deposition partial bleaching can affect the OSL signal of the minerals. We show that the minerals from the internal part of a nodule have low overdispersion values using either pseudo-single grain or small aliquot measurements, which suggests that this mineral population is unaffected by partial bleaching and/or pedogenic processes and is thus suitable for OSL dating. Moreover, the carbonate precipitated from surficial waters and, in this context, the ^{238}U-series is likely to be in disequilibrium. We found that only 76% of U could be considered in disequilibrium, the other 24% being derived from the trapped residual soil fraction and thus assumed to be in secular equilibrium. Considering this context, the worst-case disequilibrium scenario is when all ^{234}U daughters are absent, which results in a decrease of the environmental dose rate by 19 ± 3% (~0.7 Gy ka^{-1}), irrespective of the (^{238}U/^{238}U) activity ratio value included in the calculations (from 0.5 to 3). However, the effect of disequilibrium on the final OSL age is shown to be strongly dependent on the carbonate nodule precipitation age. As the carbonate nodules are expected to have precipitated during the AHP, the maximum uncertainty on the OSL ages should be c. 20% and the maximum error induced by the disequilibrium should be <10%. To conclude, the assessment of the carbonate nodule age is important for OSL age calculations, when using minerals trapped within carbonate nodules. It is advisable to

combine independent methods to assess the time of carbonate formation. However, this alternative dating approach is useful when fieldwork/logistical issues prevent the possibility of collecting soil or sediment samples for OSL dating. Moreover, our proposed method is promising and has the potential to constrain soil formation and associated pedogenic processes inducing secondary carbonate precipitation. Beyond being geochemical proxies, pedogenic carbonate nodules are thus also valuable sedimentary time archives.

Acknowledgements

The authors want to thank the two anonymous reviewers for their constructive comments. They also want to thank Rachel Smedley and Simon Armitage for useful discussions on single grain measurements and disequilibrium. Thank you to Karin Verrecchia for reading the text. Finally, Olivier Reubi (ISTE, University of Lausanne) is thanked for microprobe analyses and Jean-Claude Lavanchy (ISTE, University of Lausanne) for XRF analyses. The Swiss National Science Foundation supported this work (grant no. 200021-147038 to E.P.V, grant Ambizione PZ00P2_148191 to P.G.V., G.E.K. was supported by grant no. PP00P2-38956).

Appendix A. Supplementary data

Supplementary data related to this article can be found at http://dx.doi.org/10.1016/j.quageo.2016.08.008.

References

Achyuthan, H., Flora, O., Braida, M., Shankar, N., Stenni, B., 2010. Radiocarbon ages of pedogenic carbonate nodules from Coimbatore region, Tamil Nadu. J. Geol. Soc. India 75, 791–798.
Ahmad, N., 1983. Vertisols. In: Wilding, L.P., et al. (Eds.), Pedogenesis and Soil Taxonomy, The Soil Orders, vol. II. Elsevier Science, New York, USA, pp. 91–123.
Aitken, M.J., 1998. An Introduction to Optical Dating: the Dating of Quaternary Sediments by the Use of Photon-stimulated Luminescence. Oxford University Press, Oxford, UK.
Aitken, M.J., Xie, J., 1990. Moisture correction for annual gamma dose. Anc. TL 8, 6–9.
Aitken, M.J., 1985. Thermoluminescence Dating. Academin Press, Inc., London, UK.
Alonso-Zarza, A.M., Tanner, L.H., 2010. Carbonates in Continental Settings. In: Geochemistry, Diagenesis and Applications. Elsevier, Amsterdam.
Andersen, M.B., Erel, Y., Bourdon, B., 2009. Experimental evidence for ^{234}U–^{238}U fractionation during granite weathering with implications for $^{234}U/^{238}U$ in natural waters. Geochim. Cosmochim. Acta 73, 4124–4141.
Armitage, S.J., 2015. Optically stimulated luminescence dating of ocean drilling program core 658B: compilations arising from authigenic uranium uptake and lateral sediment movement. Quat. Geochronol. 30, 270–274.
Armitage, S.J., Bristow, C.S., Drake, N.A., 2015. West african monsoon dynamics inferred from abrupt fluctuations of lake Mega-Chad. PNAS 112, 8543–8548.
Auclair, M., Lamothe, M., Huot, S., 2003. Measurement of anomalous fading for feldspar IRSL using SAR. Radiat. Meas. 37, 487–492.
Balescu, S., Lamothe, M., 1993. Thermoluminescence dating of the Holsteinian marine formation of Herzeele, northern France. J. Quat. Sci. 8, 117–124.
Bateman, M.D., Frederick, C.D., Jaiswal, M.K., Singhvi, A.K., 2003. Investigations into the potential effects of pedoturbation on luminescence dating. Quat. Sci. Rev. 22, 1169–1178.
Bell, W.T., 1980. Alpha Attenuation in quartz grains for thermoluminescence dating. Anc. TL 12, 4–8.
Brabant, P., Gavaud, M., 1985. Les Sols et les Ressources en Terres du Nord-Cameroun. ORSTOM, Paris, France, p. 369.
Buylaert, J.-P., Jain, M., Murray, A.S., Thomsen, K.J., Thiel, C., Sohbati, R., 2012. A Robust feldspar luminescence dating method for middle and late pleistocene sediments. Boreas 41, 435–451.
Buylaert, J.-P., Murray, A.S., Thomsen, K.J., Jain, M., 2009. Testing the potential of an elevated temperature IRSL signal from K-feldspar. Radiat. Meas. 44, 560–565.
Cerling, T.E., 1984. The stable isotopic composition of modern soil carbonate and its relationship to climate. Earth Planet. Sci. Lett. 71, 229–240.
Chabaux, F., Bourdon, B., Riotte, J., 2008. U-Series geochemistry in weathering profiles, river waters and lakes. In U-Th series nuclides in aquatic systems edited by S. Krishnaswami and J. Kirk Cochran. Radioactivity in the Environment 13.
Chabaux, F., Riotte, J., Dequincey, O., 2003. U-Th-Ra fractionation during weathering and river transport. Rev. Mineral. Geochem. 52, 533–576.
Chkir, N., Guendouz, A., Zouari, K., Hadj Ammar, F., Moulla, A.S., 2009. Uranium isotopes in groundwater from the continental intercalaire aquifer in Algerian Tunisian Sahara (Northern Africa). J. Environ. Radioact. 100, 649–656.
DeMenocal, P.B., Tierney, E.J., 2012. Green Sahara: african humid periods paced by earth's orbital changes. Nat. Educ. 3, 12.
DeMenocal, P.B., Ortiz, J., Guilderson, T., Adkins, J., Sarnthein, M., Baker, L., Yarusinsky, M., 2000. Abrupt onset and termination of the african humid period: rapid climate responses to gradual insolation forcing. Quat. Sci. Rev. 19, 347–361.
Deocampo, D.M., 2010. The geochemistry of continental carbonates. In: Alonso-Zarza, A.M., Tanner, L.H. (Eds.), Carbonates in Continental Settings: Geochemistry, Diagenesis and Applications. Elsevier, Amsterdam, The Netherland.
DePaolo, D.J., Maher, K., Christensen, J.N., McManus, J., 2006. Sediment transport time measured with u-series isotopes: results from ODP North Atlantic Drift Site 984. Earth Planet. Sci. Lett. 248, 394–410.
Diaz, N., Dietrich, F., Cailleau, G., Sebag, D., Ngounou Ngatcha, B., Verrecchia, E.P., 2016. Can mima-like mounds be Vertisol relics (Far North region of Cameroon, Chad Basin)? Geomorphology 261, 41–56.
Ding, Z.L., Yang, S.L., 2000. C_3/C_4 vegetation evolution over the last 7.0 Myr in the Chinese loess plateau: evidence from pedogenic carbonate $\delta^{13}C$. Palaeogeogr. Palaeoclimatol. Palaeoecol. 160, 291–299.
Dosseto, A., Bourdon, B., Turner, S.P., 2008. Uranium-series ISOTOPES IN RIVER MATERials: insights into the timescales of erosion and sediment transport. Earth Planet. Sci. Lett. 265, 1–17.
Duller, G.A.T., 1992. Luminescence Chronology of Raised Marine Terraces, Southwest North Island, New Zealand, Institute of Earth Studies (Unpublished Ph.D. thesis). University of Wales, Aberystwyh, pp. 1–236.
Duller, G.A.T., 2015. The analyst software package for luminescence data : overview and recent improvements. Anc. TL 33, 35–42.
Duller, G.A.T., 2008. Single-grain optical dating of quaternary sediments: Why aliquot size matters in luminescence dating. Boreas 37, 589–612.
Durand, N., Gunnell, Y., Curmi, P., Ahmad, S.M., 2007. Pedogenic carbonates on precambrian silicate rocks in South India: origin and paleoclimatic significance. Quat. Int. 162–163, 35–49.
Durcan, J.A., King, G.E., Duller, G.A.T., 2015. DRAC: dose rate and age calculator for trapped charge dating. Quat. Geochronol. 28, 54–61.
Dworkin, S.I., Nordt, L., Atchley, S., 2005. Determining terrestrial paleotemperatures using the oxygen isotopic composition of pedogenic carbonate. Earth Planet. Sci. Lett. 237, 56–68.
Eswaran, H., Reich, P.F., Kimble, J., Beinroth, F.H., Padmanabham, E., Moncharoen, P., 2000. Global carbon sinks. In: Lal, R., Kimble, J., Stewart, B.A. (Eds.), Global Climate Change and Pedogenic Carbonates. CRC Press LLC, Boca Raton, Florida, USA.
FAO, 2014. World Reference Base for Soil Resources 2014. International Soil Classification System for Naming Soils and Creating Legends for Soil Maps. World soil resources reports 106, Rome, Italy.
Ferronsky, V.I., Polyakov, V.A., 2012. Isotopes of the Earth's Hydrosphere. Springer, London, UK.
Galbraith, R.F., Roberts, R.G., Laslett, G.M., Yoshida, H., Olley, J.M., 1999. Optical dating of single and multiple grains of quartz from jinmium rock shelter, Northern Australia: part I, experimental design and statistical models. Archaeometry 41, 339–364.
Gocke, M., Pustovoytov, K., Kuzyakov, Y., 2012. Pedogenic carbonate formation: recrystallization versus migration-process rates and periods assessed by ^{14}C Labeling. Glob. Biogeochem. Cycles 26, GB1018.
Guérin, G., Mercier, N., Nathan, R., Adamiec, G., Lefrais, Y., 2012. On the use of the infinite matrix assumption and associated concepts: a critical review. Radiat. Meas. 47, 778–785.
Guérin, G., Mercier, N., Adamiec, G., 2011. Dose-rate conversion factors: update. Anc. TL 29, 5–8.
Guibert, P., Lahaye, C., Bechtel, F., 2009. The Importance of U-series disequilibrium of sediments in luminescence dating: a case study at the Roc de Marsal Cave (Dordogne, France). Radiat. Meas. 44, 223–231.
Hervieu, J., 1970. Influence des changements des climats Quaternaires sur le relief et les sols du Nord-Cameroun. Bull. Ass. Sénég. Quatern. Ouest afr 25, 97–105.
Huntley, D.J., Lamothe, M., 2001. Ubiquity of anomalous fading in K-feldspars and the measurement and correction for it in optical dating. Can. J. Earth Sci. 38, 1093–1106.
Israelson, C., Björck, S., Hawkesworth, C.J., Possnert, G., 1997. Direct U-Th dating of organic- and carbonate-rich lake sediments from Southern Scandinavia. Earth Planet. Sci. Lett. 153, 251–263.
Kreutzer, S., Schmidt, C., Fuchs, M.C., Dietze, M., Fischer, M., Fuchs, M., 2012. Introducing an R Package for luminescence dating analysis. Anc. TL 30, 1–8.
Lal, R., Kimble, J.M., 2000. Pedogenic carbonates and the global carbon cycle. In: Lal, R., Kimble, J.M., Eswaran, H., Stewart, B.A. (Eds.), Global Climate Change and Pedogenic Carbonates. CRC Press LLC, Florida, USA, pp. 1–14.
Lamothe, M., Barré, M., Huot, S., Ouimet, S., 2012. Natural luminescence and anomalous fading in K-feldspar. Radiat. Meas. 47, 682–687.
Lézine, A.-M., Hély, C., Grenier, C., Braconnot, P., Krinner, G., 2011. Sahara and sahel vulnerability to climate changes, lessons from holocene hydrological data. Quat. Sci. Rev. 30, 3001–3012.
Mayya, Y.S., Morthekai, P., Murari, M.K., Singhvi, A.K., 2006. Towards quantifying beta microdosimetric effects in single-grain quartz dose distribution. Radiat. Meas. 41, 1032–1039.
Murray, A.S., Wintle, A.G., 2003. The single aliquot regenerative dose protocol:

potential for improvements in reliability. Radiat. Meas. 37, 377–381.
Neudorf, C.M., Roberts, R.G., Jacobs, Z., 2012. Sources of overdispersion in a K-rich feldspar sample from north-central India: insights from De, K content and IRSL age distributions for individual grains. Radiat. Meas. 47, 696–702.
Nicholson, S.E., 2009. A revised picture of the structure of the "monsoon" and land ITCZ over west Africa. Clim. Dyn. 32, 1155–1171.
Olley, J.M., Murray, A., Roberts, R.G., 1996. The effects of disequilibria in the Uranium and Thorium decay chains on burial dose rates in Fluvial Sediments. Quat. Sci. Rev. 15, 751–760.
Osmond, J.K., Cowart, J.B., Ivanovich, M., 1983. Uranium isotopic disequilibrium in ground water as an indicator of anomalies. Int. J. Appl. Radiat. Isotopes 34 (1), 283–308.
Prescott, J.R., Hutton, J.T., 1994. Cosmic ray contributions to dose rates for luminescence and ESR dating: large depths and long-term time variations. Radiat. Meas. 23, 497–500.
Quade, J., Garzione, C., Eiler, J., 2007. Paleoelevation reconstruction using pedogenic carbonates. Rev. Mineral. Geochem. 66, 53–87.
Quade, J., Cerling, T.E., Bowman, J.R., 1989. Systematic variations in the carbon and oxygen isotopic composition of pedogenic carbonate along elevation transects in the Southern Great Basin, United States. Geol. Soc. Am. Bull. 101, 464–475.
Reimann, T., Thomsen, K.J., Jain, M., Murray, A., Frechen, M., 2012. Single-grain dating of young sediments using the pIRIR signal from feldspar. Quat. Geochronol. 11, 28–41.
Retallack, G.J., 2005. Pedogenic carbonate proxies for amount and seasonality of precipitation in paleosols. Geology 33, 333–336.
Riotte, J., Chabaux, F., 1999. ($^{234}U/^{238}U$) Activity ratios in freshwaters as tracers of hydrological processes: the strengbach watershed (Vosges, France). Geochim. Cosmochim. Acta 63, 1263–1275.
Roberts, H.M., 2012. Testing Post-IR IRSL protocols for minimising fading in feldspars, using Alaskan loess with independent chronological control. Radiat. Meas. 47, 716–724.
Shanahan, T.M., McKay, N.P., Hugen, K.A., Overpeck, J.T., Otto-Bliesner, B., Heil, C.W., King, J., Scholz, C.A., Peck, J., 2015. The time-transgressive termination of the African humid period. Nat. Geosci. 8, 140–144.
Short, S.A., Lowson, R.T., Ems, J., Price, D.M., 1989. Thorium-uranium disequilibrium dating of late quaternary ferruginous concretions and rinds. Geochim. Cosmochim. Acta 53 (6), 1379–1389.
Singhvi, A.K., Banerjee, D., Ramesh, R., Rajaguru, S.N., Gogte, V., 1996. A Luminescence method for dating 'dirty' pedogenic carbonates for paleoenvironmental reconstruction. Earth Planet. Sci. Lett. 139, 321–332.
Smedley, R.K., Duller, G.A.T., Roberts, H.M., 2015. Bleaching of the Post-IR IRSL signal from individual grains of k-feldspar: implications for single-grain dating. Radiat. Meas. 79, 33–42.
Southard, R.J., Driese, S.G., Nordt, L.C., 2011. Vertisols. In: Huang, P.M., Li, Y., Sumner, M.E. (Eds.), Handbook of Soil Sciences Properties and Processes. CRC Press Taylor and Francis Group, USA, pp. 33–82.
Stokes, S., Ingram, S., Aitken, M.J., Sirocko, F., Anderson, R., Leuschner, D., 2003. Alternative chronologies for late quaternary (Last Interglacial–Holocene) deep sea sediments via optical dating of silt-sized quartz. Quat. Sci. Rev. 22, 925–941.
Tanner, L.H., 2010. Continental carbonates as indicators of paleoclimate. In: Alonso-Zarza, A.M., Tanner, L.H. (Eds.), Carbonates in Continental Settings: Geochemistry, Diagenesis and Applications. Elsevier, Oxford, UK, pp. 179–206.
Thiel, C., Buylaert, J.-P., Murray, A., Terhorst, B., Hofer, I., Tsukamoto, S., Frechen, M., 2011. Luminescence dating of the stratzing loess profile (Austria) – testing the potential of an elevated temperature post-IR IRSL protocol. Quat. Int. 234, 23–31.
Thomsen, K.J., Murray, A.S., Jain, M., Bøtter-Jensen, L., 2008. Laboratory fading rates of various luminescence signals from feldspar-rich sediment extracts. Radiat. Meas. 43, 1474–1486.
Trauerstein, M., Lowick, S.E., Preusser, F., Schlunegger, F., 2014. Small aliquot and single grain IRSL and post-IR IRSL dating of fluvial and alluvial sediments from the Pativilca valley, Peru. Quat. Geochronol. 22, 163–174.
Vigier, N., Bourdon, B., Turner, S.P., Allègre, C.J., 2001. Erosion timescales derived from u-decay series measurements in rivers. Earth Planet. Sci. Lett. 193, 549–563.
Violette, A., Riotte, J., Braun, J.-J., Oliva, P., Marechal, J.-C., Sekhar, M., Jeandel, C., Subramanian, S., Prunier, J., Barbiero, L., Dupre, B., 2010. Formation and preservation of pedogenic carbonates in South India, links with Paleo-monsoon and pedological conditions: clues from Sr isotopes, U–Th series and REEs. Geochim. Cosmochim. Acta 74, 7059–7085.
Wallinga, J., Bos, A.J.J., Dorenbos, P., Murray, A.S., Schokker, J., 2007. A test case for anomalous fading correction in IRSL dating. Quat. Geochronol. 2, 216–221.
Wieder, M., Yaalon, D.H., 1974. Effect of matric composition on carbonate nocule crystallisation. Geoderma 11, 95–121.
Wilding, L.P., 2004. Advancement in the knowledge base of vertisols genesis, classification, distribution and management. Rev. Cientìfica Agropecu. 8 (1), 45–54.
Williams, G.E., Polach, H.A., 1971. Radiocarbon dating of arid-zone calcareous paleosols. Geol. Soc. Am. Bull. 82, 3069–3086.
Yang, S., Ding, Z., Gu, Z., 2014. Acetic acid-leachable elements in pedogenic carbonate nodules and links to the East-Asian summer monsoon. Catena 117, 73–80.
Zamanian, K., Pustovoytov, K., Kuzyakov, Y., 2016. Pedogenic carbonates: forms and formation processes. Earth-Science Rev. 157, 1–17.
Zander, A., Hilgers, A., 2013. Potential and limits of OSL, TT-OSL, IRSL and $pIRIR_{290}$ dating methods applied on a middle pleistocene sediment record of Lake El'gygytgyn, Russia. Clim. Past 9, 719–733.
Zimmerman, K.A., 1971. Thermoluminescent dating using fine grains from pottery. Archaeometry 13, 29–52.

References Part

Aassoumi, H., Brouti, J., El Wartiti, M., Freytet, P., Koeniguer, J.-C., Quesada, C., Simancas, F., Toutin-Morin, N., 1992. Pedological nodules with cone in cone structure in the Permian of Sierra Morena (Spain) and Central Morocco. Carbonates and Evaporites 7, 140-149.

Abafoni, J.D., Arabi, A.S., Funtua, I.I., 2014. Luminescence chronology of the Bama Beach Ridge, Chad Basin, north eastern Nigeria. Quaternary International 338, 42-50.

Abdelsalam, M.G., Liégeois, J.-P., Stern, R.J., 2002. The Saharan Metacraton. Journal of African Earth Sciences 34, 119-136.

Achyuthan, H., Flora, O., Braida, M., Shankar, N., Stenni, B., 2010. Radiocarbon Ages of Pedogenic Carbonate Nodules from Coimbatore Region, Tamil Nadu. Journal Geological Society of India 75, 791-798.

Adderley, W.P., Simpson, I.A., Kirscht, H., Adam, M., Spencer, J.Q., Sanderson, D.C.W., 2004. Enhancing ethno-pedology: integrated approaches to Kanuri and Shuwa Arab definitions in the Kala-Balge region, northeast Nigeria. Catena 58, 41-64.

Adegbie, A.T., Schneider, R.R., Röhl, U., Wefer, G., 2003. Glacial millennial-scale fluctuations in central African precipitation recorded in terrigenous sediment supply and freshwater signals offshore Cameroon. Palaeogeography, Palaeoclimatology, Palaeoecology 197, 323-333.

Ahmad, N., 1983. Vertisols. In: L. P. Wilding et al. (Editors), Pedogenesis and Soil Taxonomy. Vol. II, The Soil Orders. Elsevier Science, New York, USA, 91-123.

Aitken, M.J., 1998. An Introduction to Optical Dating: The Dating of Quaternary Sediments by the Use of Photon-stimulated Luminescence. Oxford University Press, Oxford, UK.

Aitken, M.J., Xie, J., 1990. Moisture Correction for Annual Gamma Dose. Ancient TL 8, 6-9.

Aitken, M.J., 1985. Thermoluminescence Dating. Academin Press, Inc., London, UK.

Alley, R.B., Agùstsdòttir, A.M., 2005. The 8k event: cause and consequences of a major Holocene abrupt climate change. Quaternary Science Reviews 24, 1123-1149.

Alley, R.B., Mayewski, P.A., Sowers, T., Stuvier, M., Taylor, K.C., Clark, P.U., 1997. Holocene climatic instability: A prominent, widespread event 8200 yr ago. Geology 25, 483-486.

Alonso-Zarza, A.M., Tanner, L.H., 2010. Carbonates in continental settings - Facies, environments and processes. Elsevier, Amsterdam.

Alonso-Zarza, A.M., 2003. Palaeoenvironmental significance of palustrine carbonates and calcretes in the geological record. Earth-Science Reviews 60.

Alonso-Zarza, A.M., Esther Sanz, M., Calvo, J.P., Estévez, P., 1998. Calcified root cells in Miocene pedogenic carbonates of the Madrid Basin: evidence for the origin of Microcodium b. Sedimentary Geology 16, 81-97.

Andersen, M.B., Erel, Y., Bourdon, B., 2009. Experimental Evidence for $^{234}U-^{238}U$ Fractionation during Granite Weathering with Implications for $^{234}U/^{238}U$ in Natural Waters. Geochimica et Cosmochimica Acta 73, 4124-4141.

Aoudjit, H., Robert, M., Elsass, F., Curmi, P., 1995. Detailed study of smectite genesis in granitic saprolites

by analytical electron microscopy. Clay Minerals 30, 135-147.

Applin, D.M., Izawa, M.R.M., Cloutis, E.A., 2016. Reflectence spectroscopy of oxalate minerals and relevance to Solar System carbon inventories. Icarus 278, 7-30.

Aravena, R., Schiff, S., Trumbore, S.E., Dillon, P., Elgood, R., 1992. Evaluating dissolved inorganic carbon cycling in a forested lake watershed using carbon isotopes. Radiocarbon, 34, 636-645.

Armitage, S.J., 2015. Optically Stimulated Luminescence Dating of Ocean Drilling Program Core 658B: Compiliations arising from Authigenic Uranium Uptake and Lateral Sediment Movment. Quaternary Geochronology 30, 270-274.

Armitage, S.J., Bristow, C.S., Drake, N.A., 2015. West African Monsoon Dynamics Inferred from Abrubt Fluctuations of Lake Mega-Chad. PNAS 112, 8543-8548.

Arora, V.K., 2002. The use of the aridity index to assess climate change effect on annual runoff. Journal of Hydrology 265, 164-177.

Ashley, G.M., Deocampo, D.M., Kahmann-Robinson, J., Driese, S.G., 2013. Groundwater-fed wetland sediments and paleosols: It's all about water table, in: Driese, S.G., Nordt, L., McCarthy, P.J. (Eds.), New frontiers in paleopedology and terrestrial paleoclimatology. Paleosols and soil surface analog systems. SEPM (Society for sedimentary geology), Oklahoma, USA, pp. 47-61.

Auclair, M., Lamothe, M., Huot, S., 2003. Measurement of Anomalous Fading for Feldspar IRSL using SAR. Radiation Measurements 37, 487-492.

Balesdent, J., Mariotti, A., Guillet, B., 1987. Natural ^{13}C abundance as a tracer for studies of soil organic matter dynamics. Soil Biology and Biochemistry 19, 25-30.

Balescu, S., Lamothe, M., 1993. Thermoluminescence dating of the Holsteinian marine formation of Herzeele, northern France. Journal of Quaternary Science 8, 117-124.

Baran, E.J., 2014. Review: Natural oxalates and their analogous synthetic complexes. Journal of Coordination Chemistry 67, 3734-3768.

Barshad, I., 1966. Factors affecting the frequency distribution of clay minerals in soils, Clays & Clay Minerals Conference Proc.

Bateman, M.D., Frederick, C.D., Jaiswal, M.K., Singhvi, A.K., 2003. Investigations into the Potential Effects of Pedoturbation on Luminescence Dating. Quaternary Science Reviews 22, 1169-1178.

Bell, W.T., 1980. Alpha Attenuation in Quartz Grains for Thermoluminescence Dating. Ancient TL 12, 4-8.

Beltrando, G., 2004. Les climats. A. Colin, Paris.

Bennett, J.G., 1980. Aeolian deposition and soil parent materials in northern Nigeria. Catena 24, 241-255.

Berner, R.A., Lasaga, A.C., Garrels, R.M., 1983. The carbonate-silicate geochemical cycle and its effect on atmospheric carbon dioxide over the past 100 million years. American Journal of Science 283, 641-683.

Bertrand, J.-M., Caby, R., Leblanc, M.J., 1983. La zone mobile Pan-Africaine de l'Afrique de l'Ouest, in: Fabre, J. (Ed.), Afrique de l'Ouest: Introduction géologique et termes stratigraphiques. Pergamon Press, Oxford, pp. 35-42.

Blott, S.J., Pye, K., 2001. GRADISTAT: A Grain-size distribution and Statistics Package for the Analysis of Unconsolidated Sediments. Earth Surface Processes and Landforms 26, 1237-1248.

Bocquier, G., 1973. Genèse et Evolution de Deux Toposéquences de Sols Tropicaux du Tchad. Interprétation Biogéodynamique. Mémoires de l'ORSTOM, Paris, France, pp 327.

Bouchette, F., Schuster, M., Ghienne, J.-F., Denamiel, C., Roquin, C., Moussa, A., Marsaleix, P., Duringer, P., 2010. Hydrodynamics in Holocene Lake Mega-Chad. Quaternary Research 73 (2), 226-236.

Brabant, P., Gavaud, M., 1985. Les sols et les ressources en terres du Nord-Cameroun, ORSTOM ed. ORSTOM, Paris.

Brasier, A.T., 2011. Searching for Travertines, Calcretes and Speleothems in Deep Time: Processes, Apparances, Predictions and the Impact of Plants. Earth-Science Reviews 104, 213-239.

Broecker, W.S., Peng, T.-H., 1982. Tracers in the sea. Lamont-Doherty Geological Observatory, New York.

Bristow, C.S. and Armitage, S.J., 2016. Dune ages in the sand deserts of the southern Sahara and Sahel. Quaternary International 410, 46-57.

Brook, B.W., Ellis, E.C., Perring, M.P., Mackay, A.W., Blomqvist, L., 2013. Does the terrestrial biosphere have planetary tipping points? Trends in ecology & evolution 28, 396-401.

Brown, S.L., Warwick, N.W., Prychid, C.J., 2013. Does aridity influence the morphology, distribution and accumulation of calcium oxalate crystals in Acacia (Leguminosae: Mimosoideae)? Plant physiology and biochemistry 73, 219-228.

Bruijnzeel, L.A., 1991. Nutrient input-output budgets of tropical forest ecosystems: a review. Journal of Tropical Ecology 7, 1-24.

Budd, D.A., Pack, S.M., Fogel, M.L., 2002. The destruction of paleoclimatic isotopic signals in Pleistocene carbonate soil nodules of Western Austratlia. Palaeogeography, Palaeoclimatology, Palaeoecology 188, 249-273.

Bullard, J., Livingstone, I., 2002. Interactions between Aeolian and Fluvial Systems in Dryland Environments. Area 34, 8-16.

Bullock, P., Fedoroff, N., Jongerius, A., Stoops, G., Tursina, T., Babel, U., 1985. Handbook for soil thin section description. Waine Researcher Publications, Wolvergampton, UK.

Butler, D.R., (1995). Zoogeomorphology: Animals as Geomorphic Agents. Cambridge University Press, Cambridge, UK.

Buylaert, J.-P., Jain, M., Murray, A.S., Thomsen, K.J., Thiel, C., Sohbati, R., 2012. A Robust Feldspar Luminescence Dating Method for Middle and Late Pleistocene Sediments. Boreas 41, 435-451.

Buylaert, J.-P., Murray, A.S., Thomsen, K.J., Jain, M., 2009. Testing the Potential of an Elevated Temperature IRSL Signal from K-feldspar. Radiation Measurements 44, 560-565.

Cailleau, G., Sebag, D., Bindschedler, S., Pons, S., 2012. Fieldwork and sampling in Cameroon. Unpublished work.

Cailleau, G., Braissant, O., Dupraz, C., Aragno, M., Verrecchia, E.P., 2005. Biologically induced accumulations of $CaCO_3$ in orthox soils of Biga, Ivory Coast. Catena 59, 1-17.

Cairns, J., 2004. Ecological tipping points : a major challenge for experimental sciences. Asian Journal of Experimental Sciences 18, 1-16.

Campy, M., Macaire, J.-J., 2003. Géologie de la surface. Erosion, transfert et stockage dans les environnements continentaux. Dunod, Paris, France.

Cerling, T.E., 2014. Stable Isotope Evidence for Hominin Environments in Africa, in: Holland, H., Turekian, K. (Eds.), Treatise on Geochemistry. Elsevier, Amsterdam, Netherland, 157-167.

Cerling, T.E., Wang, Y., 1996. Stable carbon and oxygen isotopes in soil CO_2 and soil carbonate: theory, practice, and application to some prairie soils of upper midwestern North America. In: Boutton, T.W., Yamasaki, S. (Eds.), Mass Spectrometry of Soils. Marcel Dekker, Inc., New York, 113-132.

Cerling, T.E., Quade, J., 1993. Stable Carbon and Oxygen isotopes in soil carbonates, in: Swart, P.K., Lohmann, K.C., Mckenzie, J., Savin, S. (Eds.), Climate change in continental isotopic records. American Geophysical Union, USA, 217-231.

Cerling, T.E., Solomon, D.K., Quade, J., Bowman, J.R., 1991. On the isotopic composition of carbon in soil carbon dioxide. Geochimica et Cosmochimica Acta 55, 3403-3405.

Cerling, T.E., Quade, J., Wang, Y., Bowman, J., 1989. Carbon isotopes in soils and palaeosols as ecology and palaeoecology indicators. Nature 341, 138-139.

Cerling, T.E., 1984. The stable isotopic composition of modern soil carbonate and its relationship to climate. Earth and Planetary Science Letters 71, 229-240.

Chabaux, F., Bourdon, B., Riotte, J., 2008. U-Series Geochemistry in Weathering Profiles, River Waters and Lakes. In U-Th Series Nuclides in Aquatic Systems edited by S. Krishnaswami and J. Kirk Cochran. Radioactivity in the Environment 13.

Chabaux, F., Riotte, J., Dequincey, O., 2003. U-Th-Ra Fractionation During Weathering and River Transport. Reviews in Mineralogy and Geochemistry 52, 533-576.

Chafetz, H.S., Buczynski, C., 1992. Bacterially induced lithification of microbial mats. Palaios 7, 277-293.

Chase, B.M., Meadows, M.E., Carr, A.S., Reimer, P.J., 2010. Evidence for progressive Holocene aridification in southern Africa recorded in Namibian hyrax middens: Implications for African Monsoon dynamics and the African Humid Period. Quaternary Research 74, 36-45.

Chase, B.M., 2009. Evaluating the use of dune sediments as a proxy for palaeo-aridity: A southern African case study. Earth-Science Reviews 93, 31-45.

Chkir, N., Guendouz, A., Zouari, K., Hadj Ammar, F., Moulla, A.S., 2009. Uranium Isotopes in Groundwater from the Continental Intercalaire Aquifer in Algerian Tunisian Sahara (Northern Africa). Journal Environment Radioactivity 100, 649-656.

Clark, P. J. and Evans, F. C., 1954. Distance to Nearest Neighbor as a Measure of Spatial Relationships in

Populations. Ecology, 35(4), 445-453.

Clark, P.U., Dyke, A.S., Shakun, J.D., Carlson, A.E., Clark, J., Wohlfarth, B., Mitrovica, J.X., Hostetler, S.W., McCabe, M.A., 2009. The Last Glacial Maximum. Science 325, 710-714.

Clark, I.D., Fritz, P., 1997. Environmental Isotopes in Hydrology. CRC Press LLC, United States of America.

Collins, J.A., Govin, A., Mulitza, S., Heslop, D., Zabel, M., Hartmann, J., Röhl, U., Wefer, G., 2013. Abrupt shifts of the Sahara-Sahel boundary during Heinrich stadials. Climate of the Past 9, 1181-1191.

Coulombe, C.E., Dixon, J.B., Wilding, L.P., 1996a. Mineralogy and chemistry of Vertisols, in: Ahmad, N., Mermut, A.R. (Eds.), Vertisols and Technologies for their Management. Elservier Science, Amsterdam, The Netherlands, pp. 115-188.

Coulombe, C. E., Wilding, L. P., Dixon, J. B., 1996b. Overview of Vertisols : Characteristics and Impacts on Society. Adv. Agron., 57, 289-357.

Cox, G.W., 1984. The distribution and origin of mima mounds grasslands in San Diego County, California. Ecology 65, 1397-1405.

Cramer, M.D., Barger, N.N., 2014. Are mima-like mounds the consequence of long-term stability of vegetation spatial patterning? Palaeogeography, Palaeoclimatology, Palaeoecology 409, 72-83, http://dx.doi.org/10.1016/j.palaeo.2014.04.026.

Cramer, M.D., Midgley, J.J., 2015. The distribution and spatial patterning of mima-like mounds in South Africa suggests genesis through vegetation induced aeolian sediment deposition. J. Arid Env. 119, 16-26.

Cramer, M.D., Innes, S.N., Midgley, J.J., 2012. Hard Evidence that Heuweltjie Earth Mounds are Relictual Features Produced by Differential Erosion. Palaeogeography, Palaeoclimatology, Palaeoecology 350-352, 189-197.

Cratchley, C., Louis, P., Ajakaiye, D., 1984. Geophysical and geological evidence for the Benue-Chad Basin Cretaceous rift valley system and its tectonic implications. Journal of African Earth Sciences (1983) 2, 141-150.

Crouvi, O., Amit, R., Enzel, Y., Gillespie, A.R., 2010. Active sand seas and the formation of desert lœss. Quaternary Science Reviews 29 (17-18), 2087-2098, doi:10.1016/j.quascirev.2010.04.026.

Dalrymple, J. B. and Jim, C. Y., 1984. Experimental Study of Soil Microfabrics Induced by Isotropic Stresses of Wetting and Drying. Geoderma 34, 43-68.

Dansgaard, E., 1964. Stable isotopes in precipitation. Tellus 16, 436-468.

Davis, W. M., 1902. Basel-level, Grade and Peneplain. Journal of Geology 10, 77-111.

Delneuf, M., 1998. Les recherches archéologiques menées par l'ORSTOM au Cameroun septentorial, in: Delneuf, M., Essomba, J.-M., Froment, A. (Eds.), Paléo-anthropoligie en Afrique Centrale. L'Harmattan, Paris, France, 91-124.

deMenocal, P.B. and Tierney, E.J., 2012. Green Sahara: African Humid Periods Paced by Earth's Orbital Changes. Nature Education 3 (10), 12 pp.

deMenocal, P.B., Ortiz, J., Guilderson, T., Adkins, J., Sarnthein, M., Baker, L., Yarusinsky, M., 2000. Abrupt Onset and Termination of the African Humid Period: Rapid Climate Responses to Gradual Insolation Forcing. Quaternary Science Reviews 19, 347-361.

Deocampo, D.M., 2010. The Geochemistry of Continental Carbonates, in: Alonso-Zarza, A.M., Tanner, L.H. (Eds.), Carbonates in Continental Settings: Geochemistry, Diagenesis and Applications. Elsevier, Amsterdam, The Netherland.

DePaolo, D.J., Maher, K., Christensen, J.N., McManus, J., 2006. Sediment Transport Time Measured with U-series Isotopes: Results from ODP North Atlantic Drift Site 984. Earth and Planetary Science Letters 248, 394-410.

Deutz, P., P., M.I., Monger, H.C., Morrison, J., 2001. Morphology and isotope heterogeneity of Late Quaternary pedogenic carbonates: Implications for paleosol carbonates as paleoenvironmental proxies. Palaeogeography, Palaeoclimatology, Palaeoecology 166, 293-317.

Dewolf, Y., Bourrié, G., 2008. Les formations superficielles. Genèse - typologie - classification - paysages & environnements - ressources & risques. Ellipses Edition Marketing, Paris, France.

Dhonneur, G., 1974. Nouvelle Approche des Réalités Météorologiques de l'Afrique Occidentale et Centrale. Thèse Doctorale Ing., Université de Dakar, ASECNA, Dakar.

Diaz, N., Dietrich, F., Cailleau, G., Sebag, D., Ngounou Ngatcha, B., Verrecchia, E.P., 2016a. Can mima-like mounds be Vertisol relics (Far North Region of Cameroon, Chad Basin)? Geomorphology 261, 41-56.

Diaz, N., King, G.E., Valla, P.G., Herman, F., Verrecchia, E., 2016b. Pedogenic carbonate nodules as soils time archives: Challenges and investigations related to OSL dating. Quaternary Geochronology 36, 120-133.

Diaz, N., Dietrich, F., Sebag, D., King, G.E., Valla, P.G., Durand, A., Deschamps, P., Herman, F., Verrecchia, E.P., in prep. Quaternary palaeoenvironmental reconstruction of the southwestern Chad Basin: the invaluable legacy of soil relics. Quaternary Science Reviews.

Dietrich, F., Diaz, N., Deschamps, P., Ngatcha, B.N., Sebag, D., Verrecchia, E.P., 2017. Origin of calcium in pedogenic carbonate nodules from silicate watersheds in the Far North Region of Cameroon: Respective contribution of in situ weathering source and dust input. Chemical Geology 460, 54-69.

Dietrich, F., Diaz, N., Deschamps, P., Sebag, D., verrecchia, E.P., *in prep.* Calcium transfer over the last 20 Ky: from granitic sources to carbonate nodule sinks (Far North Cameroon). Palaeogeography, Palaeoclimatology, Palaeoecology.

Ding, Z.L., Yang, S.L., 2000. C3/C4 Vegetation Evolution over the last 7.0 Myr in the Chinese Loess Plateau: Evidence from Pedogenic Carbonate $\delta^{13}C$. Palaeogeography, Palaeoclimatology, Palaeoecology 160, 291-299.

Dosseto, A., Bourdon, B., Turner, S.P., 2008. Uranium-series Isotopes in River Materials: Insights into the Timescales of Erosion and Sediment Transport. Earth and Planetary Science Letters 265, 1-17.

Drever, J.I., 1973. The preparation of oriented clay mineral specimens for X-ray diffraction analysis by a filter-membrane peel technique. American Mineralogist 58, 553-554.

Driese, S.G., Mora, C.I., 1993. Physico-chemical environment of pedogenic carbonate formation in Devonian vertic palaeosols, central Appalachians, USA. Sedimentology 40, 199-216.

Duchaufour, P., 1990. La formation et l'évolution des complexes organo-minéraux dans les sols et leur rôle dans la pédogenèse. Science du sol 28, 273-284.

Ducloux, J., Butel, P., 1983. Micromorphology of calcretes in a slope deposit in the Poitevine Plain, France, in: Bullock, P., Murphy, C.P. (Eds.), Soil Micromorphology. Kluwer, Dordrecht.

Dudal, R. and Eswaran, H., 1988. Distribution, Properties and Classification of Vertisols. In : L. P. Wilding and R. Puentes (Editors), Vertisols : Their Distribution, Properties, Classification and Management. SMSS-Texas AandM University, 1-22.

Duller, G.A.T., 2016. Challenges involved in obtaining luminescence ages for long records of aridity: Examples from the Arabian Peninsula. Quaternary International 410, 1-6.

Duller, G.A.T., 2015. The Analyst Software Package for Luminescence Data : Overview and Recent Improvements. Ancient TL, 33, 35-42.

Duller, G.A.T., 2008. Single-Grain Optical Dating of Quaternary Sediments: Why Aliquot Size Matters in Luminescence Dating. Boreas 37, 589-612.

Duller, G.A.T., 1992. Luminescence Chronology of raised Marine Terraces, south-west north Island, New Zealand, Institute of Earth Studies. University of Wales, Aberystwyh, pp. 1-236.

Dupont, L.M., Jahns, S., Marret, F., Ning, S., 2000. Vegetation change in equatorial West Africa: time-slices for the last 150 ka. Palaeogeography, Palaeoclimatology, Palaeoecology 155, 95-122.

Durand, A., Garba, Z., Le Coz, M., Ngounou Ngatcha, B., Sebag, D., 2011. Qu'en est-il du réseau hydrographique attribué à un mégalac Tchad holocène: le fleuve Tafassasset a t-il existé? L'Angamma est-il un paléodelta? Quand le Logone est-il devenu un affluent du Tchad, in: Ngounou Ngatcha, B., Sebag, D., Diedhiou, A., Durand, A., Servat, E. (Eds.), Colloque international : sciences de l'eau, du climat et de l'environnement pour un dvveloppement durable de l'Afrique, Ngaoundéré, Cameroon.

Durand, A., 1999. Fieldwork and sampling in Mali. Unpublished work.

Durand, A., 1995. Quaternary Sediments and Climates in the Central Sahel. Africa Geoscience Review 2, 323-614.

Durand, A., Lang, J., 1986. Approche critique des méthodes de reconstitution paléoclimatique: le Sahel nigéro-tchadien depuis 40 000 ans. Bull. Soc. géol. France 8, 267-278.

Durand, A., 1982. Oscillations of Lake Chad over the Past 50,000 years: New Data and New Hypothesis. Palaeogeography, Palaeoclimatology, Palaeoecology 39, 37-53.

Durand, A., Mathieu, P., 1980. Evolution paléogéographique et paléoclimatique du bassin tchadien au Pléistocène supérieur. Revue de Géologie Dynamique et de Géographie Physique 22, 329-341.

Durand, N., Gunnell, Y., Curmi, P., Ahmad, S.M., 2007. Pedogenic Carbonates on Precambrian Silicate Rocks in South India: Origin and Paleoclimatic Significance. Quaternary International 162-163, 35-49.

Durcan, J.A., King, G.E., Duller, G.A.T., 2015. DRAC: Dose Rate and Age Calculator for Trapped Charge Dating. Quaternary Geochronology 28, 54-61.

Dworkin, S.I., Nordt, L., Atchley, S., 2005. Determining Terrestrial Paleotemperatures using the Oxygen Isotopic Composition of Pedogenic Carbonate. Earth and Planetary Science Letters 237, 56-68.

Erhart, M. H., 1954. Bassin du Moyen Logone. In: Commission Scientifique du Logone et du Tchad, Etude Pédologique du Bassin Alluvionnaire du Logone-Chari. ORSTOM, Paris, France, 17-107.

Erhart, M. H., 1967. La Genèse des Sols en Tant que Phénomène Géologique. Esquisse d'une Théorie Géologique et Géochimique. Biostasie et Rhexistasie. Masson et Cie, Seconde Edition, Paris VI, France.

Eswaran, H., Reich, P.F., Kimble, J., Beinroth, F.H., Padmanabham, E., Moncharoen, P., 2000. Global carbon sinks, in: Lal, R., Kimble, J., Stewart, B.A. (Eds.), Global Climate Change and Pedogenic Carbonates. CRC Press LLC, Boca Raton, Florida, USA.

Eswaran, H., and Wong, C. B., 1978. A Study of a Deep Weathering Profile on Granite in Peninsular Malaysia : I. Physico-Chemical and Micromorphological Properties. Soil Science Society of America Journal 42, 144-148.

Eswaran, H., Kimble J., and Cook, T., 1988. Properties, Genesis and Classification of Vertisols. Workshop Swell-shrink soils, October 24-28, National Bureau of Soil Survey and Land Use Plannign, Nagpur India, Oxford and IBH Publ. Co, New Delhi, India.

FAO, (2014). World Reference Base for Soil Resources 2014. International Soil Classification System for naming Soils and creating Legends for soil maps. World soil resources reports 106, Rome, Italy.

FAO, (2006). Guidelines for Soil Description. Food and Agriculture Organization of the United Nations (FAO), Rome, Italy.

FAO/GIEWS, (2004, on http://www.fao.org/docrep/006/J2517e/J2517e00.htm#carte). Sahel weather and crop situation report. The rainy season has started against a backdrop of worrying desert locust situation. Sahel Report, 1.

Fantong, W.Y., Satake, H., Ayonghe, S.N., Alka, F.T., Asai, K., 2009. Hydrogeochemical controls and usability of groundwater in the semi-arid Mayo Tsanaga River Basin: far north province, Cameroon. Environmental Geology 58, 1281-1293.

Farmer, D., Sivapalan, M., Jothityangkoon, C., 2003. Climate, soil and vegetation controls upon the variability of water balance in temperate and semiarid landscapes: Downward approach to water balance analysis. Water resources research 39, 1-21.

Feng, X., Faiia, A.M., Posmentier, E.S., 2009. Seasonality of isotopes in precipitation: A global perspective. Journal of Geophysical Research 114, 1-13.

Ferronsky, V.I., Polyakov, V.A., 2012. Isotopes of the Earth's Hydrosphere. Springer, London, UK.

Fitton, J., Dunlop, H., 1985. The Cameroon line, West Africa, and its bearing on the origin of oceanic and continental alkali basalt. Earth and Planetary Science Letters 72, 23-38.

Fitton, J., 1980. The Benue trough and Cameroon line - a migrating rift system in West Africa. Earth and Planetary Science Letters 51, 132-138.

Flemming, H.-C., Wingender, J., 2010. The biofilm matrix. Nature Reviews Microbiology 8, 623-633.

Flügel, E., 2004. Microfacies of carbonate rocks: Analysis, Interpretation and Application. Springer,

Berlin, Germany.

Fotius, G., 2000. Phytogéographie, in: Seignobos, C., Iyébi-Mandjek, O. (Eds.), Atlas de la Province Extrême-Nord Cameroun. Editions de l'IRD, République du Cameroun MINREST, Paris, France.

Francis, M.L., Ellis, F., Lambrechts, J.J.N., Poch, R.M., 2013. A Micromorphological View through a Namaqualand Termitaria (Heuweltjie, a Mima-like mound). Catena 100, 57-73.

Franceschi, V.R., Nakata, P.A., 2005. Calcium oxalate in Plants: Formation and Function. Annual Review of Plant Biology 56, 41-71.

Frey-Wyssling, A., 1981. Crystallography of the two hydrates of crystalline calcium oxalate in plants. American Journal of Botany 68, 130-141.

Freytet, P., Plaziat, J.-C., 1982. Continental carbonate sedimentation and pedogenesis-Late Cretaceous and Early Tertiary of southern France.

Freytet, P., Verrecchia, E.P., 2002. Lacustrine and palustrine carbonate petrography: an overview. Journal of Paleolimnology 27, 221-237.

Freytet, P., Verrecchia, E., 1989. Les carbonates continentaux du pourtour méditerranéen : microfaciès et milieux de formation. Méditerranée 68, 5-28.

Funch, R.R., 2015. Termite mounds as dominant land forms in semiarid northeastern Brazil. J. Arid Envi. 122, 27-29.

Gadd, G.M., Bahri-Esfahani, J., Li, Q., Rhee, Y.J., Wei, Z., Fomina, M., Liang, X., 2014. Oxalate production by fungi: significance in geomycology, biodeterioration and bioremediation. Fungal Biology Reviews 28, 36-55.

Galbraith, R.F., Roberts, R.G., Laslett, G.M., Yoshida, H., Olley, J.M., 1999. Optical Dating of Single and Multiple Grains of Quartz from Jinmium Rock Shelter, Northern Australia: Part I, Experimental Design and Statistical Models. Archaeometry 41, 339-364.

Gasparatos, D., Tarenidis, D., Haidouti, C., Oikonomou, G., 2005. Microscopic structure of soil Fe-Mn nodules: environmental implication. Environmental Chemistry Letters 2, 175-178.

Garcin, Y., Ménot, G., Deschamps, P., Schefuss, E., Sachse, D., de Saulieu, G., Sebag, D., Oslisly, R., Dupont, L., Brademann, B., Tjallingii, R., Brauer, A., in prep. Hydroclimate and vegetation changes in Central Africa during the Holocene: new views from the Lake Barombi Mbo (Cameroon), in: 2017, PAGES Open Science Meeting, Palaeoenvironments of Africa: Pliocene to Present session, Zaragoza, Spain.

Gasse, F., 2000. Hydrological Changes in the African Tropics Since the Last Glacial Maximum. Quaternary Science Reviews 19, 189-211.

Genik, G., 1992. Regional framework, structural and petroleum aspects of rift basins in Niger, Chad and the Central African Republic (CAR). Tectonophysics 213, 169-185.

Geyssant, J., 2001. Geology of calcium carbonate, in: Tegethoff, W. (Ed.), Calcium carbonate: From the cretaceous period into the 21^{st} century. Birkhauser, Basel, Boston, Berlin.

Ghienne, J.-F., Schuster, M., Bernard, A., Duringer, P., Brunet, M., 2002. The Holocene Giant Lake Chad

Revealed by Digital Elevation Models. Quaternary International 87, 81-85.

Giesler, R., Ilvesniemi, H., Nyberg, L., Van Hees, P., Starr, M., Bishop, K., Kareinen, T., Lundström, U.S., 2000. Distribution and mobilization of Al, Fe and Si in three podzolic soil profiles in relation to the humus layer. Geoderma 94, 249-263.

Group, G.S.D.T., 2002. Global Gridded Surfaces of Selected Soil Characteristics (IGBP-DIS). , in: System, I.G.-B.P.-D.a.I. (Ed.). Oak Ridge National Laboratory Distributed Active Archive Centre, Oak Ridge, Tennessee, USA.

Gocke, M., Pustovoytov, K., Kuzyakov, Y., 2012. Pedogenic Carbonate Formation: Recrystallization versus Migration-Process Rates and Periods assessed by ^{14}C Labeling. Global Biogeochemical Cycles, 26, GB1018.

Goudie, A.S., 2013. Arid and semi-arid geomorphology. Cambridge University Press, New York, USA.

Guérin, G., Mercier, N., Nathan, R., Adamiec, G., Lefrais, Y., 2012. On the use of the infinite matrix assumption and associated concepts: A critical review. Radiation Measurements 47, 778-785.

Guérin, G., Mercier, N., Adamiec, G., 2011. Dose-Rate Conversion Factors: update. Ancient TL 29, 5-8.

Guibert, P., Lahaye, C., Bechtel, F., 2009. The Importance of U-series Disequilibrium of Sediments in Luminescence Dating: A Case Study at the Roc de Marsal Cave (Dordogne, France). Radiation Measurements 44, 223-231.

Gumnior, M., Preusser, F., 2007. Late Quaternary river development in the southwest Chad Basin: OSL dating of sediment from the Komadugu palaeofloodplain (northeast Nigeria). Journal of Quaternary Science 22, 709-719.

Hajdas, I., 2008. Radiocarbon dating and its applications in Quaternary studies. Quaternary Science Journal 57, 2-24.

Hajdas, I., Bonani, G., Furrer, H., Mäder, A., Schoch, W., 2007. Radiocarbon chronology of the mammoth site at Niederweningen Switzerland: Results from dating bones, teeth, wood, and peat. Quaternary International 164-165, 98-105.

Hallsworth, E. G., Robertson, G. K., Gibbson, F. R., 1955. Studies in Pedogenesis in New South Wales. VII. The Gilgai Soils. Journal of Soil Science 6, 1-31.

Hasinger, O., Spangenberg, J.E., Millière, L., Bindschedler, S., Cailleau, G., Verrecchia, E.P., 2015. Carbon dioxide in scree slope deposits: A pathway from atmosphere to pedogenic carbonate. Geoderma 247-248, 129-139.

Hély, C., Braconnot, P., Watrin, J., Zheng, W., 2009. Climate and Vegetation: Simulating the African Humid Period. Comptes Rendus Geoscience 341 (8-9), 671-688.

Hervieu, J., 1970. Influence des Changements des Climats Quaternaires sur le Relief et les Sols du Nord-Cameroun. Bull. Ass. sénég. et Quatern. Ouest afr. 25, 97-105.

Hervieu, J., 1969. Le Quaternaire du Nord-Cameroun Schéma d'Evolution Géomorphologique et Relations avec la Pédogenèse. Documents de l'ORSTOM, Paris, France, 38 pp.

Holmes, J.A., Street-Perrott, F.A., Perrott, R.A., Stokes, S., Waller, M.P., Huang, Y., Eglinton, G., Ivanovich,

M., 1999. Holocene landscape evolution of the Manga Grasslands, NE Nigeria: evidence from palaeolimnology and dune chronology. Journal of Geological Society, London 156, 357-368.

Hsieh, J.C.C., Chadwick, O.A., Kelly, E.F., Savin, S., 1998. Oxygen isotopic composition of soil water: Quantifying evaporation and transpiration. Geoderma 82, 269-293.

Hubble, G. D., 1984. The cracking clay soils : definition, distribution, nature, genesis and use. In: J. W. McGarity, E. H. Hoult and H. B. So (Editors), The properties and utilization of cracking clay soils, Review in Rural Science University of New England, Armidale, Australia, 5, 3-13.

Huntley, D.J., Lamothe, M., 2001. Ubiquity of Anomalous Fading in K-feldspars and the Measurement and Correction for it in Optical Dating. Canadian Journal of Earth Sciences 38, 1093-1106.

Israelson, C., Björck, S., Hawkesworth, C.J., Possnert, G., 1997. Direct U-Th Dating of Organic- and Carbonate-rich Lake Sediments from Southern Scandinavia. Earth and Planetary Science Letters 153, 251-263.

IUSS Working Group, 2014. World reference base for soil resource 2014. International soil classification system for naming soils and creating legends for soil maps. FAO, Rome.

IUSS Working Group, 2006. Guidelines for Soil Description. FAO, Rome, Italy. Jim, C. Y. (1990). Stress, shear deformation and micromorphological clay orientation: A synthesis of various concepts. Catena 17, 431-447.

Jaillard, B., Guyon, A., Maurin, A., 1991. Structure and composition of calcified roots, and their identification in calcareous soils. Geoderma 50, 197-210.

Jenny, H., 1941. Factors of soil formation: A system of Quantitative pedology. Dover Publications, INC., New York.

Johnson, D.L., Domier, J.E.J., Johnson, D.N., 2005. Reflections on the nature of soil and its biomantle. Annals of the Association of American Geographers 95, 11-31.

Kazmierczak, J., Fenchel, T., Kühl, M., Kempe, S., B., K., Bozena, L., Krzysztof, M., 2015. CaCO3 precipitation in multilayererd cyanobacterial mats: clues to explain the alternation of micrite and sparite layers in calcareous stromatolites. Life 5, 744-769.

Ketchemen, B., Naah, E., Faye, A., Aranyossy, J.-F., 1993. Application des isotopes de l'environnement à l'étude des aquifères du Grand Yayré (Extrême Nord du Cameroun), in: AIEA (Ed.), Les ressources en eau au Sahel: études hydrogéologiques et hydrologiques en Afrique de l'Ouest par les techniques isotopiques. AIEA, Autriche, pp. 107-122.

Klappa, C.F., 1980. Rhizoliths in terrestrial carbonates: classification, recognition, genesis and significance. Sedimentology 27, 613-629.

Kocurek, G., 1998. Aeolian System Response to External Forcing Factors. In: Alsharhan, A., Glennie, K., Whittle, G., Kendall, C. (Editors), Quaternary Deserts and Climatic Change. Balkema, Rotterdam, The Netherlands, pp. 327-337.

Kolka, R.K., Grigal, D.F., Nater, E.A., 1996. Forest soil mineral weathering rates: use of multiple approaches. Geoderma 73, 1-21.

Kocir, A., 2004. Microcodium revisited: root calcification products of terrestrial plants on carbonate-rich

substrates. Journal of Sedimentary Research 74, 845-857.

Kovda, I., Mora, C.I., Wilding, L.P., 2006. Stable Isotope Compositions of Pedogenic Carbonates and Soil Organic Matter in a Temperate Climate Vertisol with Gilgai, Southern Russia. Geoderma 136 (1-2), 423-435, doi:10.1016/j.geoderma.2006.04.016

Kovda, I.V., Wilding, L.P., Drees, L.R., 2003. Micromorphology, Submicroscopy and Microprobe Study of Carbonate Pedofeatures in a Vertisol Gilgai Soil Complex, South Russia. Catena 54 (3), 457-476, doi:10.1016/S0341-8162(03)00121-8.

Kreutzer, S., Schmidt, C., Fuchs, M.C., Dietze, M., Fischer, M., Fuchs, M., 2012. Introducing an R Package for Luminescence Dating Analysis. Ancient TL 30, 1-8.

Kröpelin, S., Verschuren, D., Lézine, A.-M., Eggermont, H., Cocquyt, C., Francus, P., Cazet, J.-P., Fagot, M., Rumes, B., Russell, J.M., Darius, F., Conley, D.J., Schuster, M., Von Suchodoletz, H., Engstrom, D.R., 2008. Climate-Driven Ecosystem Succession in the Sahara: The Past 6000 Years. Science 320, 765-768.

Krumbein, W.C., Garrels, R.M., 1952. Origin and classification of chemical sediments in terms of pH and Oxidation-Reduction potentials. The Journal of Geology 60, 1-33.

Lal, R., Kimble, J.M., 2000. Pedogenic Carbonates and the Global Carbon Cycle, in: Lal, R., Kimble, J.M., Eswaran, H., Stewart, B.A. (Eds.), Global Climate Change and Pedogenic Carbonates. CRC Press LLC, Florida, USA, pp. 1-14.

Lamothe, M., Barré, M., Huot, S., Ouimet, S., 2012. Natural Luminescence and Anomalous Fading in K-feldspar. Radiation Measurements 47, 682-687.

LeGrande, A.N., Schmidt, G.A., 2009. Sources of Holocene variability of oxygen isotopes in paleoclimate archives. Climate of the Past 5, 441-445.

Leopold, L. B. and Bull, W. B., 1978. Base Level, Aggradation, and Grade. Proceedings of the American Philosophical Society 123 (3), 168-202.

Lézine, A.-M., Hély, C., Grenier, C., Braconnot, P., Krinner, G., 2011. Sahara and Sahel Vulnerability to Climate Changes, Lessons from Holocene Hydrological Data. Quaternary Science Reviews 30 (21-22), 3001-3012, doi:10.1016/j.quascirev.2011.07.006

Lézine, A.-M., Cazet, J.-P., 2005. High-resolution pollen record from core KW31, Gulf of Guinea, documents the history of the lowland forests of West Equatorial Africa since 40'000 yr ago. Quaternary Research 64, 432-443.

Lézine, A.-M., Duplessy, J.-C., Cazet, J.-P., 2005. West African monsoon variability during the last deglaciation and the Holocene: Evidence from fresh water algae, pollen and isotope data from core KW31, Gulf of Guinea. Palaeogeography, Palaeoclimatology, Palaeoecology 219, 225-237.

Lézine, A.-M., 1989. Late Quaternary Vegetation and Climate of the Sahel. Quaternary Research 32, 317-334.

L'Hôte, Y., 2000. Climatologie, in: Seignobos, C., Iyébi-Mandjek, O. (Eds.), Atlas de la Province Extrême-Nord Cameroun. Editions de l'IRD, République du Cameroun MINREST, Paris.

L'Hôte, Y., 1998. Climatologie et Agroclimatologie de la Province Extrême-North in: Seignobos, C., Iyébi-Mandjek, O. (Eds.), Atlas de la Province Extrême-Nord Cameroun. Editions de l'IRD, République

du Cameroun MINREST, Paris, France.

Likens, G.E., Driscoll, C.T., Buso, D.C., Siccama, T.G., Johnson, C.E., Lovetti, G.M., Fahey, T.J., Reiners, W.A., Ryan, D.F., Martin, C.W., Bailey, S.W., 1998. The biochemistry of calcium at Hubbard Brook. Biogeochemistry 41, 89-173.

Lin, H., 2010. Earth's Critical Zone and hydropedology: concepts, characteristics, and advances. Hydrology and Earth System Sciences 14, 25-45.

Loisy, C., Verrecchia, E., Dufour, P., 1999. Microbial origin for pedogenic micrite associated with a carbonate paleosol (Champagne, France). Sedimentary Geology 126, 193-204.

Louis, P., 1970. Contribution géophysique à la connaissance géologique du bassin du lac Tchad, Mémoires ORSTOM, Paris, p. 312.

Machel, H.-G., 2000. Application of cathodoluminescence to carbonate diagenesis, in: Pagel, M., Barbin, V., Blanc, P., Ohnenstetter, D. (Eds.), Cathodoluminescence in Geosciences. Springer, Berlin, Germany, pp. 271-301.

Machel, H.-G., 1985. Cathodoluminescence in calcite and dolomite and its chemical interpretation. Geoscience Canada 12, 139-147.

Mahop, F., Van Ranst, E., Boukar, S., 1995. Influence de l'aménagement des sols sur l'efficacité des pluies au Nord-Cameroun. Etude et Gestion des Sols 2, 105-117.

Maley, J., 2010. Climate and Palaeoenvironment Evolution in North Tropical Africa from the End of the Tertiary to the Upper Quaternary. Palaeoecology of Africa 30, 227-278.

Maley, J., 2004. Le Bassin du Tchad au Quaternaire Récent: Formations Sédimentaires, Paléoenvironnements et Préhistoire. La Question des Paléotchads. In: A.-M. Sémah and J. Renault-Miskovsky, Guide de la Préhistoire mondiale. Artcom,Äô ,Äì Errance, Paris, France, 179-217.

Maley, J., 2000. Last Glacial Maximum lacustrine and fluviatile Formations in the Tibesti and other Saharan mountains, and large-scale climatic teleconnections linked to the activity of the Subtropical Jet Stream. Global and Planetary Change 26, 121-136.

Maley, J., 1983. Histoire de la Végétation et du Climat de l'Afrique Nord-Tropicale au Quaternaire Récent. Bothalia 14 (3-4), 377-389.

Maley, J., 1981. Etudes palynologiques dans le bassin du Tchad et paléoclimatologie de l'Afrique nord-tropicale de 30 000 ans à l'époque actuelle. Thèse université des Sciences et Techniques du Languedoc à Montpellier et Document de l'ORSTOM, Bondy, France, p. 614.

Maley, J., 1980. Etudes Paylnologiques dans le Bassin du Tchad et Paléoclimatologie de l'Afrique Nord-Tropicale de 30000 ans à l'Epoque Actuelle. Palaeoecology of Africa 13, 45-52.

Manning, K., Pelling, R., Higham, T., Schwenniger, J.-L., Fuller, D.Q., 2011. 4500-year old domesticated pearl millet (Pennisetum glaucum) from the Tilemsi Valley, Mali: new insights into an alternative cereal domestication pathway. Journal of Archaeological Science 38, 312-322.

Marliac, A., 1973. Prospection archéologique au Cameroun. Cah. ORSTOM, série sciences humaines X, 47-114.

Marret, F., Maley, J., Scourse, J., 2006. Climatic instability in west equatorial Africa during the Mid- and Late Holocene. Quaternary International 150, 71-81.

Martin, D., 1961. Carte Pédologique du Nord-Cameroun au 1/100.00^{e} feuille de Mora. ORSTOM-IRCAM, Yaoundé, Cameroun.

Martin, G., Guggiari, M., Bravo, D., Zopfi, J., Cailleau, G., Aragno, M., Job, D., Verrecchia, E., Junier, P., 2012. Fungi, bacteria and soil pH: the oxalate-carbonate pathway as a model for metabolic interaction. Environmental microbiology 14, 2960-2970.

Mauz, B., Felix-Henningsen, P., 2005. Palaeosols in Saharan and Sahelian dunes of Chad: Archives of Holocene North African climate changes. The Holocene 15, 453-458.

Mayewski, P.A., Rohling, E.E., Curt Stager, J., Karlén, W., Maasch, K.A., David Meeker, L., Meyerson, E.A., Gasse, F., van Kreveld, S., Holmgren, K., Lee-Thorp, J., Rosqvist, G., Rack, F., Staubwasser, M., Schneider, R.R., Steig, E.J., 2004. Holocene climate variability. Quaternary Research 62 (3), 243-255, doi:10.1016/j.yqres.2004.07.001

Mayya, Y.S., Morthekai, P., Murari, M.K., Singhvi, A.K., 2006. Towards quantifying beta microdosimetric effects in single-grain quartz dose distribution. Radiation Measurements 41, 1032-1039.

McGarry, D., 1996. The Structure and Grain-size Distribution of Vertisols, in: Ahmad, N., Mermut, A.R. (Eds.), Vertisols and Technologies for their Management. Elservier Science, Amsterdam, The Netherlands, pp. 231-259.

Mc Tainsh, G., 1984. The nature and origin of the aeolian mantles of central northern Nigeria. Geoderma 33, 13-37.

Meilhac, A., Tardy, Y., 1970. Genèse et évolution des sericites, vermiculites et montmorillonites au cours de l'altération des plagioclases un pays tempéré. Bulletin du service de la carte géologique d'Alsace et de Lorraine 23, 145-161.

Mermut, A. R., Padmanabham, E., Eswaran, H., Dasog, G. S., 1996. Pedogenesis. In: A. N. and A. R. Mermut, Vertisols and Technologies for Their Management. Elsevier Science B. V., Amsterdam, The Netherlands, 43-58.

Miller, W. L. and Bragg, A. L., 2007. Soil Characterization and Hydrological Monitoring Project, Brazoria County, Texas, Bottomland Hardwood Vertisols. The United States Department of Agriculture (USDA), Washington, D. C., USA, pp 333.

Moore D. M. and Reynolds, R.C., 1997. X-Ray Diffraction and the Identification and Analysis of Clay Minerals. Oxford University Press, New York, USA.

Moore, J.M., Picker, M.D., 1991. Heuweltjies (Earth Mounds) in the Clanwilliam District, Cape Province, South Africa: 4000-Year-Old Termite Nests. Oecologia 86, 424-432.

Morin, S., 2000. Géomorphologie, in: Seignobos, C., Iyébi-Mandjek, O. (Eds.), Atlas de la Province Extrême-Nord Cameroun. Editions de l'IRD, République du Cameroun MINREST, Paris.

Mpeck, E., 1994. Contribution des Poussières Sahariennes à la Sédimentation du Pléistocène Supérieur au Nord Cameroun: La Formation de Doyang. Thèse de Doctorat, Terre, Océan et Espace, Université Paris 6, Paris, France, pp 303.

Mücher, H., Van Steijn, H., Kwaad, F., 2010. Colluvial and Mass Wasting Deposits. In: Stoops, G., Marcelino, V., Mees, F. (Editors), Interpretation of Micromorphological Features of Soils and Regoliths. Elsevier Science, Amsterdam, The Netherlands, 37-48.

Murray, A.S., Wintle, A.G., 2003. The Single Aliquot Regenerative Dose Protocol: Potential for Improvements in Reliability. Radiation Measurements 37, 377-381.

Nakata, P.A., 2003. Advances in our understanding of calcium oxalate crystal formation and function in plants. Plant Science 164, 901-909.

Ndougsa-Mbarga, T., Manguelle-Dicoum, E., Campos-Enriquez, J.-O., Yene Atangana, Q., 2007. Gravity anomalies, sub-surface structure and oil and gas migration in the Mamfe, Cameroon-Nigeria, sedimentary basin. Geofísica internacional 46, 129-139.

Neudorf, C.M., Roberts, R.G., Jacobs, Z., 2012. Sources of overdispersion in a K-rich feldspar sample from north-central India: Insights from De, K content and IRSL age distributions for individual grains. Radiation Measurements 47, 696-702.

Nicholson, S.E., 2009. A Revised Picture of the Structure of the "Monsoon" and Land ITCZ over West Africa. Climate Dynamics 32, 1155-1171.

Ngomanda, A., Neumann, K., Schweizer, A., Maley, J., 2009. Seasonality change and the third millennium BP rainforest crisis in southern Cameroon (Central Africa). Quaternary Research 71, 307-318.

Nordt, L., Driese, S., 2010. New weathering index improves paleorainfall estimates from Vertisols. Geology 38, 407-410.

North Greenland Ice Core Project members, 2004. High-resolution record of Northern Hemisphere climate extending into the last interglacial period. Nature 2805, 1-5.

Oakes, H. and J. Thorp, 1950. Dark Clay Soils of Warm Regions of Variously Called Rendzina Black Cotton Soils, Regurs and Tirs. Soil Science Society of America, Proceedings 15, 347-354.

Olivry, J.-C., Naah, E., 2000. Hydrologie, in: Seignobos, C., Iyébi-Mandjek, O. (Eds.), Atlas de la Province Extrême-Nord Cameroun. Editions de l'IRD, République du Cameroun MINREST, Paris.

Olivry, J.-C., Chouret, A., Vuillaume, G., Lemoalle, J., Bricquet, J.-P., 1996. Hydrologie du Lac Tchad. ORSTOM, Paris, France, 301 pp.

Olley, J.M., Roberts, R.G., Yoshida, H., Bowler, J.M., 2006. Single-grain optical dating of grave-infill associated with human burials at Lake Mungo, Australia. Quaternary Science Reviews 25, 2469-2474.

Olley, J.M., Murray, A., Roberts, R.G., 1996. The Effects of Disequilibria in the Uranium and Thorium Decay Chains on Burial Dose Rates in Fluvial Sediments. Quaternary Science Reviews 15, 751-760.

Osmond, J. K., Cowart, J. B., Ivanovich, M., 1983. Uranium Isotopic Disequilibrium in Ground Water as an Indicator of Anomalies. The International Journal of Applied Radiation and Isotopes 34 (1), 283-308.

Pastouret, L., Chamley, H., Delibrias, G., Duplessy, J.-C., Thiede, J., 1978. Late Quaternary climatic changes in Western Tropical Africa deduced from deep-sea sedimentation off the Niger delta. Oceanologica Acta 1, 217-232.

Peel, M.C., Finlayson, B.L., McMahon, T.A., 2007. Updated world map of the Köppen-Geiger climate

classification. Hygrology and Earth System Sciences 11, 1633-1644.

Pias, J., 1968. Contribution à l'étude des formations sédimentaires tertiaires et quaternaires de la cuvette tchadienne et des sols qui en dérivent. Cah. ORSTOM VI, 367-377.

Pias, J. 1962. Les Sols du Moyen et Bas Logone, du Bas Chari, des Régions Riveraines du Lac Tchad et du Bahr El Ghazal. Mémoires ORSTOM, Paris, France, 434 pp.

Prescott, J. A., 1931. The soils of Australia in relation to climate. The Commonwealth Scientific and Industrial Research Organisation (CSIRO) Australia Bull., 52, 65-67.

Prescott, J.R., Hutton, J.T., 1994. Cosmic Ray Contributions to Dose Rates for Luminescence and ESR Dating: Large Depths and Long-term Time Variations. Radiation Measurements 23, 497-500.

Pye, K., Tsoar, H., 1987. The mechanics and geological implications of dust transport and deposition in deserts with particular reference to loess formation and dune sand diagenesis in the northern Negev, Israel, in: Frostick, L., Reid, I. (Eds.), Desert Sediments: Ancient and Modern. Geological Society Special Publication, 139-156.

Quade, J., Garzione, C., Eiler, J., 2007. Paleoelevation Reconstruction using Pedogenic Carbonates. Reviews in Mineralogy and Geochemistry 66, 53-87.

Quade, J., Cerling, T.E., Bowman, J.R., 1989. Systematic Variations in the Carbon and Oxygen Isotopic Composition of Pedogenic Carbonate along Elevation Transects in the Southern Great Basin, United States. Geological Society of America Bulletin 101, 464-475.

Raiswell, R., Fischer, Q.J., 2000. Mudrock-hosted carbonate concretions: a review of growth mechanisms and their influence on chemical and isotopic composition. Journal of Geological Society, London 157, 239-251.

Rajot, J.-L. and Sebag, D., 2011. Fieldwork and sampling in Burkina Faso, Niger and Cameroon. Unpublished work.

Ramsey, C.B., 2009. Bayesian analysis of radiocarbon dates. Radiocarbon 51, 337-360.

Reimann, T., Notenboom, P.D., De Schipper, M.A., Wallinga, J., 2015. Testing for Sufficient Signal Resetting During Sediment Transport using a Polymineral Multiple-Signal Luminescence Approach. Quaternary Geochronology 25, 26-36.

Reimer, P.J., Bard, E., Bayliss, A., Beck, J.W., Blackwell, P.G., Ramsey, C.B., Buck, C.E., Cheng, H., Edwards, R.L., Friedrich, M., Grootes, P.M., Guilderson, T.P., Haflidason, H., Hajdas, I., Hatté, C., Heaton, T.J., Hoffmann, D.L., Hogg, A.G., Hughen, K.A., Kaiser, K.F., Kromer, B., Manning, S.W., Niu, M., Reimer, R.W., Richards, D.A., Scott, E.M., Southon, J.R., Staff, R.A., Turney, C.S.M., Van der Plicht, J., 2013. IntCal13 and Marine13 Radiocarbon age calibration curves 0-50,000 Years CAL BP. Radiocarbon 55, 1869-1887.

Retallack, G.J., 2005. Pedogenic Carbonate Proxies for Amount and Seasonality of Precipitation in Paleosols. Geology 33, 333-336.

Retallack, G.J., 2001. Soils of the Past. An Introduction to Paleopedology. Blackwell Science Ltd, Oxford, United Kingdom.

Riotte, J., Chabaux, F., 1999. ($^{234}U/^{238}U$) Activity Ratios in Freshwaters as Tracers of Hydrological Processes: The Strengbach Watershed (Vosges, France). Geochimica et Cosmochimica Acta 63, 1263-

1275.

Risi, C., Bony, S., Vimeux, F., Descroix, L., Ibrahim, B., Lebreton, E., Mamasou, I., Sultan, B., 2008. What controls the isotopic composition of the African monsoon precipitation? Insights from event-based precipitation collected during the 2006 AMMA field campaign. Geophysical Research Letters 35, 1-6.

Roberts, H.M., 2012. Testing Post-IR IRSL protocols for minimising fading in feldspars, using Alaskan loess with independent chronological control. Radiation Measurements 47, 716-724.

Rohling, E.E., Pälike, H., 2005. Centennial-scale climate cooling with a sudden cold event around 8,200 years ago. Nature 434, 975-979.

Rotaru, M., Gaillardet, J., Steinberg, M., Trichet, J., 2006. Les climats passés de la terre. Vuibert, Paris, France.

Salzmann, U., Hoelzmann, P., Morczinek, I., 2002. Late Quaternary Climate and Vegetation of the Sudanian Zone of Northeast Nigeria. Quaternary Research 58, 73-83.

Sangen, M., Neumann, K., Eisenberg, J., 2011. Climate-induced fluvial dynamics in tropical Africa around the last glacial maximum. Quaternary Research 76, 417-429.

Schaetzl, R.J., Thompson, M.L., 2015. Soils. Genesis and Geomorphology. Cambridge University Press, New York, USA.

Schuster, M., Roquin, C., Duringer, P., Brunet, M., Caugy, M., Fontugne, M., Taïsso Mackaye, H., Vignaud, P., Ghienne, J.-F., 2005. Holocene Lake Mega-Chad palaeoshorelines from space. Quaternary Science Reviews 24, 1821-1827.

Schwertmann, U., 1988. Occurence and Formation of Iron Oxides in Various Pedoenvironments, in: Stucki, J.W., Goodman, B.A., Schwertmann, U. (Eds.), Iron in Soils and Clay Minerals. D. Reidel Publishing Company, Dordrecht, The Netherland.

Shaub, B.M., 1937. The origin of cone-in-cone and its bearing on the origin of concretions and septaria. American Journal of Science 34, 331-344.

Seignobos, C., Tourneux, H., 2002. Le Nord-Cameroun à travers ses mots. Dictionnaire de termes anciens et modernes. IRD Editions et Karthala, France.

Sepulchre, P., Schuster, M., Ramstein, G., Krinnezr, G., Girard, J.-F., Vignaud, P., Brunet, M., 2008. Evolution of Lake Chad Basin hydrology during the mid-Holocene: A premilinary approach from lake to climate modelling. Global and Planetary Change 61, 41-48.

Servant, M., 1973. Séquences Continentales et Variations Climatiques: Evolution du Bassin du Tchad au Cenozoïque supérieur, Thèse, Paris IV, 567, Documents de l'ORSTOM, Paris, France, pp. 1-567.

Servant-Vildary, S., 1978. Etude des diatomées et paléolimnologie du bassin tchadien au Cénozoique supérieur - Tome 1, ORSTOM. Université de Paris VI, Paris, p. 321.

Servant-Vildary, S., 1973. Le Plio-Quaternaire ancien du Tchad: évolution des associations de diatomées, stratigraphie, paléoécologie. Cah. ORSTOM V, 169-216.

Servant, M., Servant-Vildary, S., 1970. Les formations lacustres et les diatomées du quaternaire récent du fond de la cuvette tchadienne. Revue de Géologie Dynamique et de Géographie Physique XII, 63-76.

Shanahan, T.M., McKay, N.P., Hugen, K.A., Overpeck, J.T., Otto-Bliesner, B., Heil, C.W., King, J., Scholz, C.A., Peck, J., 2015. The Time-Transgressive Termination of the African Humid Period. Nature Geoscience 8, 140-144.

Shaub, B.M., 1937. The origin of cone-in-cone and its bearing on the origin of concretions and septaria. American Journal of Science 34, 331-344.

Short, S. A., Lowson, R. T., Ems, J., Price D. M., 1989. Thorium-uranium Disequilibrium Dating of Late Quaternary Ferruginous Concretions and Rinds. Geochimica and Cosmochimica Acta 53 (6), 1379-1389.

Sieffermann, G., 1967. Variations climatiques au Quaternaire dans le Sud-Ouest de la cuvette tchadienne, C. R. 92e Congr. Nat. Soc. Sav., Strasbourg, Colmar, France, pp. 485-494.

Sieffermann, G., 1963. Carte Pédologique du Nord-Cameroun au $1/100.000^{e}$, feuille de Kalfou. ORSTOM-IRCAM, Yaoundé, Cameroun.

Silva, L.C.R., Vale, G.D., Haidar, R.F., da S. L. Sternberg, L., 2010. Deciphering Earth Mound Origins in Central Brazil. Plant and Soil 336, 3-14.

Singhvi, A.K., Banerjee, D., Ramesh, R., Rajaguru, S.N., Gogte, V., 1996. A Luminescence Method for Dating 'Dirty' Pedogenic Carbonates for Paleoenvironmental Reconstruction. Earth and Planetary Science Letters 139, 321-332.

Smedley, R.K., Duller, G.A.T., Roberts, H.M., 2015. Bleaching of the Post-IR IRSL Signal from Individual Grains of K-Feldspar: Implications for Single-grain Dating. Radiation Measurements 79, 33-42.

Snelder, D.J., Bryan, R.B., 1995. The use of rainfall simulation tests to assess the influence of vegetation density on soil loss on degraded rangelands in the Baringo District, Kenya. Catena 25, 105-116.

Spötl, C., Vennemann, T.W., 2003. Continuous-flow isotope ratio mass spectrometric analysis of carbonate minerals. Rapid communications in mass spectrometry : RCM 17, 1004-1006.

Southard, R.J., Driese, S.G., Nordt, L.C., 2011. Vertisols. In : Handbook of Soil Sciences Properties and Processes. P. M. Huang, Y. Li and M. E. Sumner. USA, CRC Press Taylor and Francis Group, 33-82.

Sposito, G., 1994. Chemical equilibria and kinetics in soils. Oxford University Press, USA.

Stokes, S., Ingram, S., Aitken, M.J., Sirocko, F., Anderson, R., Leuschner, D., 2003. Alternative Chronologies for Late Quaternary (Last Interglacial-Holocene) Deep Sea Sediments via Optical Dating of silt-sized Quartz. Quaternary Science Reviews 22, 925-941.

Stoops, G., 2003. Guidelines for Analysis and Description of Soil and Regolith Thin Sections. Soil Science Society of America, Wisconsin, USA, 184 pp.

Stoops, G. and Jongerius, A., 1975. Proposal for a Micromorphological Classification of Soil Materials. I. A Classification of the Related Distribution of Coarse and Fine Particles. A reply. Geoderma 19, 247-249.

Stuvier, M., Polach, H.A., 1977. Discussion of ^{14}C Data. Radiocarbon 19, 355-363.

Swartzlow, C.R., 1934. Two dimensional dendrites and their origin. American Mineralogist 19, 403-411.

Swezey, C., 2001. Eolian Sediment Responses to Late Quaternary Climate Changes: Temporal and

Spatial Patterns in the Sahara. Palaeogeography, Palaeoclimatology, Palaeoecology 167, 119-155.

Tanner, L.H., 2010. Continental Carbonates as Indicators of Paleoclimate, in: Alonso-Zarza, A.M., Tanner, L.H. (Eds.), Carbonates in Continental Settings: Geochemistry, Diagenesis and Applications. Elsevier, Oxford, UK, pp. 179-206.

Tardy, Y., Bocquier, G., Paquet, H., Millot, G., 1973. Formation of clay from granite and its distribution in relation to climate and topography. Geoderma 10, 271-284.

Taupin, J.-D., 2003. Interprétation paléoclimatique et paléohydrologique de l'origine des nodules carbonatés des terrasses du Niger aux environs de Niamey (Niger) au moyen des outils isotopiques et géochimiques. Hydrological Sciences Journal 48, 473-487.

Thiel, C., Buylaert, J.-P., Murray, A., Terhorst, B., Hofer, I., Tsukamoto, S., Frechen, M., 2011. Luminescence Dating of the Stratzing Lœss Profile (Austria) - Testing the Potential of an Elevated Temperature post-IR IRSL Protocol. Quaternary International 234, 23-31.

Thomsen, K.J., Murray, A.S., Jain, M., Bøtter-Jensen, L., 2008. Laboratory Fading Rates of Various Luminescence Signals from Feldspar-rich Sediment Extracts. Radiation Measurements 43, 1474-1486.

Thornthwaite, C.W., 1948. An approach toward a rational classification of climate. Geographical Reviews 38, 55-94.

Tierney, E.J., Pausata, F.S.R., deMenocal, P.B., 2017. Rainfall regimes of the Green Sahara. Science Advances 3, 1-9.

Trauerstein, M., Lowick, S.E., Preusser, F., Schlunegger, F., 2014. Small Aliquot and Single Grain IRSL and post-IR IRSL Dating of Fluvial and Alluvial Sediments from the Pativilca Valley, Peru. Quaternary Geochronology 22, 163-174.

Turc, L., 1954. Le bilan d,Äôeau des sols. Relation entre la précipitation, l'évaporation et l'écoulement. Ann. Agron. 5, 491,Äì569.

UNEP (United Nations Environment Programme), 1997. World atlas of desertification 2ED. Eds: Middelton, N. and Thomas, D., UNEP, London.

Urey, H.C., 1952. The planets : their origin and development. Oxford University Press.

Vandenberghe, J., 2013. Grain-size of Fine-Grained Windblown Sediment: A Powerful Proxy for Process Identification. Earth-Science Reviews 121, 18-30, http://dx.doi.org/10.1016/j.earscirev.2013.03.001.

Velde, B., Meunier, A., 2008. The Origin of Clay Minerals in Soils and Weathered Rocks. Springer, Berlin, Germany.

Vepraskas, M.J., Polizzotto, M., Faulkner, S.P., 2016. Redox chemistry of hydric soils, in: Vepraskas, M.J., Craft, C.B. (Eds.), Wetland Soils: Genesis, Hydrology, Landscapes, and Classification. CRC Press, Boca Raton, London, New York.

Verrecchia, E.P., 2007. Lacustrine and palustrine geochemical sediments. Geochemical Sediments and Landscapes. Blackwell Publishing, Oxford, 298-329.

Verrecchia, E.P., Braissant, O., Cailleau, G., 2006. The oxalate-carbonate pathway in soil carbon storage: the role of fungi and oxalotrophic bacteria, in: Gadd, G.M. (Ed.), Fungi in Biogeochemical Cycles.

Cambrige University Press, Cambridge, New York, Melbourne, Madrid, Cape Town, Singapore, Sao Paulo, pp. 289-310.

Verrecchia, E.P., Dumont, J.-L., Verrecchia, K.E., 1993. Role of calcium oxalate biomineralization by fungi in the formation of calcretes: a case study from Nazareth, Israel. Journal of Sedimentary Petrology 63, 1000-1006.

Vigier, N., Bourdon, B., Turner, S.P., Allègre, C.J., 2001. Erosion Timescales Derived from U-decay Series Measurements in Rivers. Earth and Planetary Science Letters 193, 549-563.

Violette, A., Riotte, J., Braun, J.-J., Oliva, P., Marechal, J.-C., Sekhar, M., Jeandel, C., Subramanian, S., Prunier, J., Barbiero, L., Dupre, B., 2010. Formation and Preservation of Pedogenic Carbonates in South India, links with Paleo-monsoon and Pedological Conditions: Clues from Sr isotopes, U-Th series and REEs. Geochimica et Cosmochimica Acta 74, 7059-7085.

Volk, G., Lynch-Holm, V., Kostman, T., Goss, L., Franceschi, V., 2002. The role of druse and raphide calcium oxalate crystals in tissue calcium regulation in Pistia stratiotes leaves. Plant biology 4, 34-45.

Wallinga, J., Bos, A.J.J., Dorenbos, P., Murray, A.S., Schokker, J., 2007. A test case for anomalous fading correction in IRSL dating. Quaternary Geochronology 2, 216-221.

Walkington, H., 2010. Soil science applications in archaeological contexts: a review of key challenges. Earth-Science Reviews 103, 122-134.

Wanas, H.A., Soliman, H.E., 2014. Calcretes and palustrine carbonates in the Oligo-Miocene clastic-carbonate unit of the Farafra Oasis, Western Desert, Egypt: Their origin and paleoenvironmental significance. Journal of African Earth Sciences 95, 145-154.

Wanner, H., Beer, J., Bütikofer, J., Crowley, T.J., Cubasch, U., Flückiger, J., Goosse, H., Grosjean, M., Joos, F., Kaplan, J.O., Küttel, M., Müller, S.A., Prentice, I.C., Solomina, O., Stocker, T.F., Tarasov, P., Wagner, M., Widmann, M., 2008. Mid- to Late Holocene Climate Change: an Overview. Quaternary Science Reviews 27 (19-20), 1791-1828, doi:10.1016/j.quascirev.2008.06.013.

Weldeab, S., Lea, D.W., Schneider, R.R., Andersen, N., 2007. Centennial scale climate instabilities in a wet early Holocene West African monsoon. Geophysical Research Letters 34, 1-6.

West, L.T., Drees, L.R., Wilding, L.P., Rabenhorst, M.C., 1988. Differentiation of pedogenic and lithogenic carbonate forms in Texas. Geoderma 43, 271-287.

Wieder, M., Yaalon, D.H., 1974. Effect of Matric Composition on Carbonate Nodule Crystallisation. Geoderma 11, 95-121.

Wilding, L. P. and Tessier, D., 1988. Genesis of Vertisols : Shrink-swell phenomena. In: L. P. Wilding and R. Puentes (Editors), Vertisols : Their distribution, properties, classification and management. SMSS-Texas AandM University, 55-82.

Wilding, L.P., Williams, D., Miller, W., Cook, T., Eswaran, H., 1990. Close Interval Spatial Variability of Vertisols : A Case Study in Texas. In: J. M. Kimble (Editor), Proc. Sixth Int. Soil Correlation Meeting (ISCOM). Characterization, Classification and Utilization of Cold Aridisols and Vertisols. USDA, Soil Conservation Service, National Soil Survey Center, Lincoln, USA, 232-247.

Wilding, L.P., 2004. Advancement in the Knowledge Base of Vertisols Genesis, Classification, Distribu-

tion and Management. Revista Cientìfica Agropecuaria, 8(1), 45-54.

Williams, G.E., Polach, H.A., 1971. Radiocarbon Dating of Arid-Zone Calcareous Paleosols. Geological Society of America Bulletin 82, 3069-3086.

Willmott, C.J., Rowe, C.M., 1985. Climatology of the terrestrial seasonal water cycle. Journal of Climatology 5, 589-606.

Wright, V.P., Peeters, C., 1989. Origins of some Early Carboniferous calcrete fabrics revealed by cathodoluminescence: implications for interpreting the sites of calcrete formation. Sedimentary Geology 65, 345-353.

Yang, S., Ding, Z., Gu, Z., 2014. Acetic Acid-leachable Elements in Pedogenic Carbonate Nodules and links to the East-Asian Summer Monsoon. Catena 117, 73-80.

Yule, D. F. and Ritchie, J. T., 1980. Soil Shrinkage Relationships of Texas Vertisols, I : Small Cores. Soil Science Society of America Journal, 44, 1285-1291.

Zamanian, K., Pustovoytov, K., Kuzyakov, Y., 2016. Pedogenic Carbonates: Forms and Formation Processes. Earth-Science Reviews 157, 1-17.

Zander, A., Hilgers, A., 2013. Potential and Limits of OSL, TT-OSL, IRSL and $pIRIR_{290}$ Dating Methods Applied on a Middle Pleistocene Sediment Record of Lake El'gygytgyn, Russia. Climate of the Past 9, 719-733.

Zhou, J., Chafetz, H.S., 2009. The genesis of late Quaternary caliche nodules in Mission Bay Texas: stable isotopic compositions and palaeoenvironmental interpretation. Sedimentology 56, 1392-1410.

Zimmerman, K.A., 1971. Thermoluminescent Dating using Fine Grains from Pottery. Archaeometry 13, 29-52.